NORTHWESTERN UNIVERSITY

Pattern Formation in the Weakly Nonlinear and Singularly Perturbed Regimes of the Brusselator Model

A DISSERTATION

SUBMITTED TO THE GRADUATE SCHOOL

IN PARTIAL FULFILLMENT OF THE REQUIREMENTS

for the degree

DOCTOR OF PHILOSOPHY

Field of Applied Mathematics

By

Justin Cheng Tzou

EVANSTON, ILLINOIS

December 2012

Abstract

Pattern Formation in the Weakly Nonlinear and Singularly Perturbed Regimes of the Brusselator Model

Justin Cheng Tzou

This thesis is in two parts. The first part is an analytical and numerical study of patterns near a codimension two Turing Hopf point of the one dimensional Brusselator model. For the superdiffusive variant, we derive amplitude equations describing slow time evolution of the Turing and Hopf modes. The main qualitative differences from the regular diffusion analog are the presence of a second long spatial scale owing to non-quadratic behavior near the minimum of the Hopf stability curve, and that the evolution of the Hopf mode is governed by an integro-differential equation. In a numerical study farther in the nonlinear regime, we use a modified Fourier spectral method to compute spatiotemporal patterns and compare to those found in the regular diffusion model. In both cases, we find a large number of solutions characterized by the coexistence of stationary stripes and low wavenumber temporally oscillating "cells," the shapes of which depend on superdiffusion exponents. For the regular diffusion model, we employ the AUTO package to continue such Turing-Hopf solutions in parameter space. We

find that the solutions are organized on snaking branches characterized by a series of saddle-node bifurcations, analogous to those found for stationary pinning solutions. Observations in wavelength variation, location of snaking region, and direction of front depinning, are explained in terms of the amplitude equations. In the second part of this thesis, we study pulse patterns in a singularly perturbed regime of the regular diffusion model with prescribed boundary feed. We find that the boundary feed breaks the symmetric spacing of equilibrium pulse patterns. A differential-algebraic system of equations (DAE) is derived, governing asymptotically slow translations of quasi-equilibrium pulse patterns. Criteria for slow translational instabilities are determined from a stability analysis of the DAE. Fast amplitude instabilities, characterized by pulse collapse events or synchronous and asynchronous oscillations, are studied by analyzing a nonlocal eigenvalue problem. These results are related back to the slow translations, whereby it is found that the latter may dynamically trigger fast instabilities in an initially stable pulse pattern.

Acknowledgements

I would like to thank my committee members, Professors Alvin Bayliss, Bernard Matkowsky, and Vladimir Volpert, for accepting me as a student and devoting the time and energy that they did to my development. I sincerely appreciate the patience and wisdom with which they guided me. I tell everybody I know that Prof. Volpert offers the clearest explanations of anyone that I have ever encountered. He was a great adviser to me and I consider myself extremely fortunate to have had this experience with him. I do regret not having the opportunity to better know Professor Sasha Golovin as a person, and to learn from him as a researcher. To that end, I would like to especially thank Prof. Bayliss for so kindly agreeing to be one of my advisers; he gave me more of his time than I could have ever hoped. I also would like to thank my main adviser Prof. Matkowsky for providing me financial support over the years, and for overseeing the general direction of this thesis. More importantly though, I want to thank him and his wonderful wife Fraydie for inviting me into their home for the annual barbecue. The food was always incredible, and the company even more so. I also cannot thank Beth, Danielle, Edla, and Molly enough for the work that they do for the department, and for the clarity that they gave to issues that often confounded me. Finally, the longer and more difficult the road, the more you appreciate the people that travelled it with you, and I *really* appreciate the friends that I made these past five years. The students here are outstanding people, and when I leave here, it is my times with them and the friends that I made that will shape my memories of this department. They are the ones that made this worth all the while.

Outside the department, I want to thank Dr. Yi-Ping Ma and Professor Michael Ward for their collaboration on parts of this thesis. Since my times as an undergraduate, Prof. Ward has gone out of his way at almost every turn to give me whatever support that I needed, and for that I am truly grateful. I would like to thank my parents. Being the good Democrat (or Canadian equivalent) that I am, I understand the important roles that parenting and socioeconomic standing have in determining outcomes, and I cannot deny the fact that I would have no chance of being here without opportunities that I did nothing to deserve. Lastly, this thesis is dedicated to the loving memory of my grandfather.

Contents

List of Figures

CHAPTER 1

Interaction of Turing and Hopf Modes in the Superdiffusive Model Near a Codimension Two Bifurcation Point

In this chapter, spatiotemporal patterns near a codimension-2 Turing-Hopf point of the one dimensional superdiffusive Brusselator model are analyzed. The superdiffusive Brusselator model differs from its regular counterpart in that the Laplacian operator of the regular model is replaced by $\partial^\alpha/\partial\left|\xi\right|^\alpha$, $1<\alpha<2$, an integro-differential operator that reflects the nonlocal behavior of superdiffusion. The order of the operator, α, is a measure of the rate of superdiffusion, which, in general, can be different for each of the two components. A weakly nonlinear analysis is used to derive two coupled amplitude equations describing the slow time evolution of the Turing and Hopf modes. We seek special solutions of the amplitude equations, namely a pure Turing solution, a pure Hopf solution, and a mixed mode solution, and analyze their stability to long-wave perturbations. We find that the stability criteria of all three solutions depend greatly on the rates of superdiffusion of the two components. In addition, the stability properties of the solutions to the anomalous diffusion model are different from those of the regular diffusion model. Numerical computations in a large spatial domain, using Fourier spectral methods in space and second order predictor-corrector method in time are used to confirm the analysis and also to find solutions not predicted by the weakly nonlinear analysis, in the fully nonlinear regime. Specifically, we find a large number of steady state patterns consisting of a localized region or regions of stationary stripes in a background of time periodic cellular motion, as well

as patterns with a localized region or regions of time periodic cells in a background of stationary stripes. Each such pattern lies on a branch of such solutions, is stable and corresponds to a different initial condition. The patterns correspond to the phenomenon of pinning of the front between the stripes and the time periodic cellular motion. While in some cases it is difficult to isolate the effect of the diffusion exponents, we find characteristics in the spatiotemporal patterns for anomalous diffusion that we have not found for regular (Fickian) diffusion.

1.1. Introduction

Studies of anomalous diffusion have recently been appearing in the literature as more processes have been observed to exhibit behavior that cannot be described by regular (Fickian) diffusion. These processes can often be described by models with subdiffusion or superdiffusion, where, under a random walk description, the mean square displacement of a particle scales as $\langle x^2(t)\rangle \sim t^\gamma$, with $0 < \gamma < 1$ for subdiffusion, and $1 < \gamma < 2$ for superdiffusion, rather than linearly in time. Subdiffusion has been observed in many applications, including charge carrier transport in amorphous semiconductors, and nuclear magnetic resonance diffusometry in percolative and porous systems, while superdiffusion has been observed in e.g., transport in heterogeneous rocks, quantum optics, and single molecule spectroscopy [**71**]. We consider an especially interesting case of superdiffusion, Lévy flights, which is characterized by a jump length distribution having infinite moments. On the macroscopic scale, Lévy flights are described by a diffusion equation where the second order spatial derivative is replaced by a fractional derivative $\partial^\alpha/\partial\,|\xi|^\alpha$, $1 < \alpha < 2$, defined as a non-local integro-differential operator [**71**]. The definition of the operator $\partial^\alpha/\partial\,|\xi|^\alpha$, and its action in Fourier space, is given as [**25**]

$$\partial^\alpha/\partial\,|\xi|^\alpha \equiv \frac{-1}{2\cos(\alpha\pi/2)}\left[{}_{-\infty}D_\xi^\alpha + {}_\xi D_\infty^\alpha\right]\,;$$
$${}_{-\infty}D_\xi^\alpha\phi(\xi) \equiv \frac{1}{\Gamma(2-\alpha)}\frac{\partial^2}{\partial\xi^2}\int_{-\infty}^{\xi}\frac{\phi(\eta)}{(\xi-\eta)^{\alpha-1}}d\eta\,,$$
$${}_\xi D_\infty^\alpha\phi(\xi) \equiv \frac{1}{\Gamma(2-\alpha)}\frac{\partial^2}{\partial\xi^2}\int_{\xi}^{\infty}\frac{\phi(\eta)}{(\eta-\xi)^{\alpha-1}}d\eta\,,$$

and

$$\mathscr{F}[\partial^\alpha u(\xi)/\partial\,|\xi|^\alpha](k) = -|k|^\alpha\mathscr{F}[u(\xi)](k)\,, \tag{1.1}$$

where $1 < \alpha < 2$ and $\mathscr{F}[\cdot]$ denotes the Fourier transform. A description of superdiffusion as well as subdiffusion in the context of continuous time random walks with power-law-distributions for jump lengths and waiting times is given in [**54**].

Previous works on reaction-superdiffusion equations have derived and studied amplitude equations near a Hopf [**77**] bifurcation with general reaction dynamics, where it was shown that the Benjamin-Feir stability criterion is unchanged from regular diffusion, while the Eckhaus stability boundary depended on the superdiffusive exponent. For two dimensions, amplitude equations near the Turing bifurcation point of the superdiffusive Brusselator model were derived in [**38**]. It was shown that, contrary to regular diffusion, the homogeneous state could be unstable to a Turing mode even if the activator diffused faster than the inhibitor. Conversely, it was shown in [**75**] that in the case of a general reaction-subdiffusion equation that, in the limit of short wave perturbations, the homogeneous state is always stable when the subdiffusion of the inhibitor is slower than that of the activator. A generalization of this criteria was derived in [**76**] for the case where the diffusion and reaction terms were all subject to different rates of subdiffusion. For a different type of coupling between reaction and subdiffusion terms studied

in [**111**], subdiffusion of the inhibitor was shown to delay the onset of Turing instability, while subdiffusion of the activator was shown to have a destabilizing effect. The incorporation of reaction terms into subdiffusive systems has been the subject of many studies since the findings of [**93**]. Subsequent studies may be found in [**35**, **41**, **64**, **89**] and references therein.

In this chapter, we investigate the effects of superdiffusion on the interactions between Hopf and Turing instabilities of the Brusselator model by deriving amplitude equations and studying instabilities of their solutions to long-wave perturbations, thus leading to the identification of the parameter values at which new solutions may bifurcate. Similar studies near a codimension two Turing-Hopf point (C2THP) of the regular Brusselator model have been done in [**22**], [**112**]. We also discuss the results of numerical computations in both the weakly and fully nonlinear regimes. In this chapter, we consider both the regular and superdiffusive one dimensional Brusselator model and identify characteristics of spatiotemporal patterns obtained near the C2THP that are unique to each. In the anomalous case, we consider cases of equal diffusion exponents, unequal but close diffusion exponents, and where one diffusion is regular while the other is anomalous.

1.2. The model, the basic solution, and its linear stability

We consider the Brusselator model, long a paradigm for nonlinear analysis, given by

$$\frac{\partial f}{\partial \tau} = D_f \frac{\partial^\alpha f}{\partial |\xi|^\alpha} + E - (B+1)f + f^2 g\,, \qquad \tau > 0\,, \qquad \xi \in \mathbb{R}\,, \tag{1.2a}$$

$$\frac{\partial g}{\partial \tau} = D_g \frac{\partial^\beta g}{\partial |\xi|^\beta} + Bf - f^2 g, \qquad \tau > 0\,, \qquad \xi \in \mathbb{R}\,. \tag{1.2b}$$

The diffusion coefficients D_f, D_g, the activator input rate E, and the control parameter B, are positive quantities. The equilibrium (basic) state of this system is $(f, g) = (E, B/E)$ for all values of the parameters.

Rescaling (1.2a) and (1.2b) using $f = E + u_* u$, $g = B/E + v_* v$, $\tau = t$, and $\xi = \ell_* x$, where $u_* = (D_g/D_f^{\beta/\alpha})^{1/2}$, $v_* = 1/u_*$, and $\ell_* = D_f^{1/\alpha}$, the Brusselator system becomes

$$\frac{\partial u}{\partial t} = \frac{\partial^\alpha u}{\partial |x|^\alpha} + (B-1)u + Q^2 v + \frac{B}{Q}u^2 + 2Quv + u^2 v\,, \qquad t > 0\,, \qquad x \in \mathbb{R}\,, \tag{1.3a}$$

$$\eta^2 \frac{\partial v}{\partial t} = \frac{\partial^\beta v}{\partial |x|^\beta} - Bu - Q^2 v - \frac{B}{Q}u^2 - 2Quv - u^2 v\,, \qquad t > 0\,, \qquad x \in \mathbb{R}\,. \tag{1.3b}$$

where $\eta = \sqrt{D_f^{\beta/\alpha}/D_g} > 0$, $Q = E\eta > 0$, and x and t represent the rescaled spatial and temporal variables, respectively. The equilibrium state is now at $u = v = 0$.

To determine the stability of the critical point, we consider the normal mode solution, obtaining the dispersion relation between the growth rate σ and the wave number $k > 0$, $\eta^2\sigma^2 + M_1\sigma + M_2 = 0$, where $M_1 = Q^2 + k^\beta - \eta^2(B - 1 - k^\alpha)$, and $M_2 = BQ^2 + (k^\beta + Q^2)(1 + k^\alpha - B)$.

Hopf bifurcation occurs if $M_1 = 0$ and $M_2 > 0$, which yields two pure imaginary eigenvalues. $M_1 = 0$ corresponds to $B = k^\beta/\eta^2 + k^\alpha + 1 + Q^2/\eta^2$, which has a minimum, $B_{cr}^{(H)} = 1 + Q^2/\eta^2$ at $k = 0$. The basic state is stable (unstable) for $B < B_{cr}^{(H)}$ ($B > B_{cr}^{(H)}$). In the unstable case, a spatially homogeneous oscillatory mode emerges. For $k = 0$ and $B = B_{cr}^{(H)}$, the eigenvalue $\sigma = iQ/\eta \equiv i\omega$, where ω is the frequency of the oscillatory mode, while $\mathbf{c}^\dagger = (1, Q\eta^2/(Q + i\eta))$ and $\mathbf{c} = (1, (i\eta - Q)/(Q\eta^2))^{\mathrm{T}}$ are the left and right eigenvectors, respectively.

Turing instability occurs when $M_2 = 0$ and $M_1 > 0$, which yields $B = (Q^2 + k^\beta)(1 + k^\alpha)/k^\beta$. It has a single minimum $(k_{cr}, B_{cr}^{(T)})$, given parametrically by

$$B_{cr}^{(T)} = \frac{(1+z)^2}{1+(1-s)z}\,, \qquad Q^2 = \frac{sz^{1+1/s}}{1+(1-s)z}\,, \qquad k_{cr} = z^{1/\alpha}\,,$$

where $s = \alpha/\beta$. Since Q is real, we find that $0 < z < \infty$ if $1/2 < s \leq 1$, and $0 < z < 1/(s-1)$ if $1 < s < 2$. The corresponding left and right eigenvectors of the zero eigenvalue are, respectively, $\mathbf{a}^\dagger = (1, sz\eta_c^2/(1+z))$ and $\mathbf{a} = \left(z^{1/s}, -1-z\right)^{\mathrm{T}}$. For the Turing instability, a time-independent spatially periodic pattern may emerge with spatial wave number $k = k_{cr}$.

Turing and Hopf instability thresholds coincide at the C2THP where $B = B_{cr}^{(T)} = B_{cr}^{(H)} \equiv B_{cr}$, which occurs when $\eta = \eta_c \equiv \sqrt{sz^{1/s}/(z+s+1)}$. Thus, as the control parameter B is increased beyond B_{cr}, a Turing mode and a Hopf mode simultaneously bifurcate from the basic state, giving rise to terms of the form $A\mathbf{a}e^{ik_{cr}x}$ and $C\mathbf{c}e^{i\omega t}$ in $(u,v)^{\mathrm{T}}$. We note that B_{cr}, Q, η_c, and the activator input rate, $E = Q/\eta_c$, are increasing functions of z for all allowed values of z.

1.3. Weakly nonlinear analysis

We analyze the system near the C2THP, i.e., let $\eta = \eta_c + \epsilon^2\eta_2$ $(0 < \epsilon \ll 1)$. If $\eta_2 > 0$ (< 0), the Hopf (Turing) mode appears first as the parameter B is increased. We interpret this as changing the parameter E, keeping Q constant. Thus, changing η_2 will only affect the Hopf stability curve, not the Turing curve. Also, let $B = B_{cr} + \epsilon^2\mu$, where $\mu > 0$ is a real $O(1)$ quantity. This leads to the presence of two time scales. The original time scale, t, appears with oscillation frequency ω, while the slow time scale, $T = \epsilon^2 t$, accounts for the slow time evolution of the Turing and Hopf modes. The three relevant spatial scales are x, $X_1 = \epsilon x$, and $X_{2/\alpha} = \epsilon^{2/\alpha}x$, where the scaling for $X_{2/\alpha}$ is chosen under the condition that $\alpha < \beta$. If $\alpha > \beta$,

the third spatial scale would instead be $X_{2/\beta}$. While we consider both cases in Section 1.4, the explicit expressions are for $\alpha < \beta$.

With the relevant scales established, we allow for the possibility of both A and C to be functions of the slow time scale as well as the two long spatial scales. Then, since the Turing mode may be a function of all three spatial scales and the Hopf mode a function of the two long spatial scales, we require analogs of the chain rule to obtain expressions for how the operator $\partial^\gamma / \partial |x|^\gamma$ acts on u and v. While nothing in the linear stability analysis of Section 1.2 prevents the Hopf mode from being a function of the two long spatial scales, solvability conditions discussed below in the weakly nonlinear analysis limit the Hopf mode dependence to $X_{2/\alpha}$ only. Then, since the expression obtained by applying $d^\gamma / d|x|^\gamma$ to a function of the form $F(x, X_1, X_{2/\alpha})$ does not reduce to the expression obtained by applying the operator to a function of the form $G(X_{2/\alpha})$ simply by letting $\partial/\partial x = \partial/\partial X_1 = 0$, we decompose the solutions u and v into sums of functions of the form $F(x, X_1, X_{2/\alpha}, t, T)$ and $G(X_{2/\alpha}, t, T)$. Since F accounts for all x-dependent terms, whether or not they depend on X_1 and/or $X_{2/\alpha}$, while G accounts for all x-independent terms, this decomposition captures all possible terms that can arise in u and v. We utilize the product rule [**83**] for $1 < \gamma < 2$,

$$\frac{d^\gamma (fg)}{d|x|^\gamma} = \sum_{j=0}^{\infty} \left(\begin{array}{c} \gamma \\ j \end{array} \right) \frac{d^{\gamma-j} f}{d|x|^{\gamma-j}} \frac{d^j g}{dx^j} \,,$$

to compute

$$\frac{d^\gamma F(x,X_1,X_{2/\alpha})}{d|x|^\gamma} = \left(\frac{\partial^\gamma}{\partial|x|^\gamma} + \gamma\frac{\partial^{\gamma-1}}{\partial|x|^{\gamma-1}}\left(\epsilon\frac{\partial}{\partial X_1} + \epsilon^{2/\alpha}\frac{\partial}{\partial X_{2/\alpha}}\right) + \right.$$
$$\left. + \epsilon^2\frac{\gamma(\gamma-1)}{2}\frac{\partial^{\gamma-2}}{\partial|x|^{\gamma-2}}\frac{\partial^2}{\partial X_1^2} + \dots\right)F(x,X_1,X_{2/\alpha})\,, \quad (1.4)$$

where we have discarded terms smaller than $O(\epsilon^2)$. The computation of $d^\gamma G(X_{2/\alpha})/d|x|^\gamma$ requires a simpler version of the chain rule, which gives $d^\gamma G/d|x|^\gamma = \epsilon^{2\gamma/\alpha}d^\gamma G/d|X_{2/\alpha}|^\gamma$, where γ is either α or β.

Due to the fractional powers of ϵ in (1.4), we include fractional powers in the expansions of u and v:

$$\begin{pmatrix} u \\ v \end{pmatrix} \sim \epsilon\begin{pmatrix} u_1 \\ v_1 \end{pmatrix} + \epsilon^{2/\alpha}\begin{pmatrix} u_{2/\alpha} \\ v_{2/\alpha} \end{pmatrix} + \epsilon^2\begin{pmatrix} u_2 \\ v_2 \end{pmatrix} +$$
$$\epsilon^{1+2/\alpha}\begin{pmatrix} u_{1+2/\alpha} \\ v_{1+2/\alpha} \end{pmatrix} + \epsilon^3\begin{pmatrix} u_3 \\ v_3 \end{pmatrix} + \dots\,. \quad (1.5)$$

We decompose u_i and v_i as

$$\begin{pmatrix} u_i \\ v_i \end{pmatrix} = \begin{pmatrix} u_i^{(A)}(x,X_1,X_{2/\alpha},t,T) \\ v_i^{(A)}(x,X_1,X_{2/\alpha},t,T) \end{pmatrix} + \begin{pmatrix} u_i^{(C)}(X_{2/\alpha},t,T) \\ v_i^{(C)}(X_{2/\alpha},t,T) \end{pmatrix}\,, \quad (1.6)$$

where we associate the letter A with the Turing mode (though $u_i^{(A)}$ and $v_i^{(A)}$ also account for products of pure Turing and pure Hopf terms), and the letter C with the Hopf mode. If $\alpha > 4/3$,

we must also include an $O(\epsilon^{4/\alpha})$ term in the expansion. Recalling the decomposition in (1.6), we substitute (1.5) into (1.3a) and (1.3b), and find that u_1 and v_1 satisfy

$$\left(\frac{\partial}{\partial t} - \mathbf{D}_0\mathscr{D} - \mathbf{M}_0\right)\begin{pmatrix} u_1^{(A)} \\ v_1^{(A)} \end{pmatrix} + \left(\frac{\partial}{\partial t} - \mathbf{M}_0\right)\begin{pmatrix} u_1^{(C)} \\ v_1^{(C)} \end{pmatrix} = 0\,, \tag{1.7}$$

where

$$\mathbf{D}_0 = \begin{pmatrix} 1 & 0 \\ 0 & \frac{1}{\eta_c^2} \end{pmatrix}\,, \qquad \mathscr{D} \equiv \begin{pmatrix} \frac{\partial^\alpha}{\partial|x|^\alpha} & 0 \\ 0 & \frac{\partial^\beta}{\partial|x|^\beta} \end{pmatrix}\,, \qquad \mathbf{M}_0 = \begin{pmatrix} B_{cr} - 1 & Q^2 \\ -\frac{B_{cr}}{\eta_c^2} & -\frac{Q^2}{\eta_c^2} \end{pmatrix}\,.$$

Thus

$$\begin{pmatrix} u_1 \\ v_1 \end{pmatrix} = A(X_1, X_{2/\alpha}T)\mathbf{a}e^{ik_{cr}x} + C(X_{2/\alpha}, T)\mathbf{c}e^{i\omega t} + c.c.\,,$$

where $c.c.$ denotes complex conjugate. We have allowed only A to depend on both long scales. If we had assumed that C also depended on both long scales, $O(\epsilon^\alpha)$ and $O(\epsilon^\beta)$ terms would need to be included in (1.5). In this case, solvability conditions at $O(\epsilon^{1+\alpha})$ and $O(\epsilon^{1+\beta})$ would require that C be independent of X_1. These are the solvability conditions mentioned above that dictate that the Hopf mode can only be a function of $X_{2/\alpha}$. To see this, we apply the fractional operator to a function of the form $H(X_1, X_{2/\alpha})$:

$$\frac{d^\gamma H(X_1, X_{2/\alpha})}{d|x|^\gamma} = \left(\epsilon^\gamma \frac{\partial^\gamma}{\partial |X_1|^\gamma} + \epsilon^{\gamma-1+2/\alpha} \gamma \frac{\partial^{\gamma-1}}{\partial |X_1|^{\gamma-1}} \frac{\partial}{\partial X_{2/\alpha}} + \right.$$
$$\left. + \epsilon^{\gamma-2+4/\alpha} \frac{\gamma(\gamma-1)}{2} \frac{\partial^{\gamma-2}}{\partial |X_1|^{\gamma-2}} \frac{\partial^2}{\partial X_{2/\alpha}^2} + \dots \right) H(X_1, X_{2/\alpha}) \,. \quad (1.8)$$

The presence of an $O(\epsilon^\gamma)$ term in (1.8) would require that we include terms of $O(\epsilon^\alpha)$, $O(\epsilon^\beta)$, $O(\epsilon^{1+\alpha})$, and $O(\epsilon^{1+\beta})$ in the expansion of u in (1.5), among terms of other orders. The right hand side of the $O(\epsilon^{1+\alpha})$ equation would then contain a secular-producing term

$$\begin{pmatrix} 1 \\ 0 \end{pmatrix} \frac{\partial^\alpha C}{\partial |X_1|^\alpha} e^{i\omega t} \,,$$

which is not orthogonal to $\mathbf{c}^\dagger$, and thus the solvability condition is not met. A similar violation of the solvability condition is also seen at $O(\epsilon^{1+\beta})$, and also in the case of $\alpha = \beta$. To avoid this, we do not allow C to depend on X_1.

The $O(\epsilon^{2/\alpha})$ equation is the same as the $O(\epsilon)$ equation, with $u_{2/\alpha}$ and $v_{2/\alpha}$ satisfying the same homogeneous equation as u_1 and v_1. Thus we may take $u_{2/\alpha} = v_{2/\alpha} = 0$ without loss of generality (the same applies for $u_{4/\alpha}$ and $v_{4/\alpha}$).

While the left hand side of the $O(\epsilon^2)$ equation is the same as that in (1.7), its right hand side contains secular-producing terms proportional to $e^{ik_{cr}x}$. However, the solvability condition is satisfied (the secular-producing terms are orthogonal to $\mathbf{a}^\dagger$), which leads to the solution

$$\begin{pmatrix} u_2 \\ v_2 \end{pmatrix} = A^2\mathbf{p}_{2s}e^{i2k_{cr}x} + C^2\mathbf{p}_{2t}e^{i2\omega t} + AC\mathbf{p}_L e^{i\phi_L} + AC^*\mathbf{p}_R e^{i\phi_R} + |A|^2\mathbf{p}_{0s} + |C|^2\mathbf{p}_{0t} + \mathbf{p}_s e^{ik_{cr}x} + c.c.\,,$$

where $\phi_L = k_{cr}x + \omega t$ and $\phi_R = k_{cr}x - \omega t$.

The $O(\epsilon^{1+2/\alpha})$ equation, like the $O(\epsilon^2)$ equation, contains secular-producing terms orthogonal to $\mathbf{a}^\dagger$. However, while $u_{1+2/\alpha}$ and $v_{1+2/\alpha}$ are non-zero, they do not enter the $O(\epsilon^3)$ equation. Upon solving for the vectors $\mathbf{p}_{2s}$, $\mathbf{p}_{2t}$, etc., and applying the solvability condition at $O(\epsilon^3)$, we obtain, upon rescaling, the amplitude equations

$$\frac{\partial A}{\partial T} = A + \frac{\partial^2 A}{\partial X_1^2} + \zeta A|A|^2 + \psi_2 A|C|^2\,, \tag{1.9a}$$

$$\frac{\partial C}{\partial T} = \rho C + (\alpha_1 + i\alpha_2)\frac{\partial^\alpha C}{\partial |X_{2/\alpha}|^\alpha} + (-|\beta_1| + i\beta_2)\,C|C|^2 + (\delta_1 + i\delta_2)\,C|A|^2\,, \tag{1.9b}$$

where $\zeta = \pm 1$, depending on the values of α, β, and z, while ψ_2, α_1, α_2, β_1, β_2, δ_1, and δ_2, are real functions of α, β, and z. The coefficient ρ, while also real, is a function of α, β, and z, as well as μ and η_2. Finally, it can be shown that $\alpha_1 > 0$.

We restrict z to the interval I such that $\zeta = -1$, i.e., there exists nonlinear saturation of the Turing mode. We also note that (1.9a) and (1.9b) were derived under the necessary condition that C be independent of X_1. Since (1.9b) contains terms involving both A and C, $|A|$ must be spatially homogeneous. Thus, (1.9a) and (1.9b) describe only amplitudes A whose dependence on X_1 takes the form $e^{ih(X_1)}$ for a real function h. Since A can depend on both X_1 and $X_{2/\alpha}$, there are no restrictions on the way in which C can depend on $X_{2/\alpha}$.

Lastly, the techniques used here resemble those used for the regular diffusion Brusselator model. There are, however, important differences, one being that two long spatial scales are present instead of the single long scale X_1 in the regular model. Secondly, the expansions of u and v include fractional orders of ϵ, whereas only integer powers were required in the regular model. Thirdly, the rules of differentiation require that the solution be decomposed into separate functions that depend differently on the relevant variables. The resulting form of the amplitude equations are also different in that the equation for C is now an integro-differential equation. A shorter version of this section is presented in [**98**].

1.4. Solutions of the amplitude equations and their long-wave instabilities

In this section, we seek special solutions of (1.9a) and (1.9b), namely a pure Turing solution, a pure Hopf solution, and a mixed mode solution. We then study the instabilities of these solutions to long-wave perturbations. We first consider the pure Turing solution, given by $C = 0$ and $A = \tilde{A}e^{iK_A X_1}$ with $\tilde{A} = (1 - K_A^2)^{1/2}$. To study its stability, we linearize around it using $A = (\tilde{A} + a(X_1, T))e^{iK_A X_1}$, and $C = c(X_{2/\alpha}, T)$. The resulting linearized equations decouple, so we analyze each separately. A long-wave perturbation $a(X_1, T)$ yields the familiar Eckhaus stability criterion

$$|K_A| < \frac{1}{\sqrt{3}}\,. \tag{1.10}$$

If (1.10) is not satisfied, the perturbation grows, changing the spatial frequency of the solution. A long-wave perturbation $c(X_{2/\alpha}, T)$ with wave number $k \ll 1$ results in the dispersion relation $\sigma = \rho - \alpha_1|k|^\alpha + \tilde{A}^2\delta_1 \pm i|-\alpha_2|k|^\alpha + \tilde{A}^2\delta_2|$, whose real part must be negative for long-wave stability. If the real part is positive, the perturbation grows, changing the spatial structure of the

solution and also introducing a time-oscillatory component. The long-wave stability criterion is $\rho + \tilde{A}^2\delta_1 < 0$. If $\delta_1 < 0$, long-wave perturbations of the Hopf amplitude decay for all $\rho < 0$, or even if $\rho > 0$ as long as ρ remains sufficiently small. If $\delta_1 > 0$, long-wave perturbations of the Hopf amplitude can grow even for $\rho < 0$, as long as ρ is sufficiently close to 0.

For the regular diffusion model, $\delta_1 > 0$ for $z \lesssim 0.26$, or equivalently, $\eta_c \lesssim 0.34$, meaning that the inhibitor (g) diffuses significantly faster than the activator (f). In the anomalous model, we obtain an analogous result for α and β, since these two parameters have a greater impact on the rate of diffusion than do the diffusion coefficients. In contrast to the regular model, δ_1 can be positive even if $\alpha < \beta$, that is, if the inhibitor diffuses more slowly than the activator. For $\alpha \lesssim 1.65$, $\delta_1 < 0$ for all $z \in I$, meaning that sufficiently fast diffusion of the activator makes it impossible for long-wave perturbations of the Hopf mode to grow if $\rho < 0$. This behavior is not seen in the regular model.

Next, we consider the pure Hopf solution, given by $A = 0$ and $C = \tilde{C}e^{iK_C X_{2/\alpha} + i\Omega T}$ with $\tilde{C} = ((\rho - \alpha_1|K_C|^\alpha)/|\beta_1|)^{1/2}$ and $\Omega = -\alpha_2|K_C|^\alpha + \beta_2\tilde{C}^2$. We note that, since the quantity $\rho - \alpha_1|K_C|^\alpha$ must be positive, ρ must be positive for the pure Hopf solution to exist. Long-wave perturbations of the form $e^{\sigma T + ikX_{2/\alpha}}$ yield two growth rates, one of which is negative, the other of which has the expansion for small k, $\sigma = a_1 k + a_2 k^2 + O(k^3)$, where

$$a_1 = -i\frac{\alpha\left(\alpha_1\beta_2 + \alpha_2|\beta_1|\right)|K_C|^{\alpha-1}}{|\beta_1|},$$

and

$$a_2 = \frac{\alpha(\alpha-1)\left(\alpha_2\beta_2 - \alpha_1|\beta_1|\right)}{2|\beta_1|} + \frac{\alpha^2\alpha_1^2(\beta_1^2+\beta_2^2)|K_C|^\alpha}{2|\beta_1|^3\tilde{C}^2}.$$

Requiring $a_2 < 0$ for stability leads to the generalized Eckhaus criterion,

$$|K_C|^\alpha < \frac{\rho}{R\alpha_1}\,, \tag{1.11}$$

where

$$R = 1 + \frac{\alpha\alpha_1\left(\beta_1^2 + \beta_2^2\right)}{(\alpha-1)|\beta_1|(\alpha_1|\beta_1| - \alpha_2\beta_2)}\,.$$

Thus, if (1.11) is not satisfied, both the spatial and temporal structures of the solution are altered as a long-wave perturbation grows with amplitude oscillating at a frequency different from Ω. As in the regular diffusion case, the magnitude of R is greater than unity for all $z \in I$. However, if $\alpha < \beta$, unlike the regular diffusion case, R is positive only for z sufficiently small. Beyond this interval, R becomes negative so that (1.11) is never satisfied, in which case the pure Hopf solution must be long-wave unstable. Restricting z to sufficiently small values for which R is positive implies that B_{cr}, Q, η_c, and E, must all be sufficiently small. For example, η_c must be less than ~ 0.62, and thus, while the rate of diffusion is dominated by the diffusion exponents α and β, η_c still impacts whether or not the Hopf mode can be long-wave stable. Note, however, that η_c is not a strict comparison between the diffusion coefficients D_f and D_g, as these parameters do not even have the same units. The qualitative behavior of R in the $\alpha > \beta$ case is the same as for regular diffusion, where $R > 1$ for all $z \in I$, suggesting that faster diffusion of the activator versus the inhibitor may contribute to instability of the pure Hopf solution.

Finally we consider the mixed mode solution, given by $A = \tilde{A}e^{iK_A X_1}$, $C = \tilde{C}e^{iK_C X_{2/\alpha} + i\Omega T}$ with

$$\tilde{A} = \left(\frac{\psi_2 \left(\rho - \alpha_1 |K_C|^\alpha \right) + |\beta_1| \left(1 - K_A^2 \right)}{\Delta} \right)^{1/2},$$

$$\tilde{C} = \left(\frac{\rho - \alpha_1 |K_C|^\alpha + \delta_1 \left(1 - K_A^2 \right)}{\Delta} \right)^{1/2},$$

where $\Delta = |\beta_1| - \psi_2 \delta_1$, and $\Omega = -\alpha_2 |K_C|^\alpha + \beta_2 \tilde{C}^2 + \delta_2 \tilde{A}^2$. Of course, we must restrict K_A and K_C so that $\tilde{A}$ and $\tilde{C}$ are real. Linearizing (1.9a) and (1.9b) around this mixed mode solution with small perturbations $a(X_{2/\alpha}, T)$ and $c(X_{2/\alpha}, T)$ results in the coupled equations

$$\frac{\partial a}{\partial T} = (1 - K_A^2) a - \tilde{A}^2 (a^* + 2a) + \psi_2 \left[\tilde{A}\tilde{C} \left(c^* + c \right) + a\tilde{C}^2 \right], \tag{1.12}$$

and

$$\frac{\partial c}{\partial T} = -i\Omega c + \rho c + (\alpha_1 + i\alpha_2) \left(-|K_C|^\alpha c + i\alpha |K_C|^{\alpha - 1} \frac{\partial c}{\partial X_{2/\alpha}} + \right.$$
$$\left. + \frac{\alpha(\alpha - 1)}{2} |K_C|^{\alpha - 2} \frac{\partial^2 c}{\partial X_{2/\alpha}^2} \right) + (-|\beta_1| + i\beta_2) \tilde{C}^2 (c^* + 2c) +$$
$$+ (\delta_1 + i\delta_2) \left[\tilde{A}\tilde{C} \left(a^* + a \right) + c\tilde{A}^2 \right]. \tag{1.13}$$

Eqs. (1.12) and (1.13) contain terms involving both a and c, and so, for consistency, we require a to depend only on $X_{2/\alpha}$. We consider two types of perturbations: spatially homogeneous perturbations of a spatially dependent solution ($K_A, K_C \neq 0$), and long-wave perturbations of a spatially homogeneous solution ($K_A = K_C = 0$). For the first case, the resulting dispersion relation yields two zero eigenvalues and 2 negative eigenvalues as long as $\Delta > 0$, with one of the eigenvalues turning positive if $\Delta < 0$. If $\Delta < 0$, the solution decays to either a pure

Turing or pure Hopf mode, depending on the initial conditions [**21**], changing the temporal and spatial structures of the solution. Thus, a necessary (and sufficient) condition for stability of the spatially dependent mixed mode solution to homogeneous perturbations is $\Delta > 0$. As in the regular case, there are values of α and β for which stability is possible for both sufficiently large and small values of z. These occur for (α, β) pairs that are near $(2, 2)$. Sufficiently small (large) z refers to an interval of z that ranges from the smallest (largest) $z \in I$ to some larger (smaller) $z \in I$. For (α, β) pairs where α is sufficiently large, it is possible that $\Delta > 0$ only for z sufficiently small. More specifically, for all such (α, β) pairs, stability is possible only if $\eta_c \lesssim 0.42$. Similarly, for all (α, β) for which stability is only possible for sufficiently large z, stability is possible only if $\eta_c \gtrsim 0.65$. For some (α, β) pairs with β sufficiently small, stability is impossible.

For the spatially homogeneous solution, taking $K_A = K_C = 0$, (1.12) remains the same, while the derivative term in (1.13) is replaced by $\partial^\alpha c/\partial|X_{2/\alpha}|^\alpha$. Upon inserting long-wave perturbations of the form $e^{\sigma T + ikX_{2/\alpha}}$, the resulting dispersion relation yields two zero eigenvalues and one negative eigenvalue as long as $\Delta > 0$, while the fourth eigenvalue has the expansion for small k, $\sigma \sim a_\alpha |k|^\alpha$, where

$$a_\alpha = \frac{\alpha_2(\beta_2 + \psi_2\delta_2) - \alpha_1\Delta}{\Delta}\,.$$

Thus, long-wave stability of the spatially homogeneous solution requires $\Delta > 0$ and $a_\alpha < 0$. If either one of these conditions is not satisfied, a long-wave spatial pattern appears, breaking the spatial homogeneity. Like the regular diffusion case, there exist (α, β) pairs such that stability is possible only for sufficiently large z. More specifically, for all such (α, β) pairs, long-wave stability of the spatially homogeneous mixed mode solution is possible only if $\eta_c \gtrsim 0.65$. These

occur for α sufficiently close to β, but only for $\alpha > \beta$. As in the pure Hopf stability analysis, it appears that the $\alpha > \beta$ case more closely resembles regular diffusion in terms of stability properties. For $\alpha < \beta$ with α and β sufficiently large, stability is possible only for z sufficiently small. For all such (α, β) pairs, $\eta_c \lesssim 0.37$. For both mixed mode solutions, α and β determine whether or not there exist values of parameters, such as η_c, for which stability is possible, as for many (α, β) pairs, stability is impossible.

In summary, the evolution equations (1.9a) and (1.9b) appear similar to their regular diffusion counterparts, but differ both in the behavior of their coefficients, as well as their overall form, as (1.9b) reflects non-local effects. As a result, the stability criteria differ greatly from those of regular diffusion. In the stability analysis of the pure Turing solution, there exist (α, β) such that long-wave perturbations of the Hopf mode cannot grow if $\rho < 0$ for any value of z. This is contrary to the regular diffusion case, for which growth is possible if the inhibitor diffuses sufficiently faster than the activator. Further, we found that there exist (α, β) for which long-wave perturbations of the Hopf mode can grow for $\rho < 0$ even if the inhibitor diffuses more slowly than the activator. We also found that, for $\alpha < \beta$, there exist values of $z \in I$ such that stability of the pure Hopf solution is impossible, while for $\alpha > \beta$, stability criteria remains qualitatively similar. Finally, for the mixed mode, there exist (α, β) pairs sufficiently close to $(2, 2)$ for which stability requirements are similar to those of regular diffusion. Away from this regime, these requirements can either change or stability may simply not be possible.

1.5. Numerical results

The system (1.3a) and (1.3b) was solved on the interval $0 < x < L$ with periodic boundary conditions using Fourier spectral methods in space and a second order predictor-corrector

method in time. The diffusion terms were treated implicitly and differentiation in spectral space was computed using (1.1). The reaction terms were computed in physical space before being transformed into Fourier space, where all time-stepping was performed. A numerical method for solving superdiffusive problems with Neumann and Dirichlet boundary conditions is given in [**24**], requiring subtraction of terms that lead to singularities at the boundaries. Another approach to treat superdiffusion on a finite domain is given in [**99**], where a modified integro-differential operator is introduced, requiring reflective extensions of functions outside the domain. This operator was numerically shown to yield desirable properties such as the obeying of the first and second laws of thermodynamics, and preservation of symmetry around the midpoint of the domain.

We computed solutions in two regimes: near the stability threshold to confirm the analysis in Section 1.4, and far in the nonlinear regime to find solutions not predicted by weakly nonlinear analysis. When confirming the stability analysis of Section 1.4, a system length L was employed so that the chosen initial conditions would be periodic. To determine long-wave stability of the solutions described in Section 1.4, we set as the initial conditions the respective solution plus a small long-wave perturbation. The Fourier spectrum of the initial condition thus contained a non-zero amplitude associated with the first order solution, and comparatively smaller amplitudes associated with the long-wave perturbations. The parameter μ was set to be an $O(1)$ quantity, as was η_2. In the cases for which the solution was long-wave stable, the Fourier amplitude of the first order solution remained constant to within $\sim O(\epsilon^2)$ of the initial (predicted) amplitude, while the amplitudes of the long-wave perturbations decayed. In cases for which the solution was long-wave unstable, the amplitude of the first order solution remained near its initial value for a time of $O(1/\epsilon^2)$ before beginning to decay. The amplitude of the long-wave

perturbation saw a slow initial decay that lasted for a time of $O(1/\epsilon^2)$ before growing to the same order of magnitude as the amplitude of the first order solution. In this way, we were able to confirm results (1.10) and (1.11). Specifically, if the wavenumber of the pure Turing mode lies within the Eckhaus stable region, a pure Turing solution with that wavenumber is found numerically, while if the spatial wavenumber of the Hopf bifurcated solution lies within the generalized Eckhaus stable region, the Hopf bifurcated solution with that wavenumber is found numerically, thus confirming the results of the weakly nonlinear analysis. As a further corroboration of the weakly nonlinear analysis, in Fig. 1 we compare the oscillation frequency of the Hopf solution computed numerically to that predicted by the weakly nonlinear analysis, as a function of the bifurcation parameter μ. We see that for small μ (weakly nonlinear case) there is excellent agreement between the two.

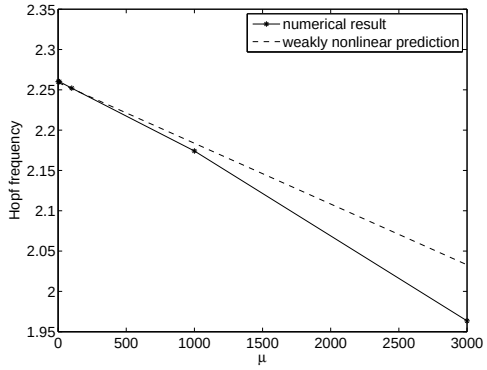

Figure 1.1. Comparison of weakly nonlinear prediction and numerical results of the frequency of spatially homogeneous oscillations as a function of the bifurcation parameter μ. The parameters are $\alpha = 1.4$, $\beta = 1.5$, $z = 1.6$, and $\eta_2 = 1$.

Results that involved components of both the Turing and Hopf modes were too computationally intensive to check. In particular, results pertaining to long-wave stability of the mixed mode were numerically inconclusive, as it appeared that a pure stable mixed mode exists only for ϵ too small to feasibly compute a steady state solution. However, it was observed that if

$\Delta < 0$, a solution that started out with both a Turing and Hopf mode decayed to either a pure Turing or pure Hopf solution, depending on the values of the parameters. If $\Delta > 0$, both modes remained present for the entire length of the computation, though the respective amplitudes were not constant, indicating that the steady state was not that of a pure mixed mode.

In the sections below, we discuss results of computations with μ of $O(1/\epsilon^2)$ so that the system is in the fully nonlinear regime. To reach what was determined to be a steady state, the system was evolved over 1.5×10^4 units of time. To verify that the time period was sufficiently long, for some results, we compared solutions obtained near $t = 1.5 \times 10^4$ with those obtained near $t = 3 \times 10^4$ to ensure that the solutions obtained were in fact in steady state. In such cases, no qualitative differences were observed between the solutions at the two times. The Fourier spectrum of the steady state solutions were also monitored to ensure that the amplitudes in the tail of the spectrum did not exceed $O(10^{-3})$ of that of magnitudes of the most dominant modes, thus indicating that aliasing was not significant for the computational results presented here. In all space-time plots presented, the spatial variable x runs horizontally while time runs vertically.

1.5.1. The fully nonlinear regime with equal diffusion exponents

Taking μ to be of $O(1/\epsilon^2)$, we computed solutions not predicted by the weakly nonlinear analysis, in the fully nonlinear regime of the regular and superdiffusive Brusselator models. The parameter η_2 was still kept as an $O(1)$ quantity so that the system remained near the C2THP. We consider only $\alpha = \beta$ in this subsection. The following subsection below discusses the $\alpha \neq \beta$ case. Figures 1.2 - 1.11 show space-time plots of u, or plots of $u(x)$ at particular instants of time, in steady states with $\alpha = \beta$, starting from random initial conditions and setting the parameters $\epsilon^2\mu = 1$, $\eta_2 = 1$, and $L = 500$ while varying z. Since it appears that different

initial conditions evolve to different steady states (cf. [**19**] for regular diffusion), we computed steady states from different random initial conditions for each set of parameters. Thus, for each $(\alpha, \beta) = (1.1, 1.1)$, $(1.5, 1.5)$ and $(2, 2)$, we computed steady states with z ranging from 0.2 to 3 in increments of 0.2. The parameters L, μ and η_2 were kept constant. For each (α, β, z) parameter set, we computed steady states from the same set of random initial conditions (i.e., the random initial conditions were generated in such a way that they were reproducible, and thus could be used again). Note that if L is lowered significantly, many of the steady state patterns disappear.

For z small (~ 0.2), setting $(\alpha, \beta) = (1.1, 1.1)$, $(1.5, 1.5)$ and $(2, 2)$, we found that all initial conditions employed resulted in a steady state consisting only of stationary stripes (a pure Turing steady state), with the dominant wave number near $Lz^{1/\alpha}/(2\pi)$, depending on the initial conditions. For $z = 0.4$, we find that the $(1.1, 1.1)$ case still yielded a pure Turing solution for all initial conditions tested. The $(1.5, 1.5)$ case yielded some pure Hopf steady states (spatially homogeneous oscillations) and some pure Turing states, depending on the initial conditions, while the $(2, 2)$ case yielded a pure Hopf solution for all initial conditions. For $z = 0.6$, both the $(1.5, 1.5)$ and $(2, 2)$ cases yielded pure Hopf steady states of the same frequency, while the $(1.1, 1.1)$ case yielded both pure Turing and pure Hopf steady states, depending on the initial conditions. Thus, anomalous diffusion with equal diffusion exponents delays the development of Hopf behavior (in terms of increasing z). For $z > 2$, all three cases yielded pure Turing steady states for all random initial conditions tested. For $1.2 \leq z \leq 1.8$, we found spatiotemporal patterns for either one or both of the $(1.5, 1.5)$ and $(2, 2)$ cases. For the values of z and the random initial conditions tested, we did not find any spatiotemporal patterns for the $(1.1, 1.1)$ case.

In the descriptions below, we will use the term "spot" to denote a local maximum of u. We will say that a spot is created when such a maximum forms, and that a spot is annihilated when the maximum disappears. We will also say that two spots that propagate away from each other are counter propagating, and that two spots that propagate toward each other are oppositely propagating. In a system with periodic boundary conditions, these definitions might appear to be confusing, as spots which are created as counter propagating can theoretically, after rotating through a full period, become oppositely propagating. However, this does not occur in our computations because the spots are prevented from going all the way around the full period by the presence of obstacles, e.g., regions of stationary stripes which halt the motion of the spots by absorbing them. These spots account for the time-oscillatory regions in the spatiotemporal patterns described below, which, in addition, often also contain stripe-like regions.

Figures 1.2(a) - 1.2(c) show spatiotemporal patterns with regular diffusion, $B = 5.84$ and $\eta = 0.612$ for different random initial conditions. Figure 1.2(a) shows breathing stripes embedded in a time-oscillatory and nearly spatially homogeneous structure. The stripes breathe while the values of the minima and maxima also oscillate in time. The dynamical behavior of this mode is illustrated in more detail in Figures 1.3(a) though 1.3(e) where we plot u versus x for selected times near the first (lowest) horizontal stripe in Figure 1.2(a). The apparently horizontal stripes are in fact slightly U-shaped, as a spot is created near $x = 4.5$ (spot A in Figures 1.3(a) and 1.3(b)), which splits into two spots that counter propagate toward opposite sides of the stripes (spots B and C in Figure 1.3(c)), after which u decays until the start of the next event. The rapid rise and gradual decay of u indicates temporal relaxation oscillations (illustrated by a plot of u at $x = 4.5$ in Figure 1.4). In the early stages of the decay, the outer spot on either side of the striped region is absorbed into the incoming spot (Figure 1.3(d)), while in the latter

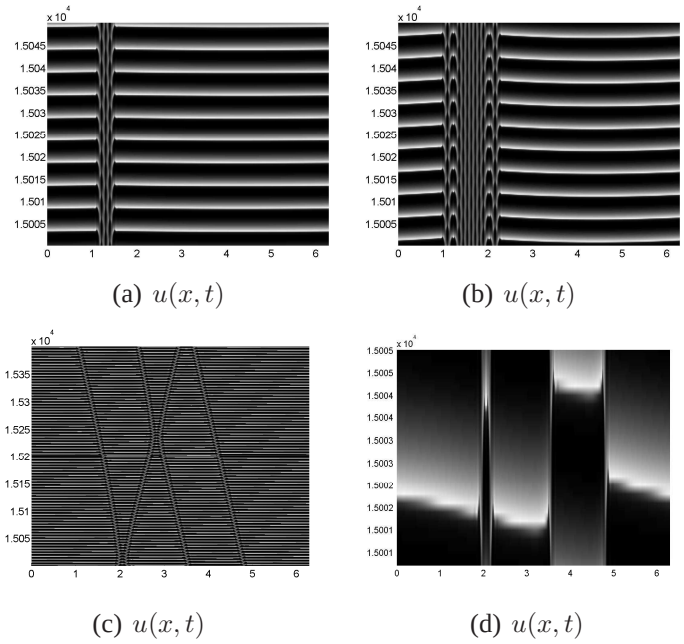

Figure 1.2. Spatiotemporal patterns of u for regular diffusion with $z = 1.2$, $B = 5.84$ and $\eta = 0.612$. The figures differ only in the random initial condition employed. Most of the patterns for this parameter set have low spatial frequency and are mainly time-oscillatory, with smaller intervals of stationary or breathing stripes. Figure (c) shows multiple propagating dislocations. Light colors indicate more positive values of u, while dark colors indicate less positive values of u. Figure (d) shows a small interval in time of (c), corresponding to the time interval depicted in Figures 1.6(a) to 1.6(i). The space-time plots of v are essentially the same, except with the colors inverted.

stages of the decay (Figure 1.3(e)), two new spots are formed at the edge of the stripe region in place of those previously absorbed.

Figure 1.2(b) has qualitative similarities to Figure 1.2(a) in that one spot splits into two counter propagating spots. The U-type behavior is more pronounced and clearly visible in Figure 1.2(b) than in Figure 1.2(a). The way that the two spots interact with the boundary of the stripes is, however, the same as in Figure 1.2(a). A slight difference is that the spot creation site is slightly closer to the right side of the stripes. As a result, the spot traveling toward the right side of the stripes is annihilated before the one traveling to the left side. However, the main

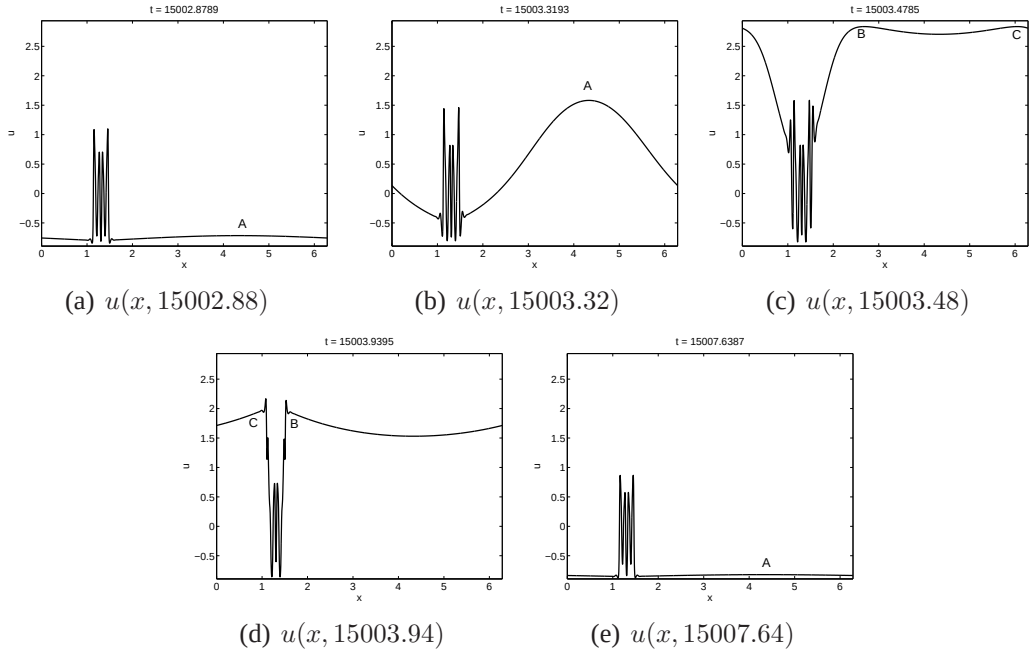

(a) $u(x, 15002.88)$ (b) $u(x, 15003.32)$ (c) $u(x, 15003.48)$

(d) $u(x, 15003.94)$ (e) $u(x, 15007.64)$

Figure 1.3. Plots of $u(x)$ at specific instants of time illustrating the creation and annihilation of spots in Figure 1.2(a). A spot (A) begins to form at $x \simeq 4.5$ in (a), which then grows ((b)) until it splits into two spots (B and C in (c)). The two spots are annihilated with the two spots straddling the striped region and decay ((d)) before the process repeats ((e)).

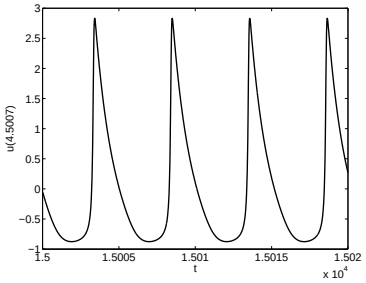

Figure 1.4. Plot of u at $x = 4.5$ as a function of time, corresponding to the bottom four stripes of Figure 1.2(a).

difference is that Figure 1.2(b) also has inverted U-shaped patterns embedded in the stripes, each of which corresponds to two spots created at the stripes that grow slowly and propagate toward one another. The dynamical behavior of this mode is illustrated in Figures 1.5(a) - 1.5(e)

where we plot u as a function of x for times near the lower part of Figure 1.2(b). These figures are plotted only over the right end of the striped region, focusing on the inverted U structure ($x \simeq 1.9$ to $x \simeq 2.15$). Two spots are centered at $x \simeq 1.95$ and $x \simeq 2.1$ and are labeled B and C, respectively. A spot in the middle (spot A in Figure 1.5(a)) grows at a rate faster than the two oppositely propagating spots (Figure 1.5(b)) and achieves a greater maximal value than the two oppositely propagating spots (Figure 1.5(c)), accounting for the bright spots at the peaks of the inverted U's in Figure 1.2(b). As the three spots decay together, the two outside spots are eventually absorbed into the larger interior spot (Figure 1.5(d)) as two new spots form in their place (spots B$'$ and C$'$ in Figure 1.5(d) and Figure 1.5(e)). Just as the two spots that are annihilated at the stripes are out of phase, so too are the oscillations of the two inverted U's.

Figure 1.2(c) shows four dislocations that propagate uniformly in time, with three that propagate to the left, and one that propagates to the right. These dislocations are sites at which a spot is born on one side and propagates away from it, and another spot generated at an adjacent dislocation is annihilated on the other side. The four dislocations divide the system into four regions and act as boundaries where spots are born and annihilated. The dislocations appear to propagate until meeting another dislocation, at which point the two appear to repel each other. The speed of the dislocations (the inverse of the absolute value of the slopes of the dislocations shown in Figure 1.2(c)) appears to be constant in time and the same for all dislocations. The time at which a spot is created in one particular region is much closer to the time at which a spot is created in the interval on the other side of its neighbor. For example, at $t = 1.5 \times 10^4$ in Figure 1.2(c), a spot creation event in the interval centered at $x \simeq 2$ will either be closely preceded or followed by a spot creation event in the interval centered at $x \simeq 4.1$. Figures 1.6(a) - 1.6(f) indicate the intervals (labeled 1-4 in the figures) and illustrate the dynamical behavior

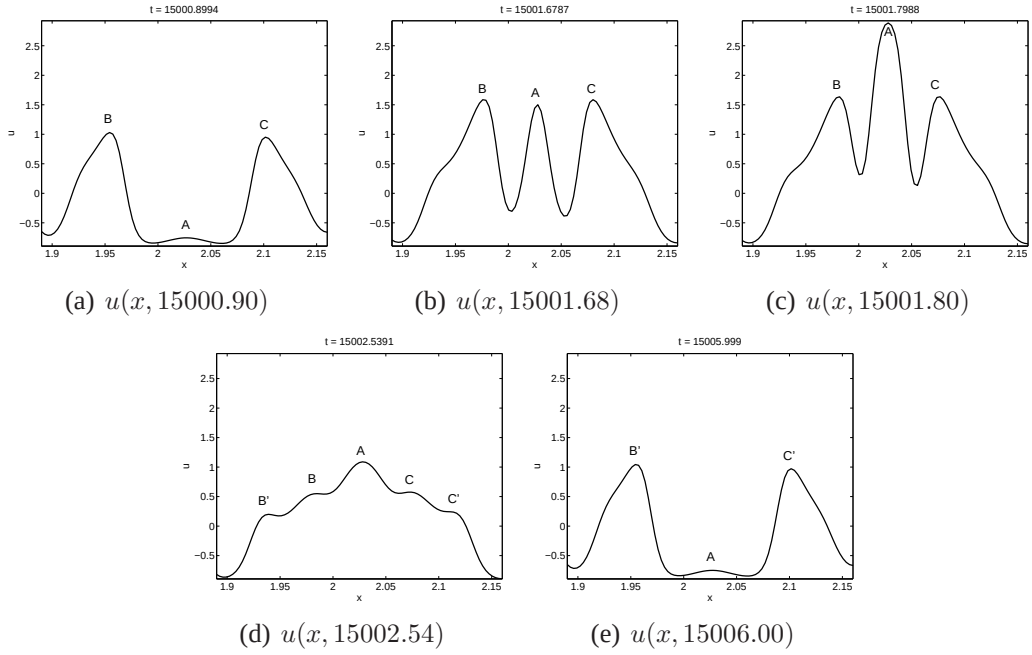

(a) $u(x, 15000.90)$ (b) $u(x, 15001.68)$ (c) $u(x, 15001.80)$

(d) $u(x, 15002.54)$ (e) $u(x, 15006.00)$

Figure 1.5. Line plots describing details of the right inverted U of Figure 1.2(b) at specific instants of time. A spot centered at $x \simeq 2.03$ grows at a faster rate than the two oppositely propagating spots centered at $x \simeq 1.95$ and $x \simeq 2.1$ ((a) and (b)). In (c), all three spots have achieved values close to their maximal value, with that of the middle spot being much larger. The three spots then decay together, appearing to merge together into one structure ((d)), from which two new spots are born to replace the two outer spots ((e)).

within each interval. The figures represent the dynamical evolution of the pattern for times near the lower part of Figure 1.2(c). Figure 1.6(a) shows the two regions centered at $x \simeq 2$ (region 2) and $x \simeq 4.1$ (region 4) near the end of a decay process, just as a spot has formed in the region centered at $x \simeq 3$ (region 3). This spot then grows (Figure 1.6(b)) and propagates to the left (Figure 1.6(c)) just as a spot begins to form to the left of $x = 2$ in the region centered near $x \simeq 0$ (region 1). This spot grows and propagates to the left as the spot in region 3 is annihilated and the whole interval begins to decay (Figure 1.6(d)). The spot in region 1 continues to propagate to the left until it is annihilated near $x = 5$ (Figure 1.6(e)). As intervals 1 and 3 decay, spots

begin to form in regions 2 and 4 (Figure 1.6(f)). The spot in region 2 reaches its maximum (Figure 1.6(g)) before the spot in region 4 forms and propagates to the left (Figure 1.6(h) and 1.6(i)). Regions 2 and 4 then decay, and the process starts over again.

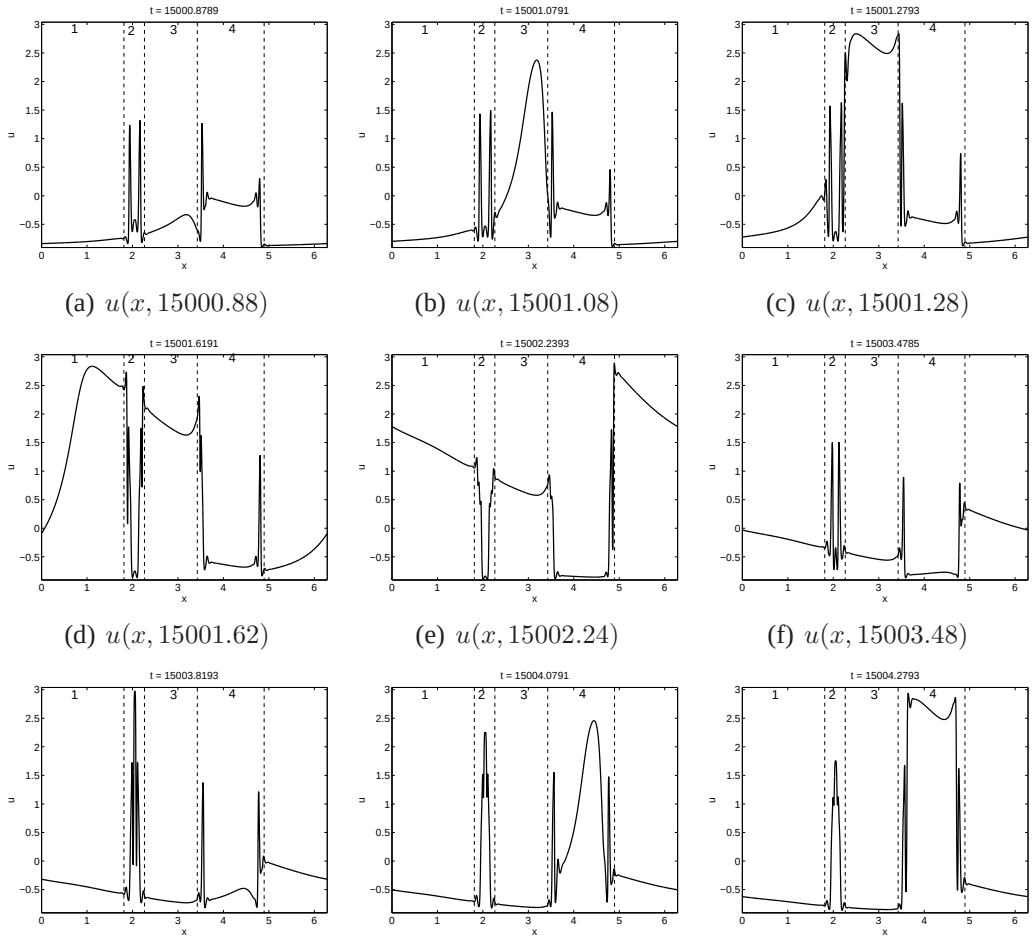

(a) $u(x, 15000.88)$ (b) $u(x, 15001.08)$ (c) $u(x, 15001.28)$

(d) $u(x, 15001.62)$ (e) $u(x, 15002.24)$ (f) $u(x, 15003.48)$

(g) $u(x, 15003.82)$ (h) $u(x, 15004.08)$ (i) $u(x, 15004.28)$

Figure 1.6. Plots of $u(x)$ at specific instants of time illustrating the structure of the regions in Figure 1.2(c). Regions 2 and 4 are near the end of a decay cycle in (a) as a spot in region 3 begins to form. The spot grows and propagates to the left ((b) and (c)) as a spot grows just to the left of $x = 2$ in region 1. The spot in region 1 grows and propagates to the left before being annihilated at $x \simeq 5$ ((d) and (e)). As regions 1 and 3 decay ((f)), spots begin to form in regions 2 and 4 ((g) and (h)). The growth of region 2 occurs slightly before that of region 4, and so it decays earlier ((i)).

With $\alpha = \beta = 1.5$ and $z = 1.2$, the only steady states found using the same initial conditions as those used for the regular diffusion computations were those of spatially homogeneous oscillations.

For $z = 1.4$, $B = 6.76$, and $\eta = 0.642$ (Figures 1.7(a) - 1.7(f)), we found spatiotemporal patterns for both the $(\alpha, \beta) = (1.5, 1.5)$ and $(2, 2)$ cases. Figures 1.7(a) and 1.7(d) correspond to the same initial conditions, only the diffusion coefficients differ ($(\alpha, \beta) = (1.5, 1.5)$ and $(2, 2)$ respectively), similarly for Figures 1.7(b) and 1.7(e) and Figures 1.7(c) and 1.7(f).

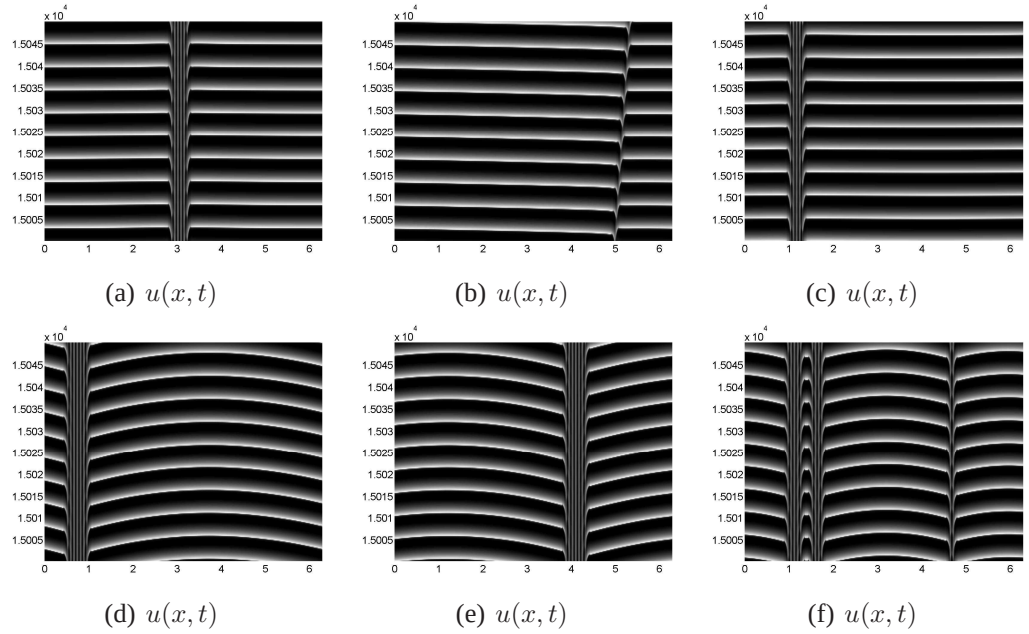

(a) $u(x,t)$ (b) $u(x,t)$ (c) $u(x,t)$

(d) $u(x,t)$ (e) $u(x,t)$ (f) $u(x,t)$

Figure 1.7. Spatiotemporal patterns of u for $\alpha = \beta = 1.5$ ((a), (b), (c)) and $\alpha = \beta = 2$ ((d), (e), (f)), with $z = 1.4$, $B = 6.76$, and $\eta = 0.642$. Each pair (a) and (d), (b) and (e), and (c) and (f) are generated from the same set of random initial conditions. As with Figure 1.2, most of the patterns for this parameter set have low spatial frequency and are mainly time-oscillatory. The main difference is in the presence of the inverted U's of the regular diffusion figures versus the flat oscillatory structures of the anomalous figures.

Figure 1.7(a) resembles Figure 1.2(a) in that the apparently horizontal lines are slightly U-shaped. The stripes for the anomalous case, however, do not breathe as do those in the regular

diffusion case. Comparing Figures 1.7(a) and 1.7(d), we see that for the regular diffusion case, instead of there being a spot created away from the stripes that splits into two spots that are annihilated on either side of the stripes (U-shape), two spots are generated on either side of the stripes, which then oppositely propagate and are annihilated between the generation sites, resulting in an inverted U-shape. In Figure 1.7(d), the left spot fires first, resulting in an annihilation site that is closer to the right side of the stripes than to the left. Thus, for the anomalous case, there is creation away from the stripes and annihilation at the stripes (U-shaped), while for regular diffusion, there is creation at the stripes and annihilation away from the stripes (inverted U).

Figure 1.7(b) (anomalous) shows a single traveling dislocation that propagates to the right. Periodically, a spot is generated on the left side of the dislocation, which then propagates until it hits the right side of the dislocation. This steady state is similar to but simpler than the pattern in Figure 1.2(c). There are three periods associated with this steady state: the time it takes for a newly formed spot to travel from one side of the dislocation to the other (~ 1.08 time units), the time between two spot-creation events (~ 5.2092 time units), and the time it takes for the dislocation to travel one length of the system (~ 939.039 time units). None of the ratios computed from these periods appear to be a simple rational number. While all results of the computation are necessarily rational, this suggests that in reality the periods are incommensurate, a situation that can lead to chaos, but does not seem to do so in this case. Figure 1.7(c) is similar to Figure 1.7(a), the only difference being the number of stripes. Figures 1.7(d) and 1.7(e) appear to be the same solution modulo a shift in space.

In Figure 1.7(f), unlike in Figure 1.7(d), all spots appear to fire simultaneously. The small inverted U's embedded in the stripes are similar to those found in Figure 1.2(b). The dynamical

behavior of one of the larger inverted U's centered at $x \simeq 3.2$ of Figure 1.7(f) is illustrated in more detail in Figures 1.8(a) - 1.8(d), where u is plotted against x for a restricted x interval. They correspond to the inverted U that occurs between $t = 1.5005 \times 10^4$ and $t = 1.501 \times 10^4$. Figure 1.8(a) shows the formation of two spots A and B. They co-propagate and grow (Figure 1.8(b)) before meeting and annihilating in the middle while two new spots are formed in their place (Figures 1.8(c) and 1.8(d)). The new spots are labeled A′ and B′ in Figure 1.8(d).

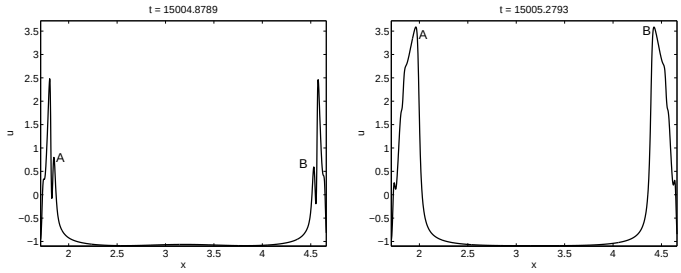

(a) $u(x, 15004.88)$ (b) $u(x, 15005.28)$

(c) $u(x, 15006.80)$ (d) $u(x, 15010.12)$

Figure 1.8. Line plots describing details of the spatiotemporal cell centered at $x \simeq 3.2$ in Figure 1.7(f). Two spots are created at the stripes ((a)), which then co-propagate and grow ((b)) before meeting and annihilating in the middle while two new spots are formed in their place ((c) and (d)).

Figures 1.9(a) - 1.9(c) show spatiotemporal patterns of single or multiple localized structures in a sea of stripes for $\alpha = \beta = 1.5$, $z = 1.6$, $B = 7.76$ and $\eta = 0.67$. Figure 1.9(d) is a close-up of Figure 1.9(c). Using the same initial conditions, only stationary stripes were found for the case of regular diffusion.

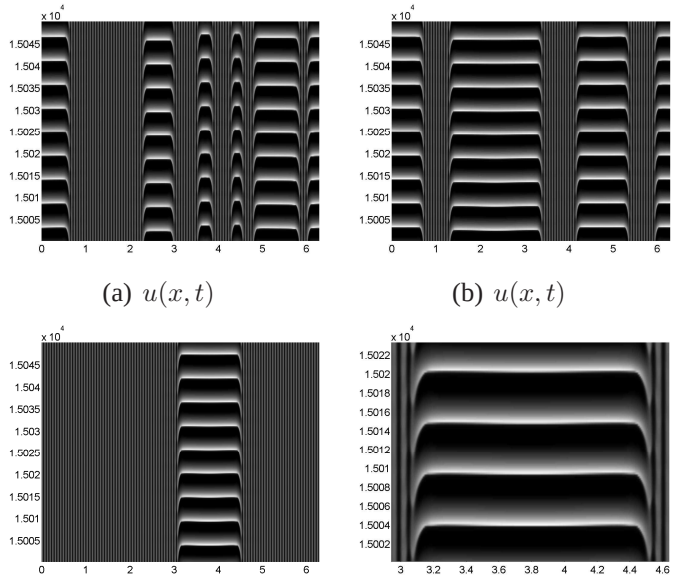

(a) $u(x,t)$ (b) $u(x,t)$

(c) $u(x,t)$ (d) $u(x,t)$

Figure 1.9. Spatiotemporal patterns of u for anomalous diffusion with $\alpha = \beta = 1.5$, $z = 1.6$, $B = 7.76$ and $\eta = 0.67$. The figures differ only in initial condition. Compared to Figures 1.2(a)-1.2(c) and Figures 1.7(a) - 1.7(f), these figures show a more Turing-dominant structure in which time-oscillatory structures are embedded. (d) is a close-up of the spatiotemporal cell of (c). Depending on the initial conditions, the spatiotemporal cells can occur in any size, number, and with any relative spacing.

The predominant structures seen for this parameter set are the square-shaped spatiotemporal cells that take on the shape of an inverted U with a flat apex, which we did not find for regular diffusion. It appears that, depending on the initial conditions, these cells can occur in different sizes and numbers, and can have any relative spacing between them. Some square cells behave in a similar fashion as the inverted U's of Figure 1.7(f) in that a small spot arises rapidly between two slowly growing and oppositely propagating spots, which are subsequently absorbed into the interior spot. However, there are some significant differences described below. For some square cells this is a spatially symmetric process that results in a concentrated bright spot at the apex. Other square cells can exhibit either symmetric or slightly asymmetric behavior. In either case,

the interior spot is much wider and is less localized than that of the inverted U's in Figure 1.2(b), accounting for the absence of a bright spot at the apex.

Figures 1.10(a)-1.10(d) illustrate the detailed dynamics of the symmetric square cell shown in Figure 1.9(c) (closeup in Figure 1.9(d)). These figures are plotted only over a restricted x interval corresponding to the extent of the square cell. An interior spot (spot A in Figures 1.10(a) and 1.10(b)) grows in the middle of two oppositely propagating spots (spots B and C in Figures 1.10(a) and 1.10(b)). Spot A then splits into two counter propagating spots (spots D and E in Figure 1.10(c)), which merge with spots B and C (Figure 1.10(c)). The solution over the entire interval then decays as two new spots form at the edge of the square cells to replace spots B and C (spots B$'$ and C$'$ in Figure 1.10(d)). The process then repeats periodically. The primary difference between these patterns and the inverted U's found with regular diffusion, e.g., Figure 1.2(b), is that the interior spot splits into two rapidly counter propagating spots over such a rapid timescale that the apex appears flat and the interval of the cell appears to "fire" as one (essentially flat) unit.

In an asymmetric square cell, (e.g., the cell centered at $x \simeq 5.3$ in Figure 1.9(a)), either a spot forms closer to one of the oppositely propagating spots, or one of the oppositely propagating spots itself grows and propagates more quickly. The dynamics of this square cell exhibiting the latter scenario is illustrated in Figures 1.11(a)-1.11(d). A growing spot (spot B in Figure 1.11(a) and 1.11(b)) propagates toward the more slowly growing spot (spot A). The two spots then merge leading to an asymmetric structure (Figure 1.11(d)).

We next consider the effect of deterministic initial conditions. Figures 1.12(a) - 1.12(g) are generated using $u = \cos mx$ and $v = \sin mx$ for various m as initial conditions. All other parameters are the same for all of the figures and are the same as the parameters employed in

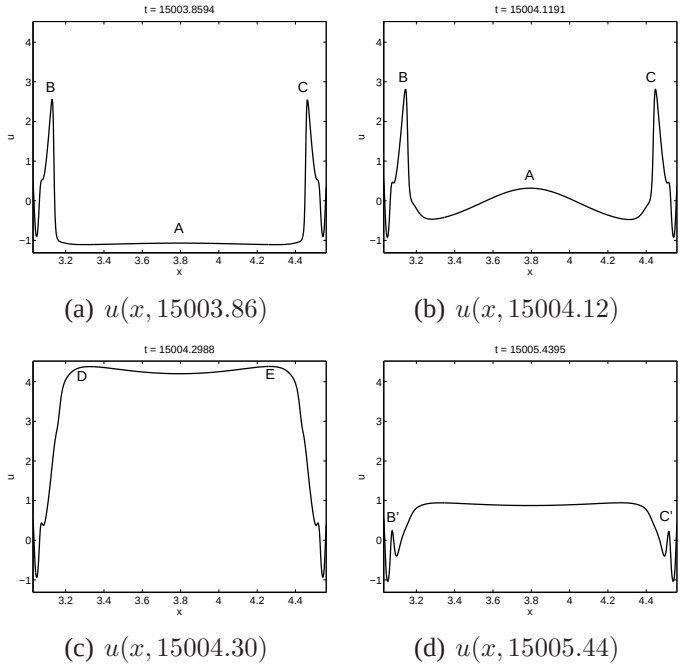

(a) $u(x, 15003.86)$ (b) $u(x, 15004.12)$

(c) $u(x, 15004.30)$ (d) $u(x, 15005.44)$

Figure 1.10. Line plots describing details of the symmetric spatiotemporal cell of Figure 1.9(d) at specific instants of time. A spot is created in between two oppositely propagating spots ((a) and (b), which splits into two counter propagating spots that are annihilated with the oppositely propagating spots (c). Two new spots are formed to replace the two oppositely propagating spots (d).

Figures 1.9(a)-1.9(c). For $m = 1, \ldots, 10$, in cases when we found spatiotemporal cells (when $m = 1, 2, 3, 4, 5, 8, 9$), aside from the two cells in the $m = 1$ case (Figure 1.12(a)), the number of square cells was equal to m. The square cells were all uniformly spaced, symmetric and of the same size. For $m = 6, 7, 10$, we found stationary stripes. For $m > 10$ we have only computed for $m = 60$ and $m = 180$ which yielded pure Hopf (horizontal stripes) and pure Turing (stationary vertical stripes), respectively.

The individual square cells are similar to the symmetric square cells obtained for random initial conditions, e.g., Figure 1.9(c). The primary effect of the deterministic initial conditions is that the steady state involves uniformly spaced and equal sized square cells. The effect of

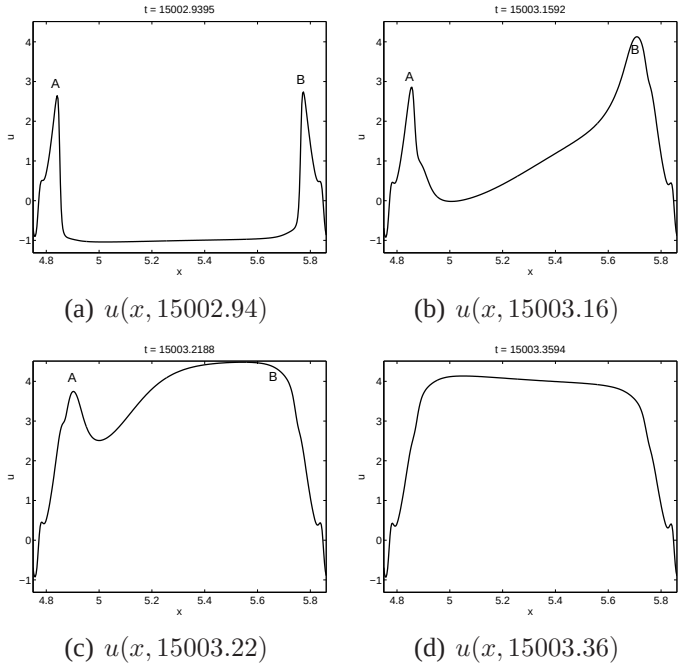

(a) $u(x, 15002.94)$ (b) $u(x, 15003.16)$

(c) $u(x, 15003.22)$ (d) $u(x, 15003.36)$

Figure 1.11. Line plots describing details of an asymmetric spatiotemporal cell of Figure 1.9(a) centered at $x \simeq 5.3$ at specific instants of time. Spot B grows and propagates more quickly than spot A ((b) and (c)) so that the spots merge at a location closer to spot A ((d)).

sinusoidal initial data for regular diffusion was similar, as in most cases we obtained cells equal in number to m. In some cases, we obtained identical evenly spaced cells that were either symmetric or asymmetric, depending on the value of m. In other cases, the cells differed in size,were not evenly spaced, and differed in number from m. For certain values of m, we also obtained breathing stripes. In all cases, the apex of all cells had a marked inverted U shape, in contrast to the cells with flat apexes obtained in the anomalous case.

In summary, for all three (α, β) pairs, stationary stripe patterns were observed for small z, followed by mainly spatially homogeneous oscillations (horizontal stripes) for larger z. In the case of $(\alpha, \beta) = (1.1, 1.1)$, the steady states returned to stationary stripes as z was increased.

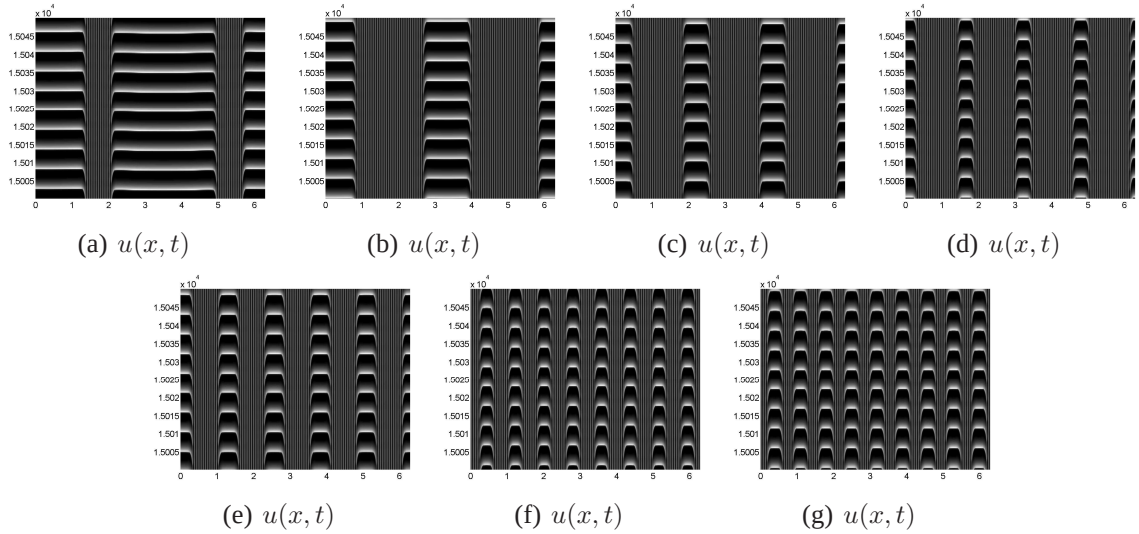

(a) $u(x,t)$ (b) $u(x,t)$ (c) $u(x,t)$ (d) $u(x,t)$

(e) $u(x,t)$ (f) $u(x,t)$ (g) $u(x,t)$

Figure 1.12. Spatiotemporal patterns of u for anomalous diffusion with $\alpha = \beta = 1.5$, $z = 1.6$, $B = 7.76$ and $\eta = 0.67$. Initial conditions were $u = \cos mx$, $v = \sin mx$ with (a) $m = 1$, (b) $m = 2$, (c) $m = 3$, (d) $m = 4$, (e) $m = 5$, (f) $m = 8$, and (g) $m = 9$. With the exception of (a), the number of spatiotemporal cells is equal to m and all cells in each figure are of the same size and spaced evenly, and also oscillate in phase. For $m = 1$, the number of cells is $2m = 2$, and while the cells are spaced evenly, they are not equal in size and oscillate out of phase.

In the case of $(\alpha, \beta) = (1.5, 1.5)$ and $(2, 2)$, steady states with spatiotemporal patterns were observed as z was increased before the steady states returned to mainly stationary stripes.

Spatiotemporal patterns were observed with $(\alpha, \beta) = (2, 2)$ for $z = 1.2$ and 1.4, while for $(\alpha, \beta) = (1.5, 1.5)$, they were observed for $z = 1.4$, 1.6, and 1.8 (the $z = 1.8$ case yielded nothing that had not been seen with $z = 1.4$ and $z = 1.6$ and is not shown). For both regular and anomalous diffusion there seem to be a large number of stable steady states, as in virtually all cases different initial conditions gave different steady states. In both cases, as z was increased, the steady states became more stripe-dominated, while for the same z, regular diffusion yielded more stripe-dominated steady states.

In general, patterns obtained with regular diffusion were more diverse, as breathing stripes (Figure 1.2(a)), inverted U's with a pronounced peak (Figure 1.2(b)), multiple traveling dislocations (Figure 1.2(c)), and inverted U's (Figure 1.7(d)) were not observed for anomalous diffusion. For anomalous diffusion, the predominant pattern appears to be that of spatiotemporal cells in the shape of inverted U's with a square apex, embedded in a mainly Turing structure of vertical stripes. This is something that we did not find with regular diffusion. With random initial data, the cells occur in different sizes and numbers, and stable steady states with essentially any inter-cell spacing and number of cells appear possible.

For sinusoidal initial conditions with wave number m only steady states with symmetric and uniformly spaced cells (with flat apexes) were found. With $m = O(1)$ the resulting steady state had exactly m cells with the exceptions described above. For larger values of m, only pure Turing and pure Hopf steady states were found. In the case of regular diffusion, breaks in the symmetry of the steady states were observed, as described above, and the number of cells was not always equal to m.

1.5.2. The fully nonlinear regime with unequal diffusion exponents

We next consider the case $\alpha \neq \beta$. In this case s is no longer equal to 1 so that for the same value of z the values of B_{cr} and η_c are slightly different from the $\alpha = \beta$ case. Since we do not change the values of μ and η_2, both B and η change as a result of the unequal diffusion exponents. To keep these parameters from changing would require altering how far the system is into the nonlinear regime as well as its closeness to the C2THP, and this could result in a significant qualitative change in the patterns not attributable to unequal diffusion exponents.

We first kept $\beta = 1.5$ while setting α to 1.4 and then to 1.6. For each α, we computed steady states starting from three sets of initial conditions: the same random initial conditions used in Section 1.5.1, the same sinusoidal initial conditions used in Section 1.5.1, and the steady states computed from random initial conditions with $\alpha = \beta = 1.5$ and $z = 1.6$. In this last case, we took the solutions $u(x)$ and $v(x)$ at $t = 1.5 \times 10^4$ and set them as initial conditions for computations with the same z and different α.

For $\alpha = 1.6$, $\beta = 1.5$, and $z = 1.6$ ($B = 8.57$, $\eta = 0.672$), the only steady states we found were stationary stripes. In contrast, for $\alpha = 1.4$, $\beta = 1.5$ we did find spatiotemporal patterns. Figures 1.13(a) - 1.13(c) show steady states for this case obtained from the same initial conditions employed in Figures 1.9(a) - 1.9(c). Figure 1.13(d) is a closeup of the solution shown in Figure 1.13(c).

There are two primary differences between Figures 1.13(a) - 1.13(c) (unequal diffusion exponents) and Figures 1.9(a) - 1.9(c) (equal diffusion exponents). In the former case regions of vertical stripes (Turing type modes) are very much reduced compared to the equal diffusion exponent case. For the unequal diffusion case, the solution appears to be dominated by nearly spatially homogeneous regions that oscillate in time (i.e., Hopf type regions). The second difference is that in contrast to the very slight U-shaped apexes for the $\alpha = \beta$ case solutions with $(\alpha, \beta) = (1.4, 1.5)$ have a very marked inverted U-shaped apex, similar to those seen in Figures 1.7(d) - 1.7(f) for $(\alpha, \beta) = (2, 2)$.

A similar difference was observed when the initial conditions were set as sinusoidal functions. Figures 1.14(a) - 1.14(j) show more Hopf-dominated steady states than do Figures 1.12(a) - 1.12(g), which correspond to steady states with $\alpha = \beta = 1.5$. Further, unlike the $\alpha = \beta = 1.5$

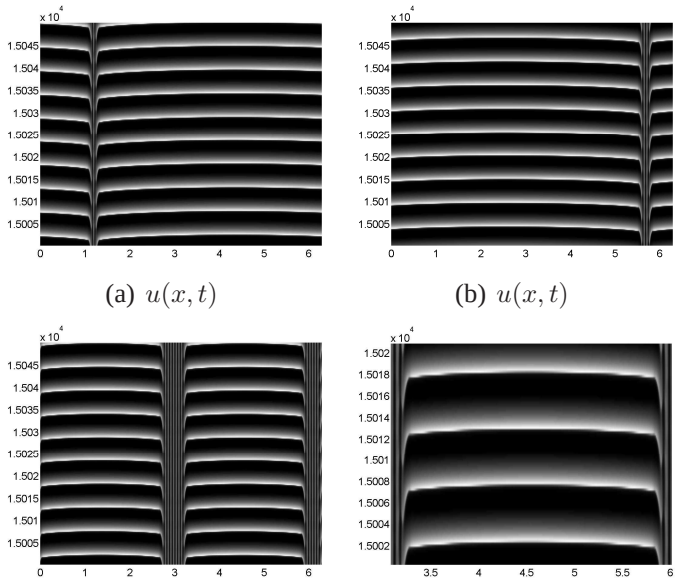

Figure 1.13. Spatiotemporal patterns of u for anomalous diffusion with $\alpha = 1.4$, $\beta = 1.5$, $z = 1.6$, $B = 7.11$ and $\eta = 0.66$. The figures differ only in initial condition. The same random initial conditions were used in Figures 1.9(a) - 1.9(c), and match up according to letter label. In comparison to Figures 1.9(a) - 1.9(c), these show a more Hopf-dominant set of steady states. Figure (d) is a close up of the right spatiotemporal cell of (c). The cells in (a) - (d) also exhibit a noticeable inverted U shape, compared to those of Figures 1.9(a) - 1.9(d), which exhibit a very slight U-shape. (a) and (b) are similar but differ in the number of stripes.

case, spatiotemporal patterns were obtained for sinusoidal initial conditions of all wave numbers $m = 1, \ldots, 10$.

As in the case with equal diffusion exponents, the $m = 1$ case (Figure 1.14(a)) appears to be an exception. For $m = 2, 3, 4$ (Figures 1.14(b) - 1.14(d)), we see m pairs of cells so that the total number of cells is $2m$. This is in contrast to the $m = 1$ case for which there is only one square cell. This is also in contrast to the case of equal diffusion exponents, where generally the number of square cells was m, not $2m$. This suggests that the cells split as $\beta - \alpha$ increases from zero. The $m = 2$ case is also an exception in that there are cells of unequal size that oscillate

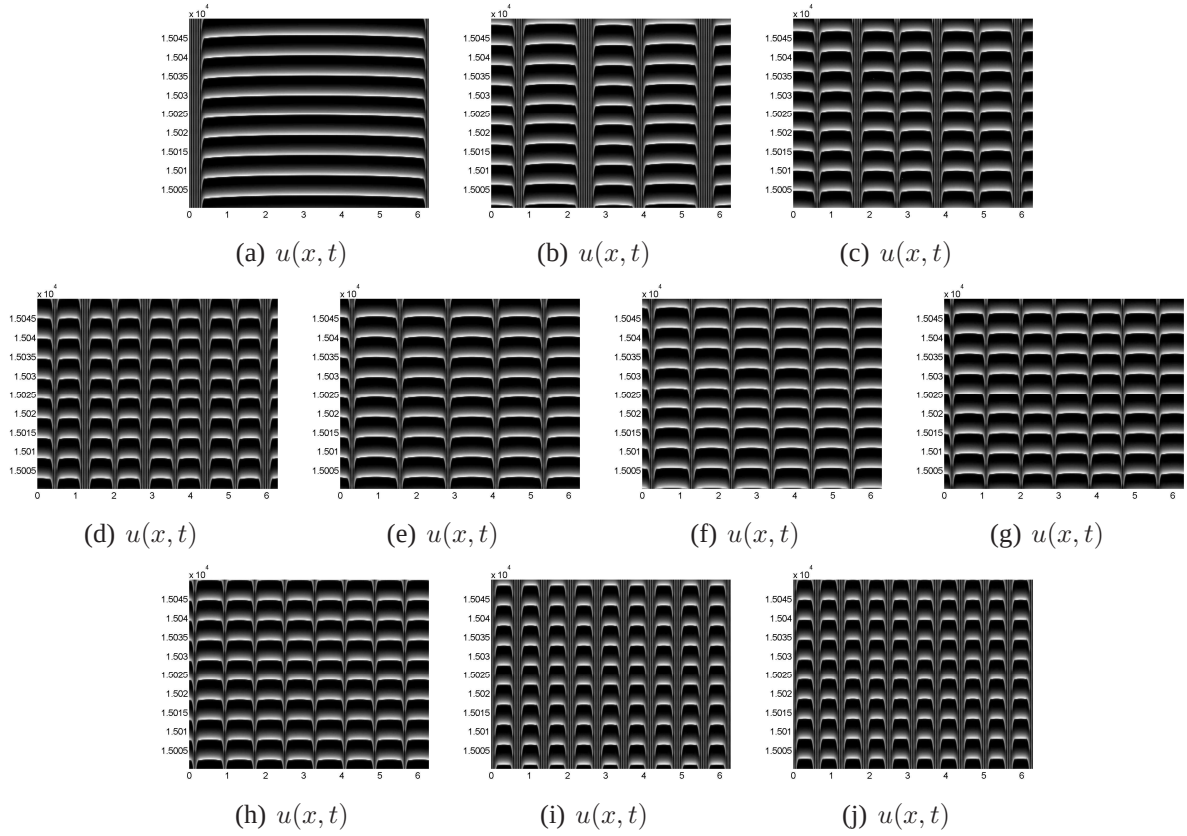

(a) $u(x,t)$ (b) $u(x,t)$ (c) $u(x,t)$

(d) $u(x,t)$ (e) $u(x,t)$ (f) $u(x,t)$ (g) $u(x,t)$

(h) $u(x,t)$ (i) $u(x,t)$ (j) $u(x,t)$

Figure 1.14. Spatiotemporal patterns of u for anomalous diffusion with $\alpha = 1.4$, $\beta = 1.5$, $z = 1.6$, $B = 7.11$ and $\eta = 0.66$. Initial conditions were $u = \cos mx$, $v = \sin mx$ with (a) $m = 1$, (b) $m = 2$, (c) $m = 3$, (d) $m = 4$, (e) $m = 5$, (f) $m = 6$, (g) $m = 7$, (h) $m = 8$, (i) $m = 9$, and (j) $m = 10$. Unlike in Figure 1.12(a), the $m = 1$ case ((a)) contains only one spatiotemporal cell. (b) - (d) contain pairs of cells equal in number to m. In (b), the two smaller cells oscillate in phase with each other, as do the two larger cells. All cells in all other figures are of equal size and oscillate in phase. In (e) - (j), the trend is the same as in the case of equal diffusion exponents in that the number of cells is equal to m.

with a phase difference. In all other cases, the cells are of equal size and oscillate in phase. In Figures 1.14(e) - 1.14(j) we do not find cell splitting and the number of cells equals m, similar to the $\alpha = \beta$ case.

When we used the steady state solutions found in Figures 1.9(a) - 1.9(c) as initial conditions for the $(\alpha, \beta) = (1.4, 1.5)$ runs, there were cases when the steady state became more Turing

dominated and the spatiotemporal cells attain a more inverted U shape (e.g. Figure 1.15(a)) and cases when the difference was only in the shape of the cells (e.g. Figures 1.15(b) and 1.15(c)). Note that Figure 1.15(a) is a continuation of Figure 1.9(a) with a different value for α, Figure 1.15(b) of Figure 1.9(b), and Figure 1.15(c) of Figure 1.9(c).

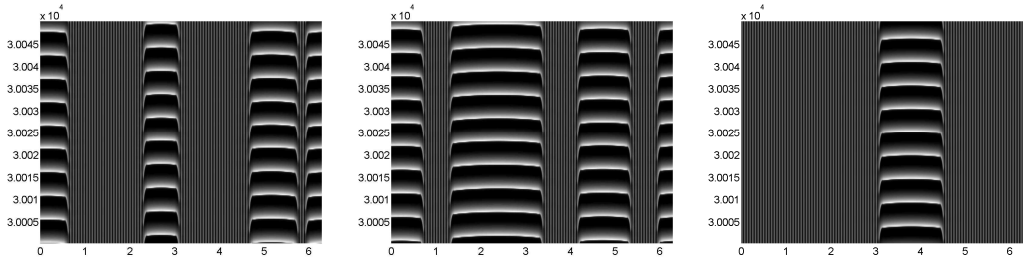

(a) $u(x,t)$ (b) $u(x,t)$ (c) $u(x,t)$

Figure 1.15. Steady states with $\alpha = 1.4$, $\beta = 1.5$ using as initial conditions the steady states computed with $\alpha = \beta = 1.5$ (Figures 1.9(a) - 1.9(c), respectively). The only difference between (b) and 1.9(b) and (c) and 1.9(c) is that the cells of (b) and (c) have a more rounded apex. Going from Figure 1.9(a) to (a), we see that, in addition to the more rounded cells, the number of cells has decreased, yielding a more Turing-dominant solution.

For the $(\alpha, \beta) = (1.6, 1.5)$ case, while we obtained only pure Turing steady states with $z = 1.6$, we found spatiotemporal patterns with $z = 1.4$ ($B = 7.35$ and $\eta = 0.649$) when starting with the same random initial conditions used throughout. Compared to the $z = 1.4$ runs with equal diffusion exponents, Figures 1.16(a) - 1.16(c) show more Turing-dominant steady states.

The predominant feature in Figures 1.16(a) - 1.16(c) is the presence of spatiotemporal cells with a U-shaped apex, which are described in Section 1.5.1. They indicate that a spot, born away from the stripes, splits into two counter propagating spots, which are then annihilated at the stripes. The difference between the cells of Figures 1.16(a) - 1.16(c) and those described in Section 1.5.1 is that, in the former, the two spots on either side of the cell do not grow as

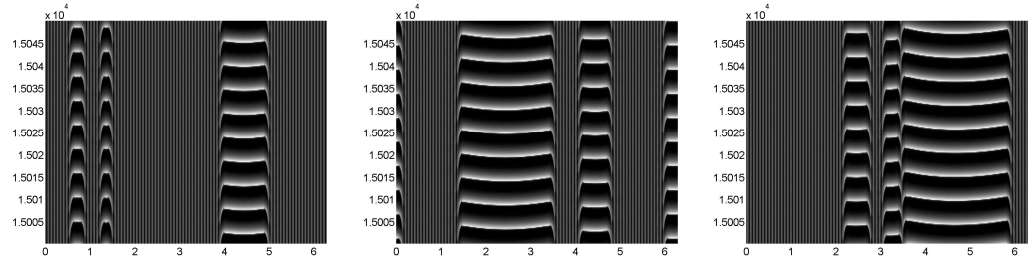

(a) $u(x,t)$ (b) $u(x,t)$ (c) $u(x,t)$

Figure 1.16. Spatiotemporal patterns of u for anomalous diffusion with $\alpha = 1.6$, $\beta = 1.5$, $z = 1.4$, $B = 7.35$ and $\eta = 0.649$. The figures differ only in initial condition. The two smaller cells of (a) resemble the inverted U's of Figure 1.7(f). The cells in (b) are all qualitatively similar, while there are two immediately adjacent asymmetric cells in (c).

large as they do in the latter, which is why the U-shape is much more noticeable in the former. The two smaller cells in Figure 1.16(a) are similar to the small inverted U's of Figure 1.7(f) and oscillate in phase. The cells of Figure 1.16(b) are qualitatively similar, while in Figure 1.16(c), we see an asymmetric spatiotemporal cell immediately adjacent to a U-shaped cell, which is also asymmetric in that the left spot decays slightly more slowly than does the right.

When we set one of the diffusion exponents equal to 2 (regular diffusion) and the other to a value less than 2 (anomalous diffusion), most of the patterns that we found were comparable to those described above. However, for $(\alpha, \beta) = (2, 1.4)$, and $z = 1.4$ ($B = 87.4$, $\eta = 0.708$), starting with random initial conditions, we found a steady state consisting entirely of spatiotemporal spots (Figures 1.17(a) and 1.17(b)). Different random initial conditions yielded qualitatively very similar steady states, the only difference being the size of the individual spots. While the pattern of spots may be due in part to the much larger value of B, from the limited number of computations that we performed, we did not find any similar steady states for the same or comparable values of B under regular diffusion. Note a similar spot pattern was found

by De Wit et al. for regular diffusion in [**22**] with $B = 10.3$, closer to the weakly nonlinear regime and farther from the C2THP.

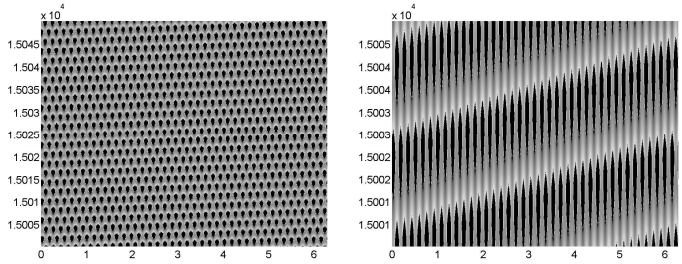

(a) $u(x,t)$ (b) $u(x,t)$

Figure 1.17. Spatiotemporal patterns of u for anomalous diffusion with $(\alpha, \beta) = (2, 1.4)$, $z = 1.4$, $B = 87.4$, and $\eta = 0.708$. (b) shows a closeup of the bottom portion of (a).

The dynamics of the spots of Figures 1.17(a) and 1.17(b) is illustrated in Figures 1.18(a) - 1.18(d), which depict half of a period (approximately 2 units of time) and correspond to the lower half of Figure 1.17(b). The dark spots in Figures 1.17(a) and 1.17(b) are due to the global minima of u in Figures 1.18(a) - 1.18(d), while the lightest regions are due to the traveling pulse that appears to be traveling at a constant or near constant speed, seen centered at $x \simeq 4.8$ in Figure 1.18(a), $x \simeq 0.6$ in Figure 1.18(b), $x \simeq 2.7$ in Figure 1.18(c) and back to $x \simeq 4.8$ in Figure 1.18(d). The valleys accounting for the black spots change in width, which can be seen in Figures 1.17(a) and 1.17(b), as a spot is very narrow near the beginning and end of its duration, and wider during the middle. Locations at which valleys exist turn into locations of peaks when the pulse arrives. Once the pulse passes, the valleys reappear, but with a shift in space relative to their previous locations, which can be clearly seen in Figure 1.17(a). The result in the space-time plot is that one row of spots runs diagonally, and a row is displaced by one

spot's width relative to a neighboring row. Over one full period (approximately 4 units of time), the valleys return to the same locations.

In summary, it appeared that the $(\alpha, \beta) = (1.4, 1.5)$ steady states with $z = 1.6$ were more Hopf-dominant than the cases with $(\alpha, \beta) = (1.5, 1.5)$. In the case of the continuation runs, however, this trend was not seen. In the case of $(\alpha, \beta) = (1.6, 1.5)$ with $z = 1.4$, the steady states appeared to be more Turing-dominant than the same runs with $(\alpha, \beta) = (1.5, 1.5)$. This trend seems more consistent, as pure Turing steady states were found for $z = 1.6$ for all initial conditions mentioned above. Further, the spatiotemporal cells, which appear to have a flat apex in the $(\alpha, \beta) = (1.5, 1.5)$ case, take on an inverted U shape in the $(\alpha, \beta) = (1.4, 1.5)$ case and a U-shape in the $(\alpha, \beta) = (1.6, 1.5)$ case. In the case when one component undergoes regular diffusion and the other anomalous, we found a series of adjacent valleys that periodically turn into peaks when a traveling pulse arrives, accounting for the dark spots and their arrangement in Figure 1.17(a). Similar structures were found for regular diffusion in [**22**].

Since in all of these cases, B and η change as described above it is difficult to infer whether these differences are due solely to the difference in diffusion exponents.

1.6. Discussion

Using weakly nonlinear analysis, we derived a pair of coupled amplitude equations that describe the evolution of the Turing and Hopf modes over a long time scale near a C2THP of the superdiffusive Brusselator model. The amplitude equations have a similar form to those of the regular model, but differ in three regards: the two spatial derivatives in the pair of equations are with respect to two different length scales, the equation describing the evolution of the Hopf mode contains an integro-differential operator, which reflects the non-local effect of

anomalous diffusion, and finally, the coefficients of the amplitude equations differ from those of the regular amplitude equations. The latter two differences contribute to the differences in the long wave stability criteria of the special solutions, which are described in Section 1.4. Two of these criteria were confirmed with numerical computations in the weakly nonlinear regime, while criteria involving both the Turing and Hopf modes were inconclusive due to numerical difficulties arising from small ϵ.

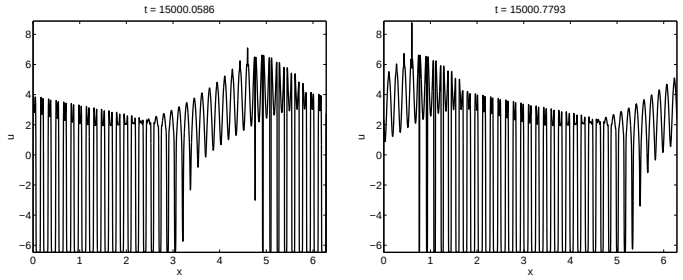

(a) $u(x, 15000.06)$ (b) $u(x, 15000.78)$

(c) $u(x, 15001.42)$ (d) $u(x, 15002.08)$

Figure 1.18. Line plots describing details of the spots of Figures 1.17(a) and 1.17(b) at specific instants of time. The global minima, account for the dark spots in Figures 1.17(a) and 1.17(b).

In computations in the fully nonlinear regime, one of the dominant spatiotemporal structures that we found under anomalous diffusion were the square-shaped spatiotemporal cells with either a flat apex ($\alpha = \beta$), an inverted U shaped apex ($\alpha < \beta$), or a U-shaped apex ($\alpha > \beta$).

Qualitatively similar structures were found under regular diffusion with a similar range in values of z, though the square and flat cells embedded in a mainly Turing structure was something that we did not find under regular diffusion. There was also behavior that we found under regular diffusion that we did not find with anomalous diffusion, such as breathing stripes and multiple traveling dislocations that appear to repel each other. With equal diffusion exponents, it appeared that the effect of anomalous diffusion was to delay the onset of Hopf-type behavior in terms of increasing z, and also to inhibit spatiotemporal pattern formation, as was seen when we found only pure Turing and pure Hopf solutions with $\alpha = \beta = 1.1$. The main effect of unequal but close diffusion exponents appeared to be to alter the apex shape of the spatiotemporal cells from the case of equal diffusion exponents. When one diffusion was regular and the other anomalous, we found spatiotemporal spots corresponding to valleys whose sizes and positions changed periodically, similar to structures presented in [**22**]. More generally, we found a large number of steady state patterns consisting of a localized region or regions of stationary stripes in a background of time periodic cellular motion, as well as a localized region or regions of time periodic cells in a background of stationary stripes. Each such pattern lies on a branch of such solutions, is stable and corresponds to a different initial condition. The patterns correspond to the phenomenon of pinning of the front between the stripes and the time periodic cellular structure. The different branches live in a region called the pinning region in which such solution branches snake back and forth. The idea of pinning was originally suggested by Pomeau [**88**], who referred to pinning as locking. The idea has been considered and extended by a number of researchers, including Knobloch and coauthors [**1**, **10**, **12**], who considered localized stationary patterns in a background of a stationary, spatially uniform state, as well as in a background of small amplitude traveling waves, Bensimon et. al. [**5**], who considered localized traveling rolls

(stripes) in a background of a stationary, spatially uniform state, and Malomed et. al [**69**], who considered localized hexagonal patterns in a background of stationary stripes. These scenarios involve a subcritical bifurcation leading to bistability between the basic state and the bifurcated state after the latter turns around to become stable. In contrast, our study involves bistability between two stable supercritical branches which exist near a codimension two bifurcation point. We note that many of these patterns disappear when the size L of the domain is considerably reduced. In the next chapter, we analyze in detail solutions exhibiting Turing-Hopf coexistence near the C2THP when both branches are stable and bifurcate supercritically from the homogeneous state. These solutions are qualitatively similar to those in this chapter (e.g., Figure 1.12). However, while only stable solutions may be computed by the time-evolution method of this chapter, we employ the method of continuation to compute both stable and unstable solutions in the next chapter. In this way, we obtain the snaking structure of the entire branch of solutions.

CHAPTER 2

Homoclinic Snaking Near a Codimension Two Turing-Hopf Bifurcation Point

In this chapter, spatiotemporal Turing-Hopf pinning solutions near the codimension two Turing-Hopf point of the one dimensional Brusselator model are studied. Both the Turing and Hopf bifurcations are supercritical and stable. The pinning solutions exhibit coexistence of stationary stripes of near critical wavelength and time periodic oscillations near the characteristic Hopf frequency. Such solutions of this nonvariational problem are in contrast to the stationary pinning solutions found in the subcritical Turing regime for the variational Swift-Hohenberg equations, characterized by a spatially periodic pattern embedded in a spatially homogeneous background state. Numerical continuation was used to solve periodic boundary value problems in time for the Fourier amplitudes of the spatiotemporal Turing-Hopf pinning solutions. The solution branches are organized in a series of saddle-node bifurcations similar to the known snaking structures of stationary pinning solutions. We find two intertwined pairs of such branches, one with a defect in the middle of the striped region, and one without. Solutions on one branch of one pair differ from those on the other branch by a π phase shift in the spatially periodic region, i.e., locations of local minima of solutions on one branch correspond to locations of maxima of solutions on the other branch. These branches are connected to branches exhibiting collapsed snaking behavior, where the snaking region collapses to almost a single value in the bifurcation parameter. Solutions along various parts of the branches are described

in detail. Time dependent depinning dynamics outside the saddle-nodes are illustrated, and a time scale for the depinning transitions is numerically established. Wavelength variation within the snaking region is discussed, and reasons for the variation are given in the context of amplitude equations. Finally, we compare the pinning region to the Maxwell line found numerically by time evolving the amplitude equations. This chapter is based on joint work with Yi-Ping Ma of the Department of Geophysical Sciences at the University of Chicago and Department of Engineering Sciences and Applied Mathematics at Northwestern University.

2.1. Introduction

Localized stationary solutions of reaction-diffusion systems characterized by the coexistence of a flat, i.e., stationary (time independent), spatially homogeneous state with a spatially periodic state have recently been the subject of much analysis. In the context of variational systems, a stationary front between two stationary states is expected when both states possess equal free energy. The point (or curve) in parameter space at which the free energies are equal is referred to as a Maxwell point (curve). When the coexistence is between two flat states, a perturbation from the Maxwell point results in a time dependent invasion of the energetically favored state into the other. In [**88**], Pomeau explains that when the coexistence is between a flat and spatially periodic state, there is a broadening of the Maxwell point. Thus, within a finite-width region in parameter space around the Maxwell point, a continuum of such solutions exist. The broadening of the Maxwell point may be explained by the fact that the energy difference must be sufficiently large in order to displace the front connecting the coexisting states by one wavelength of the periodic pattern. Equivalently, displacement of the front only occurs sufficiently far from the Maxwell point. This effect has been referred to (e.g., [**10**] and

references therein) as the pinning of the spatially periodic front. By assembling two such fronts back-to-back, one can construct stationary solutions in which a finite region of spatially periodic states is embedded in a background of flat state. Such solutions are known as spatially localized states in other contexts (cf. [**55**]), but in this chapter we refer to them as pinning solutions. The pinning phenomenon is explained in detail in [**88**].

The (variational) 2–3 and 3–5 Swift-Hohenberg equations for a real scalar field $u(x,t)$, which exhibit quadratic–cubic, and cubic–quintic nonlinearities, respectively, have been studied extensively to illustrate the phenomenon of pinning. Most of these studies have focused on the subcritical Turing regime where there is bistability between the flat and spatially periodic states. In [**10**] for the 2–3 Swift-Hohenberg equation on an unbounded domain, a continuum of pinning solutions was shown to exist on branches that "snake" back and forth in the bifurcation diagram forming a series of saddle-node bifurcations. As predicted in [**88**], the snaking region was found to straddle the Maxwell point. Solutions on these branches are even in space and thus preserve the spatial reversibility symmetry $(x \to -x, u \to u)$ of the 2–3 Swift-Hohenberg equation. The snaking region consists of two intertwined branches, with solutions on one branch having a local maximum in the central part of the spatially periodic region, and solutions on the other branch having a local minimum. Solutions at different points along one branch differ in the width of the spatially periodic region. In particular, traversal through two saddle-nodes or equivalently one back and forth cycle on the snaking branch corresponds to two wavelengths of the spatially periodic state being added or subtracted at the edges of the spatially periodic region. In addition to the two snaking branches of symmetric solutions, a series of pitchfork bifurcations near the saddle-nodes on these branches were found to be connected through a series of rungs (or ladders) of asymmetric solutions. The entire bifurcation diagram of stationary

pinning solutions was therefore dubbed snakes-and-ladders. Outside the snaking region, a depinning transition was shown to occur in which wavelengths were either nucleated or destroyed at the edges of the spatially periodic region. The speed of depinning was calculated analytically and confirmed numerically. The conservation of a spatial Hamiltonian was shown to select the wavelength of the spatially periodic state within the snaking region, and the wavelength variation across the snaking region was qualitatively explained based on the free energy variation of the flat and spatially periodic states. Studies of stationary pinning solutions whose analogs are not addressed in this chapter include the effects of finite domain lengths on snaking. In [**6**], it was shown that snaking branches in a spatially periodic domain terminate on branches of spatially periodic states whose wavenumber depends on the domain length. It was also determined that these termination points corresponded to the Eckhaus instability boundary. In [**42**], it was found that non-periodic and non-Neumann boundary conditions eliminated entirely spatially periodic states of the Swift-Hohenberg equation, replacing them with states with defects at or near the boundary. In this case, instead of terminating on spatially periodic branches, the snaking branches either exit the snaking region and develop into branches of large amplitude patterns, or they may turn back toward small amplitude and terminate at other primary bifurcation points on the flat state. In [**8**], a multiple scale analysis was used to derive an envelope equation for pinning solutions of the non-symmetric generalized Swift-Hohenberg equation. More recently, the entire snakes-and-ladders bifurcation diagram, including in particular the width of the pinning region, was analytically determined through a multiple scale analysis beyond all algebraic orders for the 2–3 Swift Hohenberg equation near the onset of subcriticality (cf. [**14**]). For the 3–5 Swift-Hohenberg equation, the additional up-down symmetry $(x \to x, u \to -u)$ admits two additional snaking branches of odd solutions (cf. [**11**, **23**]). In contrast to the 2–3 case,

traversal through four saddle-nodes on one snaking branch is required to add two wavelengths at the edges of the spatially periodic region in the 3–5 Swift-Hohenberg equation (cf. [**9**]).

Another explanation for the existence of stationary pinning solutions has been given in terms of reversible spatial dynamics (see e.g., [**11**, **17**, **18**, **67**], or [**27**–**30**] for spike patterns in singularly perturbed reaction-diffusion systems). In this framework, the locations in the complex plane of the spatial eigenvalues (in the case of flat states) or spatial Floquet multipliers (in the case of spatially periodic states), along with spatial reversibility are the key components responsible for the existence of pinning solutions. The most complete account to date of the snakes-and-ladders bifurcation diagram from this perspective can be found in [**4**], which formulated a set of hypotheses about the connecting orbit between the flat and spatially periodic states that guarantees snaking. Whereas the free-energy description is limited only to pinning solutions of variational systems, the spatial dynamics framework extends the theory of pinning to a much broader class of systems. In particular, a cubic-quintic Ginzburg-Landau equation can be derived as a truncated normal form near weakly subcritical Turing bifurcations, and its solutions yield insights into the location of the pinning region in both variational and nonvariational systems. While no true snaking is possible in this equation due to phase rotation symmetry of the spatial dynamical system, branches emanating from Eckhaus bifurcation points exhibiting snake-like behavior (termed “protosnaking”) were found near the nonvariational analog of the Maxwell point (cf. [**50**]). Stationary pinning solutions organized along snaking branches have indeed been observed in many nonvariational systems. In [**39**], two snaking branches were computed for the Lugiato-Lefever equation; in addition, it was shown that there are other pinning solutions found by directly computing the invariant manifolds to the flat and spatially periodic states. A study of a nonvariational extension of the 3–5 Swift-Hohenberg equation

in [**43**] stressed that asymmetric pinning solutions on the ladders are expected to travel in nonvariational systems. In [**67**], the forced complex Ginzburg-Landau equations were shown to exhibit a different growth mechanism by which periodic structures were nucleated or destroyed in the middle of the spatially periodic region as opposed to the edges. In this case the codimension two point marking the onset of snaking corresponds to the simultaneous occurrence of a (codimension-one) heteroclinic orbit between two inequivalent flat states and a (codimension-one) supercritical Turing bifurcation on one of them. Hence the nature of the bistability between flat and spatially periodic states in this study differs from the aforementioned studies that mainly focused on subcritical Turing bifurcations.

Nonvariational systems allow for temporal oscillations, which have not been considered in the context of snaking structures of pinning solutions. In particular, pinning solutions characterized by a coexistence of Turing and Hopf states have been observed in [**22**] in the vicinity of a codimension two Turing-Hopf point (C2THP) of the (nonvariational) Brusselator model (see e.g., [**79**, **85**, **100**] and the references therein), where both the Turing and Hopf bifurcations were supercritical and stable. The Brusselator model, describing a simplified autocatalytic reaction, has long been a paradigm of nonlinear analysis and is given by

$$u_t = Du_{xx} + E - (B+1)u + vu^2\,, \qquad x \in \mathbb{R}, \qquad t > 0; \tag{2.1a}$$

$$v_t = v_{xx} + Bu - vu^2\,, \qquad x \in \mathbb{R}, \qquad t > 0, \tag{2.1b}$$

subject to appropriate initial and boundary conditions. Note that, unlike the Swift-Hohenberg equations, the spatial dynamics of (2.1) are not Hamiltonian. Spatiotemporal patterns near the Brusselator C2THP have also been computed for the superdiffusive variant of (2.1) in [**96**]. Both

of these studies were restricted to using only time evolution techniques to compute the pinning solutions, which only yielded a very narrow view of all possible Turing-Hopf pinning solutions, since only stable solutions can be computed with a standard initial boundary value problem (IBVP) code. Furthermore, the manner in which these solutions are organized on solution branches is difficult to ascertain. In this chapter, we use AUTO [**26**] to solve boundary value problems in time for the $0, \ldots, N$ spatial Fourier amplitudes of the solutions u and v to (2.1) for appropriately large N, under the assumption of spatial periodicity (the $-N, \ldots, -1$ modes are also accounted for since we only consider real solutions). In this way, we obtain both stable and unstable solution branches, and the structure of these branches is readily obtained. Solutions on these branches resemble stationary pinning solutions, only with the flat state replaced by Hopf-like temporal oscillations. The respective growth rates of the Turing and Hopf modes near the C2THP assume the roles of the free energies of the coexisting states in variational systems, with larger growth rates implying greater dominance. While the equality of growth rates is not the analogous Maxwell condition, the "physical" roles of the growth rates and the free energies in the respective systems are analogous. We remark that space-time solutions presented in this chapter involve interfaces between regions in space that oscillate in time, and regions that are spatially periodic and stationary in time. Such interfaces cannot be assigned to any of the four classes of defects solutions proposed in [**90**] for time-periodic solutions of reaction-diffusion systems, as the defects discussed generically serve as interfaces between only traveling waves of nonzero speed.

This chapter is organized as follows. In §2.2, we briefly review the derivation of the amplitude equations near the C2THP of (2.1) and give conditions for Turing-Hopf bistability. These results are used to facilitate a search in parameter space for Turing-Hopf pinning solutions. In

§2.3.1, we describe the equations used to compute the pinning solutions using the method of continuation in AUTO. We then present in §2.3.2 the snaking branches on which the pinning solutions exist and discuss their relationship to the pure Turing and pure Hopf branches. We describe the solutions found on these branches and how they vary as the solution branch is traversed. In §2.3.3, we illustrate the process by which solutions depin when parameters are set a distance δ outside of the snaking region, and give a numerical estimate of the scaling of the depinning speed with respect to δ. We give a qualitative explanation for the direction of depinning based on the relative dominance of the Turing and Hopf modes. In §2.3.4, we illustrate the dependence of the wavelength of the spatially periodic state on the parameters of the Brusselator model. In §2.3.5, we offer an explanation for the observed dependence in the framework of properties of the amplitude equations derived in §2.2. We then conclude and discuss open problems in §2.4.

2.2. Turing-Hopf Bistability

In this section, we briefly outline the derivation of the evolution equations for the amplitudes of the Turing and Hopf modes near the C2THP. For a detailed analysis, see [**53**], or [**96**] for the superdiffusive variant of Brusselator model. See [**110**] for a review of normal form theory near the codimension two point, and [**85**] and [**38**] for a weakly nonlinear analysis of Turing patterns of the regular and superdiffusive Brusselator models in two dimensions. Stability results from analysis of the amplitude equations will yield the regime of Turing-Hopf bistability in which pinning behavior is possible, as it is in this regime of bistability that the pure Turing and pure Hopf modes may coexist in physical space.

The system (2.1) has one spatially homogeneous steady state $(u, v)^\top = (E, B/E)^\top$. Here, $\top$ denotes the transpose. As B is increased past $B_H = 1 + E^2$, the basic state loses stability through a Hopf bifurcation yielding spatially homogeneous temporal oscillations of frequency $\omega_c = E$. As B is increased past $B_T = (1 + E\sqrt{D})^2$, a steady state Turing bifurcation occurs, yielding a stationary spatially periodic pattern with critical wavenumber $k_c = [E/(\sqrt{1+E^2} - 1)]^{1/2}$. When the Hopf and Turing bifurcations occur simultaneously, i.e., when $B_H = B_T$, the point in parameter space is referred to as a codimension two Turing-Hopf point. This condition is satisfied when $D = D_c = [(\sqrt{1+E^2} - 1)/E]^2$. To analyze the slow time evolution of the two modes near the C2THP, we let $B = B_H + \epsilon^2\mu$ and $D = D_c + \epsilon^2\rho$, where $0 < \epsilon \ll 1$ and μ and ρ are both $\mathcal{O}(1)$. When $\rho > 0$ ($\rho < 0$), the Hopf (Turing) bifurcation is the first to occur as B is increased. Introducing the slow time scale $T = \epsilon^2 t$ and the long spatial scale $X = \epsilon x$ and perturbing the steady state by $(u, v)^\top = (E, B/E)^\top + \epsilon \boldsymbol{a} A(X,T) e^{ik_c x} + \epsilon \boldsymbol{c} C(X,T) e^{i\omega_c t} + c.c.$, where $\boldsymbol{a} = ((E^2 + k_c^2)/B_H, 1)^\top$, $\boldsymbol{c} = (-E(E+i)/B_H, 1)^\top$, and $A(X,T)$ and $C(X,T)$ are the complex amplitudes of the Turing and Hopf modes, respectively, the amplitude equations are readily calculated as

$$A_T = \zeta A_{XX} + \gamma A - g|A|^2 A - \lambda |C|^2 A\,, \tag{2.2a}$$

$$C_T = (\kappa_r + i\kappa_i) C_{XX} + \nu C - (\beta_r + i\beta_i)|C|^2 C - (\delta_r + i\delta_i)|A|^2 C\,. \tag{2.2b}$$

The constants in (2.2) are given in the appendix. All constants in (2.2) are real and, with the exception of ν and γ, only functions of the parameter E. The coefficient ν is given by $\nu = \mu/2$, while γ is a function of μ, ρ, and E. The conditions for supercriticality of the Turing and Hopf bifurcations are $g > 0$ and $\beta_r > 0$, where the latter condition is always satisfied for the

Brusselator model. A value of E for which the former is satisfied is $E = 1.4$, which is the value used in all computations presented herein. For this value of E and $\rho > 0$, the bifurcation scenario is given in Figure 9(g) of [**53**]. The pure Turing mode stabilizes when μ (and thus the amplitude of the pure Turing mode) is sufficiently large to suppress growth of the Hopf mode. This value of μ can be readily computed from a linear stability analysis of (2.2). These weakly nonlinear results were used in the initial search for a pinning region in parameter space.

2.3. Snaking Structure and Pinning Solutions

In this section, we first introduce the numerical procedure to be used to compute the pinning solutions. Both time evolution of the PDE system (2.1) and continuation for a system of ODEs (given in §2.3.1), gotten by representing the solutions by a finite number of Fourier modes, are employed. We then present the main results regarding the existence of a robust region in parameter space in which stationary striped structures and time periodic oscillations coexist in the same spatial domain. Such solutions vary continuously with the parameters of (2.1) and lie on snaking branches, each of which is characterized by a series of saddle-node bifurcations similar in appearance to the well known snaking structures found in studies of stationary pinning solutions. Two intertwined pairs of such solution branches are shown to exist. The main difference between solutions on these two pairs of branches is that on one pair, a defect is present at the center of the striped region, and on the other pair, no defect exists. Solutions on one branch of one pair differ from those on the other branch by a π phase shift in the spatially periodic region, i.e., locations of local minima (maxima) of solutions on one branch correspond to locations of maxima (minima) of solutions on the other branch. We discuss where these branches bifurcate,

and describe the differences between solutions on different parts of each branch. For the non-defect pair of solutions, we discuss the depinning transition and wavelength selection. Lastly, we relate the results back to properties of the amplitude equations.

2.3.1. Numerical Methods

We employ two approaches to numerically determine the bifurcation branches and the structure and stability of the solutions on those branches. In the first approach we solve the IBVP for the PDE system (2.1) and evolve the initial conditions to their eventual steady states. To determine the structure and stability of the solution branches, we employ AUTO, a continuation package which follows solutions along the various branches and determines their stability. The IBVP solver was used to 1) perform parameter searches to determine the parameters for pinning, and 2) provide appropriate initial guesses to be used in the AUTO computations. AUTO was then used to compute all the solution branches that we found and determine their stability.

We now describe the process by which we employed time evolution to compute pinning solutions. To locate the region in parameter space where pinning is possible, we first solved the IBVP system (2.1) with $E = 1.4$ using a Fourier spectral method in space and a semi-implicit second order two step predictor-corrector method in time. The diffusion terms of (2.1) were treated implicitly while the reaction terms were treated explicitly. The latter were first computed in physical space before being transformed into Fourier space, where all time stepping was performed. The initial conditions for u and v were set as

$$(u,v)^\top = (E, B/E)^\top + \epsilon \text{Re}\left[\boldsymbol{a} e^{ik_c x}\theta(x) + \boldsymbol{c}(1-\theta(x))\right] ,$$
$$\theta(x) \equiv H(x+\ell/2) - H(x-\ell/2)\,; \qquad \ell < L\,, \tag{2.3}$$

on a domain of length L subject to periodic boundary conditions, where $H(x)$ is the Heaviside step function. Thus, the initial condition (2.3) contains a pure Turing mode on the interval $[-\ell/2, \ell/2]$ and a pure Hopf mode on $[-L/2, -\ell/2) \cup (\ell/2, L/2]$. The u component of (2.3) is depicted in Figure 2.1(a). Note that the basic state of u is $u = E = 1.4$.

Fixing $E = 1.4$ and setting μ (equivalently, B) sufficiently large as determined in §2.2 so that the pure Turing mode is stable, we varied ρ (equivalently, D) until (2.1) yielded a time periodic solution marked by the coexistence of Turing and Hopf modes on the same spatial domain. The large time behavior of such a solution is depicted in the space-time plot in Figure 2.1(b), which shows a nearly stationary striped region embedded in a background of low wavenumber Hopf-like oscillations. Note that the locations of the interfaces between the Turing and Hopf regions remain constant in time. In all space-time plots, the spatial variable x is plotted on the horizontal axis, the temporal variable t is plotted on the vertical axis, and dark (light) regions indicate larger (smaller) values of $u(x,t)$. Space-time plots of $v(x,t)$ simply appear as black-and-white inverted plots of u, and are thus not included.

Most of the solutions shown in this section resemble an interval in time of Figure 2.1(b) consisting of one complete cycle of the oscillatory region. Analogous to the well studied problems in homoclinic snaking of stationary solutions, (2.1) admits an infinite multiplicity of solutions similar to Figure 2.1(b) that differ in the width of the striped region. While Figure 2.1(b) appears to be time periodic, all solutions that we have computed by means of time evolution have

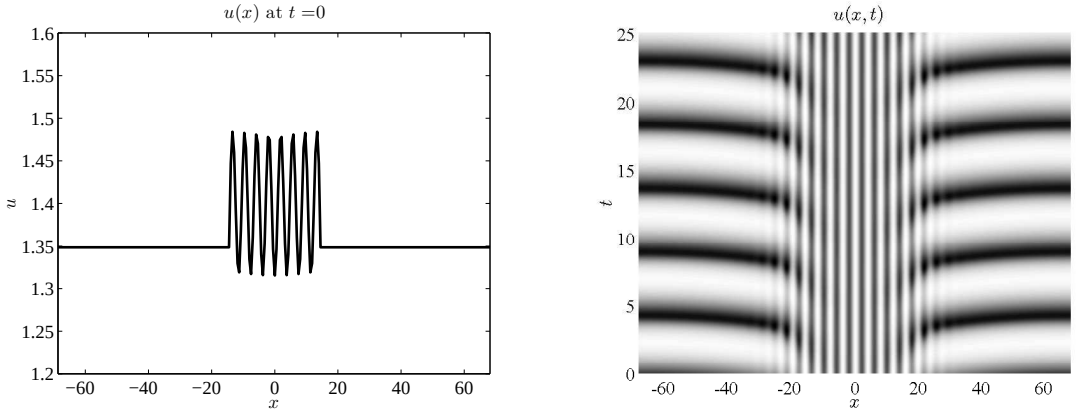

(a) typical initial condition for u (b) large time spatiotemporal behavior of u

Figure 2.1. (a) Line plot of a typical initial condition of u for $L \approx 137.37$, $E = 1.4$, $\epsilon = 0.1$, $\mu = 25$, and $\rho = 0.178$ (equivalently, $B = 3.21$, $D \approx 0.2666$). (b) Space-time plot of u for large time starting from the initial condition in (a). Turing and Hopf modes coexist on the same spatial domain in a time periodic solution.

exhibited a slight aperiodicity, possibly due to the difference between the oscillation frequencies of the pure Hopf mode and the mixed mode between Hopf and Turing. However, time periodic solutions do exist and can be found using AUTO, which was the main tool in obtaining the results reported in this chapter.

One of the main capabilities of AUTO is the computation and continuation of limit cycles of systems of ordinary differential equations. To exploit this capability, we used AUTO to solve the time periodic BVP

$$\frac{1}{T}\frac{d\hat{u}_k}{dt} = -D\left(\frac{2\pi k}{L}\right)^2 \hat{u}_k + \hat{F}(u,v)_k\,, \quad \hat{u}_k(0) = \hat{u}_k(1)\,, \quad k = 0,\ldots,N\,, \tag{2.4a}$$

$$\frac{1}{T}\frac{d\hat{v}_k}{dt} = -\left(\frac{2\pi k}{L}\right)^2 \hat{v}_k + \hat{G}(u,v)_k\,, \quad \hat{v}_k(0) = \hat{v}_k(1)\,, \quad k = 0,\ldots,N\,, \tag{2.4b}$$

where $\hat{f}_k$ denotes the amplitude of the k-th mode of the $(N+1)$-mode Fourier transform of f. In (2.4), $F(u,v)$ and $G(u,v)$ are the reaction terms on the right-hand sides of (2.1a) and (2.1b), respectively, and T is the period of the solution as determined by AUTO. As in the time stepping code, the reaction terms were computed first in physical space before being transformed into Fourier space. This formulation allowed use of the basic elements of the time evolution code described above, exploiting the fact that the IBVP solver directly computes the right-hand side of (2.4). The initial guess used to initialize the AUTO computations was the Fourier modes of $u(x,t)$ and $v(x,t)$ taken between the times $t_0 \leq t \leq t_1$, where $u(-L/2,t_0)$ and $u(-L/2,t_1)$ are both local maxima; in Figure 2.1(b), this condition corresponds to all slices in time between two consecutive horizontal black stripes, or between one complete oscillation of the Hopf mode. Here, $u(x,t)$ and $v(x,t)$ are solutions computed by time evolution. While, as noted previously, $u(x,t_0)$ is not identical to $u(x,t_1)$, the aperiodicity is not so severe that AUTO is unable to converge onto a time periodic solution from the initial guess. Indeed, the solutions that AUTO computes are exactly periodic in time. We suspect that such time periodic solutions to (2.1) exist, though with an extremely small domain of attraction.

We make the following observations. First, in the example in Figure 2.1 with $L \approx 137.37$, results of the bifurcation diagram and solutions for u and v hardly changed as the number of Fourier modes was increased from $N = 128$ to $N = 256$. Comparing two corresponding saddle-nodes in the snaking region, the value of D at the saddle-nodes differed in the two resolutions by less than 0.004%. Thus, $N = 128$ was used in the computations. The length L was chosen so that exactly 36 wavelengths of a pure Turing solution with wavenumber $k = k_c$ would fit in the domain. However, as we will show below, only 35 wavelengths are present when the solution is continued to a near-pure Turing state. Second, a pinning region in parameter

space further into the nonlinear regime was documented in [**22**]. This regime was found to exhibit highly relaxational temporal oscillations that required a higher temporal resolution in AUTO to resolve. This was not conducive to this study, as the number of modes required to resolve the spatial variation already led to time-intensive computations. Further, results from AUTO indicate that solutions of the more nonlinear parameter regime may not be connected through the familiar snaking structure that will be presented in the next section for the weakly nonlinear regime. Lastly, the norm used as the measure of the solutions and plotted on the y-axis of the bifurcation diagrams below is given by

$$L_{2F} = \sqrt{\int_0^1 \sum_{k=0}^{N} \left[\hat{u}_k^2(t) + \hat{v}_k^2(t)\right] \, dt} \, . \tag{2.5}$$

The norm (2.5) is close to but not exactly equivalent to the L_2 space-time norm, differing by a factor of two under the square root for $k \neq 0$. Also, since only even solutions are considered, $\hat{u}_k(t)$ and $\hat{v}_k(t)$ are real for all k and t.

2.3.2. Main Results

The complete bifurcation diagram of all solutions found is shown in Figure 2.2, where the diffusivity D is treated as the bifurcation parameter and plotted on the horizontal axis, and the norm (2.5) as the measure of the solutions plotted on the vertical axis. Heavy (light) segments indicate stable (unstable) solution branches. Representative solutions from each branch are shown in the figures below. We begin with a broad overview of each branch and discuss how they are located with respect to each other. We then describe each branch, and the corresponding solutions, in detail. We note that all branches and their solutions, stationary and time periodic,

were computed by AUTO; different options were used to direct AUTO to compute each type of solution.

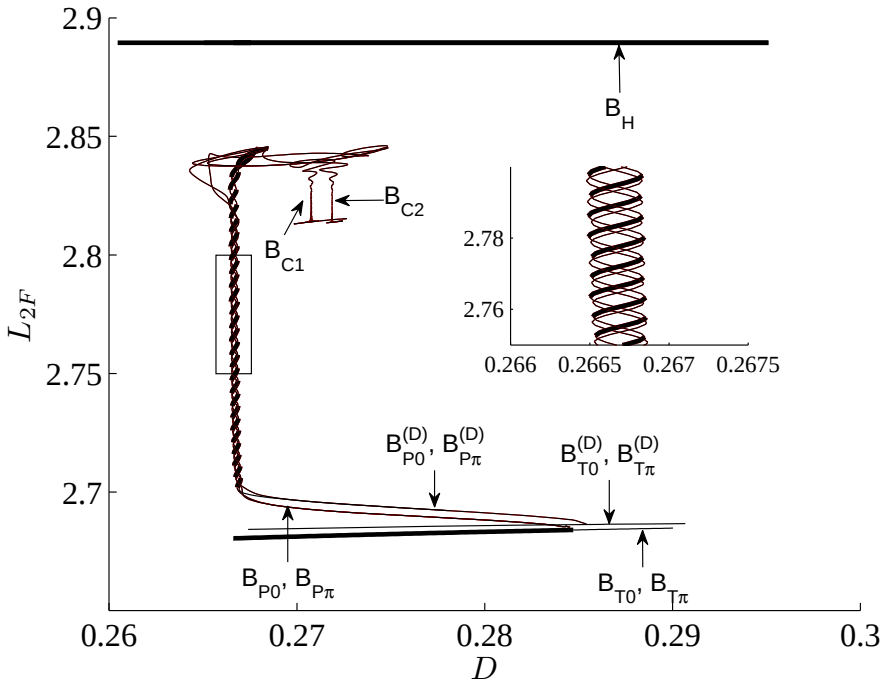

Figure 2.2. Complete bifurcation diagram for $B = 3.21$, $E = 1.4$, $L \approx 137.37$. The bottom two branches B_T and $B_T^{(D)}$ are the stationary pure Turing and defect branches, respectively. The top branch B_H is the pure Hopf branch. The main snaking region on the left consists of two pairs of intertwined branches B_{P0} and $B_{P\pi}$, and $B_{P0}^{(D)}$ and $B_{P\pi}^{(D)}$. Connected to these branches in the manner describe in Figure 2.5 are two distinct branches B_{C1} and B_{C2} exhibiting collapsed snaking behavior. The inset is a magnification of the main snaking region inside the rectangle.

Figure 2.2 includes two pure Turing branches B_{T0} (local maximum at $x = 0$) and $B_{T\pi}$ (local minimum at $x = 0$), indistinguishable by the measure L_{2F}. These two branches arise from the rotational invariance of the solutions of (2.2a). In particular, $A = \sqrt{(\gamma - \zeta k^2)/g}e^{i(kx+\phi)}$ ($|k| \leq \sqrt{\gamma/\zeta}$) is a solution to (2.2a) for any ϕ when $C = 0$. However, within (2.1), the phases $\phi = 0, \pi$ are the only ones that preserve the spatial reversibility symmetry. The stability

transition on the pure Turing branches occurs at a Hopf bifurcation point at $D \approx 0.28471$. An analysis of (2.2) (not presented here as it is straightforward) predicts that, with $\epsilon^2 = 0.01$ and $\mu = 25$, the transition occurs at $D \approx 0.28531$, a difference of approximately 6×10^{-4}. The point of stability transition also corresponds to the bifurcation point of the mixed mode. For clarity, we have plotted only a portion of the two pure Turing branches, and chosen not to plot the (unstable) mixed-mode branch. The pure Hopf branch, denoted by B_H, corresponds to the time periodic solution to (2.2b) with $A = 0$. The period of oscillations on the pure Hopf branch is $T \approx 4.6623$.

The two Turing-Hopf pinning branches B_{P0} and $B_{P\pi}$ are connected through a saddle-node bifurcation near the stability transition of the pure Turing branches. At this saddle-node point, the solution resembles solutions along the pure Turing branches B_{T0} and $B_{T\pi}$, with a small amplitude oscillation in time of period $T \approx 4.4179$. As is the case with all solutions described below, the period of oscillations is close to but not equal to the period of the pure Hopf oscillations. The space-time plot of the solution for u at the saddle-node, along with two line plots of two particular slices in time, are shown in Figure 2.3. While the length of the domain is able to accommodate exactly 36 Turing wavelengths of critical wavenumber $k = k_c$, only 35 are present in Figure 2.3. Hence among the discrete band of pure Turing solutions, each with a slightly different wavenumber allowed by the length of the domain, we have shown in Figure 2.2 only the two pure Turing branches for which there are 35 wavelengths corresponding to the same number as seen in Figure 2.3. This pattern can be shown to be Eckhaus stable by analyzing (2.2a) with $C = 0$.

The branches B_{P0} and $B_{P\pi}$ continue towards decreasing values of D before beginning a snaking process in which the two branches intertwine. In the snaking region, the solutions on

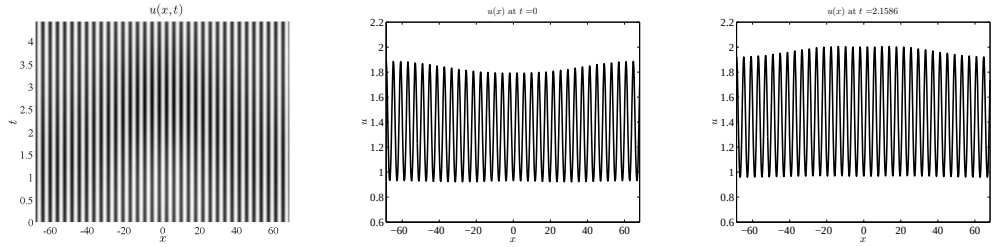

(a) space-time solution for u (b) time slice at $t = 0$ (c) time slice at $t \approx 2.1586$

Figure 2.3. Space-time plot of u at the saddle-node bifurcation point of the two Turing-Hopf pinning branches B_{P0} and $B_{P\pi}$. The solution resembles a pure Turing solution with a small amplitude temporal oscillation of period $T \approx 4.4179$ in the shape of the spatial envelope. The oscillations of the envelope can be inferred from (b) (time slice of (a) at $t = 0$) and (c) (time slice of (a) at $t \approx 2.1586$). The parameters are $B = 3.21$, $E = 1.4$, $L = 137.37$, and $D \approx 0.2843$. There are a total of 35 Turing wavelengths present.

these branches resemble that of one temporal period of Figure 2.1(b). Because the L_{2F} norm of the pure Hopf branch is larger than that of the pure Turing branch, solutions higher up on the Turing-Hopf pinning branches B_{P0} and $B_{P\pi}$ have a narrower striped region (i.e., fewer stripes) than those on the lower branches. Analogous to the distinction between the B_{T0} and $B_{T\pi}$ branches, the two pinning branches are distinguished by solutions on B_{P0} having a local maximum at the center of the striped (Turing) region, and solutions on $B_{P\pi}$ having a local minimum. The upward sloping segments in the snaking region are stable; all other solutions along the two branches are unstable.

Another pair of intertwined pinning branches, $B_{P0}^{(D)}$ and $B_{P\pi}^{(D)}$, is also characterized by striped regions embedded in a background of Hopf-like oscillations. However, solutions on these two branches exhibit a defect in the central part of the striped region. All solutions along these two branches are unstable. In the same way that the branches B_{P0} and $B_{P\pi}$ begin near a Hopf bifurcation point on the stationary pure Turing branch, the $B_{P0}^{(D)}$ and $B_{P\pi}^{(D)}$ branches begin

near a Hopf bifurcation point on a pair of stationary defect branches $B_{T0}^{(D)}$ and $B_{T\pi}^{(D)}$ (indistinguishable by L_{2F}). The space-time solution for u at the bottom of the $B_{P0}^{(D)}$ branch is shown in Figure 2.4(a), while Figures 2.4(b) and 2.4(c) are line plots of u at two instants of time, indicating a slight temporal oscillation in the form of the spatial envelope. Figures 2.4(d) and 2.4(e) show time slices of the solution at the bottom of the $B_{P\pi}^{(D)}$ branch, characterized by a local minimum, instead of a local maximum, at the center of the defect, centered at $x = 0$. Within the spatial envelope, 35 wavelengths are present. The stationary defect solutions on the $B_{T0}^{(D)}$ and $B_{T\pi}^{(D)}$ branches were described analytically in [**67**] in the framework of (2.2a) near a supercritical Turing bifurcation. As in the case of two branches of pure Turing solutions, the stationary defect solutions have either a local minimum or maximum at the center of the defect.

Finally, to the right of the four snaking branches of pinning solutions are two separate branches B_{C1} and B_{C2} that exhibit properties similar to collapsed snaking (cf. [**67**] for stationary collapsed snaking), where the snaking region collapses to almost a single value in the bifurcation parameter. Solutions on these two branches consist of two regions in space of approximately antiphase pure Hopf-like oscillations separated by striped Turing-like structures. Solutions at different locations on each branch differ in the relative width of the two regions. A schematic of the connections between all branches discussed is shown in Figure 2.5.

All solutions on the branches described are even about $x = 0$. We have not been able to find any solutions that are odd. By time evolving (2.1) initialized with particular initial conditions, we attempted to compute odd solutions in which two Hopf regions separated by a striped region oscillate antiphase. However, due to the apparent presence of weak coupling of the Hopf regions through the striped region, the initially antiphase oscillations synchronize over time. We were also unable to compute asymmetric solutions that, in the stationary pinning solutions of the

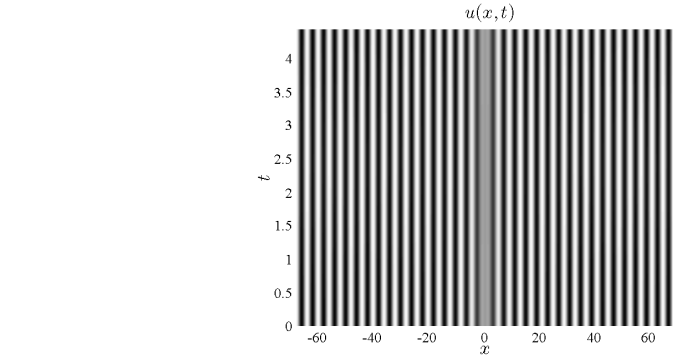

(a) space-time solution for u on $B_{P0}^{(D)}$

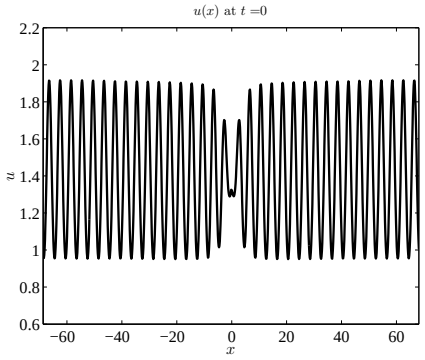

(b) time slice of (a) at $t = 0$

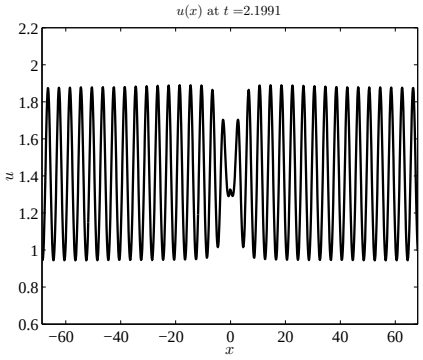

(c) time slice of (a) at $t \approx 2.1991$

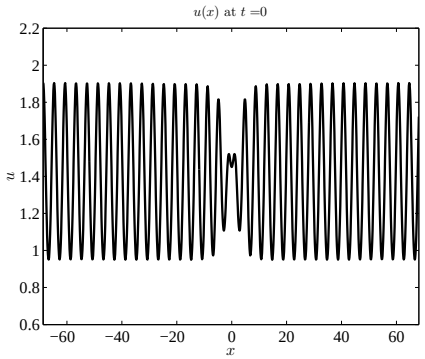

(d) time slice on $B_{P\pi}^{(D)}$ at $t = 0$

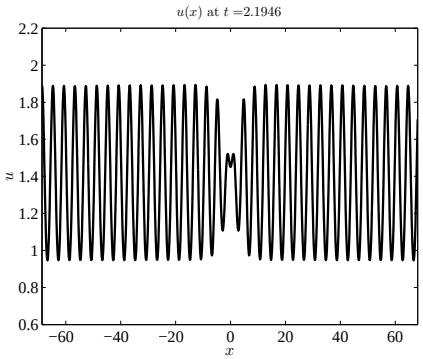

(e) time slice on $B_{P\pi}^{(D)}$ at $t \approx 2.1946$

Figure 2.4. Solutions at the bottom of the $B_{P0}^{(D)}$ and $B_{P\pi}^{(D)}$ branches. The oscillations of the spatial envelope ($T \approx 4.4167$) can be inferred from (b) (time slice of (a) at $t = 0$) and (c) (time slice of (a) at $t \approx 2.1991$) for the $B_{P0}^{(D)}$ branch. Time-slices for the $B_{P\pi}^{(D)}$ branch are shown in (d) and (e) ($T \approx 4.4166$). The parameters are $B = 3.21$, $E = 1.4$, $L = 137.37$, and $D \approx 0.28544$. Within the spatial envelope, 35 wavelengths are present.

Swift-Hohenberg equations (see e.g., [**11**] and [**14**]), make up the "rungs" that connect two intertwined snaking branches. Such solutions can be constructed by "gluing" together parts of solutions on one branch. However, when considering time periodic solutions, as we do here, each component must have the same temporal period, which is generally not the case. As a result, AUTO will not be able to converge to a time periodic solution. This is a fundamental difficulty with the present model, not encountered in previous studies of stationary pinning regimes.

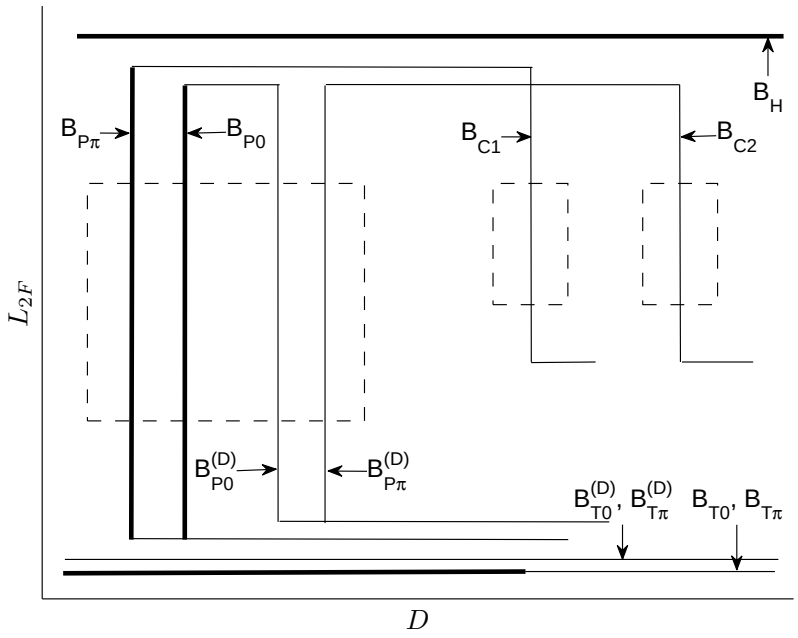

Figure 2.5. Schematic bifurcation diagram of Figure 2.2 illustrating connections between branches. The dashed boxes represent snaking regions. Dark segments indicate the existence of branches of stable solutions.

We now discuss each pair of branches in detail starting with the two pure Turing branches. In Figure 2.6, we show the solutions at the point of the stability transition where a Hopf bifurcation

occurs, marked by a solid circle in Figure 2.6(a), on the branches B_{T0} and $B_{T\pi}$. The four pinning branches are also visible in Figure 2.6(a); in particular, the saddle-node point from which the B_{P0} and $B_{P\pi}$ branches bifurcate can be seen to be located near the aforementioned Hopf bifurcation point on the pure Turing branches. Multiple Hopf bifurcation points occur on the B_{T0} and $B_{T\pi}$ branches; the one marked by the solid circle located at the stability transition point is the one that occurs at the smallest value of D. The corresponding (stationary) solutions for u are plotted in Figure 2.6(b), which has a local maximum at $x = 0$ (B_{T0}) and Figure 2.6(c), which has a local minimum at $x = 0$ ($B_{T\pi}$). For clarity, only the interval $x \in [-20, 20]$ is shown. The entire domain contains 35 wavelengths.

As stated above, the two Turing-Hopf pinning branches B_{P0} and $B_{P\pi}$ bifurcate from the saddle-node point located near the stability transition point of the two pure Turing branches B_{T0} and $B_{T\pi}$. In Figures 2.7(b) and 2.7(c), we show one space-time solution for u from the lower part of each branch to illustrate how the solutions on the branches differ from that of the saddle-node shown in Figure 2.3(a). Similarities between Figures 2.7(b) and 2.7(c) are immediate when spatial and temporal periodicity of the space-time plots are considered. This similarity is apparent when comparing Figure 2.7(c) to Figure 2.7(d), the latter of which has been periodically shifted in both space and time from Figure 2.7(b). The center of the striped region occurs at $x = 0$ (or, by periodicity, the leftmost point in space of Figure 2.7(b)). In Figure 2.7(d), the center of the striped region is a local maximum (dark stripe) while in Figure 2.7(c), it is a local minimum (white stripe). These two solutions differ slightly both in the temporal period and the wavelength of the striped region. The mechanism(s) that affect these two quantities is an open problem. Experiments involving the time evolution of (2.1) suggest that the selection of the wavelength of the striped region is independent of initial conditions.

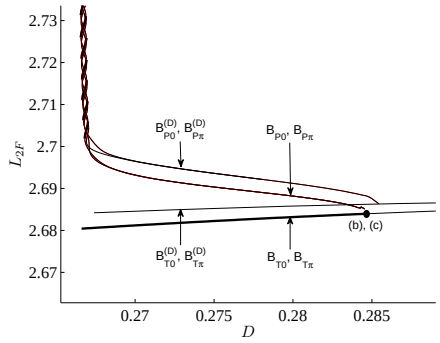

(a) closeup of pure Turing branches

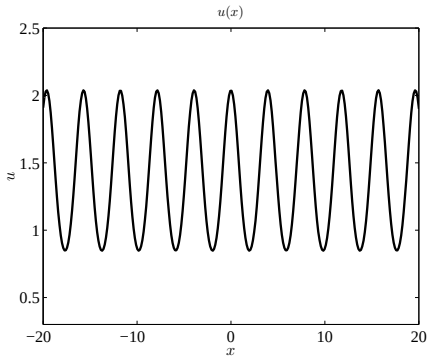

(b) solution on branch B_{T0}

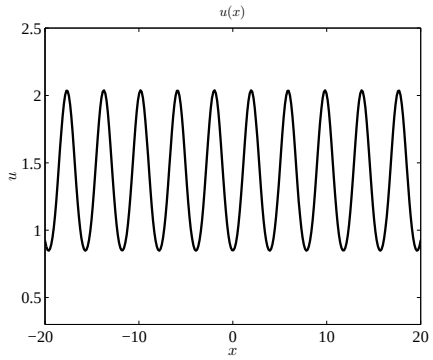

(c) solution on branch $B_{T\pi}$

Figure 2.6. Closeup of stability transition point (indicated by solid circle) on the pure Turing branches (a) and the corresponding solutions for u on B_{T0} (b) and $B_{T\pi}$ (c). The pure Turing branches are indistinguishable by the measure L_{2F}. The parameters are $B = 3.21$, $E = 1.4$, $L \approx 137.37$, and $D \approx 0.2847$.

Snaking higher up the B_{P0} and $B_{P\pi}$ branches, the spatial extent of the striped region is reduced through a series of saddle-node bifurcations. In Figure 2.8, we show the solutions at two saddle-nodes in the snaking region of the $B_{P\pi}$ indicated in Figure 2.8(a) (the $B_{P0}^{(D)}$ and $B_{P\pi}^{(D)}$ branches have been removed for clarity). We note in Figure 2.8(a) that, while the saddle-nodes exhibit an approximate "lining-up property" (cf. [**34**]) where saddle-nodes occur at approximately the same value of the bifurcation parameter, we observe a nonmonotonic convergence of saddle-nodes in the parameter D, a departure from previous results on stationary snaking

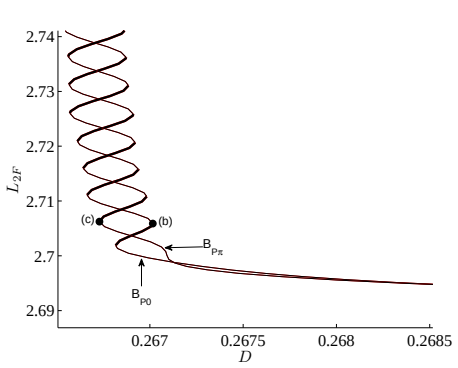

(a) lower portion of B_{P0} and $B_{P\pi}$

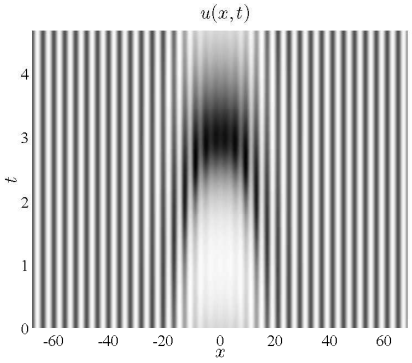

(b) solution on branch B_{P0} with $D \approx 0.26702$

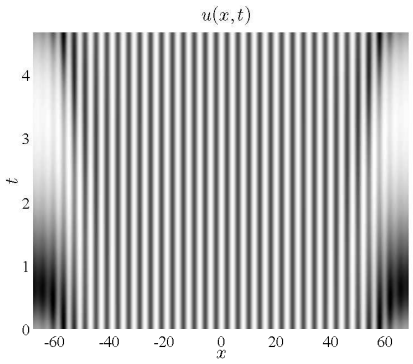

(c) solution on branch $B_{P\pi}$ with $D \approx 0.26673$

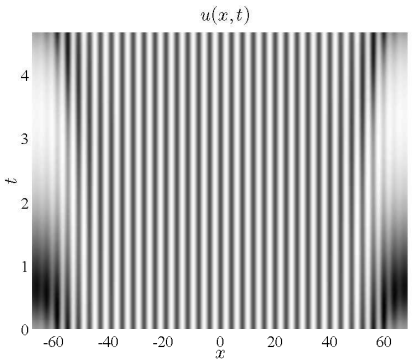

(d) same as (b), flipped in x and shifted in t

Figure 2.7. Solutions on the lower part of the Turing-Hopf pinning branches B_{P0} (b) and $B_{P\pi}$ (c). The temporal periods are, respectively, $T \approx 4.6450$ and $T \approx 4.6452$. In (d), we show a periodically (temporally and spatially) shifted plot of (b), illustrating the similarity between (b) and (c). The parameters are $B = 3.21$, $E = 1.4$, $L \approx 137.37$.

branches. The solution at the lower saddle-node, shown in Figure 2.8(b), is Turing-dominated while the one at the higher saddle-node, Figure 2.8(c), is Hopf dominated, consistent with the fact that in Figure 2.2, the stationary Turing branches have the smallest values of L_{2F} and the pure Hopf branch the largest. The periods of the solutions also differ slightly, with that of the solution higher on the branch closer to the period of the pure Hopf solution. While the number of stripes is difficult to quantify due to temporal oscillations and the interaction between Turing

and Hopf regions, the process by which solutions gain or lose stripes can be clearly seen by comparing solutions at particular points in time.

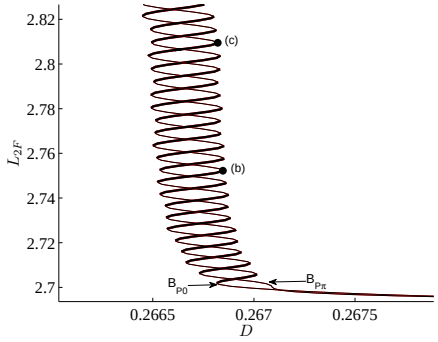

(a) closeup of non-defect pinning branches

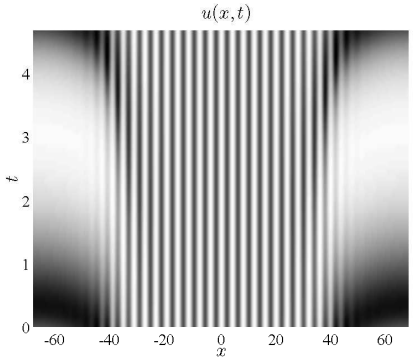

(b) solution on low saddle-node of $B_{P\pi}$

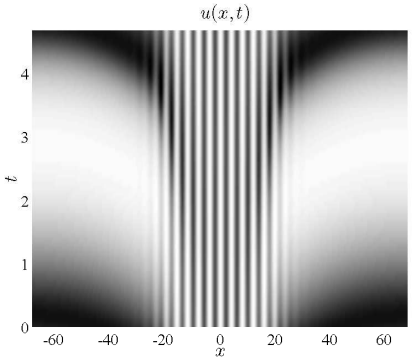

(c) solution on high saddle-node of $B_{P\pi}$

Figure 2.8. Progression of solutions along the snaking region (a) of the $B_{P\pi}$ branch. In (b), the striped region occupies the majority of the spatial domain, while in (c), the time oscillatory region is dominant. The temporal periods of the solutions are $T \approx 4.6573$ (b) and $T \approx 4.6597$ (c). The parameters are $B = 3.21$, $E = 1.4$, $L \approx 137.37$, $D \approx 0.26685$ (b) and $D \approx 0.26682$ (c).

In Figure 2.9 we show the process of the nucleation of a Turing cell, or stripe, as the $B_{P\pi}$ branch is traversed downwards. In particular, for a typical segment of the snaking branch, we illustrate the difference between solutions at three consecutive saddle-nodes by plotting $u(x, t_0)$, where $t_0 \in [0, T]$ is the instant in time when the center of the oscillatory region in u attains a local minimum in time. In Figure 2.9(a), we indicate the three saddle-node points of interest

as well as two intermediate points. In Figure 2.9(b), the solution at saddle-node point (b) has a main Turing region containing 10 local maxima at which u has a value between 2 and 2.5. The main Turing region is bounded between two pairs of local maxima of lesser value. As the branch is traversed downwards, the two pairs of local maxima grow in amplitude, as seen in Figure 2.9(c), 2.9(d), 2.9(e), while very little is changed in the main Turing region. Once the saddle-node point (f) is reached (Figure 2.9(f)), the larger of the pair of maxima has grown to approximately equal height as the outer pair of maxima of the main Turing region. Thus, as the branch was traversed from saddle-node point (b) through saddle-node point (d) to saddle-node point (f), the main Turing region gained one pair of maxima, or two Turing wavelengths.

We make some remarks regarding the process illustrated in Figure 2.9. First, the mechanism of nucleation at the edge of the Turing region, including in particular the nucleation of two Turing wavelengths for every two saddle-nodes, is the same as that reported for the 2–3 Swift-Hohenberg equation in [**9**]. Second, comparing Figures 2.9(b) and 2.9(f) reveals that the larger the extent of the Turing region, the more the central stripes resemble that of the pure Turing stripes at the same value of D. This trend suggests that there is weak coupling between the two Turing-Hopf interfaces through the Turing region, and that the coupling strength weakens the greater the distance between the two Turing-Hopf interfaces. Third, all corresponding space-time solutions of Figures 2.9(b)–2.9(f) have slightly different temporal periods, given in the caption of Figure 2.9. Lastly, we observe the same nucleation characteristics for the defect pinning branches.

Solutions on the $B_{T0}^{(D)}$ and $B_{T\pi}^{(D)}$ branches are characterized by a spatially periodic pattern contained within a spatially varying envelope. Solutions on $B_{T0}^{(D)}$ ($B_{T\pi}^{(D)}$) have a local maximum (minimum) at $x = 0$. As indicated in Figure 2.10(a), both stationary defect branches are

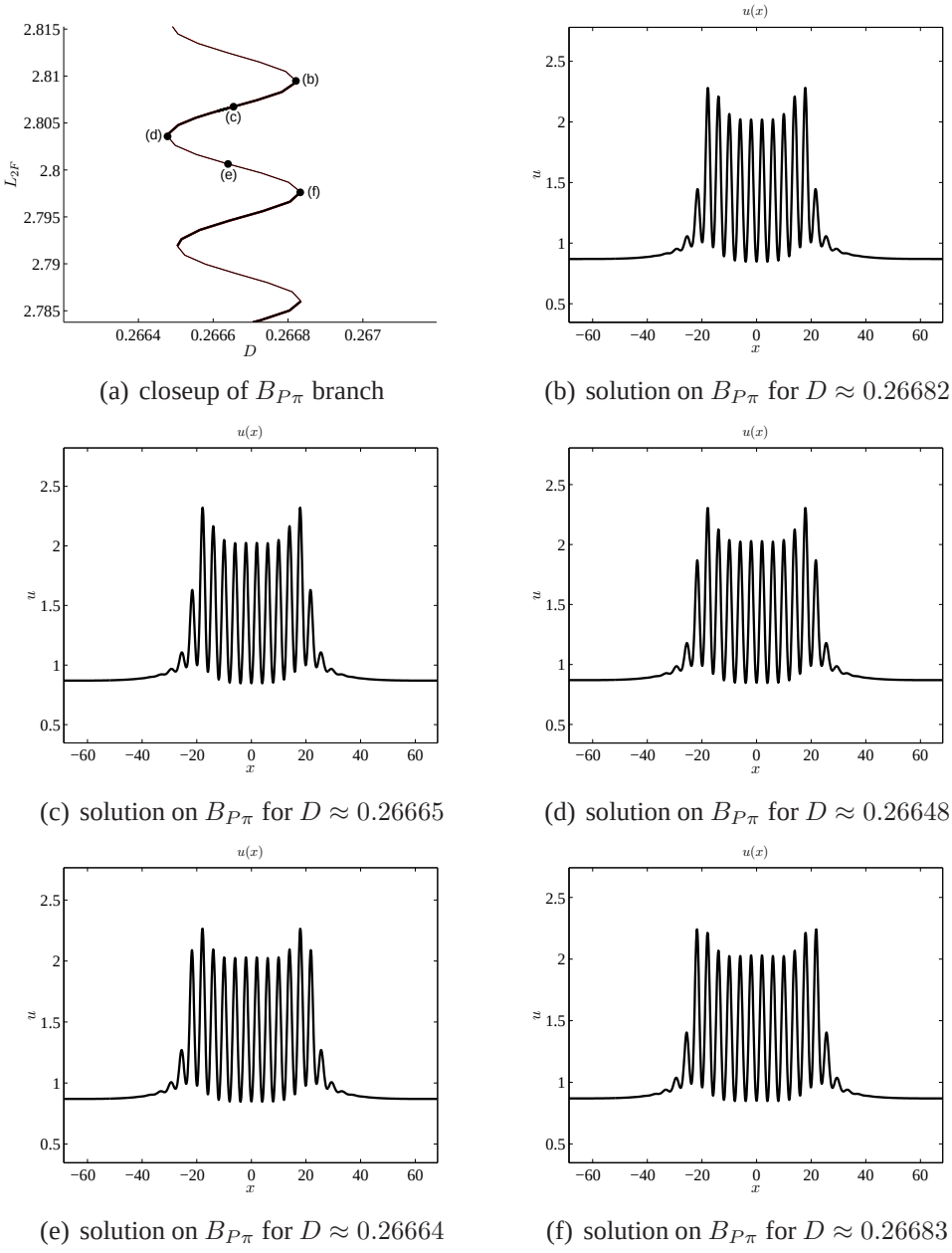

(a) closeup of $B_{P\pi}$ branch

(b) solution on $B_{P\pi}$ for $D \approx 0.26682$

(c) solution on $B_{P\pi}$ for $D \approx 0.26665$

(d) solution on $B_{P\pi}$ for $D \approx 0.26648$

(e) solution on $B_{P\pi}$ for $D \approx 0.26664$

(f) solution on $B_{P\pi}$ for $D \approx 0.26683$

Figure 2.9. Illustration of the nucleation process that occurs at the edge of the Turing region. In (a), the locations on the $B_{P\pi}$ branch of the subsequent figures are indicated. In the progression (b)–(f), the Turing region grows by a width of two wavelengths through the increase in amplitude of a pair of local maxima at its edges. The temporal periods of the solutions are $T \approx 4.6597$ (b), $T \approx 4.6597$ (c), $T \approx 4.6596$ (d), $T \approx 4.6595$ (e), $T \approx 4.6594$ (f). The parameters are $B = 3.21$, $E = 1.4$, and $L \approx 137.37$.

unstable. Multiple Hopf bifurcation points occur on the two branches; the one marked by the solid circle is the one that occurs nearest the bifurcation point of the defect Turing-Hopf pinning branches $B_{P0}^{(D)}$ and $B_{P\pi}^{(D)}$. The two solutions at the Hopf bifurcation points are shown in Figures 2.10(b) and 2.10(c). Like the space-time solution at the bifurcation points of the $B_{P0}^{(D)}$ and $B_{P\pi}^{(D)}$ branches in Figure 2.4, 35 wavelengths are present inside the spatial envelope.

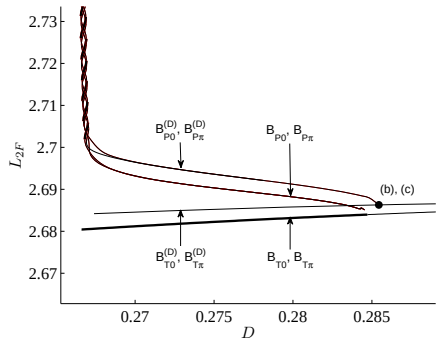

(a) closeup of stationary defect branches

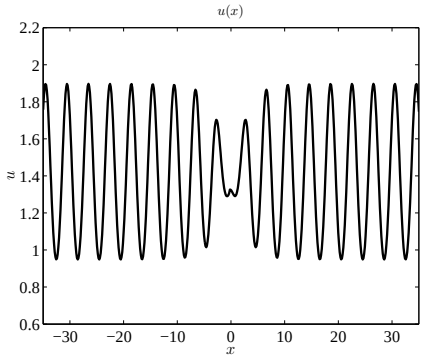

(b) solution on branch $B_{T0}^{(D)}$

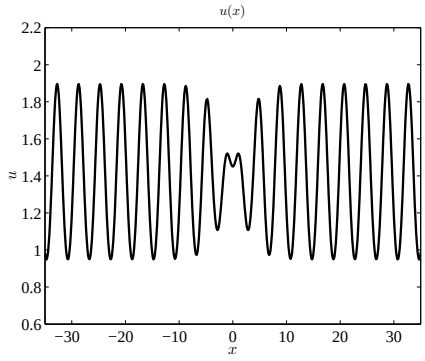

(c) solution on branch $B_{T\pi}^{(D)}$

Figure 2.10. Closeup of the Hopf bifurcation point (indicated by solid circle) nearest the saddle-node bifurcation point of $B_{P0}^{(D)}$ and $B_{P\pi}^{(D)}$ on the stationary defect branches (a) and the corresponding solutions for u on $B_{T0}^{(D)}$ (b) and $B_{T\pi}^{(D)}$ (c). The stationary defect branches are indistinguishable by the measure L_{2F}. The parameters are $B = 3.21$, $E = 1.4$, $L \approx 137.37$, and $D \approx 0.28544$.

As seen in Figure 2.10(a), the defect Turing-Hopf pinning branches $B_{P0}^{(D)}$ and $B_{P\pi}^{(D)}$ begin near a Hopf bifurcation on the stationary defect branches $B_{T0}^{(D)}$ and $B_{T\pi}^{(D)}$. The space-time solution at the bifurcation point is shown in Figure 2.4(a). The similarity between this solution and the stationary defect solution at the Hopf bifurcation point is immediate upon comparing Figure 2.4(b) to Figure 2.10(b) and Figure 2.4(d) to Figure 2.10(c). In Figure 2.11, we show two typical defect Turing-Hopf pinning solutions at low and high saddle-node points on the $B_{P\pi}^{(D)}$ branch (Figure 2.11(a)). Other solution branches have been removed for clarity. The defect can be seen to be centered around $x = 0$ in Figures 2.11(b) and 2.11(c). As with the non-defect pinning branches B_{P0} and $B_{P\pi}$, solutions lower on the branch have a larger striped region than those higher on the branch. The manner in which Turing wavelengths are nucleated on the branches B_{P0} and $B_{P\pi}$ also applies to solutions on the defect pinning branches, and thus is not shown. We remark that although stationary defect pinning solutions have not been observed in the Swift-Hohenberg equations, they have been found in a periodically forced Ginzburg-Landau equation originally proposed in [**7**] and subsequently studied in detail in [**13**]. In this example the two "hybrid" snakes formed by defect pinning solutions coexist in the same snaking region as the two "primary" snakes formed by non-defect pinning solutions, precisely as in Figure 2.2. Besides, it was theoretically predicted in [**13**] that as the spatially periodic region of the pinning solution becomes wider along the snaking branches, the locations of the saddle-nodes on the two hybrid snakes approach their limiting values from the other direction and more slowly compared to those on the two primary snakes, which again agrees with the upper portion of Figure 2.2.

The collapsed snaking branches B_{C1} and B_{C2} lie to the right of the four main snaking branches described above. All solutions on the two branches are unstable. The B_{C1} branch

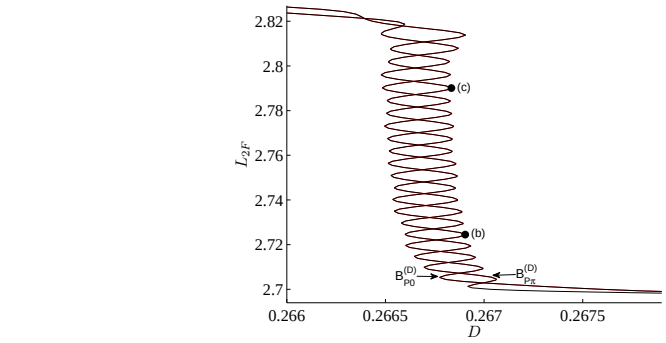

(a) closeup of defect pinning branches

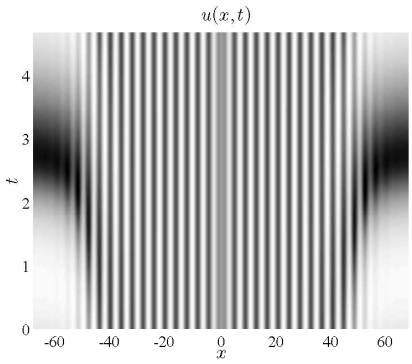

(b) solution on low saddle-node of $B^{(D)}_{P\pi}$

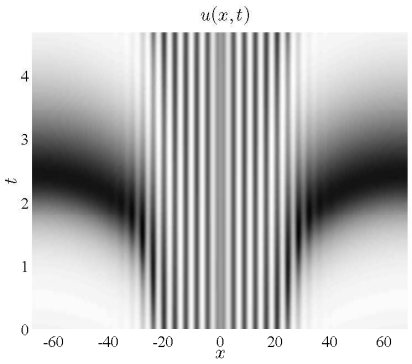

(c) solution on high saddle-node of $B^{(D)}_{P\pi}$

Figure 2.11. Progression of solutions along the snaking region (a) of the $B^{(D)}_{P\pi}$ branch. In (b), the striped region occupies the majority of the spatial domain, while in (c), the time oscillatory region is dominant. The temporal periods of the solutions are $T \approx 4.6533$ (b) and $T \approx 4.6592$ (c). The parameters are $B = 3.21$, $E = 1.4$, $L \approx 137.37$, $D \approx 0.26690$ (b) and $D \approx 0.26683$ (c).

connects to $B_{P\pi}$, and B_{C2} connects to $B^{(D)}_{P\pi}$, both through a complex array of saddle-nodes that will not be described here. A simplified schematic of these connections is shown in Figure 2.5. In Figure 2.12(a), we show a closeup of the two collapsed snaking branches. As the branch is traversed beginning from the top, the snaking region appears to collapse to a single value in D in a back-and-forth manner before broadening out at the bottom. Two typical solutions on the

lower (Figure 2.12(b)) and upper (Figure 2.12(c)) part of the B_{C1} branch are shown. The solutions on the lower and upper part of the collapsed snaking branches differ in the relative widths of the mainly spatially homogeneous regions undergoing approximately antiphase temporally periodic oscillations. This is in direct contrast to the regular snaking behavior discussed above in which solutions on lower and upper parts of the branch differed in the widths of the spatially periodic region, i.e., the number of Turing stripes. The fact that in the latter case, stripes are nucleated or destroyed as the branch is traversed, while in the former case, only the widths of predominantly spatially homogeneous structures are altered, offers a simple explanation for the fact that solutions such as those in Figures 2.12(b) and 2.12(c) lie on a collapsed snaking branch, while those in, e.g., Figure 2.8(b), lie on a snaking branch with finite width. The difference between the solutions in Figure 2.12 and those on the other collapsed snaking branch B_{C2} will be illustrated below.

We make two remarks regarding Figure 2.12. First, the time oscillatory regions of space in Figures 2.12(b) and 2.12(c) are flatter than those of solutions described above (e.g., Figure 2.11(c)). Further, the frequency of these oscillations is closer to that of the pure Hopf frequency. These characteristics suggest that there is very little coupling between the time oscillatory regions and the interfaces in between them. Second, the nearly antiphase temporal oscillations in Figures 2.12(b) and 2.12(c) are separated by spatially oscillatory structures, while the corresponding branches in Figure 2.12(a) snake back and forth in their approach to a single value in the bifurcation parameter. A direct analog of this scenario for stationary solutions, where two spatially homogeneous states are connected by spatially oscillatory fronts, is given in [**67**]. There, the spatially oscillatory fronts were explained by the spatial eigenvalues of the two spatially homogeneous states. In this case, they form a quartet in the complex plane with nonzero

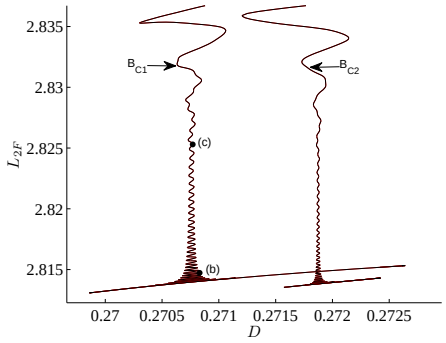

(a) closeup of collapsed snaking branches

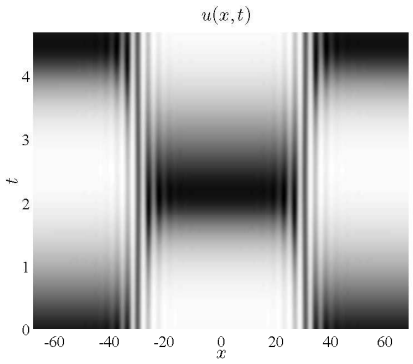

(b) solution on low saddle-node of B_{C1}

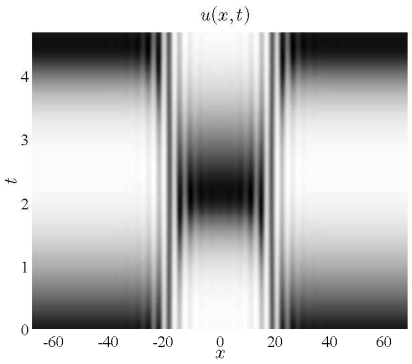

(c) solution on high saddle-node of B_{C1}

Figure 2.12. Progression of solutions along the collapsed snaking region (a) of the B_{C1} branch. The solutions in (b) and (c) (locations on the branch indicated in (a)) differ in the ratio between the widths of the time oscillatory regions. The temporal periods of the solutions are $T \approx 4.66234$ (b) and $T \approx 4.66231$ (c). The parameters are $B = 3.21$, $E = 1.4$, $L \approx 137.37$, $D \approx 0.27083$ (b) and $D \approx 0.27077$ (c).

real and imaginary parts, with the nonzero imaginary parts responsible for the spatially oscillatory front. For stationary solutions, the difference between regular snaking and collapsed snaking behavior has been understood as follows. Collapsed snaking solutions are explained in [**56**] as the intersection of the two dimensional stable and unstable manifolds of two "stationary" (in space) states in a four-dimensional spatial dynamical system. This codimension one intersection is the reason behind the collapsed snaking structure of the solution branches; a

slight perturbation in the value of the control parameter would lead to the breaking of the non-robust intersection of the manifolds. In contrast, the robust snaking region of regular snaking solutions can be explained by a codimension zero intersection between a two dimensional unstable manifold of a stationary (in space) state with a three-dimensional center-stable manifold of a periodic orbit in space, with spatial reversibility guaranteeing the return orbit to the stationary state. Extension of this description to the present case of time dependent snaking behavior involves dimension counting in the style of [**90**] in the infinite dimensional phase space of (2.1), and is left as future work.

In Figure 2.13(b), we illustrate the difference between two comparable solutions on the B_{C1} and B_{C2} branches, respectively. The solid curve shows the solution $u(x)$ of Figure 2.12(b) at the time where $u(0,t)$ is a local maximum. The dashed curve shows the same slice of a similar solution on the other collapsed snaking branch B_{C2}. The respective locations of the two solutions are shown in Figure 2.13(a). As has been the distinction between the 0 and π regular snaking branches, points in space where solutions on B_{C1} attain a local maximum (minimum) are approximately points where those on B_{C2} attain a local minimum (maximum). This antiphase relationship between the two collapsed snaking branches is not as exact as in the regular snaking branches, perhaps due to the separation of the collapsed branches in parameter space.

2.3.3. Depinning Transition

Within the regular snaking region described above, the solutions are time periodic and the relative widths of the striped and time oscillatory regions remain constant in time. That is, the Turing-Hopf front is pinned while the solution is inside the snaking region. Outside the snaking

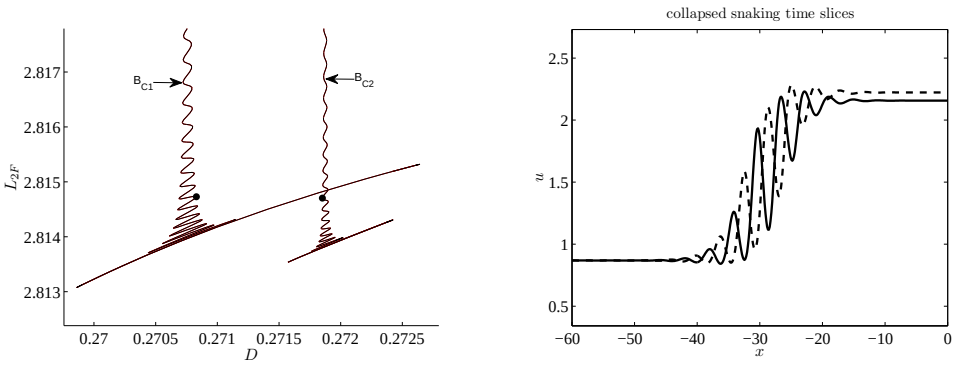

(a) bottom of collapsed snaking branches B_{C1} and B_{C2} (b) time slices of collapsed snaking solutions

Figure 2.13. In (a), the bottom of the B_{C1} and B_{C2} branches are shown. In (b), two slices of space-time solutions on B_{C1} (solid) and B_{C2} (dashed) are shown. Their locations on the respective branches are indicated in (a) by solid circles. The spatially periodic regions of the two solutions oscillate approximately antiphase with periods $T \approx 4.66234$ (solid) and $T \approx 4.66229$ (dashed). The parameters are $B = 3.21$, $E = 1.4$, $L = 137.37$ and $D \approx 0.27083$ (solid) and $D \approx 0.27185$ (dashed).

region, the fronts are expected to depin, as was the case for the 2–3 Swift-Hohenberg equation in [**10**]. The direction of depinning may be inferred from the weakly nonlinear analysis. In §2.2, we found that when $\rho > 0$, or equivalently $D > D_c$, the Hopf bifurcation occurs first as B is increased. This suggests that when D is increased, the Hopf mode becomes more dominant relative to the Turing mode. Thus, when D is set to the right of the pinning region, the Hopf region is expected to invade the striped region. Figure 2.14 illustrates the depinning dynamics that occur in this scenario. Figure 2.14(b) shows a space-time plot of u where the temporal oscillations have been removed for clarity by only recording times at which the center of the time oscillatory region attained a local minimum in time. As expected, the Hopf region (white) invades the striped region. The time evolution of (2.1) was initialized with one slice in time of the space-time solution of u and v at a particular saddle-node as computed by AUTO. The

parameter D was set at $D = D_s + \delta$ with $\delta > 0$, where D_s is the value at the particular saddle-node marked by a solid circle in Figure 2.14(a). Invasion of the striped region was observed when the process was repeated with D set to the left of the snaking region (Figure 2.15).

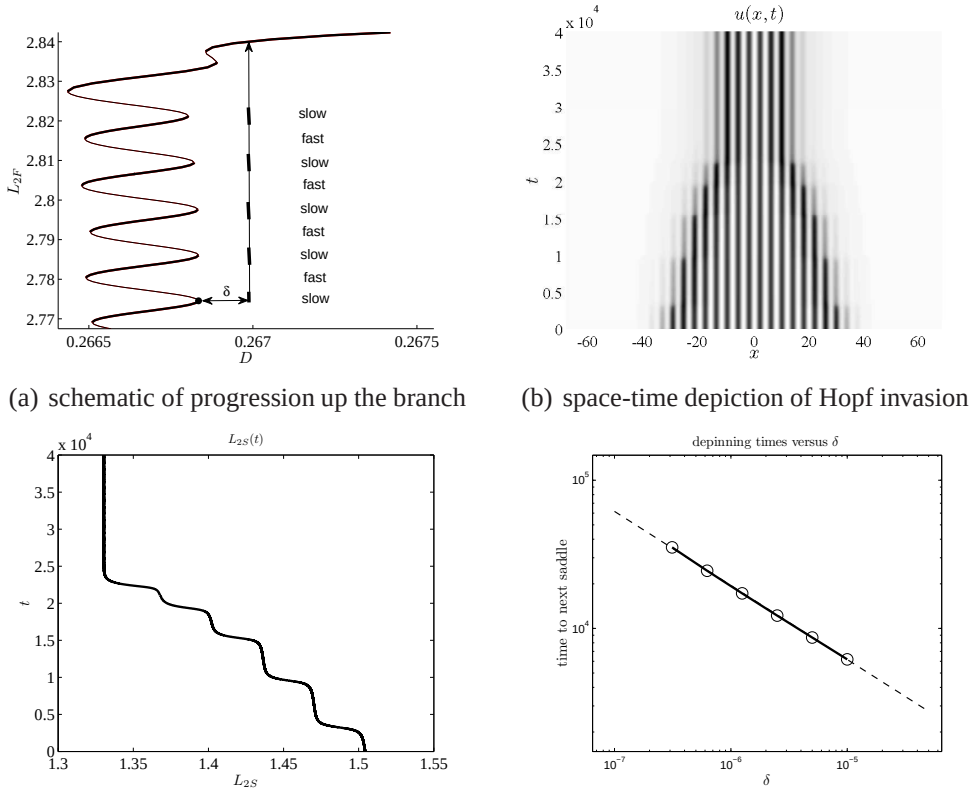

(a) schematic of progression up the branch

(b) space-time depiction of Hopf invasion

(c) evolution of $L_{2S}(t)$

(d) log-log plot of depinning time versus δ

Figure 2.14. Shown in (a) is a closeup of the $B_{P\pi}$ branch with the location of the initial condition indicated by the solid circle. At the saddle-node, $D = D_s \approx 0.26683$. The evolution up the branch at δ distance outside the snaking region is depicted by the vertical arrow. The space-time depiction of the solution starting from this initial condition is shown in (b) for $\delta = 1 \times 10^{-5}$. Only the time slices at which the center of the time oscillatory region is at a local minimum are included. The slow-fast-slow evolution of $L_{2S}(t)$ of the time slices of (b) is shown in (c) with time t on the horizontal axis. The corresponding slow and fast regions are indicated in (a). The $\delta^{-1/2}$ scaling of the time of traversal between two saddle-nodes is shown in the log-log plot in (d). The solid line is a least squares fit through the data points (empty circles). The dashed line has a slope of $-1/2$.

The progression of the solution mirrors the depinning of stationary pinning solutions in [**10**]. Initialized in the neighborhood of a saddle-node, the solution evolves in a manner so as to approach the solution at the saddle-node either below it, if the striped state invades, or above it, when the Hopf state invades. This progression can be inferred from Figure 2.8, as stripe-dominated solutions populate the lower portions of the branch. As in [**10**], we observe that the rate of evolution is slow in the vicinity of a saddle-node, increases away from the saddle-node, and decreases again near the next saddle-node. This slow-fast-slow progression past saddle-nodes has also been observed in nonlinear pulse splitting regimes (see e.g., [**34**, **59**, **82**]). Figure 2.14(c) illustrates the slow-fast dynamics by tracking the spatial norm $L_{2S}(t)$ of each slice in time of Figure 2.14(b). The L_{2S} norm is defined as

$$L_{2S}(t) = \sqrt{\frac{1}{L}\int_{-L/2}^{L/2} u^2(x,t)\,dx}\,.$$

Note that, unlike the L_{2F} norm in (2.5), $L_{2S}(t)$ decreases as the width of the striped region decreases. As seen in Figure 2.14(c), the norm decreases in a step-like progression in time, suggesting a sequence of destruction events separated by long intervals of relatively little change. Because the saddle-nodes do not line up exactly, times spent near each saddle-node are not uniformly distributed. We finally remark that the destruction events do not continue until the system reaches a pure Hopf state. This is due to the presence of stable branches that extend beyond the snaking region to the right, which can be seen in Figure 2.14(a) as well as in Figure 2.2. However, the progression of a Turing-Hopf pinning solution down the left side of the snaking region does evolve to a pure Turing state, seen in Figure 2.15(b). This is suggested by the snaking diagram shown in Figure 2.15(a). A wavelength adjustment occurs at $t \approx 2 \times 10^4$

in Figure 2.15(b) so that the final state, like the pure Turing solutions described in §2.3.2, has 35 wavelengths.

Repeating the above procedure for various δ, we observe that the time of traversal from one saddle-node to the next scales approximately as $\delta^{-1/2}$, the same scaling found in [**10**] for the 2–3 Swift-Hohenberg equation. This scaling was determined only by the time to traverse from the starting saddle-node, indicated in Figure 2.14(a) to the one immediately above it. We numerically determined the time by calculating the difference between the appropriate time slice $u(x, t_0)$ of the solution computed by AUTO at the second saddle-node to every time slice of Figure 2.14(b). The time at which the L_{2S} norm of the difference was minimized was taken to be the time at which the solution was considered to have reached the second saddle-node. The log-log relation of the traversal time to the distance δ from the saddle-node is shown in Figure 2.14(d); the solid line is a least squares fit through numerical data (empty circles), and the dashed line has slope $-1/2$. We finally remark that the aforementioned slight aperiodicity of the temporal oscillations in time evolved solutions of (2.1) makes it difficult to determine whether an integer number of temporal oscillations occur between saddle-node transitions. This difficulty is exacerbated by the vast difference in the time scales between one temporal period and the transition time.

2.3.4. Wavelength Selection

In studies of pinning solutions in the stationary Swift-Hohenberg equations, the wavelength of the periodic state was shown to vary within the snaking region. This variation can be understood by the conservation of a spatial Hamiltonian (cf. [**12**]), a property not available in the Brusselator model. However, in the latter case, the wavelength of the Turing state also varies within the

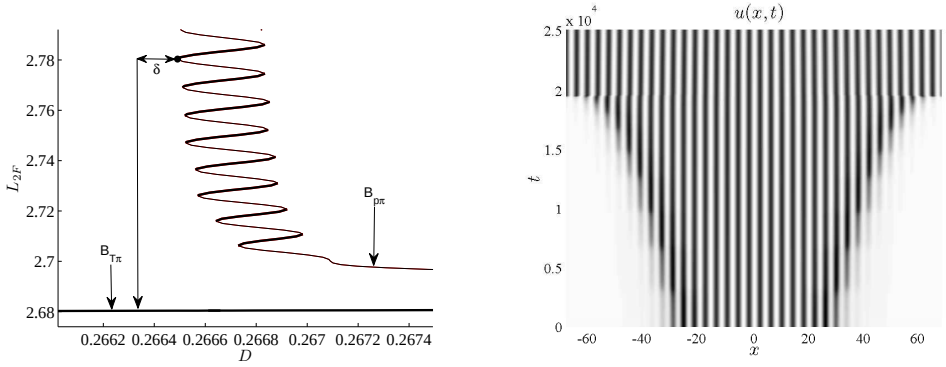

(a) schematic of progression down the branch (b) space-time depiction of Turing invasion

Figure 2.15. Shown in (a) is a closeup of the $B_{P\pi}$ branch with the location of the initial condition indicated by the solid circle. At the saddle-node, $D = D_s \approx 0.26649$. The evolution down the branch at δ distance outside the snaking region is depicted by the large vertical arrow. The space-time depiction of the solution starting from this initial condition is shown in (b) for $\delta = -1 \times 10^{-5}$. Only the time slices at which the center of the time oscillatory region is at a local minimum are included. A wavelength adjustment occurs at $t \approx 2 \times 10^4$. The final pure Turing state contains 35 wavelengths. The parameters are $B = 3.21$, $E = 1.4$, and $L = 137.37$.

snaking region and is distributed evenly among all stripes. We illustrate this phenomenon for solutions on the $B_{P\pi}$ branch. Figure 2.16(a) shows a scatter plot of the wavelength of the striped region for solutions in the snaking region. It shows that, generally, the wavelength λ increases as the parameter D increases. Deviation from the trend near the top of Figure 2.16(a) occurs for solutions near the top of the snaking branch. For those solutions, the Hopf region has significant influence on the entire striped region as a result of the Turing-Hopf coupling. For a typical solution, Figure 2.16(b) shows the x locations of each individual local maximum. The linear relationship implies a spatially uniform wavelength throughout the striped region. We note that the critical wavelength λ_c is $\lambda_c \approx 3.8158$ and the value of D at the C2THP is $D_c \approx 0.26483$. Thus, Figure 2.16(a) shows that when D is closer to D_c, the wavelength λ is

closer to λ_c. We also observe this trend with the parameter B; the closer B is to B_H, the closer λ is to λ_c.

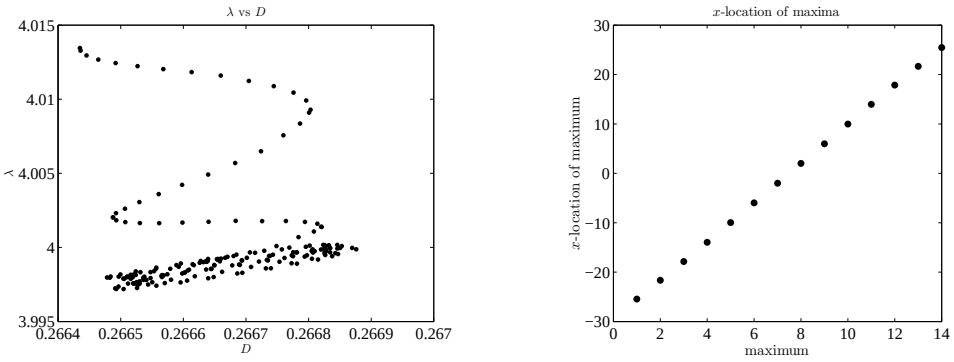

(a) scatter plot of wavelengths λ versus D (b) locations of local maxima of typical solution

Figure 2.16. Shown in (a) is a scatter plot of the wavelengths λ of the striped region of solutions on the snaking segments of the $B_{P\pi}$ branch. Most of the data points are concentrated in the lower region of the plot and suggest a positive correlation of λ with D. The approximately linear behavior shown in (b) of the locations of local maxima of a typical solution indicates equally spaced peaks and spatially uniform wavelengths. The parameters are $B = 3.21$, $E = 1.4$, and $L = 137.37$.

There is an important difference, however, between the wavelength selection in Figure 2.16(a) and that found for the (variational) 3–5 Swift-Hohenberg equation in [**12**]. In the case of the latter, the snaking region straddles a Maxwell point, a point of energy balance between the homogeneous and spatially periodic states. Deviation from the Maxwell point in the direction that favors the periodic state causes it to expand, resulting in a uniform increase in wavelength of the entire spatially periodic region. Further deviation beyond the snaking region triggers a depinning transition where the spatially periodic state invades the homogeneous state leading to a picture similar to Figure 2.15(b). The reverse is true when deviation from the Maxwell point energetically favors the homogeneous state. In this case, the picture would resemble Figure 2.14(b). Thus, the variation of the wavelength within the snaking region is consistent with the

depinning process: when the bifurcation parameter is varied so as to increase the wavelength, further variation of the parameter in the same direction to outside the snaking region would lead to an invasion of the periodic state. Conversely, when the parameter is varied so as to decrease the wavelength, further variation to outside the snaking region would result in an invasion of the homogeneous state. This relation between wavelength selection and depinning direction does not apply in the case of the Turing-Hopf pinning solutions, however. Given the depinning results of §2.3.3, the reasoning above would suggest that the wavelength of the striped region should decrease (increase) when D increases (decreases). Figure 2.16(a) suggests that the opposite is true for the Turing-Hopf pinning solutions. Thus, the wavelength selection within the snaking region is unrelated to the direction of depinning. The latter is determined by the relative dominance between the Turing and Hopf modes and was explained in §2.3.3. An explanation for the former is given in the next subsection.

2.3.5. Comparison of Pinning Region to Results Based on Amplitude Equations

Like the Turing-Hopf pinning solutions described in §2.3.2 for the full Brusselator model (2.1), there also exist Turing-Hopf solutions of the amplitude equations (2.2). In such solutions as that in Figure 2.17(a), regions in space where $(|A|, |C|) = (0, C_0)$ are connected by approximately exponential monotonic fronts (close up in Figure 2.17(b)) to regions where $(|A|, |C|) = (A_0, 0)$. We note that while $|C|$ is stationary, $C(x, t)$ is complex and oscillates periodically in time. The widths of the Turing and Hopf regions are arbitrary and thus a continuum of solutions exists for an appropriate parameter set. Such solutions of the amplitude equations translate to solutions similar to that shown in Figure 2.8 for the full Brusselator model. However, these solutions of the amplitude equations exist only on a codimension one subset in parameter space, while the

snaking region of the Brusselator model is codimension zero. This point is developed further below. We remark that while Figure 2.17(a) resembles the mesa patterns constructed in [**57**] for a particular scaling of (2.1), that analysis does not appear to be applicable to (2.2).

Above, $A_0 = \sqrt{\gamma/g}$ is the spatially homogeneous pure Turing amplitude, while the amplitude of the Hopf mode $C_0 \approx \sqrt{\nu/\beta_r}$ is slightly affected by interaction with the Turing mode; its exact determination is beyond the scope of this chapter. The reason that only the spatially homogeneous Turing amplitude needs to be considered is the property that the spatial dynamics of (2.2a) conserves a quantity in X (see e.g., [**44**]) that uniquely selects the wavelength. In particular, a solution $A = R(X)e^{i\theta(X)}$ must conserve the "angular momentum" $h(X) = R^2(X)d\theta/dX$. If $R(X) = 0$ for any X, then $h(X) = 0$ for all X. Thus, at any point at which $R(X)$ is nonzero, $d\theta/dX = 0$ must hold, leading to a spatially homogeneous Turing region. By this conservation law, for any solution to (2.2) such that (2.2a) reaches a steady state, if there exists a region in space such that $(|A|, |C|) = (0, C_0)$, regions for which $|C| = 0$ may only admit the spatially homogeneous $A = A_0$ state. Indeed, when time evolving (2.2) initialized with A spatially periodic in the $C = 0$ region, a coarsening of the Turing state occurs until the region is spatially homogeneous. This wavelength selection within the amplitude equations may explain the observation in §2.3.4 that the wavelength λ of the striped region is closer to the critical value λ_c the closer (B, D) are to (B_H, D_c), their values at the C2THP.

The front solution to (2.2) shown in Figure 2.17(a) only exists on a positively sloped line in (μ, ρ)–space through the origin (dashed line in Figure 2.18(a)), a codimension one subset in parameter space. The μ–ρ relationship was obtained numerically by time evolving (2.2) for various μ and ρ and observing pairs (μ, ρ) for which the Turing-Hopf front remained stationary. The line shown in Figure 2.18(a) is a least squares fit through the computed data points

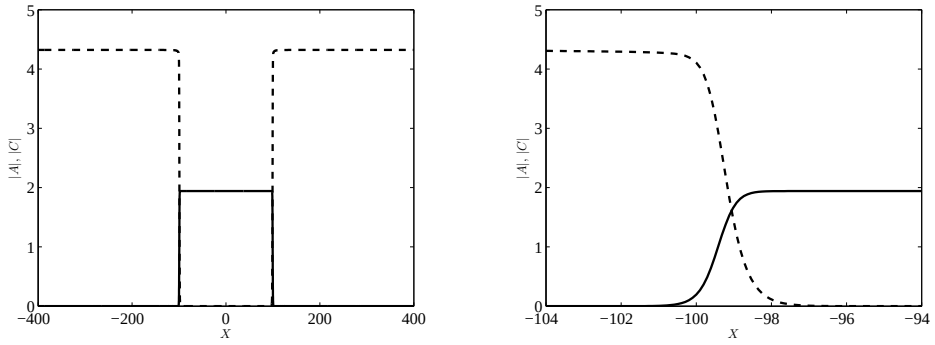

(a) magnitudes of Turing-Hopf solution of amplitude equation

(b) closeup of left fronts

Figure 2.17. Shown in (a) is a plot of the stationary amplitudes of a Turing-Hopf solution of the amplitude equations. The Turing (Hopf) amplitude is the solid (dashed) line. The widths of the Turing and Hopf regions are arbitrary. The parameters are $\mu = 25$, $\rho = 0.1682$, and $E = 1.4$. A close-up of the left front is shown in (b).

(empty circles). We refer to this line as the Maxwell line, even though the problem is not variational. The significance of the Maxwell line is that the snaking region is expected to straddle the Maxwell line, regardless of whether the system is variational. Another nonvariational example can be found in [**63**], where a higher order analytical approximation to the Maxwell curve for stationary solutions of the (nonvariational) Lugiato-Lefever model was calculated from a seventh order Ginzburg-Landau equation near the codimension two point corresponding to weakly subcritical Turing bifurcation. This curve was shown to be straddled by a numerically determined snaking region of [**39**].

Below the Maxwell line in Figure 2.18(a), the Turing mode becomes less dominant in relation to the Hopf mode, and the Hopf mode invades the Turing mode. Above this line, the opposite is true. By comparing the Turing and Hopf growth rates γ and ν given in the appendix, it is easily shown that the ratio γ/ν decreases as D (or ρ) increases. Unlike the full Brusselator model that has a codimension zero snaking region within the parameter space in which a

continuum of solutions exist, the Turing-Hopf solutions of the amplitude equations only exist on a codimension one subset. The reason is that the amplitude equations do not capture the nonadiabatic effects of (2.1) responsible for the pinning of periodic fronts (see e.g., [**22**, **63**, **88**] and references therein), or equivalently, the broadening of the Maxwell curve. The black dots in Figure 2.18(a) are computed limits of the snaking region for various values of B for a domain length of $L = 250$. We observed that the limits of the snaking region shift more to the left, i.e., closer to straddling the Maxwell line, the larger the value of L. Comprehensive results for lengths significantly larger than $L = 250$ were difficult to obtain due to computational constraints. Besides the length of the domain, another reason for the slight discrepancy may be the lowest order approximation of (2.1). In [**63**], it was shown that the weakly nonlinear analysis must be carried out to higher orders for the Maxwell curve to be straddled by the limits of the snaking region near a codimension two point. In Figure 2.18(b), we show a semi-log plot of the width of the snaking region in D for various values of $-(B - B_H)^{-1}$. The dashed line is a least squares fit through the data points (empty circles). The linear relation indicates that, near the C2THP, the width of the pinning region in D is exponentially narrow in $-(B - B_H)^{-1}$, consistent with the scaling analytically determined in [**14**].

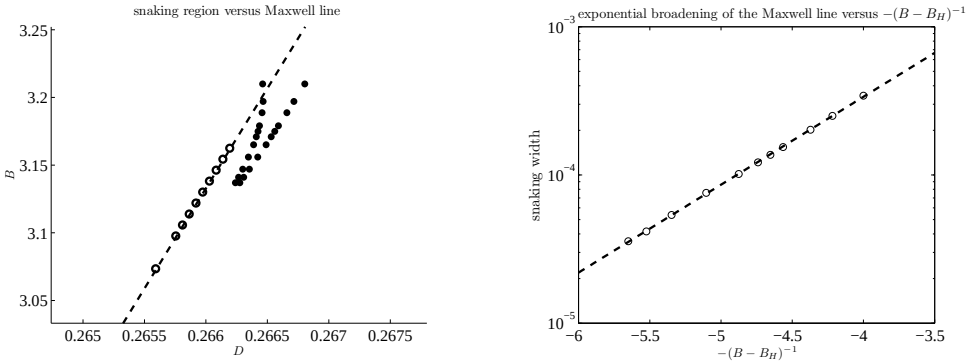

(a) snaking region versus Maxwell line (b) exponential broadening of the Maxwell line

Figure 2.18. Figure (a) depicts the relationship between the numerically determined Maxwell line (dashed) and the limits of the pinning region (solid circles). The dashed line is a least squares fit through data points indicated by empty circles. The relationship between the Turing and Hopf growth rates γ and ν on the Maxwell line is approximately linear, as can be seen from (a) along with the expressions for γ and ν in the appendix. Figure (b) is a semi-log plot of the width of the snaking region in D as a function of $-(B - B_H)^{-1}$. For B near B_H, the width is approximately exponential in $-(B - B_H)^{-1}$.

2.4. Discussion

In this chapter, we have extended the study of homoclinic snaking of stationary pinning solutions to solutions exhibiting time periodicity. Whereas most studies in the past have focused on the subcritical Turing regime of variational models, we have demonstrated snaking behavior near a C2THP of a nonvariational system where both the Turing and Hopf bifurcations are supercritical. In the region of Turing-Hopf bistability, we found multiple branches of solutions characterized by a coexistence of temporal oscillations and stationary stripes. By using AUTO to solve boundary value problems in time for the Fourier amplitudes of the space-time solutions, we were able to compute both stable and unstable solution branches. Two pairs of branches were found. Each solution on one pair contained a defect at the center of the striped region, while solutions on the other pair did not. The solutions on either pair of branches differ

by a π phase shift in the spatially periodic pattern. We found that these branches displayed a similar structure to those found for stationary pinning solutions. Further similarities discovered include the manner in which striped structures of the space-time solutions were destroyed or nucleated when traversing up or down the branches. The scaling of the speed of the depinning transition with respect to distance from the nearest saddle-node was also found to be the same as that observed in studies of stationary pinning solutions. Lastly, within the framework of the amplitude equations valid near the C2THP, we numerically determined a Maxwell line, and showed that the pinning region was located nearby, with the separation decreasing as the length of the domain increased. There are, however, also important differences. The saddle-nodes of the snaking branches found did not monotonically converge to a single value in the bifurcation parameter. Also, instead of terminating on the pure Hopf branch the way that stationary pinning branches terminate on the homogeneous branches, the snaking branches found here connect to a pair of collapsed snaking branches through a series of complex saddle-nodes. Wavelength selection of the striped region along the snaking branches is also different. In particular, wavelength variation appears unrelated to the direction of depinning as was the case in the Hamiltonian spatial dynamics of the Swift-Hohenberg equations.

There are many open problems to pursue that would increase the understanding of time periodic pinning solutions. A qualitative interpretation, analogous to the spatial dynamics framework applied to the stationary pinning solutions, would provide valuable insights into the nature of the solutions found in this study. A quantitative determination of the $\delta^{-1/2}$ scaling of the depinning time-scale is also a key open problem. Other paths of analysis may include calculating the Maxwell point of the system of amplitude equations, or extending the method of [**14**] to analytically determine the pinning region. A higher order system of amplitude equations may be

derived to confirm that the corresponding higher order Maxwell line compares more favorably to the snaking region. Lastly, it would be interesting to see if Turing-Hopf pinning solutions also exist in two dimensions, and if so, if the solutions are also organized on branches that share the same structure as those found in this chapter and for stationary pinning solutions in the two dimensional Swift-Hohenberg equations [**2**, **66**]. Turing-Hopf coexistence in two dimensions near the supercritical C2THP has been numerically observed in [**49**].

CHAPTER 3

Localized Pulses in the Singularly Perturbed Regime: The Small Eigenvalues

Recent attention has focused on deriving localized pulse solutions to various systems of reaction-diffusion equations. In this chapter, we consider the evolution of localized pulses in the Brusselator activator-inhibitor model, long considered a paradigm for the study of nonlinear equations, in a finite one dimensional domain with feed of the inhibitor through the boundary and global feed of the activator. We employ the method of matched asymptotic expansions in the limit of small activator diffusivity and small activator and inhibitor feeds. The disparity of diffusion lengths between the activator and inhibitor leads to pulse-type solutions in which the activator is localized while the inhibitor varies on an $O(1)$ length scale. In the asymptotic limit considered, the pulses become pulses described by Dirac delta functions and evolve slowly in time until equilibrium is reached. Such quasi-equilibrium solutions with N activator pulses are constructed and a differential-algebraic system of equations (DAE) is derived, characterizing the slow evolution of the locations and the amplitudes of the pulses. We find excellent agreement for the pulse evolution between the asymptotic theory and the results of numerical computations. An algebraic system for the equilibrium pulse amplitudes and locations is derived from the equilibrium points of the DAE system. Both symmetric equilibria, corresponding to a common pulse amplitude, and asymmetric pulse equilibria, for which the pulse amplitudes are different, are constructed. We find that for a positive boundary feed rate, pulse spacing of

symmetric equilibria is no longer uniform, and that for sufficiently large boundary flux, pulses at the edges of the pattern may collide with and remain fixed at the boundary. Lastly, stability of the equilibrium solutions is analyzed through linearization of the DAE, which, in contrast to previous approaches, provides a quick way to calculate the small eigenvalues governing weak translation-type instabilities of equilibrium pulse patterns.

3.1. Introduction

Since Turing [**95**] showed that diffusion-driven instabilities of a spatially homogeneous steady-state could give rise to spatially complex patterns in a mixture of chemically reacting species, reaction-diffusion equations have been paradigms of spatio-temporal pattern formation. Much of the analysis since has been weakly nonlinear, involving small amplitude patterns arising from small perturbations of the unstable uniform steady state. However, numerical studies (see e.g. [**84**] for numerical simulations of the two dimensional Gray-Scott model) have shown that large-amplitude perturbations can lead to the formation of localized structures, solutions far from equilibrium and thus not amenable to weakly nonlinear analysis. Instead, the method of matched asymptotic expansions has been applied to construct such localized solutions. Early works involving the one dimensional Gray-Scott model on the infinite line include [**30**], [**28**] and [**29**], where a dynamical systems approach was taken to construct localized pulse solutions and study their stability by analyzing a nonlinear eigenvalue problem (NLEP). In [**73**], stability analysis of a one dimensional pulse to transverse perturbations in the second dimension was performed. Extensions of these results to incorporate finite domain effects for models such as the Gray-Scott (e.g. [**59**] and [**16**]), Gierer-Meinhardt (e.g. [**47**] and [**46**]), and Schnakenberg (e.g [**105**] and [**61**]) models have been of recent interest. In one dimension, behaviors such as

slow pulse evolution, pulse-splitting, and pulse oscillations have been predicted analytically and confirmed numerically. In [**103**], the dynamics of a one-pulse solution to a simplified Gierer-Meinhardt model were analyzed under the influence of a precursor gradient, which was shown to pin the pulse at a location different from that of equilibrium in the absence of the gradient. In this work, we consider the slow evolution of multiple pulses in the one dimensional activator-inhibitor Brusselator model (see e.g., [**100**] and references therein), long a paradigm of nonlinear analysis.

The Brusselator model describes the space-time dependence of the concentrations of the intermediate products U (the activator) and V (the inhibitor) in the sequence of reactions

$$E \to U\,, \qquad B + U \to V + P\,, \qquad 2U + V \to 3U\,, \qquad U \to Q\,. \tag{3.1}$$

The global reaction is $E + B \to P + Q$, corresponding to the transformation of reactants E and B into products P and Q. The third reaction of sequence (3.1) is autocatalytic in that U drives its own production; thus, U is the activator. The autocatalytic reaction requires the presence of V to proceed; the depletion of V in the autocatalytic process acts as an inhibition mechanism to limit the growth of U. Thus, V is the inhibitor and is subject to low concentrations in regions of high activator concentration. A different scenario is seen in the Gierer-Meinhardt model [**37**] where the autocatalytic reaction is impeded by the presence of an inhibitor. In this case, high concentrations of the inhibitor are observed in regions of high activator concentration.

Due to the third reaction in (3.1), the Brusselator model shares the same cubic nonlinearity as the Gray-Scott and Schnakenberg models but differs in that the former contains a global feed term of the activator and not of the inhibitor. The feed of the activator comes from the first reaction in (3.1). The result of a global activator feed term is that localized pulses in the

concentration of the activator can decay to either a zero or non-zero value away from their centers, depending on the value of the feed term. We find that the absence or presence of the activator feed term has an important role in the evolution of the pulses. This is in contrast to the Gray-Scott and Schnakenberg models, where pulses always decay to zero away from their centers. Further, while many previous studies considered pure Neumann boundary conditions for both the activator and inhibitor, we allow for the possibility of a boundary feed term of the inhibitor, which we find alters the equilibrium solutions as well as the interaction between pulses and boundaries.

In [**79**], localized solutions were computed numerically and analyzed for a variation of the conventional Brusselator model. Instead of the concentration of the reactant E being kept constant as is the case in most studies of the Brusselator model, it was allowed to vary with space and time. The diffusion rate of E was also taken to be significantly larger than those of U and V. Localized structures exhibited by the conventional Brusselator model near a codimension two point were numerically observed under periodic [**97**] and, additionally, pure Neumann [**22**] boundary conditions with similar diffusivities of the activator and inhibitor. In the following analysis, we consider a singular perturbation of the conventional Brusselator model with an asymptotically small activator-inhibitor diffusivity ratio, leading to the formation of localized pulses in the concentration of the activator. Assuming (without loss of generality) that all rate constants of the reactions in (3.1) are unity, the conventional dimensionless Brusselator model in a one dimensional domain with slow diffusion of the activator and constant influx of the inhibitor from the boundaries can be written as

$$u_t = \epsilon^2 u_{xx} + \mathcal{E} - (B+1)u + vu^2\,, \qquad -1 < x < 1\,, \quad u_x(\pm 1, t) = 0\,, \quad t > 0\,, \quad \text{(3.2a)}$$

$$v_t = Dv_{xx} + Bu - vu^2\,, \qquad -1 < x < 1\,, \quad v_x(\pm 1, t) = \pm\mathcal{A}\,, \quad t > 0\,, \quad \text{(3.2b)}$$

supplemented by appropriate initial conditions, where $u \geq 0$ is the activator concentration (which will be seen to be the localized variable), $v \geq 0$ is the inhibitor, $0 < \epsilon \ll 1$, and $\mathcal{A}$, B, D and $\mathcal{E}$ are non-negative constants. In a study of mesa-type patterns, [**57**] considers a slightly different form in which the first and last steps of (3.1) occur much more slowly than the other reactions, leading to the kinetic terms of (3.2a) being $r\mathcal{E} - (B+r)u + vu^2$ with r small.

The activator drives its own reaction through a positive feedback (the vu^2 term in (3.2a)), while its growth is controlled by the inhibitor, for which there is negative feedback, represented by the $-vu^2$ term in (3.2b) ([**51**]). The condition that the inhibitor diffuses significantly faster than the activator ($D \gg \epsilon^2$) is essential for the formation of pulses, as in [**72**]. Indeed, the self-production of the activator in a region of length $O(\epsilon)$ cannot be sufficiently suppressed by the inhibitor as the strong inflow of the inhibitor from the peripheral regions continues to feed the production of the activator ([**52**], [**51**]). It is for this reason, along with the slow diffusion of the activator, that we expect the formation of localized pulses in the activator, while the inhibitor varies over an $O(1)$ length scale. As a result, the leading order interaction between pulses is due to the slow spatial variation of the inhibitor variable, this interaction having thusly been termed semi-strong [**31**]. This regime is in contrast to the weak interaction regime, in which

$D = O(\epsilon^2)$, $\epsilon \ll 1$ and studied in [**81**] and [**82**] for the Gray-Scott model, yielding both pulse-splitting behavior and pulse collisions. In this latter regime, both the activator and the inhibitor are localized, hence the weaker pulse interaction.

As mentioned, pulse patterns in reaction-diffusion models in one dimension (e.g., [**46**], [**59**], [**105**]) have previously been considered with no-flux boundary conditions, leading to repulsive pulse-boundary interactions. In contrast, we will show that, in this Brusselator model with boundary flux, the boundaries of the domain can be attracting for large enough boundary flux. We begin in §3.3 by using matched asymptotic expansions to derive a system of differential algebraic equations (DAE) describing the slow evolution of N-pulse quasi-equilibrium patterns (see [**32**] for a treatment of slow pulse evolution in a regularized Gierer-Meinhardt model). Considering special two and three-pulse cases, we demonstrate that pulses at the edges of the pulse pattern (edge-pulses) can be captured by the boundary when the boundary feed increases such that their equilibrium positions no longer lie inside the domain. The term "capture" herein will refer to the event in which a pulse collides with and remains fixed at the boundary and, in the cases that we considered, its amplitude changes dramatically over a relatively short time. The presence of boundary flux also affects equilibrium pulse spacing and requires modification of the "gluing" construction for equilibrium pulse patterns employed in [**104**] and [**60**] for the Gierer-Meinhardt and Gray-Scott models. Instead, in §3.4, we construct equilibrium solutions by deriving an algebraic system for equilibrium pulse amplitudes and locations from equilibrium points of the DAE. As in the aforementioned studies, symmetric equilibria, corresponding to a common pulse amplitude, and asymmetric pulse equilibria, for which pulse amplitudes are different, are found. For symmetric equilibria, we show that pulse spacing is non-uniform due to boundary flux, and we also give a general criterion for edge-pulses to be captured by the

boundary. Finally, in §3.5, the stability of the equilibrium points of DAE dynamics is calculated analytically which, in contrast to the approach in [**104**] and [**60**] for Gierer-Meinhardt and Gray-Scott models, provides a quick way to calculate the small eigenvalues governing the weak translation-type instabilities of pulse patterns. In this chapter, however, no analysis of $O(1)$ time-scale fast instabilities of the pulse profile, typically governed by a nonlocal eigenvalue problem (see e.g., [**105**], [**58**]), is carried out.

3.2. Scalings

To motivate the scalings with respect to ϵ of the parameters and variables in (3.2), we first note that u is the localized variable for which the inner region of each pulse has $O(\epsilon)$ width. We also assume that, since v is the slowly varying global variable, it is of the same order in both the inner region and the outer region away from each pulse. Thus, in order to balance v_x to the boundary feed rate term $\mathcal{A}$ in (3.2b), $v = O(\mathcal{A})$ in all regions. In the inner region, we let $u = O(U_{in})$ and assume that $U_{in} \gg \mathcal{E}$. In order for the cubic term in (3.2a) to balance the derivative and linear terms and yield a homoclinic solution in u, we require that $U_{in}\mathcal{A} = O(1)$, or $U_{in} = O(\mathcal{A}^{-1})$. In the outer region, the term vu^2 in (3.2b) as $\epsilon \to 0$ can be represented as a delta sequence with weight $O(\epsilon U_{in}^2\mathcal{A})$, which must balance the v_{xx} term, yielding $\mathcal{A} = O(\epsilon U_{in}^2\mathcal{A})$. Thus, $U_{in} = O(\epsilon^{-1/2})$ and $\mathcal{A} = O(\epsilon^{1/2})$. The same scaling is obtained from repeating this argument for the Bu term in (3.2b) with $B = O(1)$. Finally, from (3.2a), assuming $vu^2 \ll u$, we have $u = O(U_{out}) = O(\mathcal{E})$ in the outer region, which must balance the v_{xx} term in (3.2b), so that $O(\mathcal{E}) = O(\epsilon^{1/2})$. Thus, $u = O(\epsilon^{-1/2})$ in the inner region while $u = O(\epsilon^{1/2})$ in the outer region. Globally, $v = O(\epsilon^{1/2})$. With these scalings for $\mathcal{A}$ and $\mathcal{E}$, we rewrite (3.2) as

$$u_t = \epsilon^2 u_{xx} + \epsilon^{1/2} E - (B+1)u + vu^2\,, \qquad -1 < x < 1\,, \quad u_x(\pm 1, t) = 0\,, \quad t > 0\,, \tag{3.3a}$$

$$v_t = Dv_{xx} + Bu - vu^2\,, \qquad -1 < x < 1\,, \quad v_x(\pm 1, t) = \pm\epsilon^{1/2} A\,, \quad t > 0\,. \tag{3.3b}$$

All subsequent analysis and computations will be performed on this system.

3.3. Evolution of Multiple Pulses

Using matched asymptotic expansions, we now construct an N-pulse quasi-equilibrium solution to (3.3) that evolves on an asymptotically slow time-scale $T = \epsilon^2 t$; the scale determined by enforcing consistency in the solvability condition in the inner problem. Assuming an $O(1)$ separation distance between adjacent pulses and between edge-pulses and the boundaries, we separately consider the inner problem for each individual pulse j. That is, in the j^{th} inner region, we recall the inner scalings in §3.2 and introduce the inner variables

$$\begin{aligned} u &\sim \frac{1}{\epsilon^{1/2}} U_j(y_j) = \frac{1}{\epsilon^{1/2}} \left(U_{j_0} + \epsilon U_{j_1} + \dots\right)\,; \qquad y_j = \frac{x - x_j(T)}{\epsilon}\,, \\ v &\sim \epsilon^{1/2} V_j(y_j) = \epsilon^{1/2} \left(V_{j_0} + \epsilon V_{j_1} + \dots\right)\,; \qquad y_j = \frac{x - x_j(T)}{\epsilon}\,, \end{aligned} \tag{3.4}$$

where we assume $x_i < x_j$ for $i < j$. The solution is thus characterized by N pulses whose form remains constant while their center and amplitude may vary on a slow time-scale. Substituting (3.4) into (3.3), we find the leading order equations for U_{j_0} and V_{j_0}:

$$U_{j_0}'' - (B+1)U_{j_0} + V_{j_0} U_{j_0}^2 = 0\,, \qquad -\infty < y_j < \infty\,, \tag{3.5a}$$

$$U_{j_0} \to 0 \;\text{ as }\; |y_j| \to \infty\,, \tag{3.5b}$$

and

$$DV_{j_0}'' = 0\,, \qquad -\infty < y_j < \infty\,, \tag{3.6a}$$

$$V_{j_0} \ \text{ bounded as } \ |y_j| \to \infty\,, \tag{3.6b}$$

where the decay condition on U_{j_0} at $\pm\infty$ and the boundedness condition on V_{j_0} are required to match to the outer solution. We remove the translational invariance of (3.5) by requiring that $U_{j_0}'(0) = 0$. Here, the primes indicate differentiation with respect to y_j. Since (3.6) leads to V_{j_0} being a constant, the leading order inner equations are uncoupled. We can then readily solve (3.5) and (3.6) as

$$V_{j_0} = \bar{V}_j(x_1, \ldots, x_N) \equiv \bar{V}_j\,, \qquad j = 1, \ldots, N\,,$$

and

$$U_{j_0}(y_j) = \frac{3(B+1)}{2\bar{V}_j}\text{sech}^2\left(\frac{\sqrt{B+1}}{2}y_j\right)\,, \tag{3.7}$$

where $\bar{V}_j$ is spatially independent but can depend on $x_1, \ldots, x_N$. In [**74**], it was shown that the exponential decay in the tail of (3.7) is replaced by an algebraic decay when the activator is superdiffusive. We refer to the pre-factor in (3.7) as the pulse amplitude, which is inversely proportional to $\bar{V}_j$. We will see below that, like x_j, $\bar{V}_j$ evolves on an $O(\epsilon^2)$ time-scale. At the next order, we obtain for U_{j_1} and V_{j_1}

$$U_{j_1}'' - (B+1)U_{j_1} + 2\bar{V}_j U_{j_0} U_{j_1} = -x_j'(T)U_{j_0}' - V_{j_1}U_{j_0}^2 - E\,, \qquad -\infty < y_j < \infty\,, \tag{3.8a}$$

$$U_{j_1} \to \frac{E}{B+1} \quad \text{as} \quad |y_j| \to \infty\,, \tag{3.8b}$$

and

$$DV_{j_1} = V_{j_0}U_{j_0}^2 - BU_{j_0}\,, \qquad -\infty < y_j < \infty\,. \tag{3.9}$$

The limiting condition (3.8b) follows from the fact that in the outer region $u \sim \epsilon^{1/2}E/(B+1)$, which can be deduced from applying the outer region scaling $u = O(\epsilon^{1/2}) = v$ and solving for u in (3.3a). In the far-field, we allow V_{j_1} to grow linearly in y_j, with the precise conditions to come from matching to the outer solution. The solution to (3.9) can then be readily obtained, which we write as

$$V_{j_1}(y) = -\frac{3(B+1)}{2D\bar{V}_j}\text{sech}^2\left(\frac{\sqrt{B+1}}{2}y_j\right) + \frac{6}{D\bar{V}_j}\log\left(\cosh\left(\frac{\sqrt{B+1}}{2}y_j\right)\right) + c_{j_1}y_j + c_{j_2}\,, \tag{3.10}$$

where c_{j_1} and c_{j_2}, which may depend on $x_1, \ldots, x_N$, are integration constants. The former determines the linear behavior of V_{j_1} in the far-field, and will be calculated when the inner solution is matched to the outer. Determining c_{j_2} requires higher order matching, and is not needed for our purposes.

To use the Fredholm alternative to find an expression for $x_j'(T)$ from (3.8a), we make the substitution $U_{j_1} = W_j + E/(B+1)$ to obtain

$$W_j'' - (B+1)W_j + 2\bar{V}_j U_{j_0} W_j =$$

$$-2U_{j_0}\bar{V}_j \frac{E}{B+1} - x_j'(T)U_{j_0}' - V_{j_1}U_{j_0}^2\,, \qquad -\infty < y_j < \infty\,, \quad \text{(3.11a)}$$

$$W_j \to 0 \ \text{ as } \ |y_j| \to \infty\,. \qquad \text{(3.11b)}$$

Differentiating (3.5a) with respect to y_j, we find that $W = U_{j_0}'$ is a solution to the homogeneous problem of (3.11a) satisfying (3.11b); thus, the right-hand side of (3.11a) must satisfy the Fredholm condition

$$\int_{-\infty}^{\infty} U_{j_0}' \left(-2U_{j_0}V_{j_0}\frac{E}{B+1} - x_j'(T)U_{j_0}' - V_{j_1}U_{j_0}^2 \right) dy_j = 0\,. \qquad \text{(3.12)}$$

Noting that V_{j_0} is a constant and that U_{j_0} is an even function (from (3.7)), we use (3.10) to obtain from (3.12)

$$\frac{dx_j}{dT} = \frac{2c_{j_1}}{\bar{V}_j}\,, \qquad j = 1, \ldots, N\,.$$

Here, c_{j_1}, introduced in (3.10), and $\bar{V}_j$ will be determined by matching the inner solution of v to the outer solution along with a solvability condition. In general, c_{j_1} and $\bar{V}_j$ can depend on x_j, $j = 1, \ldots, N$, resulting in coupling between the N pulses. Since x_j varies slowly in time, so too will $\bar{V}_j$, $j = 1, \ldots, N$, and consequently, the pulse amplitudes.

To solve for v in the outer region, we proceed as in [**105**] and use the assumption of sufficiently separated pulses to express each term involving u in (3.3b) as a sum of N appropriately

weighted delta masses, with each delta mass representing a pulse. With weights equal to the area under each function involving u, we approximate the Bu term in (3.3b) as

$$Bu \sim \epsilon^{1/2}\frac{BE}{B+1}+\sum_{j=1}^{N} w_{j_1}\delta(x-x_j)\,; \qquad w_{j_1}=\epsilon^{1/2}\int_{-\infty}^{\infty} U_{j_0}\,dy_j=\epsilon^{1/2}\frac{6B\sqrt{B+1}}{\bar{V}_j}\,, \tag{3.13}$$

and the vu^2 term in (3.3b) as

$$vu^2 \sim \sum_{j=1}^{N} w_{j_2}\delta(x-x_j)\,; \qquad w_{j_2}=\epsilon^{1/2}\int_{-\infty}^{\infty} V_{j_0}U_{j_0}^2\,dy_j=\epsilon^{1/2}\frac{6(B+1)^{3/2}}{\bar{V}_j}\,. \tag{3.14}$$

Then, using (3.13) and (3.14) in (3.3b), and rescaling $v=\epsilon^{1/2}\nu$, we find that, to leading order, ν satisfies

$$\begin{gathered} D\nu_{xx}+\frac{BE}{B+1}-6\sqrt{B+1}\sum_{j=1}^{N}\frac{1}{\bar{V}_j}\delta(x-x_j)=0\,, \\ -1<x<1\,, \qquad \nu_x(\pm 1)=\pm A\,. \end{gathered} \tag{3.15}$$

Integrating (3.15) over $-1<x<1$ and applying the boundary conditions on ν_x, we find that $\bar{V}_j$ must satisfy the solvability condition

$$\sum_{j=1}^{N}\frac{1}{\bar{V}_j}=\frac{AD+F}{3\sqrt{B+1}}\,, \tag{3.16}$$

where

$$F\equiv\frac{BE}{B+1}\,. \tag{3.17}$$

With the constraint (3.16), we solve for $\nu(x)$ up to an arbitrary constant $\bar{\nu}$ in terms of a modified Green's function $G(x;x_j)$,

$$\nu = \bar{\nu} + \frac{A}{2}x^2 + 6\sqrt{B+1}\sum_{j=1}^{N}\frac{1}{\bar{V}_j}G(x;x_j)\,, \tag{3.18}$$

where $G(x;x_j)$ satisfies

$$\begin{aligned} DG_{xx}(x;x_j) + \frac{1}{2} &= \delta(x-x_j), \qquad -1 < x < 1\,, \\ G_x(\pm 1;x_j) &= 0, \qquad \int_{-1}^{1} G(x;x_j)\,dx = 0\,, \end{aligned} \tag{3.19}$$

with uniqueness achieved through the constraint in (3.19). The solution to (3.19) is

$$G(x;x_j) = -\frac{1}{4D}(x^2+x_j^2) + \frac{1}{2D}|x-x_j| - \frac{1}{6D}\,.$$

Now to determine $\bar{\nu}$ and c_{i_1}, we match the behavior of ν and V_i near x_i for $i = 1,\ldots,N$. Expanding $\nu(x)$ in (3.18) in powers of $(x-x_i)$ as $x \to x_i^+$, we find

$$\begin{aligned} \nu \sim \bar{\nu} + \frac{A}{2}x_i^2 + 6\sqrt{B+1}\sum_{j=1}^{N}\frac{1}{\bar{V}_j}G(x_i;x_j) + \\ \left(Ax_i + 6\sqrt{B+1}\sum_{j=1}^{N}\frac{1}{\bar{V}_j}G_x(x_i^+;x_j)\right)(x-x_i)\,, \end{aligned} \tag{3.20}$$

which must match the behavior of V_i as $y_i \to \infty$:

$$V_i \sim \bar{V}_i + \epsilon\left(\frac{3\sqrt{B+1}}{D\bar{V}_i}y_j + c_{i_1}y_j + c_{i_2} - \log 2\right)\,. \tag{3.21}$$

Matching the appropriate terms in (3.20) and (3.21) while recalling that $y_i = (x - x_i)/\epsilon$, we find that

$$\bar{\nu} = \bar{V}_i - \frac{A}{2}x_i^2 - 6\sqrt{B+1}\sum_{j=1}^{N}\frac{1}{\bar{V}_j}G(x_i;x_j)\,,$$

and

$$c_{i_1} = -\frac{3\sqrt{B+1}}{D\bar{V}_i} + Ax_i + 6\sqrt{B+1}\sum_{j=1}^{N}\frac{1}{\bar{V}_j}G_x(x_i^+;x_j)\,, \tag{3.22}$$

where $\bar{\nu}$ is independent of i. Matching the behaviors of ν and V_i as $x \to x_i^-$ and $y_i \to -\infty$, respectively, yields the equivalent expression

$$c_{i_1} = \frac{3\sqrt{B+1}}{D\bar{V}_i} + Ax_i + 6\sqrt{B+1}\sum_{j=1}^{N}\frac{1}{\bar{V}_j}G_x(x_i^-;x_j)\,. \tag{3.23}$$

We now summarize the results for an N-pulse quasi-equilibrium solution to (3.3) in the following result:

Principal Result I: *Let $\epsilon \to 0$ in* (3.3) *and assume $O(1)$ separation between adjacent pulses as well as $O(1)$ separation between edge-pulses and nearest boundaries. Then the leading order quasi-equilibrium N-pulse solutions for u and v are given by*

$$u(x) \sim \frac{1}{\epsilon^{1/2}}\left(\sum_{j=1}^{N}\frac{3(B+1)}{2\bar{V}_j}\text{sech}^2\left(\frac{\sqrt{B+1}}{2}\frac{x-x_j}{\epsilon}\right)\right) + \epsilon^{1/2}\left(\frac{E}{B+1} + \sum_{j=1}^{N}W_j\left(\frac{x-x_j}{\epsilon}\right)\right)\,, \tag{3.24a}$$

$$v(x) \sim \epsilon^{1/2} \left(\bar{\nu} + \frac{A}{2} x^2 + 6\sqrt{B+1} \sum_{j=1}^{N} \frac{1}{\bar{V}_j} G(x; x_j) \right) , \tag{3.24b}$$

where W_j *is the even solution to* (3.11)*, and* $\bar{\nu}$ *and* $\bar{V}_j$*,* $j = 1, \ldots, N$ *are determined by the system of* $N + 1$ *equations*

$$\bar{\nu} - \bar{V}_i + 6\sqrt{B+1} \sum_{j=1}^{N} \frac{1}{\bar{V}_j} G(x_i; x_j) = -\frac{A}{2} x_i^2 , \qquad i = 1, \ldots, N , \tag{3.25a}$$

$$\sum_{j=1}^{N} \frac{1}{\bar{V}_j} = \frac{AD + \frac{BE}{B+1}}{3\sqrt{B+1}} . \tag{3.25b}$$

The $O(\epsilon^2)$ *time-scale evolution of the pulse locations can be computed from*

$$\frac{dx_i}{dt} = \epsilon^2 \frac{2c_{i_1}}{\bar{V}_i} , \qquad i = 1, \ldots, N , \tag{3.26}$$

where c_{i_1} *is computed from* (3.22) *and* $\bar{V}_i$*,* $i = 1, \ldots, N$ *are computed from* (3.25)*. Eqns.* (3.25) *and* (3.26) *with* (3.22) *form a differential-algebraic system of equations (DAE) for the evolution of the pulse locations and* $\bar{V}_i$*, the inverse proportionality constant of pulse amplitude, which along with* $\bar{\nu}$*, uniquely parameterize a quasi-equilibrium state.*

We now consider special cases for which simplifications of the DAE are possible. The simplest is the one-pulse case for which, by (3.25b), $\bar{V}_1$ remains constant for all time. To leading orders, the solution of u and v are then given by

$$u(x) \sim \frac{1}{\epsilon^{1/2}} \frac{(AD+F)(B+1)}{2} \operatorname{sech}^2 \left(\frac{\sqrt{B+1}}{2} \frac{x - x_1}{\epsilon} \right) + \epsilon^{1/2} \left[\frac{E}{B+1} + W_1 \left(\frac{x - x_1}{\epsilon} \right) \right] , \tag{3.27a}$$

$$v(x) \sim \epsilon^{1/2} \left[-\frac{F}{2D}(x^2 - x_1^2) + \left(A + \frac{F}{D} \right) |x - x_1| + \frac{3\sqrt{B+1}}{AD+F} \right] , \tag{3.27b}$$

while the center of the pulse evolves on a slow time-scale as

$$x_1(t) = x_1(0) e^{-\epsilon^2 k_1 t} ; \qquad k_1 \equiv 2 \frac{EB\,(AD+F)}{3(B+1)^{3/2} D} , \tag{3.28}$$

where $x_1(0)$ is the initial position of the pulse and F is defined in (3.17). From (3.27a), we see that if $E = 0$, that is, if the pulse decays to a trivial background state, no pulse can exist unless $A > 0$. This is because the nontrivial background state of activator acts as a source for the inhibitor through the Bu term in (3.3b), and without this source, feed of the inhibitor must enter through boundaries. Further, for $E = 0$ and $A > 0$, (3.28) predicts that the pulse will remain stationary to all orders of ϵ. However, in this case, exponentially slow dynamics due to the failure of the pulse profile to satisfy the no-flux boundary conditions become important. This is analogous to the metastable pulse solution in a nonlocal reaction-diffusion equation derived from a certain limit of the Gierer-Meinhardt model ([**45**]) and is addressed in Appendix C.

The evolution of two pulses centered at $(-\alpha(t), \alpha(t))$ can also be obtained explicitly, the evolution of $\alpha(t)$ given by

$$\alpha(t) = \left[\alpha(0) - \frac{AD+F}{2F} \right] e^{-\epsilon^2 k_2 t} + \frac{AD+F}{2F} ; \qquad k_2 \equiv \frac{BE\,(AD+F)}{3(B+1)^{3/2} D} . \tag{3.29}$$

Comparing (3.29) to (3.28), we see that the evolution of a symmetric two pulse pattern when $A = 0$ is simply that of a one pulse pattern on a domain of half the size. When $A > 0$, the equilibrium locations of the pulses are given by $\alpha = (AD+F)/(2F)$ so that when A exceeds the critical value A_{c_2} given by

$$A_{c_2} = \frac{F}{D}\,, \tag{3.30}$$

equilibrium locations of the pulses are outside of the domain. We will illustrate the importance of this threshold below.

For a three-pulse pattern symmetric about $x = 0$ with pulses located at $(x_1(t), x_2, x_3(t)) = (-\alpha(t), 0, \alpha(t))$, we argue by symmetry that $\bar{V}_1 = \bar{V}_3 \equiv \bar{V}$. Then the evolution of $\alpha(t)$ is given by

$$\frac{d\alpha}{dt} = \epsilon^2 \frac{2}{\bar{V}} \left(-\alpha \frac{F}{D} + A + \frac{F}{D} - \frac{3\sqrt{B+1}}{\bar{V} D} \right)\,, \tag{3.31}$$

where $\bar{V}$ is solved in terms of α using (3.25). As we discuss in §3.5, only symmetric patterns are stable; thus, in equilibrium, all pulse amplitudes are equal so that $\bar{V}_i = 9\sqrt{B+1}/(AD+F)$, $i = 1, 2, 3$. Applying this in (3.31), we find that in equilibrium, $\alpha = 2(AD+F)/(3F)$, leading to the three-pulse threshold for existence of equilibrium locations inside the domain

$$A_{c_3} = \frac{F}{2D}\,. \tag{3.32}$$

When the boundary feed exceeds the respective thresholds above, pulses at the edges of the pattern are captured by the boundary. Thus, whereas when the boundary feed rate is sufficiently small, the boundaries repel the pulses, when the boundary feed is sufficiently large, the boundaries become attractive, leading to equilibrium patterns where pulses are centered at the boundary. We illustrate this point in the figures below in which we compare asymptotic results to those obtained numerically from solving (3.3) using the `MATLAB` function `pdepe()`. The locations of the centers of the pulses are simply taken to be the locations on the grid where local

maxima of u occur; we do not perform an interpolation near the maxima to compute a more accurate location. The asymptotic results may be obtained from either numerically solving the DAE (3.25) and (3.26) with (3.22), or from (3.29) and (3.31). In all plots containing u and v, the plotted quantities are $\epsilon^{1/2}u$ (solid line) and $\epsilon^{-1/2}v$ (dashed line). Lastly, in plots comparing the asymptotic prediction of the pulse location(s), the solid line represents the numerical result while the circles represent the asymptotic result.

In Figures 3.1(a)-3.1(c), we show the case of repulsive boundaries resulting from $A < A_{c_2}$. Figure 3.1(a) shows the quasi-equilibrium initial conditions for u and v. In Figure 3.1(b), we compare the asymptotic prediction of the pulse locations to that of the numerical solution. As predicted, the pulses evolve to symmetric equilibrium locations inside the domain as seen in Figure 3.1(c). Note that, as expected, locations of activator maxima coincide with locations of inhibitor minima. Figures 3.1(d)-3.1(f) show the $A > A_{c_2}$ case for attractive boundaries. In Figure 3.1(d), we see that the asymptotic prediction of the pulse locations is accurate until the pulses become sufficiently close to the boundary, at which point the asymptotic results become invalid. Figure 3.1(e) shows the evolution of the right pulse as it approaches and and is captured by the boundary at $x = 1$. From the times given in the caption, it is seen that the capture process is rapid relative to the evolution of the pulse when sufficiently far from the boundary. During this time as the pulse approaches the boundary, its amplitude doubles. Thus, as the pulses approach the boundaries, their amplitudes change dramatically in a short time. Lastly, we plot the equilibrium pattern in Figures 3.1(f) with two pulses centered at the boundary with twice their original amplitudes due to the fact that only half of each pulse is inside the domain. The Neumann conditions for v are met by boundary layers near $x = \pm 1$.

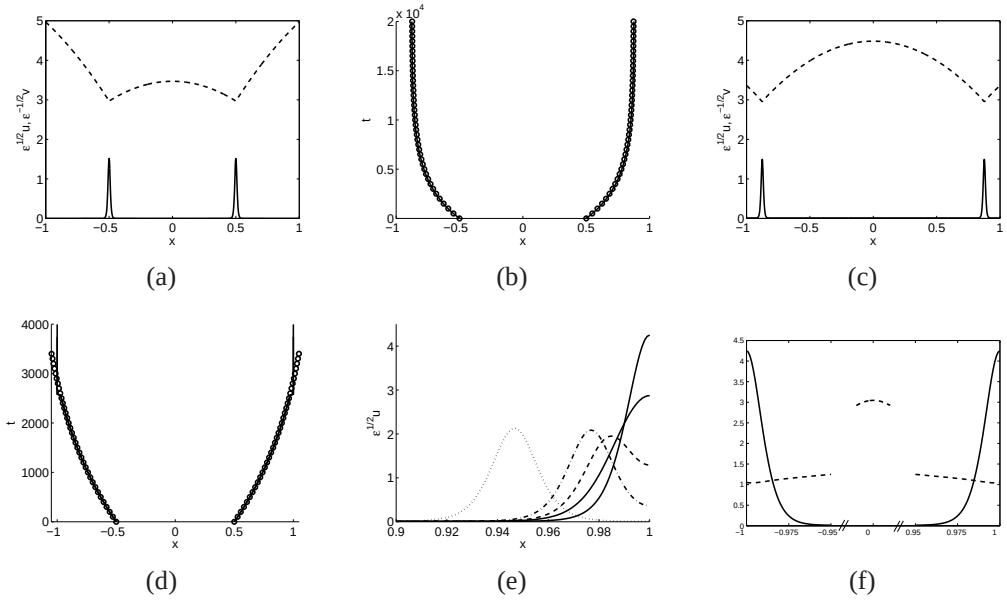

Figure 3.1. Illustration of the effect of boundary feed rate on the behavior of boundaries with $\epsilon = 0.01$, $B = 2$, $D = 0.5$, and $E = 3$ so that $A_{c_2} = 4$. In (a)-(c), $A = 3$ while in (d)-(f), $A = 6$. In both cases, the initial conditions (plotted for the former case in (a)) are $(x_1, x_2) = (-0.5, 0.5)$. When $A < A_{c_2}$, the boundaries are repulsive and the pulses evolve to equilibrium locations inside the domain ((b) and (c)). When $A > A_{c_2}$, the boundaries are attractive so that the pulses are captured by the boundaries ((d) and (f)). Note the axis breaks in (f). In (e), we show the evolution of the right pulse as it propagates to the right towards boundary at $x = 1$. The dotted line is a snapshot of $\epsilon^{1/2}u$ taken at $t = 2341$, the dashed-dotted line at $t = 2561$, and the dashed line at $t = 2576$. The two solid lines correspond to $t = 2577$ and $t = 2583$, the taller pulse being the equilibrium shape.

In Figures 3.2 we show the case of attracting boundaries for a three-pulse example symmetric about $x = 0$. The center pulse remains stationary, while the two edge-pulses drift toward the boundaries. As before, the asymptotics are able to predict the evolution of the pulses until they are too close to the boundaries (Figures 3.2(a) and 3.2(b)). In contrast to the two-pulse case, the pulse amplitudes must be calculated as a function of the pulse locations, and thus vary in time (Figure 3.2(b)). The difference between the asymptotic and numerical results in Figure 3.2(b) can be attributed to not including the second term in the expansion for u in (3.4). In

Figure 3.2(c), we show the equilibrium state with one pulse in the center and two pulses centered at the boundaries. Stability of near-boundary pulses were studied in [**68**] for the shadow Gierer-Meinhardt system, where it was shown that Robin boundary conditions could give rise to instabilities while Neumann conditions could not.

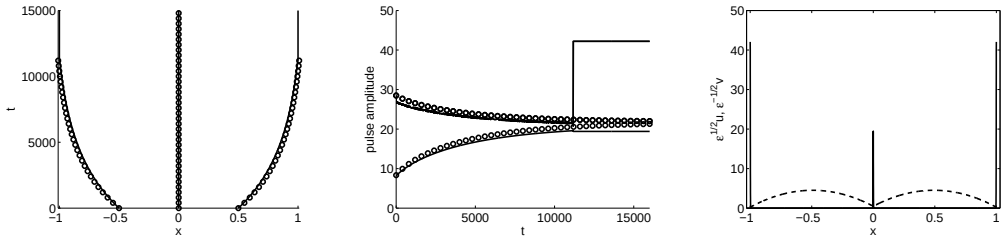

(a) (b) (c)

Figure 3.2. Illustration of the effect of boundary feed rate on the behavior of boundaries with $\epsilon = 0.00125$, $B = 5$, $D = 1$, and $E = 40$ so that $A_{c_3} = 16.67$. Here, $A = 20 > A_{c_3}$ so that the two edge-pulses are captured by the boundary. In (a) and (b), we compare the asymptotic to numerical results for pulse locations and amplitudes. In (c), we plot the equilibrium state with two pulses centered on the boundary.

In further numerical computations (not shown), we observed that any quasi-equilibrium pattern evolves to a symmetric equilibrium as long as pulses are not captured by the boundaries (rapid pulse collapse events, discussed briefly in §3.6, leading to a decrease in the number of pulses are possible, and are studied in the next chapter). In the next section of this chapter, we construct such equilibria by deriving an algebraic system from equilibrium points of the DAE obtained in this section. In addition, we construct asymmetric equilibria characterized by pulses of different amplitudes and find conditions for their existence.

3.4. Symmetric and Asymmetric Equilibria

In this section, we construct equilibrium states of (3.3) by finding equilibrium solutions of the DAE (3.25)-(3.26). By (3.26), equilibrium solutions for x_i, $\bar{V}_i$, $i = 1\ldots, N$, and $\bar{\nu}$

must satisfy the system (3.25) along with $c_{i_1} = 0$, $i = 1, \ldots, N$, where c_{i_1} is given in (3.22). We begin by considering symmetric equilibria for which all pulse amplitudes have a common value, but for which inter-pulse spacing may be non-uniform in the presence of a boundary feed rate. We will find that a positive boundary feed rate increases both the pulse amplitudes as well as inter-pulse spacing. Also, in particular, we derive a threshold for the boundary feed rate at which the interaction between the boundary and the edge-pules changes from repulsive to attractive. In previous similar studies with no boundary feed, the boundaries were shown to be repulsive. The other main focus of this section is to show that, in addition to symmetric equilibria, there exist asymmetric equilibria in which the pulse amplitudes can differ from one another. The existence of asymmetric equilibria arises from the multi-valued property of the inverse of a function obtained from solving (3.25) and $c_{i_1} = 0$. No general statement can be made about the effect of boundary feed on asymmetric equilibria; its effect depends on specific cases and will not be discussed here.

We begin by obtaining a general relation between equilibrium pulse locations and their amplitudes, applicable to both symmetric and asymmetric patterns. We then consider the two cases separately. Using (3.23) for c_{i_1}, we obtain

$$\frac{3b}{D\bar{V}_i} + Ax_i + 6b\sum_{j=1}^{N} \frac{1}{\bar{V}_j} G_x(x_i^-; x_j) = 0\,, \tag{3.33}$$

where

$$b \equiv \sqrt{B+1}\,. \tag{3.34}$$

Using

$$G_x(x; x_j) = -\frac{x}{2D} + \frac{1}{2D}\text{sgn}(x - x_j)$$

in (3.33), we find that the equilibrium pulse locations satisfy

$$\frac{1}{\bar{V}_i} - x_i \sum_{j=1}^{N} \frac{1}{\bar{V}_j} + \sum_{j=1}^{N} \frac{1}{\bar{V}_j}\text{sgn}(x_i^- - x_j) = -\frac{AD}{3b} x_i \,. \tag{3.35}$$

Using (3.25b) for the first sum in (3.35), and defining ℓ_j in terms of $\bar{V}_j$ by

$$\bar{V}_j = \frac{3b}{(AD + F)\ell_j} \,, \tag{3.36}$$

we split the second sum in (3.35) according to sgn$(x - x_j)$ and simplify to find

$$\ell_i + \sum_{j=1}^{i-1} \ell_j - \sum_{j=i}^{N} \ell_j = C x_i \,, \tag{3.37}$$

where

$$C \equiv \frac{F}{AD + F} \leq 1 \,. \tag{3.38}$$

Note that equality in (3.38) holds if $A = 0$. We make two remarks about ℓ_j. First, since $\bar{V}_j$ is inversely proportional to the amplitude of pulse j, ℓ_j is proportional to the amplitude. Second, the equivalent statement to (3.25b) in terms of ℓ_j is

$$\sum_{j=1}^{N} \ell_j = 1 \,, \tag{3.39}$$

which we use to write the second sum in (3.37) in terms of the first sum to calculate an expression for x_i in terms of ℓ_j, $j \leq i$:

$$x_i = \frac{1}{C}\left(2\sum_{j=1}^{i-1}\ell_j - 1 + \ell_i\right) . \tag{3.40}$$

From (3.40), we obtain the recursion relation for the pulse locations

$$x_1 = \frac{1}{C}\left(-1+\ell_1\right) , \qquad x_{i+1} = x_i + \frac{1}{C}\left(\ell_i + \ell_{i+1}\right) , \qquad x_N = \frac{1}{C}\left(1-\ell_N\right) . \tag{3.41}$$

If $C = 1$, the quantity $2\ell_j$ can be interpreted as the space occupied by pulse j. This interpretation was used in [**105**] to construct asymmetric pulse equilibria to the zero-boundary-flux Schnakenberg model, where equilibrium solutions allowed for pulses of two different amplitudes. The method of constructing the asymmetric equilibria was different from that employed in this section, as single pulses solved for on a domain of length $2\ell_j$ were "glued" together to form a multi-pulse solution. The method does not extend as naturally here because we allow for non-homogeneous boundary conditions. However, we will see below that asymmetric equilibria of the Brusselator model arise in the same manner as in the Schnakenberg model.

We first consider the simple case of symmetric solutions. Since all pulse amplitudes are equal, (3.39) yields $\ell_j = 1/N$ for all $j = 1, \ldots, N$, leading to $\bar{V}_j = 3\sqrt{B+1}N/(AD+F)$. Since pulse amplitudes are inversely proportional to $\bar{V}_j$, we see that increasing boundary feed leads to increasing pulse amplitudes in the case of symmetric solutions. The recursion relation (3.41) also simplifies, yielding

$$x_j = \frac{1}{C}\left(-1 + \frac{2j-1}{N}\right) . \tag{3.42}$$

With C given in (3.38), it is evident from (3.42) that the presence of boundary feed increases inter-pulse spacing and also leads to equilibrium edge-pulse locations closer to the boundaries. The condition for all pulses to be inside the domain is $x_N < 1$, or $C > (N-1)/N$. That is, as the boundary feed increases to some critical value A_{c_N}, the edge-pulses become centered on the boundary, and as the feed is increased past this threshold, no equilibrium positions within boundaries exist for the edge-pulses. In terms of the slow evolution of §3.3, the boundaries when $A > A_{c_N}$ are said to be attracting. This leads to the main result of this section:

Principal Result II: *Let $\epsilon \to 0$ in* (3.3) *and assume $O(1)$ separation between adjacent pulses as well as $O(1)$ separation between edge-pulses and nearest boundaries, and consider the slow evolution of the quasi-equilibrium pattern given in Principal Result I. Then the threshold A_{c_N} for the boundary feed A at which the boundaries change from repelling to attracting the pulses at the edges of an N-pulse pattern is given by*

$$A_{c_N} = \frac{F}{(N-1)D}\,. \tag{3.43}$$

When $A < A_{c_N}$, the boundaries repel pulses at the edges of the pattern, while when $A \geq A_{c_N}$, the boundaries attract the edge-pulses.

We note that the result (3.43) is consistent with those obtained in (3.30) and (3.32) for the two and three-pulse cases, and also that $E > 0$ is required for equilibrium locations inside the boundaries to exist. Because it appears that all asymmetric equilibria are unstable, as we will discuss in §3.5, this analysis is not worth repeating for asymmetric solutions, as quasi-equilibrium patterns will always evolve toward symmetric equilibrium points.

To construct asymmetric equilibria, we compute ℓ_j using (3.25a) to find $N-1$ equations of the form

$$\bar{V}_{i+1} - 6b\sum_{j=1}^{N}\frac{1}{\bar{V}_j}G(x_{i+1};x_j) - \frac{A}{2}x_{i+1}^2 = \bar{V}_i - 6b\sum_{j=1}^{N}\frac{1}{\bar{V}_j}G(x_i;x_j) - \frac{A}{2}x_i^2\,, \qquad i = 1,\ldots,N-1\,. \quad (3.44)$$

Using (3.36) to write $\bar{V}_j$ in terms of ℓ_j, (3.44) becomes

$$\frac{3b}{AD+F}\left(\frac{1}{\ell_{i+1}} - \frac{1}{\ell_i}\right) = 2(AD+F)\sum_{j=1}^{N}\ell_j\left(G(x_{i+1};x_j) - G(x_i;x_j)\right) + \frac{A}{2}\left(x_{i+1}^2 - x_i^2\right)\,. \quad (3.45)$$

We calculate the sum in (3.45) to be

$$\sum_{j=1}^{N}\ell_j\left(G(x_{i+1};x_j) - G(x_i;x_j)\right) = -\frac{1}{4D}\left(x_{i+1}^2 - x_i^2\right) + \frac{1}{2CD}\left(\ell_i + \ell_{i+1}\right)\left(\sum_{j=1}^{i}\ell_j - \sum_{j=i+1}^{N}\ell_j\right)\,. \quad (3.46)$$

To write the difference of squares term in (3.46) in terms of ℓ_i and ℓ_{i+1}, we write

$$x_{i+1}^2 - x_i^2 = (x_{i+1}-x_i)(x_{i+1}-x_i+2x_i) = (x_{i+1}-x_i)^2 + 2x_i(x_{i+1}-x_i)\,,$$

and, upon applying (3.40) for x_i and (3.41) for $(x_{i+1}-x_i)$, we find that

$$x_{i+1}^2 - x_i^2 = \frac{1}{C^2}(\ell_{i+1} + \ell_i)\left(4\sum_{j=1}^{i}\ell_j + \ell_{i+1} - \ell_i - 2\right). \tag{3.47}$$

Using (3.47) and (3.46) in (3.45) and recalling (3.39), we find that, upon rearranging,

$$\frac{1}{\ell_{i+1}} - \frac{1}{\ell_i} = \frac{(AD+F)^3}{6bDF}(\ell_i^2 - \ell_{i+1}^2)\,. \tag{3.48}$$

Making the substitution

$$\ell_i = qz_i\,, \qquad q \equiv \frac{(6bDF)^{1/3}}{AD+F}\,, \tag{3.49}$$

in (3.48) and (3.39), we find that z_i must satisfy

$$\beta(z_i) = \beta(z_{i+1})\,, \qquad i = 1, \ldots, N-1\,, \tag{3.50a}$$

$$\sum_{j=1}^{N} z_j = \frac{1}{q}\,. \tag{3.50b}$$

where $\beta(z) \equiv z^2 + \frac{1}{z}$. Note that the amplitude of pulse j is proportional to z_j. The function $\beta(z)$, plotted for a select range of z in Figure 3.3(a), has a global minimum at $z = z_c$, where

$$z_c = 2^{-1/3}\,. \tag{3.51}$$

Further, $\beta'(z) < 0$ on $(0, z_c)$ and $\beta'(z) > 0$ on (z_c, ∞). Thus, for any $z \in (0, z_c)$, there exists a unique point $\tilde{z} \in (z_c, \infty)$ such that $\beta(z) = \beta(\tilde{z})$. That is, the inverse function $\beta^{-1}(z)$ is multi-valued. Consequently, because (3.50a) must be satisfied for $i = 1, \ldots, N-1$, z_i can take on two and only two possible values, yielding two possible pulse amplitudes in a given equilibrium state. It is not restricted, however, in which value it does take on, meaning that the left-to-right

order in which the pulses appear in the domain is arbitrary. Since the amplitude of pulse i is proportional to z_i, $z_i = z$ would correspond to a small pulse at location i, while $z_i = \tilde{z}$ would correspond to a large pulse at location i. The system (3.50) is the same system that also led to the possibility of two pulse amplitudes in equilibrium solutions constructed in [**105**].

To find solutions to (3.50), we first solve $\beta(\tilde{z}) = \beta(z)$ for $\tilde{z} > z$ in terms of z. There are two positive solutions for $\tilde{z}$; clearly one solution is $\tilde{z} = z$. The other is given by

$$\tilde{z} = f(z) = \frac{-z + \sqrt{z^2 + 4/z}}{2} > z\,.$$

The function $f(z)$ is plotted in Figure 3.3(b).

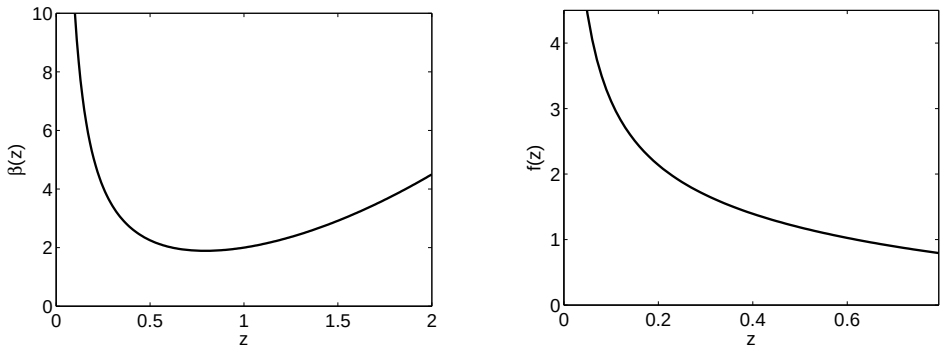

(a) (b)

Figure 3.3. Plots of the functions $\beta(z)$ (left) and $f(z)$ (right). The domain over which $f(z)$ is plotted is $z \in (0, z_c)$.

Letting N_1 be the number of small pulses and $N_2 = N - N_1$ the number of large pulses, allowing (3.50b) to be written as $N_1 z + N_2 \tilde{z} = 1/q$, we find that an equilibrium solution exists if there is at least one intersection between the curves

$$\tilde{z} = -\frac{N_1}{N_2} z + \frac{1}{qN_2}\,, \tag{3.52a}$$

$$\tilde{z} = \frac{-z + \sqrt{z^2 + 4/z}}{2}\,. \tag{3.52b}$$

Analysis concerning the existence and uniqueness of solutions to (3.52) can be found in [**105**]. We give here a short discussion leading to the results. The important properties of the function $f(z)$ are that $f(z_c) = z_c$, $f''(z) > 0$ on $(0, z_c)$, $f'(0) = -\infty$, and $f'(z_c) = -1$. We can then conclude that $f'(z) < -1$ on $(0, z_c)$. Thus, if $N_1/N_2 \leq 1$, there can be at most one intersection between the two curves in (3.52) in the interval $z \in (0, z_c)$. For a given N_1 and N_2, the value of $\tilde{z}$ at which the intersection occurs decreases as q increases; that is, the line (3.52a) shifts downwards as q increases. As q increases above a critical value q_m, the two curves can no longer intersect. When $q = q_m$, the intersection occurs at $(z, \tilde{z}) = (z_c, z_c)$. Using this fact in (3.52a), we find that

$$q_m = \frac{1}{N z_c}\,, \tag{3.53}$$

where $N = N_1 + N_2$ is the total number of pulses, and z_c is given in (3.51). The intersection of the two curves at $(z, \tilde{z}) = (z_c, z_c)$ when $q = q_m$ leads to the small and large pulses being of equal amplitude. Thus, when $N_1 \leq N_2$, asymmetric equilibria exist only when $q < q_m$.

If $N_1/N_2 > 1$, there can be either zero, one, or two points of intersection in the interval $z \in (0, z_c)$. The three ways in which intersections can occur are depicted for $N_1 = 3$ and $N_2 = 1$ in Figure 3.4. Similar to the previous case, as q increases past a critical value q_{m_1}, no intersection is possible. When $q = q_{m_1}$, the two curves are tangent at $z = z_*$ (the bottommost curve in Figure 3.4), where $0 < z_* < z_c$ is given by

$$z_* = \left[\frac{2(1+\gamma^2) - 2\sqrt{(1+\gamma^2)^2 - (1-\gamma^2)}}{(1-\gamma^2)}\right]^{1/3}, \qquad \gamma = 1 - \frac{2N_1}{N_2}\,. \tag{3.54}$$

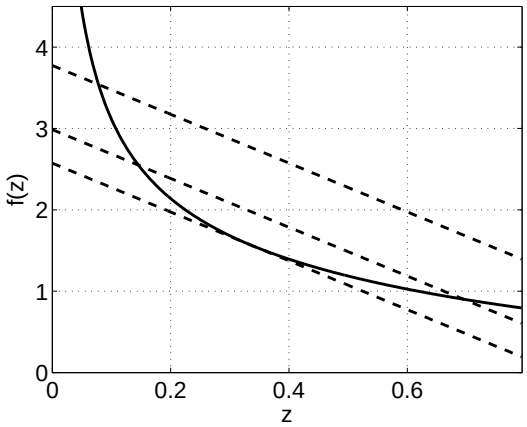

Figure 3.4. Plot of $f(z)$ (solid curve) and the linear function (3.52a) (dashed lines) for $N_1 = 3$, $N_2 = 1$. When $q = q_{m_1}$, the two curves are tangent. When $q_m < q < q_{m_1}$, there are two intersections, and when $q < q_m$, there is only one intersection. Here, $q_m \approx 0.31498$ and $q_{m_1} \approx 0.3886$. The three values of q, from lowest line to highest line, are $q \approx 0.3886$, $q \approx 0.33498$, and $q \approx 0.26498$.

Using (3.54) in (3.52a), we obtain the expression for q_{m_1}

$$q_{m_1} = \frac{1}{N_1 z_* + N_2 f(z_*)} \,. \tag{3.55}$$

As q decreases below q_{m_1}, the curves intersect in two locations (the middle line in Figure 3.4) until the rightmost intersection point reaches $(z, \tilde{z}) = (z_c, z_c)$. The value of q at which this occurs is $q = q_m$. For $q < q_m$, only one intersection on $z \in (0, z_c)$ is possible (the uppermost line in Figure 3.4).

We now summarize the results of asymmetric equilibria. The forms of u and v are the same as those of the quasi-equilibrium solution given in (3.24), where the pulse locations x_j are given by the recursion relation (3.41), with $\ell_j = qz$ corresponding to a small pulse centered at $x = x_j$, or $\ell_j = q\tilde{z}$ corresponding to a large pulse centered at $x = x_j$. Here, q is defined in (3.49), and $(z, \tilde{z})$ is given by an intersection of the right-hand sides of (3.52a) and (3.52b). The inverse

proportionality constant of the amplitude of each pulse, $\bar{V}_j$, is given in terms of ℓ_j by (3.36). The last parameter needed to construct the solution is $\bar{\nu}$, which may be calculated from x_j and $\bar{V}_j$ independent of i. The left-to-right ordering of small and large pulses is arbitrary.

In Figures 3.5, we demonstrate the arbitrary left-to-right ordering of small and large pulses using a five-pulse example with $N_1 = 2$ and $N_2 = 3$. Even though the same parameters were used to generate Figures 3.5(a) and 3.5(b), the arbitrary left-to-right ordering predicted above allows for different equilibrium states. However, since $N_1 < N_2$, only two possible pulse amplitudes are possible. That is, while other left-to-right orderings are possible, the pulse amplitudes in Figure 3.5 are the only amplitudes allowed by the parameter set.

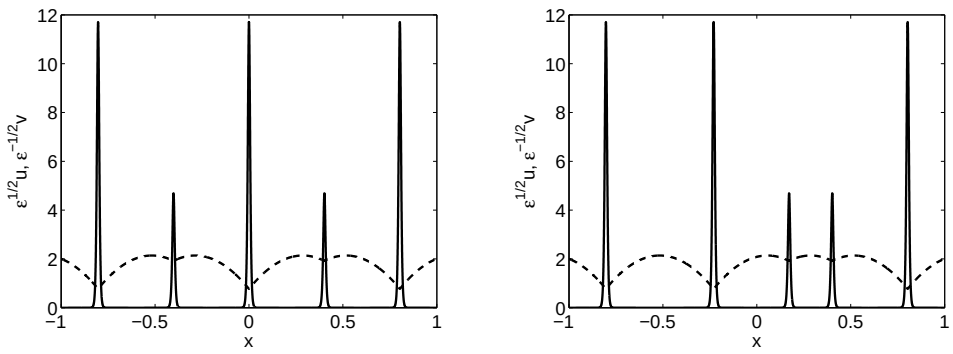

Figure 3.5. Two asymmetric equilibrium states with $N_1 = 2$ and $N_2 = 3$ and the same parameters but different left-to-right ordering of small and large pulses. The parameters are $\epsilon = 0.01$, $A = 3$, $B = 5$, $D = 1$ and $E = 40$. The small and large pulses of (a) are of the same amplitude as those in (b).

In Figures 3.6, we demonstrate the non-uniqueness of the solutions to (3.52) when $N_1 > N_2$. We illustrate the point on a four-pulse example with $N_1 = 3$ and $N_2 = 1$. The parameters are the same as those used to generate the middle line in Figure 3.4. With the same left-to-right ordering of small and large pulses, we plot the solutions corresponding to the left (solid) and

right (dashed) intersections in Figure 3.4. The left intersection corresponds to more disparate values for z and $\tilde{z}$, leading to more disparate pulse amplitudes and inter-pulse spacings while the right intersection corresponds to less disparate values for z and $\tilde{z}$, and thus the pulse amplitudes are less disparate with the pulses more evenly distributed across the domain.

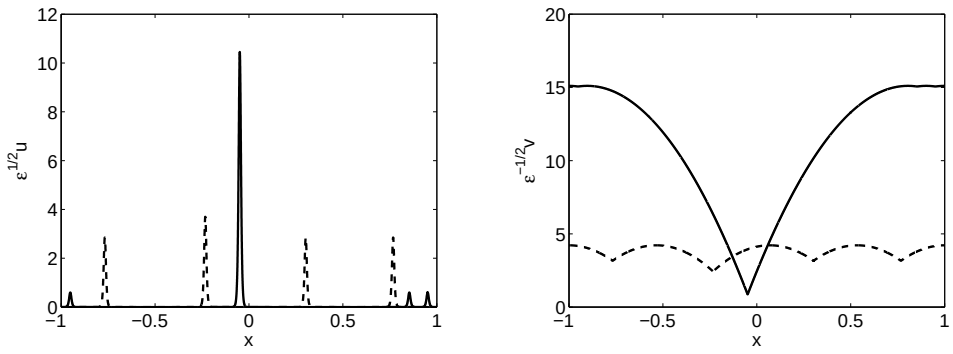

(a) (b)

Figure 3.6. Four-pulse asymmetric solutions with $N_1 = 3$ and $N_2 = 1$ and the same left-to-right ordering but corresponding to different intersections of $f(z)$ and the middle curve of Figure 3.4. The parameters are $\epsilon = 0.01$, $A = 0$, $B = 5$, $D \approx 0.25576$, and $E = 12$ so that $q_m \approx 0.31498$, $q_{m_1} \approx 0.3886$, and $q \approx 0.34498$. We plot $\epsilon^{1/2}u$ in (a) and $\epsilon^{-1/2}v$ in (b). The solid curves correspond to the left intersection, while the dashed curves correspond to the right intersection.

In §3.5, we analyze the stability of N-pulse equilibria to small ($O(\epsilon^2)$) eigenvalues corresponding to perturbations that either grow or decay on an $O(\epsilon^2)$ time-scale. They do not account for pulse collapse events in which one or more pulses collapse relatively rapidly on an $O(1)$ time-scale, nor do they predict oscillations of pulse amplitudes. Such instabilities are governed by large ($O(1)$) eigenvalues and are not studied here.

3.5. Stability of Equilibria to Small Eigenvalues

In this section, we study the stability of the equilibrium solutions constructed in §3.4 to $O(\epsilon^2)$ eigenvalues. The class of perturbations that we consider accounts only for slow drift

instabilities that occur on an $O(\epsilon^2)$ time-scale; analysis of these perturbations cannot predict instabilities that occur on an $O(1)$ time-scale. Thus, stability with respect to this class of perturbations does not guarantee that such solutions are stable, though solutions found to be unstable to these perturbations are certainly unstable. Two approaches were taken to analyze the stability to such perturbations. The first approach, in which an eigenvalue problem is derived by linearizing the system (3.3) around an N-pulse equilibrium solution, is analogous to that taken in the small eigenvalue analysis of [**105**]. As in [**105**], we found that the eigenvalues scaled as $O(\epsilon^2)$ and were eigenvalues of a certain $N \times N$ matrix $\mathcal{M}_P$. In the other approach, instead of linearizing (3.3), we linearize the DAE system (3.25)-(3.26) around an N-pulse equilibrium solution. The associated eigenvalues are eigenvalues of an $N \times N$ matrix $\mathcal{M}_D$. Since the DAE evolves on an $O(\epsilon^2)$ time-scale, perturbations of the DAE also grow or decay on an $O(\epsilon^2)$ time-scale, consistent with the first approach. Moreover, further calculations (not shown) show that $\mathcal{M}_D = r\mathcal{M}_P$, where r is a positive constant. The two analyses thus yield the same results in terms of stability and are equivalent. Because of the length of the first analysis and its similarity to that given in [**105**], we only present the stability analysis of the DAE in this section.

We first introduce the two N-dimensional column vectors $\boldsymbol{x} = (x_1, \ldots, x_N)^{\mathrm{T}}$ and $\boldsymbol{V} = (\bar{V}_1, \ldots, \bar{V}_N)^{\mathrm{T}}$ containing the pulse locations and inverse pulse amplitudes, respectively, where T denotes the transpose. We also denote

$$\boldsymbol{C}(\boldsymbol{x}, \boldsymbol{V}) = (C_1(\boldsymbol{x}, \boldsymbol{V}), \ldots, C_N(\boldsymbol{x}, \boldsymbol{V}))^{\mathrm{T}}\,, \tag{3.56a}$$

$$C_i(\boldsymbol{x}, \boldsymbol{V}) \equiv c_{i_1} = -\frac{3b}{D\bar{V}_i} + Ax_i + 6b\sum_{j=1}^{N}\frac{1}{\bar{V}_j}G_x(x_i^+; x_j)\,, \qquad i = 1, \ldots, N\,, \tag{3.56b}$$

where c_{i_1} was defined in (3.22). We lastly rewrite the $N+1$ algebraic equations in (3.25) in vector form as

$$\boldsymbol{H}(\boldsymbol{x}, \boldsymbol{V}, \bar{\nu}) = 0\,, \qquad S(\boldsymbol{V}) = 0\,,$$

where

$$\boldsymbol{H}(\boldsymbol{x}, \boldsymbol{V}, \bar{\nu}) = (H_1(\boldsymbol{x}, \boldsymbol{V}, \bar{\nu}), \ldots, H_N(\boldsymbol{x}, \boldsymbol{V}, \bar{\nu}))^{\mathrm{T}}\,, \tag{3.57a}$$

$$H_i(\boldsymbol{x}, \boldsymbol{V}, \bar{\nu}) = \bar{\nu} - \bar{V}_i + 6b \sum_{j=1}^{N} \frac{1}{\bar{V}_j} G(x_i; x_j) + \frac{A}{2} x_i^2\,, \qquad i = 1, \ldots, N\,, \tag{3.57b}$$

and

$$S(\boldsymbol{V}) = \sum_{j=1}^{N} \frac{1}{\bar{V}_j} - \frac{AD + F}{3b}\,,$$

where F is defined in (3.17) and b is defined in (3.34). An equilibrium solution $(\boldsymbol{x}, \boldsymbol{V}, \bar{\nu}) = (\boldsymbol{x}_e, \boldsymbol{V}_e, \bar{\nu}_e)$ thus satisfies the $2N+1$ system of equations

$$\boldsymbol{C}(\boldsymbol{x}_e, \boldsymbol{V}_e) = 0\,, \tag{3.58a}$$

$$\boldsymbol{H}(\boldsymbol{x}_e, \boldsymbol{V}_e, \bar{\nu}_e) = 0\,, \tag{3.58b}$$

$$S(\boldsymbol{V}_e) = 0\,. \tag{3.58c}$$

To derive the eigenvalue problem that determines stability, we perturb the equilibrium solutions according to

$$\boldsymbol{x} = \boldsymbol{x}_e + \delta\boldsymbol{\xi}\,, \qquad \boldsymbol{V} = \boldsymbol{V}_e + \delta\boldsymbol{\phi}\,, \qquad \bar{\nu} = \bar{\nu}_e + \delta\mu\,, \tag{3.59}$$

with $\delta \ll 1$. We then use (3.58b) and (3.58c) to determine $\boldsymbol{\phi}$ and μ in terms of $\boldsymbol{\xi}$, which we then use in (3.58a) to compute $\boldsymbol{C}(\boldsymbol{x}, \boldsymbol{V}) = \delta \mathcal{M} \boldsymbol{\xi}$ for some matrix $\mathcal{M}$. Using this for $\boldsymbol{C}$ in (3.26), the leading order terms yield the eigenvalue problem $d\boldsymbol{\xi}/dt = 2\epsilon^2 \mathcal{V}^{(e)} \mathcal{M} \boldsymbol{\xi}$, where $\mathcal{V}^{(e)}$ is the matrix

$$\mathcal{V}^{(e)} \equiv \begin{pmatrix} 1/\bar{V}_{1e} & 0 & \dots & 0 \\ 0 & \ddots & \cdots & 0 \\ \vdots & \vdots & \ddots & \vdots \\ 0 & 0 & \cdots & 1/\bar{V}_{Ne} \end{pmatrix}, \tag{3.60}$$

where V_{ie} is the i^{th} component of $\boldsymbol{V}_e$. The eigenvalues of the matrix $\mathcal{V}^{(e)} \mathcal{M}$ then determine the stability of the equilibrium solutions with respect to perturbations of the DAE.

We begin by substituting the perturbed solutions (3.59) into (3.58b) and expanding to first order in δ to calculate that

$$\mathcal{H}_{\boldsymbol{x}}^{(e)} \boldsymbol{\xi} + \mathcal{H}_{\boldsymbol{V}}^{(e)} \boldsymbol{\phi} + \mu \boldsymbol{H}_{\bar{\nu}}^{(e)} = 0\,, \tag{3.61}$$

where, for some N-dimensional column vector vector $\boldsymbol{w}$, scalar s, and N-dimensional vector function $\boldsymbol{F}$, $\mathcal{F}_{\boldsymbol{w}}(\boldsymbol{w}, s)$ denotes the Jacobian matrix

$$(\mathcal{F}_{\boldsymbol{w}}(\boldsymbol{w}, s))_{ij} = \frac{\partial F_i}{\partial w_j}\,, \qquad 1 \le i, j \le N\,; \qquad \boldsymbol{F} = (F_1, \dots, F_N)^{\mathrm{T}}\,, \qquad \boldsymbol{w} = (w_1, \dots, w_N)^{\mathrm{T}}\,,$$

and $\boldsymbol{F}_s$ denotes the derivative of $\boldsymbol{F}$ with respect to s, $(\boldsymbol{F}_s)_i = \frac{\partial F_i}{\partial s}$. The superscript $^{(e)}$ indicates that the quantity is evaluated at the equilibrium solution $(\boldsymbol{x}, \boldsymbol{V}, \bar{\nu}) = (\boldsymbol{x}_e, \boldsymbol{V}_e, \bar{\nu}_e)$. Next, expanding (3.58c) to first order in δ, we find that $\nabla \boldsymbol{S}^{(e)\mathrm{T}} \boldsymbol{\phi} = 0$.

Since we require $\boldsymbol{\phi}$ in terms of $\boldsymbol{\xi}$, we must first calculate μ in terms of $\boldsymbol{\xi}$. We first use (3.61) to write

$$\boldsymbol{\phi} = -\mathcal{H}_{\boldsymbol{V}}^{(e)-1}\left(\mathcal{H}_{\boldsymbol{x}}^{(e)}\boldsymbol{\xi} + \mu \boldsymbol{e}_N\right) , \tag{3.62}$$

where we have used (3.57) to calculate that $\boldsymbol{H}_{\tilde{\nu}}^{(e)}$ is the N-dimensional vector $\boldsymbol{e}_N \equiv (1, \ldots, 1)^{\mathrm{T}}$. Then using (3.62) for $\boldsymbol{\phi}$ in $\nabla \boldsymbol{S}^{(e)\mathrm{T}}\boldsymbol{\phi} = 0$, we find that

$$\mu = -\frac{\nabla \boldsymbol{S}^{(e)\mathrm{T}}\left(\mathcal{H}_{\boldsymbol{V}}^{(e)-1}\mathcal{H}_{\boldsymbol{x}}^{(e)}\boldsymbol{\xi}\right)}{\nabla \boldsymbol{S}^{(e)\mathrm{T}}\mathcal{H}_{\boldsymbol{V}}^{(e)-1}\boldsymbol{e}_N} . \tag{3.63}$$

Using (3.63) for μ in (3.61), we arrive at

$$\mathcal{H}_{\boldsymbol{V}}^{(e)}\boldsymbol{\phi} = -\mathcal{H}_{\boldsymbol{x}}^{(e)}\boldsymbol{\xi} + \frac{\nabla \boldsymbol{S}^{(e)\mathrm{T}}\left(\mathcal{H}_{\boldsymbol{V}}^{(e)-1}\mathcal{H}_{\boldsymbol{x}}^{(e)}\boldsymbol{\xi}\right)}{\nabla \boldsymbol{S}^{(e)\mathrm{T}}\mathcal{H}_{\boldsymbol{V}}^{(e)-1}\boldsymbol{e}_N}\boldsymbol{e}_N ,$$

which, upon some matrix algebra, yields $\boldsymbol{\phi} = \mathcal{R}\boldsymbol{\xi}$, where $\mathcal{R}$ is defined as

$$\mathcal{R} = \mathcal{H}_{\boldsymbol{V}}^{(e)-1}\left[-\mathcal{H}_{\boldsymbol{x}}^{(e)} + \frac{1}{\nabla \boldsymbol{S}^{(e)\mathrm{T}}\mathcal{H}_{\boldsymbol{V}}^{(e)-1}\boldsymbol{e}_N}\boldsymbol{e}_N\left(\nabla \boldsymbol{S}^{(e)\mathrm{T}}\mathcal{H}_{\boldsymbol{V}}^{(e)-1}\mathcal{H}_{\boldsymbol{x}}^{(e)}\right)\right] . \tag{3.64}$$

Finally, to derive the eigenvalue problem, we rewrite (3.26) in matrix form as

$$\frac{d\boldsymbol{x}}{dt} = 2\epsilon^2 \mathcal{V}\boldsymbol{C}(\boldsymbol{x}, \boldsymbol{V}), \qquad \mathcal{V} \equiv \begin{pmatrix} 1/\bar{V}_1 & 0 & \ldots & 0 \\ 0 & \ddots & \cdots & 0 \\ \vdots & \vdots & \ddots & \vdots \\ 0 & 0 & \cdots & 1/\bar{V}_N \end{pmatrix} , \tag{3.65}$$

where $\boldsymbol{C}$ is defined in (3.56). Using the perturbations (3.59) for $\boldsymbol{x}$ and $\boldsymbol{V}$ in (3.65) and expanding to the first order in δ, we arrive at the eigenvalue problem

$$\frac{d\boldsymbol{\xi}}{dt} = 2\epsilon^2 \mathcal{V}^{(e)} \mathcal{M} \boldsymbol{\xi}\,, \qquad \mathcal{M} \equiv \mathcal{C}_{\boldsymbol{x}}^{(e)} + \mathcal{C}_{\boldsymbol{V}}^{(e)} \mathcal{R}\,, \tag{3.66}$$

where $\mathcal{V}^{(e)}$ and $\mathcal{R}$ are defined in (3.60) and (3.64), respectively. This leads to the main result of this section:

Principal Result III: *Let $\epsilon \to 0$ in* (3.3) *and assume $O(1)$ separation between adjacent pulses as well as $O(1)$ separation between edge-pulses and nearest boundaries, and consider an equilibrium solution as constructed in §3.4 parameterized by $(\boldsymbol{x}, \boldsymbol{V}, \bar{\nu}) = (\boldsymbol{x}_e, \boldsymbol{V}_e, \bar{\nu}_e)$. Then the solution is stable with respect to small eigenvalues if all eigenvalues of the matrix $\mathcal{V}^{(e)}\mathcal{M}$ have negative real parts. Here, $\mathcal{V}^{(e)}$ and $\mathcal{M}$ are defined in* (3.60) *and* (3.66)*, respectively. It is unstable if at least one of the eigenvalues has positive real part. The entries of the vectors and matrices defined above are given as follows:*

$$(\mathcal{H}_{\boldsymbol{x}}^{(e)})_{ij} = \begin{cases} \frac{6\sqrt{B+1}}{\bar{V}_{je}} \frac{\partial}{\partial x_j} G(x_{ie}; x_j)\Big|_{x_j = x_{je}}\,, & i \neq j\,, \\ A x_{ie} + 6\sqrt{B+1} \sum_{k=1}^{N} \frac{1}{\bar{V}_{ke}} \frac{\partial}{\partial x_i} G(x_i; x_{ke})\Big|_{x_i = x_{ie}}\,, & i = j\,, \end{cases}$$

$$(\mathcal{H}_{\boldsymbol{V}}^{(e)})_{ij} = -\delta_{ij} - \frac{6\sqrt{B+1}}{\bar{V}_{je}^2} G(x_{ie}; x_{je})\,,$$

where δ_{ij} is the Kronecker delta function, and

$$\begin{gathered} (\nabla \boldsymbol{S}^{(e)\mathrm{T}})_i = -\frac{1}{\bar{V}_{ie}^2}\,, \\ (\mathcal{C}_{\boldsymbol{V}}^{(e)})_{ij} = \delta_{ij} \frac{3\sqrt{B+1}}{D\bar{V}_{ie}^2} - \frac{6\sqrt{B+1}}{\bar{V}_{je}^2} G_x(x_{ie}^+; x_{je})\,, \qquad (\mathcal{C}_{\boldsymbol{x}}^{(e)})_{ij} = -\delta_{ij} \frac{F}{D}\,, \end{gathered} \tag{3.67}$$

where F is defined in (3.17)*. This stability result is equivalent to that obtained from analyzing perturbations within the original system* (3.3)*.*

While, as expected, the above analysis predicts that some symmetric solutions are stable, it predicts that some asymmetric solutions are also stable. However, when solving (3.3) numerically with such asymmetric solutions as initial conditions, we have observed in all cases a pulse collapse event in which one or more pulses collapse relatively rapidly on an $O(1)$ time-scale. Thus, it appears that no asymmetric solutions are stable. In the symmetric case with $A = 0$, the matrix $\mathcal{V}^{(e)}\mathcal{M}$ reduces to a positive multiple of a matrix analyzed in [**48**], the eigenvalues ω_j of which were calculated as

$$\omega_1 = -\frac{N}{2D}\,, \qquad \omega_j = -\frac{N}{2D}\left[\frac{\left(1-\left(\frac{q_m}{q}\right)^3\right)\tan^2\left(\frac{\theta_j}{2}\right)}{\tan^2\left(\frac{\theta_j}{2}\right)-\left(\frac{q_m}{q}\right)^3\sec^2\left(\frac{\theta_j}{2}\right)}\right]\,, \qquad j=2,\ldots,N\,,$$

where $\theta_j = \pi(j-1)/N$, $j = 2,\ldots,N$, and q and q_m are defined in (3.49) and (3.53), respectively. Thus, we find that w_2 crosses into the right-half plane on the real axis when q is increased from q_m^- to q_m^+. When $q = q_m$, there are $N-1$ eigenvalues equal to 0, equaling the number of asymmetric branches that bifurcate from the symmetric branch (ignoring the permutations in left-to-right ordering of small and large pulses). We note that, for q sufficiently larger than q_m, all eigenvalues w_j become negative. However, it has been observed that these symmetric solutions are unstable to relatively rapid pulse collapse events (Figure 3.8(c)). We note that increasing ϵ from $\epsilon = 0.01$ to $\epsilon = 0.015$ in Figure 3.8(c) did not change the time at which the middle pulse collapsed, indicating an $O(1)$ instability.

Notice that the value $q = q_m$ at which stability changes is also the value at which asymmetric patterns bifurcate from a symmetric branch with $A = 0$. This is found to be true also for $A > 0$, and is illustrated in Figures 3.7, where we plot bifurcation diagrams for one and two pulses (3.7(a)) and three pulses (3.7(b)). The horizontal axis is the bifurcation parameter A, while the vertical axis is the norm defined by

$$|u|_2 = \left[\sum_{i=1}^{N} \left(\frac{3(B+1)}{2\bar{V}_j} \right)^2 \right]^{1/2}.$$

In the annotations, s_N is the symmetric N-pulse branch, and a 101 label represents a *large-small-large* ordering of a three-pulse asymmetric pattern. Parts of the branch that are stable (unstable) to small eigenvalues are depicted by a solid (dashed) line. Note that permutations of such a pattern would trace out the same curve, though we have plotted the curve for the permutations for which the pulse locations are between -1 and 1 for the values of A depicted. Lastly, A_m and A_{m_1} are values of A such that $q = q_m$ and $q = q_{m_1}$, respectively, where q, q_m and q_{m_1} are given in (3.49), (3.53), and (3.55). As previously stated in terms of q, stability of the symmetric branches changes at when $A = A_m$. In Figure 3.7(b), two 001 solutions exist in the interval $A_{m_1} < A < A_m$ as found in §3.4 for the $N_1 > N_2$ case. The lower branch corresponds to the solution of (3.52) with large z and small $\tilde{z}$, while the opposite is true for the upper branch. The upper branch ends when the location of an edge-pulse is outside of the domain. If the 010 solution were plotted instead, the stability properties of the branches would change. In all cases, asymmetric equilibria are unstable to small eigenvalues for A sufficiently near A_m, the value where they bifurcate from the symmetric branch. We emphasize that while some parts of asymmetric branches may be stable to small eigenvalues sufficiently far from the bifurcation point, numerical computations on (3.3) show that such solutions are unstable to

rapid collapse events; we have not numerically observed a stable asymmetric solution. Lastly, in the context of the DAE, there is no contradiction in the existence of multiple stable equilibria for a given value of A; different solutions of the algebraic part of the DAE lead to different systems of differential equations whose stationary points (and their stability) are independent of one another.

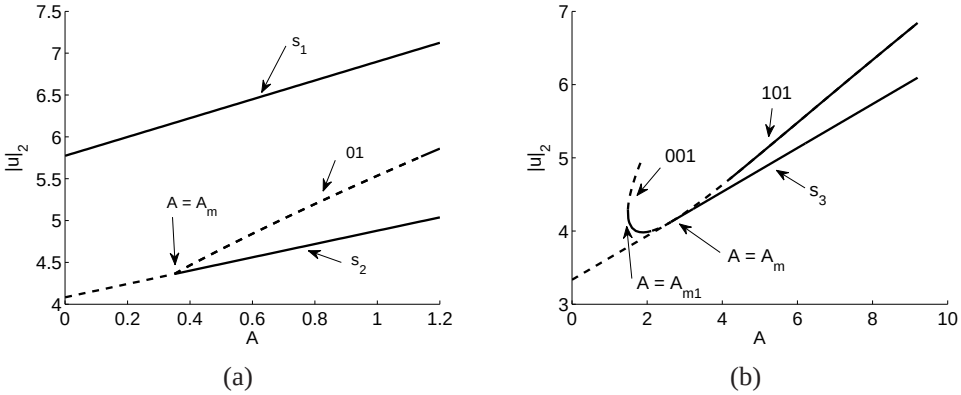

Figure 3.7. Bifurcation diagrams for one and two pulses ((a)) and three pulses ((b)) with $B = 2$ and $E = 10$. In (a), $D = 1.3$ while in (b), $D = 0.6$. The solid (dashed) lines indicate solutions that are stable (unstable) to slow instabilities. In (a) a single asymmetric branch (ignoring the 10 permutation) bifurcates from s_2 when $A = A_m$. In (b), two branches (again ignoring permutations) bifurcate from s_3 when $A = A_m$. In the region $A_{m_1} < A < A_m$, two 001 solutions exist.

In Figures 3.8(a) and 3.8(b), we show space-time plots of symmetric solutions starting from perturbations of two different three-pulse equilibria, both of which are stable to large eigenvalues, one for which $q < q_m$ (stable, Figure 3.8(a)) and the other for which $q > q_m$ (unstable, Figure 3.8(b)). The perturbation in the pulse locations was taken to be in the $(-1/\sqrt{2}, 0, 1/\sqrt{2})$ direction, with the perturbation in Figure 3.8(a) taken to be larger for illustrative purposes. In Figure 3.8(b), the solution drifts on an $O(\epsilon^2)$ time-scale to a solution near a three-pulse asymmetric equilibrium observed numerically to be stable to large eigenvalues. However, because it

is unstable to small eigenvalues, the pattern drifts for a duration of $O(\epsilon^{-2})$ until the pulse locations are such that the right pulse collapses (if the perturbation were in the $-(-1/\sqrt{2}, 0, 1/\sqrt{2})$ direction, it is the middle pulse that collapses). As was the case for the Gierer-Meinhardt model in [**46**], stability to collapse events is sensitive to instantaneous pulse locations; thus, in Figure 3.8(b), it is likely that the slow drift instability has triggered a fast collapse instability. While, as previously stated, the collapse event in Figure 3.8(c) occurs at a time independent of ϵ, the time of the collapse event in Figure 3.8(b) scales as $O(\epsilon^{-2})$, confirming that the initial instabilities in these two figures are of different nature. We finally note that all three pulses drift in the same direction at the onset of the pulse collapse due to the fact that the unstable eigenvector $\boldsymbol{\xi}$ in (3.66) of the aforementioned asymmetric three-pulse equilibrium is in the $(0.38671, 0.83720, 0.38671)$ direction.

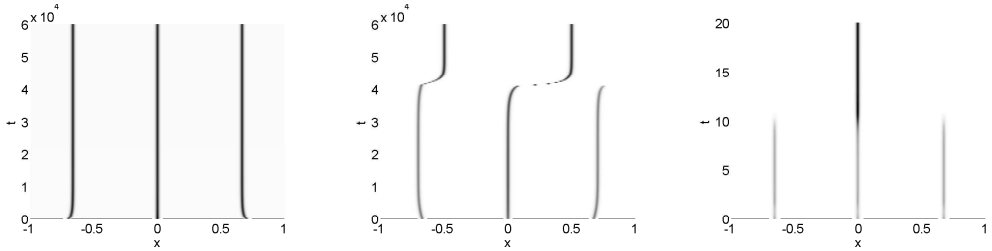

Figure 3.8. Space-time plot of $u(x,t)$ starting from perturbations of three-pulse equilibria. The dark (light) regions represent large (small) values. The parameters are $\epsilon = 0.01$, $A = 0$, $B = 2$, and $E = 10$. Here, $q_m \approx 0.41997$. The pulses are initially perturbed from their equilibrium locations at $(x_{1e}, x_{2e}, x_{3e}) = (-2/3, 0, 2/3)$. In (a), $D = 0.29$ ($q \approx 0.40778 < q_m$) so that the symmetric three-pulse equilibrium is stable. In (b), $D = 0.37$ ($q \approx 0.44228 > q_m$) so that the symmetric three-pulse equilibrium is unstable and the pulse locations drift away from the equilibrium locations. Eventually, one of the pulses collapses and the solution evolves to a stable two-pulse equilibrium ($q_m \approx 0.63 > q$). The apparent discontinuity near $t = 4 \times 10^4$ is due to the low temporal resolution used only for plotting purposes. In (c), $D = 2$ ($q \approx 0.7762$) so that $\omega_j < 0$ for $j = 1, 2, 3$. However, two pulses collapse relatively rapidly.

3.6. Discussion

The method of matched asymptotic expansions was used to construct quasi-equilibrium pulse solutions to a singularly perturbed Brusselator model in the semi-strong pulse-interaction regime. We introduced a particular scaling of the parameters of the Brusselator model to analyze the regime in which pulses move toward equilibrium positions on an $O(\epsilon^2)$ time-scale. Using solvability conditions and matching the inner and outer solutions, we derived a differential-algebraic system of equations (DAE) for the evolution of the pulse locations and inverse pulse amplitudes. We found excellent agreement between the asymptotic and numerical results computed from the Brusselator equations. We observed that the presence of a boundary feed term shifted the equilibrium positions of the edge-pulses toward the boundaries and increased inter-pulse spacings as well as pulse amplitudes. Further, based on the condition that edge-pulses of an N-pulse symmetric equilibrium lie outside of the domain, we derived a critical boundary feed rate above which the pulse-boundary interaction changes from repulsive to attractive. When the boundary feed rate exceeded this threshold, we found that edge-pulses of quasi-equilibrium solutions are captured by the boundary, leading to an equilibrium solution in which two pulses are centered on the boundary.

We also found equilibrium points of the differential-algebraic system of equations to construct equilibrium solutions. We found that, in addition to symmetric equilibria with equal pulse amplitudes, asymmetric solutions are also admitted for certain ranges of the parameter q defined in (3.49). The asymmetric equilibria are characterized by N_1 small and N_2 large pulses spaced unevenly across the domain with arbitrary left-to-right ordering. Numerical evidence suggests that asymmetric equilibria are always unstable, resulting either in a slow evolution to a symmetric equilibrium or in the rapid collapse of one or more pulses.

Finally, we analyzed the stability of N-pulse equilibria to perturbations that evolve on an $O(\epsilon^2)$ time-scale. Calculations (not shown) reveal that analyzing perturbations within the differential-algebraic system (3.25)-(3.26) is equivalent to analyzing perturbations within the original reaction-diffusion system (3.3). Combining the stability results of §3.5 with those of numerical computations, we found that only symmetric solutions may be stable to both small and large eigenvalues, and that asymmetric solutions appear to be always unstable to at least one of the modes of instability. Instability to large eigenvalues may manifest in rapid collapse events (depicted in Figure 3.8(c) for which the value of D is larger) or in pulse amplitude oscillations (not yet observed for this model). Study of such instabilities typically requires analysis of a non-local eigenvalue problem, and has been performed for the Gierer-Meinhardt ([**47**], [**46**], [**107**]) and Gray-Scott ([**58**]) models. The study of large eigenvalues for the Brusselator model is an open problem. Another interesting problem might be to find if there exists a regime such that pulse-splitting behavior may occur (as in, e.g. [**59**] and discussed qualitatively in [**29**]). Growing domains leading to pulse-splitting behavior has been proposed as a model for robust pattern formation in reaction-diffusion systems ([**3**] with noise and [**36**] with time delay). It would also be interesting to study the evolution of spots in a two dimensional singularly perturbed Brusselator model. In [**61**], spot-replication was studied for a singularly perturbed Schnakenberg model on a unit square and unit disk, while in [**33**], interaction of rings were studied with exothermic reaction kinetics. It was numerical observed that, in the parameter regime where the velocity of a traveling pulse in one dimension was fast, interactions between ring boundaries led to annihilation at the points of contact. Conversely, in the parameter regime where velocity of a traveling pulse in one dimension was slow, interactions between ring boundaries resulted in the breaking up of the rings, leading to a domain filled with spots and labyrithian-like patterns.

In the next chapter, we analyze the large eigenvalues responsible for amplitude instabilities that evolve on an $\mathcal{O}(1)$ time scale. Two possible classes of amplitude instabilities may occur. Competition instabilities result in the collapse or annihilation of one or more pulses, and are triggered when an eigenvalue crosses through the origin into the right-half plane. Oscillatory instabilities are characterized by oscillations in the amplitudes of all pulses, which occur when a pair of eigenvalues crosses the imaginary axis into the right-half plane. The oscillations may be either in phase or out of phase, depending on parameters. Both competition instabilities and the two types of oscillatory instabilities can be triggered either by a certain tuning of parameters, in which case the instabilities set in immediately at $t = 0$, or they can be dynamically triggered at a time $t_1 > 0$ by the slow dynamics studied in this chapter. Both of these scenarios are analyzed in detail in the next chapter.

CHAPTER 4

Localized Pulses in the Singularly Perturbed Regime: The Large Eigenvalues

In this chapter, in a one dimensional domain, the stability of localized pulse patterns is analyzed for two closely related singularly perturbed reaction-diffusion (RD) systems with Brusselator kinetics. For the first system, where there is no influx of the inhibitor on the domain boundary, asymptotic analysis is used to derive a nonlocal eigenvalue problem (NLEP) whose spectrum determines the linear stability of a multi-pulse steady-state solution. Similar to previous NLEP stability analyses of pulse patterns for other RD systems, such as the Gierer-Meinhardt (GM) and Gray-Scott (GS) models, a multi-pulse steady-state solution can become unstable to either a competition or an oscillatory instability depending on the parameter regime. An explicit result for the threshold value for the initiation of a competition instability, which triggers the annihilation of pulses in a multi-pulse pattern, is derived. Alternatively, in the parameter regime when a Hopf bifurcation occurs, it is shown from a numerical study of the NLEP that an *asynchronous*, rather than synchronous, oscillatory instability of the pulse amplitudes can be the dominant instability. The existence of robust asynchronous temporal oscillations of the pulse amplitudes has not been predicted from NLEP stability studies of other RD systems. For the second system, where there is an influx of inhibitor from the domain boundaries, an NLEP stability analysis of a quasi-steady-state two-pulse pattern reveals the possibility of dynamic bifurcations leading to either a competition or an oscillatory instability of the pulse amplitudes

depending on the parameter regime. It is shown that the novel *asynchronous* oscillatory instability mode can again be the dominant instability. For both Brusselator systems, the detailed stability results from NLEP theory are confirmed by rather extensive numerical computations of the full PDE system. This chapter is based on joint work with Prof. Michael Ward of the Department of Mathematics at the University of British Columbia, and Yana Nec, who at the time was a postdoctoral research at the same department.

4.1. Introduction

Spatially localized patterns arise from a wide variety of reaction-diffusion systems, with applications to chemical dynamics and biological modelling (cf. [**101**]), the spatial distribution of urban crime (cf. [**62**, **92**]), electronic gas-discharge systems (cf. [**91**]), and many other areas. In particular, it is now well-known that localized spot patterns can exhibit a wide range of different instabilities including, spot oscillation, spot annihilation, and spot self-replication behavior. Various topics related to the analysis of far-from-equilibrium patterns modeled by PDE systems are discussed in [**80**], [**40**], and [**52**].

In this broad context, in this chapter we study the stability of localized pulse-type solutions to two closely related RD systems with Brusselator-type kinetics. The Brusselator system (see e.g., [**79**], [**100**], or [**85**] and the references therein) is a well-known theoretical model for a simplified autocatalytic reaction. It describes the space-time dependence of the concentrations of the intermediate products U (the activator) and V (the inhibitor) in the sequence of reactions given in (3.1). Assuming (without loss of generality) that all rate constants of the reactions in (3.1) are unity, the conventional dimensionless Brusselator model in a one dimensional domain, with slow diffusion of the activator and constant influx of the inhibitor from the boundaries, can

be written as

$$U_t = \epsilon_0^2 U_{xx} + \mathcal{E}_0 - (B_0+1)U + vu^2\,, \quad -1<x<1\,, \quad U_x(\pm 1,t) = 0\,, \quad t>0\,, \tag{4.1a}$$

$$V_t = D_0 V_{xx} + B_0 U - VU^2\,, \qquad -1<x<1\,, \quad V_x(\pm 1,t) = \pm\mathcal{A}_0\,, \quad t>0\,, \tag{4.1b}$$

supplemented by appropriate initial conditions. Here $U \geq 0$, $V \geq 0$, $0 < \epsilon_0 \ll 1$, and $\mathcal{A}_0$, B_0, D_0 and $\mathcal{E}_0$ are all non-negative constants. The constant $\mathcal{A}_0$ represents a boundary feed term for the inhibitor, while the constant $\mathcal{E}_0$ represents a constant bulk feed for the activator. Our key assumption in the model is that there is an asymptotically large ratio of the diffusivities for U and V.

In the absence of a boundary feed-term, so that $\mathcal{A}_0 = 0$ in (4.1b), then pulses for (4.1) occur when $\mathcal{E}_0 = \mathcal{O}(\epsilon_0^{1/2})$ (see Appendix B and [**97**]). Upon writing $\mathcal{E}_0 = \epsilon_0^{1/2} E_0$ where $E_0 = \mathcal{O}(1)$, the scaling analysis in Appendix B yields

$$u_t = \epsilon^2 u_{xx} + \epsilon - u + fvu^2\,, \qquad -1<x<1\,, \quad u_x(\pm 1,t) = 0\,, \quad t>0\,, \tag{4.2a}$$

$$\tau v_t = D v_{xx} + \frac{1}{\epsilon}\left(u - vu^2\right)\,, \qquad -1<x<1\,, \quad v_x(\pm 1,t) = 0\,, \quad t>0\,, \tag{4.2b}$$

where t is a different time-scale than in (4.1). Here D, τ, ϵ, and f, are defined by

$$D \equiv \frac{D_0(B_0+1)^{3/2}}{E_0^2}\,, \qquad \tau \equiv \frac{(B_0+1)^{5/2}}{E_0^2}\,, \qquad \epsilon \equiv \frac{\epsilon_0}{\sqrt{B_0+1}}\,, \qquad f \equiv \frac{B_0}{B_0+1}\,. \tag{4.3}$$

In contrast, when both the boundary and bulk feed terms are non-vanishing, and are asymptotically small of the order $\mathcal{O}(\epsilon_0^{1/2})$ so that $\mathcal{E}_0 = \epsilon_0^{1/2} E_0$ and $\mathcal{A}_0 = \epsilon_0^{1/2} A_0$, where E_0 and A_0 are

$\mathcal{O}(1)$, then the appropriate re-scaled form of (4.1) is (see Appendix B below)

$$u_t = \epsilon^2 u_{xx} + \epsilon E - u + fvu^2\,, \qquad -1 < x < 1\,, \quad u_x(\pm 1, t) = 0\,, \quad t > 0\,, \tag{4.4a}$$

$$\tau v_t = D v_{xx} + \frac{1}{\epsilon}\left(u - vu^2\right)\,, \qquad -1 < x < 1\,, \quad v_x(\pm 1, t) = \pm 1\,, \quad t > 0\,, \tag{4.4b}$$

where D, E, τ, ϵ, and f are now defined by

$$\begin{gathered} D \equiv \frac{D_0 A_0^2 \sqrt{B_0+1}}{B_0^2}\,, \qquad E \equiv \frac{E_0 A_0}{B_0\sqrt{B_0+1}}\,, \\ \tau \equiv \frac{A_0^2 (B_0+1)^{3/2}}{B_0^2}\,, \qquad \epsilon \equiv \frac{\epsilon_0}{\sqrt{B_0+1}}\,, \qquad f \equiv \frac{B_0}{B_0+1}\,. \end{gathered} \tag{4.5}$$

The spatially uniform steady-state solution of (4.2) is $u_e = \epsilon/(1-f)$ and $v_e = \epsilon^{-1}(1-f)$. For arbitrary $\epsilon > 0$, it is well-known that this solution undergoes either a Turing or Hopf instability depending on the parameter ranges in (4.2) (cf. [**79**]). Near the bifurcation points for the onset of these instabilities, small amplitude patterns emerge and they have been well-studied in a multi-spatial dimensional context through canonical amplitude equations that are readily derived from a multi-scale weakly nonlinear analysis (see [**85**] and the references therein). For a detailed survey of normal form theory as applied to the study of 1-D pattern formation in the Brusselator model see [**110**]. More recently, a weakly nonlinear analysis was used in [**96**] to study pattern formation near a Turing-Hopf bifurcation in a Brusselator model with superdiffusion.

In contrast, with an asymptotically large diffusivity ratio as in (4.2), localized large amplitude patterns are readily observed in full numerical simulations of (4.2) with initial conditions close to the spatially uniform state (u_e, v_e). A standard calculation shows that for $f > 1/2$, $0 < \epsilon \ll 1$, and $\tau = \mathcal{O}(1)$, the band of unstable wave numbers m for an instability mode of the

form $(u, v) = (u_e, v_e) + e^{\lambda t + im}(\Phi, N)$ satisfies

$$\epsilon^{1/2}\left[(2f-1)(1-f)D\right]^{-1/2} < m < \frac{(2f-1)^{1/2}}{\epsilon}\,, \qquad \text{as} \quad \epsilon \to 0\,. \tag{4.6}$$

The maximum growth rate within this instability band is calculated as $\lambda_{\text{max}} \sim (2f-1) - 2\epsilon^2 m^2$, which occurs when $m = m_{\textbf{max}}$, where

$$m_{\text{max}} \sim \left(\frac{3f-2}{D(f-1)^2}\right)^{1/4} \epsilon^{-1/4}\,, \qquad \text{as} \quad \epsilon \to 0\,. \tag{4.7}$$

Therefore, the instability has a short wavelength of $\mathcal{O}(\epsilon^{1/4})$, In contrast, our results below (see (4.8) and (4.9)), show that stable localized pulses occur only at $\mathcal{O}(1)$ inter-pulse separation distances. This suggests that starting from initial data a coarsening process must occur, which eventually leads to localized pulses. For a particular parameter set, in Fig. 4.1 we show the formation of a two-pulse pattern as obtained from the numerical solution of (4.2).

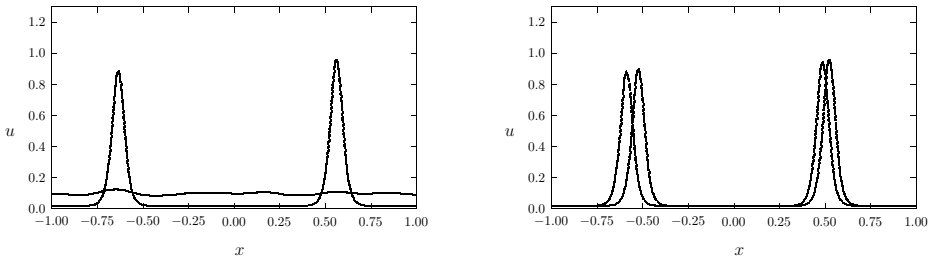

(a) u at $t = 18$ and $t = 46$ (b) u at $t = 193$ and $t = 837$

Figure 4.1. Plot of numerical solution u of (4.2) at different times for the parameter set $\epsilon = 0.02$, $f = 0.8$, $D = 0.1$, and $\tau = 0.001$, with initial condition $u(x,0) = u_e(1 + 0.02\times\text{rand})$ and $v(x,0) = v_e(1+0.02\times\text{rand})$, where $u_e = \epsilon/(1-f)$, $v_e = \epsilon^{-1}(1-f)$, and $rand$ is a uniformly generated random number in $[0,1]$. Left: the small amplitude pattern at $t = 18$ leads to the two-pulse pattern shown at $t = 46$. Right figure: As t increases from $t = 193$ to $t = 837$ the two pulses slowly drift to their equilibrium locations at $x = \pm 0.5$.

Rigorous results for the existence of large amplitude equilibrium solutions for some generalizations of the Brusselator model (4.2) in the non-singular perturbation limit $\epsilon = 1$ have recently been obtained in [**86**] and [**87**] (see also the references therein). However, to date, there is no comprehensive stability theory for these large amplitude solutions.

In a more general 1-D context, there are now many results for the existence and stability of localized equilibrium pulse patterns for various singularly perturbed two-component RD systems such as the Gierer-Meinhardt (GM) model [**27**,**47**,**106**,**108**], the Gray-Scott (GS) model [**15**,**30**,**58**,**72**,**73**], and the Schnakenberg model [**48**,**105**]. A explicit characterization of the slow dynamics of pulse patterns, and their instability mechanisms, is given in [**28**,**29**,**31**,**32**,**46**,**94**] for various RD systems in one space dimension. A central feature in all of these previous studies is that the determination of the spectrum of various classes of nonlocal eigenvalue problems (NLEP's) is critical for characterizing the stability of both equilibrium and quasi-equilibrium multi-pulse patterns. A survey of NLEP theory is given in [**109**].

The goal of this chapter is to provide a detailed analysis of the stability of multi-pulse equilibria of (4.2), and a detailed study of the dynamics and stability of two-pulse solutions for the Brusselator model (4.4) with a non-zero boundary feed term. Although much of the general theoretical framework for the pulse-stability analysis is closely related to that developed in previous works for GM, GS, and Schnakenberg RD systems, there are important differences both in the details of the analysis required and in the stability results that are obtained. The stability results obtained herein complement the results obtained in the previous chapter for the dynamics of pulses in the Brusselator model.

We now summarize our main results. In §4.2.1 we begin by briefly outlining the asymptotic construction of symmetric N-pulse equilibrium solutions to (4.2). We refer to a symmetric

N-pulse solution as one for which the pulses are equally spaced and, correspondingly, each pulse has the same amplitude. The main focus of §4.2, not considered in [**97**], is to analyze the stability of symmetric N-pulse equilibrium solutions to (4.2). A singular perturbation analysis is used in §4.2.2 to derive a nonlocal eigenvalue problem (NLEP) that determines the stability of this solution to $\mathcal{O}(1)$ time-scale instabilities. The derivation of this NLEP is rather more intricate than for related RD systems in [**27**, **30**, **47**, **48**, **58**, **73**, **105**, **106**] owing primarily to the presence of two separate nonlocal terms resulting from the $\mathcal{O}(\epsilon^{-1})$ coefficient in (4.2b), and secondarily from the nontrivial background state for the activator resulting from the constant feed term of order $\mathcal{O}(\epsilon)$ in (4.2a). From an analysis of this NLEP there are two distinct mechanisms through which the solution can go unstable as the bifurcation parameters τ and D are varied.

Firstly, for τ sufficiently small, our analysis of the NLEP in §4.2.3 reveals the existence of a critical threshold N_{c+} such that a pattern consisting of N pulses with $N > 1$ is unstable to a competition instability if and only if $N > N_{c+}$. This instability, which develops on an $\mathcal{O}(1)$ time scale as $\epsilon \to 0$, is due to a positive real eigenvalue, and it triggers the collapse of some of the pulses in the overall pattern. This critical threshold $N_{c+} > 0$ is the unique root of (see Principal Results 2.3 and 2.4 below)

$$N\left(1+\cos\left(\pi/N\right)\right)^{1/3} = \left(\frac{2f^2}{3(1-f)D}\right)^{1/3}. \tag{4.8}$$

In addition, from the location of the bifurcation point associated with the birth of an asymmetric N-pulse equilibrium solution, a further threshold N_{c-} is derived that predicts that an N-pulse equilibrium solution with $N > 1$ is stable with respect to slow translational instabilities of the

pulse locations if and only if $N < N_{c-}$, where (see (4.55))

$$N_{c-} = \left(\frac{2f^2}{3(1-f)D} \right)^{1/3} . \tag{4.9}$$

Since $N_{c-} < N_{c+}$, the stability properties of an N-pulse equilibrium solution to (4.2) with $N > 1$ and τ sufficiently small are as follows: stability when $N < N_{c-}$; stability with respect to fast $\mathcal{O}(1)$ time-scale instabilities but unstable with respect to slow translation instabilities when $N_{c-} < N < N_{c+}$; a fast $\mathcal{O}(1)$ time-scale instability dominates when $N > N_{c+}$. We remark that for (4.2) posed on a domain of length L, then by a scaling argument we need only replace D in (4.8) and (4.9) with $4D/L^2$. As an example, consider the parameter set $\epsilon = 0.02$, $f = 0.8$, and $\tau = 0.001 \ll 1$. Then, the threshold (4.9) with $N_{c-} = 2$ predicts that a two-pulse pattern is stable to both fast and slow instabilities when $D < 0.133$. The numerical results shown in Fig. 4.1 with $D = 0.1$ confirm this prediction.

For the case $\tau > 0$ in (4.2), we show that an N-pulse equilibrium solution to (4.2) is unstable when $N > N_{c+}$, or equivalently when $D > D_{c_N}$ (see Principal Result 2.3 below), where

$$D_{c_N} \equiv \frac{2f^2}{3N^3(1-f)\left(1+\cos\frac{\pi}{N}\right)} .$$

For $D < D_{c_N}$, in §4.2.4 we show from a numerical computation of the spectrum of the NLEP that there is a critical value τ_H of τ for which an N-pulse equilibrium solution undergoes a Hopf bifurcation. In contrast to the previous NLEP stability studies of [**58**, **102**, **106**] for the GM and GS models, where a synchronous oscillation in the pulse amplitudes was always the dominant instability, our results show that there is a parameter regime where the Hopf bifurcation for the Brusselator (4.2) triggers robust *asynchronous* temporal oscillations of the pulse amplitudes. Furthermore, we establish the scaling law $\tau_H \sim c/D$ as $D \to 0$ for some $\mathcal{O}(1)$ constant $c > 0$.

Therefore, in contrast to the previous analyses for the GM and GS models (cf. [**58**, **106**]) where $\tau_H = \mathcal{O}(1)$ as $D \to 0$, this new scaling law indicates that pulses that are isolated from their neighbors or from the domain boundaries (i.e. D small) do not undergo an oscillatory instability unless τ is very large.

For the boundary-flux system (4.4), in §4.3.1 we derive an ODE for the slow evolution of a two-pulse quasi-steady pattern. In the presence of boundary flux, equilibrium pulses are not equally spaced, and depending on the parameter values, slowly drifting pulses may annihilate against the domain boundaries. In §4.3.2 we derive an NLEP governing the stability of the two-pulse quasi-steady pattern to $\mathcal{O}(1)$ time-scale instabilities. From an analytical and numerical study of this NLEP, in §4.3.3 and §4.3.4 we show the possibility of dynamic bifurcations leading to either a competition or an oscillatory instability of the pulse amplitudes depending on the parameter regime. As in the study of the no-flux system (4.2), the novel *asynchronous* oscillatory instability mode can again be the dominant instability.

For both Brusselator systems, the detailed stability results are confirmed and illustrated by rather extensive numerical computations of the full PDE systems.

4.2. Stability of Symmetric N-Pulse Equilibria with No Boundary Flux

In this section, we construct N-pulse symmetric equilibrium solutions of (4.2). By a symmetric pulse solution we refer to a pattern of pulses with a common height and equal spacing. We then linearize about this equilibrium solution to derive an NLEP governing the stability of the equilibrium pattern to $\mathcal{O}(1)$ eigenvalues. Stability with respect to the small $\mathcal{O}(\epsilon^2)$ eigenvalues as well as the existence of asymmetric equilibria were studied in [**97**]. We highlight the differences between the NLEP derived here and analogous NLEP's derived for the Gray-Scott

([**58**]) and Gierer-Meinhardt ([**106**]) models. We also draw similarities to the aforementioned NLEP's and appeal to results of [**106**] to determine criteria for competition and oscillatory instabilities. Numerical results computed from (4.2) are used to validate our stability results.

4.2.1. Asymptotic Construction of N-Pulse Equilibria

To construct an N-pulse symmetric equilibrium solution, characterized by pulses of a common amplitude and equal spacing, we employ the "gluing" technique used in [**105**]. We first consider a one-pulse solution on the interval $|x| < \ell$ centered at $x = 0$. In the inner region of width $\mathcal{O}(\epsilon)$, we introduce the stretched spatial variable $y = \epsilon^{-1}x$ and let $U(y) = u(\epsilon y)$. Because v varies on an $\mathcal{O}(1)$ length scale, then $v \sim v_c$ in the inner region where the constant v_c is to be found. Then, by (4.2a), we obtain to leading order that U satisfies $U_{yy} - U + fv_cU^2 = 0$. The pulse solution to this problem is

$$U(y) = \frac{1}{fv_c} w(y)\,, \tag{4.10}$$

where $w = \frac{3}{2}\operatorname{sech}^2(y/2)$ is the homoclinic solution to

$$\begin{gathered} w'' - w + w^2 = 0\,, \qquad -\infty < y < \infty\,, \\ w \to 0 \ \text{ as } \ |y| \to \infty\,, \qquad w'(0) = 0, \qquad w(0) > 0\,, \end{gathered} \tag{4.11}$$

for which

$$\int_{-\infty}^{\infty} w\, dy = \int_{-\infty}^{\infty} w^2\, dy = 6. \tag{4.12}$$

In the outer region, we obtain from (4.2a) that $u = \mathcal{O}(\epsilon)$ so that $vu^2 \ll u$. Thus, $u \sim \epsilon$ to leading order in the outer region. The resulting leading-order composite solution for u is then

given by

$$u \sim \epsilon + \frac{1}{f v_c} w(x/\epsilon)\,, \tag{4.13}$$

where $w(y)$ is defined by (4.11). Since u is localized near $x = 0$, the terms involving u in (4.2b) can be represented in the outer region as delta functions. Upon using (4.12) and (4.13) we calculate that

$$\begin{aligned} \frac{1}{\epsilon}(u - v u^2) &\sim 1 + \left(\frac{1}{f v_c} \int_{-\infty}^{\infty} w\, dy - \frac{1}{f^2 v_c} \int_{-\infty}^{\infty} w^2\, dy \right) \delta(x) \\ &= 1 + \frac{6}{f v_c} \left(1 - \frac{1}{f} \right) \delta(x)\,. \end{aligned} \tag{4.14}$$

Therefore, in the outer region we obtain for $\epsilon \to 0$ that v satisfies

$$D v_{xx} + 1 = \frac{6}{f v_c} \left(\frac{1}{f} - 1 \right) \delta(x)\,, \qquad -\ell < x < \ell\,, \qquad v_x(\pm \ell) = 0\,. \tag{4.15}$$

Integrating this equation over $|x| \le \ell$ and imposing that $v_x = 0$ at $x = \pm \ell$, we obtain

$$v_c = \frac{3}{f \ell} \left(\frac{1}{f} - 1 \right) > 0\,, \tag{4.16}$$

since f satisfies $0 < f < 1$. To obtain an N-pulse equilibrium solution for (4.2) on the domain of length two, we must set $2 = 2N\ell$ and periodically extend our solution on $|x| < l$ to $[-1, 1]$. Thus, we identify that $l = 1/N$ and (4.16) becomes

$$v_c = \frac{3N}{f} \left(\frac{1}{f} - 1 \right)\,. \tag{4.17}$$

Before solving for the outer solution for v, we make some remarks. Firstly, v_c in (4.17) increases with N, and so, by (4.10), the common pulse amplitude decreases as the number of pulses increases. Also, the common amplitude is independent of D, which will not be the case when we construct pulse solutions under the presence of boundary flux in §4.3. Secondly, by using $\ell = 1/N$, the center of each pulse is located at

$$x_j = -1 + \frac{2j+1}{N}\,, \qquad j = 0, \ldots, N-1\,. \tag{4.18}$$

This equally-spaced pulse result will be shown not to hold in §4.3 when we allow for the presence of boundary flux. Lastly, the uniqueness of the solution to (4.15) is achieved by imposing the matching condition $v(x_j) = v_c$.

Using the last remark, we write the equation for v on the interval $-1 < x < 1$ as

$$Dv_{xx} + 1 = \frac{6}{fv_c}\left(\frac{1}{f} - 1\right)\sum_{j=0}^{N-1}\delta(x - x_j)\,, \qquad -1 < x < 1\,, \qquad v_x(\pm 1) = 0\,, \tag{4.19}$$

where v_c satisfies (4.17). The solution to (4.19) can be written in terms of the Neumann Green's function $G(x; x_j)$ as

$$v = \bar{v} + \frac{6}{fv_c}\left(\frac{1}{f} - 1\right)\sum_{j=0}^{N-1} G(x; x_j)\,, \tag{4.20}$$

for some constant $\bar{v}$ to be determined. Here $G(x; x_j)$ satisfies

$$\begin{aligned} &DG_{xx}(x; x_j) + \frac{1}{2} = \delta(x - x_j), \qquad -1 < x < 1\,, \\ &G_x(\pm 1; x_j) = 0, \qquad \int_{-1}^{1} G(x; x_j)\,dx = 0\,, \end{aligned} \tag{4.21}$$

which has the explicit solution

$$G(x;x_j) = -\frac{1}{4D}(x^2+x_j^2) + \frac{1}{2D}|x-x_j| - \frac{1}{6D}\,. \tag{4.22}$$

The constant $\bar{v}$ is determined by the matching condition $v(x_i) = v_c$, yielding

$$\bar{v} = v_c - \frac{6}{fv_c}\left(\frac{1}{f}-1\right)\sum_{j=0}^{N-1} G(x_i;x_j)\,, \tag{4.23}$$

where the right-hand side of (4.23) is readily shown to be independent of i. We summarize our result as follows:

Principal Result 4.2.1: *Let $\epsilon \to 0$ in* (4.2)*. Then, the leading order composite approximation for the symmetric N-pulse equilibrium solution for u is*

$$u_e(x) \sim \epsilon + \frac{1}{fv_c}\sum_{j=0}^{N-1} w[\epsilon^{-1}(x-x_j)]\,. \tag{4.24a}$$

Alternatively, the outer solution for v valid for $|x-x_j| \gg \mathcal{O}(\epsilon)$ and $j = 0,\ldots,N-1$ is given asymptotically by

$$v_e(x) \sim \bar{v} + \frac{6}{fv_c}\left(\frac{1}{f}-1\right)\sum_{j=0}^{N-1} G(x;x_j)\,. \tag{4.24b}$$

Here $w(y)$ satisfies (4.11)*, while v_c, x_j, $\bar{v}$, and $G(x;x_j)$ are given in* (4.17)*,* (4.18)*,* (4.23)*, and* (4.22)*, respectively.*

Next, we calculate the critical value D_{s_N} of D for which an asymmetric N-pulse equilibrium solution, characterized by pulses of different height and non-uniform spacing, bifurcates from the symmetric N-pulse symmetric solution branch. This bifurcation point corresponds to a zero eigenvalue crossing along the symmetric branch, and for τ sufficiently small it characterizes the

stability threshold of symmetric N-pulse equilibria with respect to the small eigenvalues with $\lambda \to 0$ as $\epsilon \to 0$ in the linearization of (4.2) (cf. [**97**]).

To determine this bifurcation point, we compute $v(l)$ for the one-pulse equilibrium solution to (4.2) on the domain $-l < x < l$. From (4.15) and (4.16), we readily calculate that

$$v(l) = \frac{1}{2D}\left(l^2 + \frac{b}{l}\right), \qquad b \equiv \frac{6D}{f^2}(1-f).$$

The bifurcation point for the emergence of an asymmetric N-pulse solution on a domain of length two, is obtained by calculating the minimum point of the graph of $v(l)$ versus l, and then setting $2Nl = 2$ (cf. [**97**]). This occurs at the value $D = D_{s_N}$, where

$$D_{s_N} \equiv \frac{f^2}{3(1-f)N^3}. \tag{4.25}$$

4.2.2. Derivation of Nonlocal Eigenvalue Problem

To analyze the stability of the equilibrium solution constructed above, we linearize about u_e and v_e, where u_e and v_e are given in (4.24a) and (4.24b), respectively. We substitute $u = u_e + e^{\lambda t}\Phi$ and $v = v_e + e^{\lambda t}\Psi$ into (4.2), where $|\Phi| \ll 1$ and $|\Psi| \ll 1$. This leads to the eigenvalue problem

$$\epsilon^2\Phi_{xx} - \Phi + 2fu_ev_e\Phi + fu_e^2\Psi = \lambda\Phi, \qquad -1 < x < 1, \qquad \Phi_x(\pm 1) = 0, \tag{4.26a}$$

$$D\Psi_{xx} + \frac{1}{\epsilon}\left[\Phi - 2u_ev_e\Phi - u_e^2\Psi\right] = \tau\lambda\Psi, \qquad -1 < x < 1, \qquad \Psi_x(\pm 1) = 0. \tag{4.26b}$$

To analyze the large eigenvalues that are $\mathcal{O}(1)$ as $\epsilon \to 0$, we look for a localized eigenfunction for Φ of the form

$$\Phi \sim \sum_{j=0}^{N-1} \Phi_j[\epsilon^{-1}(x - x_j)], \tag{4.27}$$

where $\Phi_j(y)$ is an even function with $\Phi_j \to 0$ exponentially as $|y| \to \infty$. In the inner region near the jth pulse we obtain from (4.26b) that $\Psi \sim \Psi_j$, where Ψ_j is a constant to be found. Since both u_e and Φ are localized near each x_j, we calculate in the sense of distributions that

$$\frac{1}{\epsilon}\left[\Phi - 2u_e v_e \Phi - u_e^2 \Psi\right] \sim \left(\int_{-\infty}^{\infty} \Phi_j \, dy - \frac{2}{f}\int_{-\infty}^{\infty} w\Phi_j \, dy - \frac{\Psi_j}{f^2 v_c^2}\int_{-\infty}^{\infty} w^2 \, dy\right)\delta(x - x_j)\,. \quad (4.28)$$

Substituting (4.27) into (4.26a) and (4.28) into (4.26b), and using (4.12) for the last integral in (4.28), we obtain that

$$\Phi_j'' - \Phi_j + 2w\Phi_j + \frac{1}{f v_c^2} w^2 \Psi_j = \lambda \Phi_j\,, \qquad -\infty < y < \infty\,, \qquad \Phi_j \to 0 \ \text{ as } \ |y| \to \infty\,, \quad (4.29a)$$

and

$$\Psi_{xx} - \mu^2 \Psi = -\sum_{j=0}^{N-1} \tilde{\omega}_j \delta(x - x_j)\,, \qquad -1 < x < 1\,, \qquad \Psi_x(\pm 1) = 0\,, \quad (4.29b)$$

where we have defined μ and $\tilde{\omega}_j$ by

$$\mu \equiv \sqrt{\frac{\tau\lambda}{D}}\,, \qquad \tilde{\omega}_j \equiv \frac{1}{D}\left[\int_{-\infty}^{\infty} \Phi_j \, dy - \frac{2}{f}\int_{-\infty}^{\infty} w\Phi_j \, dy - \frac{6\Psi_j}{f^2 v_c^2}\right]\,. \quad (4.30)$$

To derive an NLEP for Φ_j, we must compute Ψ_j for $j = 0, \ldots, N-1$ from (4.29b). To do so, we write $\Psi(x)$ as

$$\Psi = \sum_{j=0}^{N-1} G^{(\mu)}(x; x_j)\tilde{\omega}_j\,, \quad (4.31)$$

where $G^{(\mu)}(x;x_j)$ is the Green's function satisfying

$$G^{(\mu)}_{xx} - \mu^2 G^{(\mu)} = -\delta(x-x_j)\,, \qquad -1<x<1\,; \qquad G^{(\mu)}_x(\pm 1;x_j) = 0\,. \tag{4.32}$$

Evaluating (4.31) at $x = x_i$ we obtain that $\Psi(x_i) = \Psi_i = \sum_{j=0}^{N-1} G^{(\mu)}_{i,j}\tilde{\omega}_j$, where $G^{(\mu)}_{i,j} \equiv G^{(\mu)}(x_i,x_j)$ and $\tilde{\omega}_j$ is given in (4.30). In matrix form, this system can be written as

$$\boldsymbol{\Psi} = \mathcal{G}^{(\mu)}\left(\boldsymbol{\omega} - \frac{6}{f^2 v_c^2 D}\boldsymbol{\Psi}\right)\,, \tag{4.33}$$

where

$$\boldsymbol{\Psi} \equiv \begin{pmatrix} \Psi_0 \\ \vdots \\ \Psi_{N-1} \end{pmatrix}\,, \qquad \mathcal{G}^{(\mu)} \equiv \begin{pmatrix} G^{(\mu)}_{0,0} & G^{(\mu)}_{0,1} & \cdots & G^{(\mu)}_{0,N-1} \\ G^{(\mu)}_{1,0} & \ddots & \cdots & G^{(\mu)}_{1,N-1} \\ \vdots & \vdots & \ddots & \vdots \\ G^{(\mu)}_{N-1,0} & G^{(\mu)}_{N-1,1} & \cdots & G^{(\mu)}_{N-1,N-1} \end{pmatrix}\,, \tag{4.34}$$

and

$$\boldsymbol{\omega} = \frac{1}{D}\left[\int_{-\infty}^{\infty}\boldsymbol{\Phi}\,dy - \frac{2}{f}\int_{-\infty}^{\infty} w\boldsymbol{\Phi}\,dy\right]\,, \qquad \boldsymbol{\Phi} \equiv \begin{pmatrix} \Phi_0 \\ \vdots \\ \Phi_{N-1} \end{pmatrix}\,. \tag{4.35}$$

Solving for $\boldsymbol{\Psi}$ in (4.33), we obtain

$$\boldsymbol{\Psi} = \mathcal{C}^{-1}\mathcal{G}^{(\mu)}\boldsymbol{\omega}\,; \qquad \mathcal{C} \equiv \mathcal{I} + \frac{6}{f^2 v_c^2 D}\mathcal{G}^{(\mu)}\,, \tag{4.36}$$

where $\mathcal{I}$ is the $N \times N$ identity matrix.

Having obtained $\mathbf{\Psi}$ in terms of $\mathbf{\Phi}$, we now derive a vector NLEP for $\mathbf{\Phi}$. Upon defining the local operator L_0 by

$$L_0\phi \equiv \phi'' - \phi + 2w\phi\,, \tag{4.37}$$

we then use (4.35) for $\boldsymbol{\omega}$ to write (4.29a) in vector form as

$$L_0\mathbf{\Phi} + \frac{w^2}{fv_c^2D}\mathcal{C}^{-1}\mathcal{G}^{(\mu)}\left[\int_{-\infty}^{\infty}\left(\mathbf{\Phi} - \frac{2}{f}w\mathbf{\Phi}\right)\,dy\right] = \lambda\mathbf{\Phi}\,. \tag{4.38}$$

To obtain N uncoupled scalar NLEP's, we diagonalize $\mathcal{C}^{-1}$ and $\mathcal{G}^{(\mu)}$ by using the eigenpairs $\mathcal{G}^{(\mu)}\boldsymbol{v}_j = \kappa_j\boldsymbol{v}_j$ for $j = 0,\ldots,N-1$ of $\mathcal{G}^{(\mu)}$. This yields,

$$\mathcal{G}^{(\mu)} = \mathcal{S}\Lambda\mathcal{S}^{-1}\,, \qquad \mathcal{C}^{-1} = \mathcal{S}\left[\mathcal{I} + \beta_0\Lambda\right]^{-1}\mathcal{S}^{-1}\,; \qquad \beta_0 \equiv \frac{6}{f^2v_c^2D}, \tag{4.39}$$

where $\mathcal{S}$ is the non-singular matrix whose columns are the eigenvectors of $\mathcal{G}^{(\mu)}$ and Λ is the diagonal matrix of the eigenvalues $\kappa_0,\ldots,\kappa_{N-1}$. From the observation that $\left(\mathcal{G}^{(\mu)}\right)^{-1}$ is a tridiagonal matrix, explicit formulae for these eigenvalues were calculated in Proposition 2 of [**47**] as

$$\kappa_j = \frac{1}{\mu\sigma_j}\,, \qquad j = 0,\ldots,N-1\,, \tag{4.40}$$

where σ_j for $j = 0,\ldots,N-1$ are given by

$$\sigma_0 = e_\lambda + 2f_\lambda; \qquad \sigma_j = e_\lambda + 2f_\lambda\cos\left(\frac{j\pi}{N}\right)\,, \qquad j = 1,\ldots,N-1\,. \tag{4.41a}$$

Here e_λ and f_λ are defined in terms of $\mu \equiv \sqrt{\tau\lambda/D}$ by

$$e_\lambda \equiv 2\coth\left(\frac{2\mu}{N}\right)\,, \qquad f_\lambda \equiv -\operatorname{csch}\left(\frac{2\mu}{N}\right)\,. \tag{4.41b}$$

The corresponding eigenvectors of $\mathcal{G}^{(\mu)}$ are

$$\boldsymbol{v}_0^t = (1, \ldots, 1)\ ; \qquad v_{\ell,j} = \cos\left[\frac{j\pi}{N}(\ell - 1/2)\right]\ , \qquad j = 1, \ldots, N-1\,, \tag{4.41c}$$

where t denotes the transpose and $v_{\ell,j}$ denotes the ℓth component of the vector $\boldsymbol{v}_j$.

Upon substituting (4.39) into (4.38), and making use of the transformation $\boldsymbol{\Phi} = \mathcal{S}\hat{\boldsymbol{\Phi}}$, we obtain the diagonal NLEP

$$L_0\hat{\boldsymbol{\Phi}} + f\beta_0\left[\mathcal{I} + \beta_0\Lambda\right]^{-1}\Lambda w^2\left(\frac{\int_{-\infty}^{\infty}\left(\hat{\boldsymbol{\Phi}} - \frac{2}{f}w\hat{\boldsymbol{\Phi}}\right)\,dy}{\int_{-\infty}^{\infty}w^2\,dy}\right) = \lambda\hat{\boldsymbol{\Phi}}\,, \tag{4.42}$$

where β_0 is defined in (4.39), and where we have used that $\int_{-\infty}^{\infty}w^2\,dy = 6$. While the components of $\hat{\boldsymbol{\Phi}}$ are generally different, for notational convenience we lable $\hat{\boldsymbol{\Phi}} = \hat{\Phi}\boldsymbol{e}$, where $\boldsymbol{e}$ is the N-vector $(1, \ldots, 1)^t$. Since Λ is the diagonal matrix of eigenvalues κ_j, this substitution leads to N uncoupled scalar NLEP's of the form

$$L_0\hat{\Phi} + f\tilde{\chi}_j w^2\left(\frac{\int_{-\infty}^{\infty}\left(\hat{\Phi} - \frac{2}{f}w\hat{\Phi}\right)\,dy}{\int_{-\infty}^{\infty}w^2\,dy}\right) = \lambda\hat{\Phi}\,, \qquad j = 0\,, \ldots, N-1\,, \tag{4.43}$$

where $\tilde{\chi}_j$ is defined by

$$\tilde{\chi}_j \equiv \frac{\beta_0\kappa_j}{1 + \beta_0\kappa_j}\,. \tag{4.44}$$

In contrast to the NLEP problems for the Gierer-Meinhardt and Gray-Scott models analyzed in [**106**] and [**58**], the NLEP (4.43) involves the two separate nonlocal terms $\int_{\infty}^{\infty}\hat{\Phi}\,dy$ and $\int_{\infty}^{\infty}w\hat{\Phi}\,dy$. These terms arise from the fact that the $\mathcal{O}(\epsilon^{-1})$ term in (4.2b) involves the sum of two localized terms. Due to this complication, it initially appears that the general theory

developed in [**106**] is not applicable. However, as we now show, by a simple manipulation we can recast (4.43) into the same general form as the NLEP analyzed in [**106**].

To do so, we first define I_1 and I_2 as $I_1 \equiv \int_{-\infty}^{\infty} \hat{\Phi}\, dy$ and $I_2 \equiv \int_{-\infty}^{\infty} w\hat{\Phi}\, dy$. Then, by using (4.37) for $L_0\hat{\Phi}$, together with the condition that $\hat{\Phi} \to 0$ as $|y| \to \infty$, we integrate (4.43) over $-\infty < y < \infty$ to obtain

$$-I_1 + 2I_2 + f\tilde{\chi}_j \left[I_1 - \frac{2}{f} I_2 \right] = \lambda I_1 \,,$$

which is then re-arranged to yield

$$I_1 - \frac{2}{f} I_2 = -\frac{2}{f} \left[\frac{1+\lambda-f}{1+\lambda-\tilde{\chi}_j f} \right] I_2 \,. \tag{4.45}$$

Finally, using (4.45) in (4.43), we obtain the NLEP problem

$$L_0\hat{\Phi} - \chi_j w^2 \left(\frac{\int_{-\infty}^{\infty} w\hat{\Phi}\, dy}{\int_{-\infty}^{\infty} w^2\, dy} \right) = \lambda\hat{\Phi} \,, \qquad \chi_j \equiv 2\tilde{\chi}_j \left[\frac{1+\lambda-f}{1+\lambda-\tilde{\chi}_j f} \right] \,, \tag{4.46}$$

where $\tilde{\chi}_j$ is defined in terms of κ_j in (4.44).

The NLEP in (4.46) is of the form given in Proposition 2.3 of [**106**] for the GM model and in Principal Result 3.2 of [**58**] for the GS model. However, because the activator in the Brusselator model acts as two separate sources for the inhibitor, the identity (4.45) is needed, which results in a rather complicated coefficient in front of the nonlocal term in (4.46). Finally, by substituting (4.44) and (4.40) into (4.46) we obtain the following main result:

Principal Result 4.2.2: *Let $\epsilon \to 0$ in* (4.2) *and consider the N-pulse equilibrium solution constructed in §4.2.1. The stability of this solution on an $\mathcal{O}(1)$ timescale is determined by the*

spectrum of the NLEP

$$L_0\hat{\Phi} - \chi_j w^2 \left(\frac{\int_{-\infty}^{\infty} w\hat{\Phi}\, dy}{\int_{-\infty}^{\infty} w^2\, dy} \right) = \lambda\hat{\Phi}\,, \qquad -\infty < y < \infty\,, \qquad \hat{\Phi} \to 0 \;\; \textit{as} \;\; |y| \to \infty\,, \tag{4.47a}$$

where χ_j is given explicitly by

$$\chi_j = \frac{2}{1 + \mu\sigma_j/\beta_0} \left[1 + \frac{f\mu\sigma_j}{f\beta_0 - (1+\lambda)(\beta_0 + \mu\sigma_j)} \right]\,. \tag{4.47b}$$

Here σ_j is defined in terms of μ in (4.41a)*, μ is defined in terms of λ in* (4.30)*, and β_0 is defined in* (4.39)*.*

We make a few remarks concerning (4.47). Firstly, the dependence of χ_j in (4.47) on τ is strictly through the parameter $\mu = \sqrt{\tau\lambda/D}$, the importance of which will be discussed in the following section. From the explicit formula (4.41a), it follows that χ_j does not have a branch point at the origin $\lambda = 0$. Secondly, since $\hat{\Phi}$ is even, then $\int_{-\infty}^{\infty} w\hat{\Phi}\, dy \neq 0$. The spectrum of L_0 was studied in [**65**] and [**27**], where it was proved that in addition to the zero eigenvalue associated with translation invariance, L_0 has a unique positive eigenvalue $\nu_0 = 5/4$ corresponding to an eigenfunction ϕ_0 of constant sign. In addition, there is another discrete eigenvalue for L_0 on the negative real line at $\nu_2 = -3/4$ (cf. [**27**]).

Finally, the spectrum of the NLEP for (4.47) is recast into a more convenient form by first writing

$$\hat{\Phi} = \chi_j \left(\frac{\int_{-\infty}^{\infty} w\hat{\Phi}\, dy}{\int_{-\infty}^{\infty} w^2\, dy} \right) (L_0 - \lambda)^{-1} w^2\,.$$

and then multiplying both sides of this equation by w and integrating over the real line. In this way, we obtain that the eigenvalues of (4.47) are the roots of the transcendental equations $g_j(\lambda) = 0$, for $j = 0, \ldots, N-1$, where

$$
\begin{aligned}
g_j(\lambda) &\equiv C_j(\lambda) - F(\lambda)\,, \qquad C_j(\lambda) \equiv \frac{1}{\chi_j(\lambda)}\,, \\
F(\lambda) &\equiv \frac{\int_{-\infty}^{\infty} w\psi\, dy}{\int_{-\infty}^{\infty} w^2\, dy}\,, \qquad \psi \equiv (L_0 - \lambda)^{-1} w^2\,,
\end{aligned}
\tag{4.48}
$$

and where the inversion $(L_0 - \lambda)^{-1}$ is defined uniquely by requiring that ψ is an even function.

4.2.3. Competition Instabilities

In this sub-section, we seek criteria in terms of D that guarantee that there is a positive real solution to (4.48) in the limit $\tau \to 0^+$. Such a root corresponds to an unstable real positive eigenvalue of the NLEP (4.47). For $\tau \to 0^+$ it will be shown that such a linear instability is of competition type in the sense that it conserves the sum of the amplitudes of the pulses. The instability threshold condition on D will also be shown to apply to the case where $\tau > 0$.

We begin the analysis by recalling key properties of the function $F(\lambda)$ when λ is real and positive as determined in Proposition 3.5 of [**106**]. We then determine the behavior of $C_j(\lambda)$ in (4.48) in the limit $\tau \to 0^+$. Using the properties of $C_j(\lambda)$ in this limit, together with the properties of $F(\lambda)$, we obtain criteria for which there exists a positive real value of λ at which $C_j(\lambda)$ and $F(\lambda)$ intersect. Some global properties of $F(\lambda)$ when λ is real and positive, which were rigorously established in [**106**], are as follows:

$$
\begin{aligned}
&F(\lambda) > 0\,, \qquad F'(\lambda) > 0\,, \qquad F''(\lambda) > 0\,, \quad \text{for} \quad 0 < \lambda < 5/4\,; \\
&F(\lambda) < 0\,, \quad \text{for} \quad \lambda > 5/4\,.
\end{aligned}
\tag{4.49a}
$$

Furthermore, since $L_0 w = w^2$ and since the operator $(L_0 - \lambda)$ is not invertible at $\lambda = 5/4$, we obtain that

$$
F(0) = 1\,, \qquad F(\lambda) \to +\infty\,, \quad \text{as} \quad \lambda \to 5/4^-\,. \tag{4.49b}
$$

To determine the behavior of $C_j(\lambda)$ as $\tau \to 0^+$, we first write $C_j(\lambda)$ in terms of σ_j as

$$C_j(\lambda) = \frac{1}{2}\left[1 + \xi_j + \frac{f\xi_j}{1+\lambda-f}\right]; \qquad \xi_j = \frac{\mu\sigma_j}{\beta_0}, \qquad j = 0, \ldots, N-1. \tag{4.50}$$

For any branch of $\sqrt{\lambda}$, this function is analytic in the finite λ plane except at the simple pole $\lambda = -1 + f$, which is on the negative real axis since $0 < f < 1$. Upon taking the limit $\mu \to 0^+$ in σ_j in (4.41a), we see that ξ_j in (4.50) has the behavior

$$\begin{gathered} \xi_0 \to 0^+; \qquad \xi_j \to \frac{Na_j}{\beta_0}, \quad a_j \equiv 1 - \cos\left(\frac{j\pi}{N}\right), \\ j = 1, \ldots, N-1, \qquad \text{as} \quad \tau \to 0^+, \end{gathered} \tag{4.51}$$

where β_0 is defined in (4.39).

Firstly, by (4.51) and (4.50), we have that $C_0(\lambda) \equiv 1/2$ for all λ when $\tau = 0$. Thus, by (4.49), it follows that $g_0(\lambda) \neq 0$ for any $\lambda \geq 0$. Moreover, from the rigorous study of [**108**] (see Corollary 1.2 of [**108**]), we can conclude, more strongly, that when $C_0 = 1/2$ there are no roots to $g_0(\lambda) = 0$ in the unstable right-half plane $\text{Re}(\lambda) > 0$ (see (4.2.4)). Thus, the $(1, \ldots, 1)^t$ mode, governing synchronous instabilities of the amplitudes of the pulses, is always stable in the limit $\tau \to 0^+$.

Next, consider the modes $j = 1, \ldots, N-1$. Since ξ_j in (4.51) for $j > 0$ is independent of λ in the limit $\tau \to 0^+$, it follows from (4.50) that $C_j'(\lambda) < 0$ and $C_j(\lambda) > 0$ for $\lambda \geq 0$ when $j = 1, \ldots, N-1$. Thus, from (4.49), we conclude that if $\max_j C_j(0) < 1$ for $j = 1, \ldots, N-1$, then there are no real positive eigenvalues when $\tau = 0$. A simple calculation using (4.50) and (4.51) shows that as $\tau \to 0^+$, we have the ordering $C_{N-1}(0) > C_{N-2}(0) > \ldots > C_1(0)$.

Therefore, in the limit $\tau \to 0^+$, (4.47) has no real positive eigenvalues when

$$C_{N-1}(0) = \frac{1}{2}\left[\frac{1+\xi_{N-1}-f}{1-f}\right] < 1\,. \tag{4.52}$$

If $C_{N-1}(0) > 1$, there is an unstable positive real eigenvalue when $\tau \to 0^+$. The threshold value D_{c_N} of D, as given below in (4.53), is obtained by setting $C_{N-1}(0) = 1$, and then using (4.51) for ξ_{N-1} together with (4.39) for β_0.

Although for the case $\tau > 0$ it is no longer true that $C_{N-1}(\lambda)$ is monotonically decreasing, we still have that $C_{N-1}(0) > 1$ when $D > D_{c_N}$. Hence, by the properties of $F(\lambda)$ given in (4.49) it follows that there must still be a positive root to $C_{N-1}(\lambda) = F(\lambda)$. However, when $\tau > 0$ it is possible that there can now be further real positive roots where the other curves $C_j(\lambda)$ for $j = 0, \ldots, N-2$ intersect $F(\lambda)$. We summarize our instability result as follows:

Principal Result 4.2.3: *Let $\epsilon \to 0$ and $\tau \geq 0$ in* (4.2)*. Then the N-pulse equilibrium solution ($N \geq 2$) constructed in §4.2.1 is unstable when*

$$D > D_{c_N} \equiv \frac{2f^2}{3N^3(1-f)\left(1+\cos\frac{\pi}{N}\right)}\,, \qquad 0 < f < 1\,, \tag{4.53}$$

and the spectrum of the NLEP (4.47) *contains at least one unstable positive real eigenvalue. For $\tau \to 0^+$, the instability is of competition type in the sense that any linearly unstable eigenvector v_j for the pulse amplitudes must satisfy $(1, \ldots, 1) \cdot v_j = 0$.*

We now make some remarks. Firstly, for the limiting case $\tau \to 0^+$, in §4.2.4 a winding number calculation will be used to prove that there are no unstable complex eigenvalues in the right half-plane when $D < D_{c_N}$. Therefore, for $\tau \to 0^+$, the threshold D_{c_N} gives a necessary and sufficient condition for stability. Secondly, by comparing (4.53) with (4.55), we see that

as $\tau \to 0^+$, the N-pulse equilibrium solution (4.24) is stable if and only if it is stable to small eigenvalues. Thirdly, the term competition instability is due to the fact that when such an instability is triggered, some pulses grow in amplitude while other decrease. This is due to the difference in signs of the components of the eigenvectors $\boldsymbol{v}_j$ for $j = 1, \ldots, N-1$. As shown in the numerical experiments below, computed from the full Brusselator model (4.2), this linear instability triggers a nonlinear event that leads to pulse annihilation. In contrast, as was shown above, the synchronous mode corresponding to $\boldsymbol{v}_0 = (1, \ldots, 1)^t$ is always stable when τ is sufficiently small. Fourthly, D_{c_N} decreases as $\sim N^{-3}$ when N is large, which is the same scaling as for the Schnakenberg model (Corollary 3.1 of [**105**]). In contrast, the GM (Proposition 7 of [**47**]) and GS ([**58**]) models have a more robust N^{-2} scaling in terms of the ability to support additional pulses. Since D is inversely proportional to the square length of the domain, (4.53) shows that in order to maintain stability the domain size must increase as the number of pulses increases. Finally, in terms of the original Brusselator parameters B_0, D_0 and E_0 in (4.5), we have the stability criterion

$$D_0 < D_{0c_N} \equiv \frac{2E_0^2 B_0^2}{3N^3(B_0+1)^{5/2}\left(1+\cos\frac{\pi}{N}\right)}. \tag{4.54}$$

Thus a pulse pattern can be stabilized with small D_0 or large E_0. Note that, by (4.3), $E_0^2 = \mathcal{O}(\tau^{-1})$ so that $D_{0c_N} = \mathcal{O}(\tau^{-1})$ as $\tau \to 0^+$. However, if we require that $D = \mathcal{O}(1)$ with respect to τ, then D_0 must also be $\mathcal{O}(\tau^{-1})$ by (4.3). Also, if $\tau = (B_0+1)^{5/2}/E_0^2$ is held constant, then increasing B_0 in (4.54) relaxes the stability criterion. This fact is reflected in terms of the rescaled variables in (4.53), where increasing $f = B_0/(B_0+1)$ towards unity increases D_{c_N}.

Finally, we remark that the eigenvalue problem (4.26) admits another class of eigenvalues associated with translation-type instabilities, and these eigenvalues are of the order $\lambda = \mathcal{O}(\epsilon^2)$

as $\epsilon \to 0$. These eigenvalues, studied in [**97**], were found to be real negative when $\tau = \mathcal{O}(1)$ if and only if $D < D_{s_N}$, where (cf. [**97**])

$$D_{s_N} \equiv \frac{f^2}{3N^3(1-f)} < D_{c_N} \, . \tag{4.55}$$

This threshold value is the same as that calculated in (4.25) for the bifurcation point corresponding to the emergence of asymmetric N-pulse equilibria from a symmetric N-pulse equilibrium solution branch.

4.2.4. Complex Eigenvalues and Oscillatory Instabilities

For the case $D < D_{c_N}$ and $\tau = 0$, we now use a winding number argument to prove that (4.47) has no unstable eigenvalues with $\mathrm{Re}(\lambda) > 0$. To calculate the number of zeros of $g_j(\lambda)$ in the right-half plane, we compute the winding of $g_j(\lambda)$ over the contour Γ traversed in the counterclockwise direction composed of the following segments in the complex λ- plane: Γ_I^+ ($0 < \mathrm{Im}(\lambda) < iR$, $\mathrm{Re}(\lambda) = 0$), Γ_I^- ($-iR < \mathrm{Im}(\lambda) < 0$, $\mathrm{Re}(\lambda) = 0$), and Γ_R is the semi-circle in the right-half plane defined by $|\lambda| = R > 0$, $-\pi/2 < \arg(\lambda) < \pi/2$, where $R > 0$.

Each function $g_j(\lambda)$ in (4.48) for $j = 0, \ldots, N-1$ is analytic in $\mathrm{Re}(\lambda) \geq 0$ except at the simple pole $\lambda = 5/4$ corresponding to the unique positive eigenvalue of the operator L_0 in (4.37). Therefore, by the argument principle we obtain that $M_j - 1 = (2\pi)^{-1} \lim_{R\to\infty} [\arg g_j]_\Gamma$, where M_j is the number of zeros of g_j in the right half-plane, and where $[\arg g_j]_\Gamma$ denotes the change in the argument of g_j over Γ. Furthermore from (4.48), (4.50) and (4.51) it follows that $g_j \to (1+\xi_j)/2$ as $|\lambda| \to \infty$ on the semi-circle Γ_R, so that $\lim_{R\to\infty} [\arg g_j]_{\Gamma_R} = 0$. For the contour Γ_I^-, we use that $g_j(\overline{\lambda}) = \overline{g_j(\lambda)}$ so that $[\arg g_j]_{\Gamma_I^-} = [\arg g_j]_{\Gamma_I^+}$. By summing the roots of the N separate functions $g_j(\lambda)$ for $j = 0, \ldots, N-1$, we obtain that the number M of unstable

eigenvalues of the NLEP (4.47) when $\tau = 0$ is

$$M = N + \frac{1}{\pi} \sum_{j=0}^{N-1} \left[\arg g_j \right]_{\Gamma_I^+} . \tag{4.56}$$

Here $\left[\arg g_j \right]_{\Gamma_I^+}$ denotes the change in the argument of g_j as the imaginary axis $\lambda = i\lambda_I$ is traversed from $\lambda_I = +\infty$ to $\lambda_I = 0$.

To explicitly calculate $\left[\arg g_j \right]_{\Gamma_I^+}$ when $\tau = 0$, we substitute $\lambda = i\lambda_I$ into (4.50) for C_j, and separate the resulting expression into real and imaginary parts to obtain

$$C_j(i\lambda_I) = C_{jR}(\lambda_I) + iC_{jI}(\lambda_I) \,, \tag{4.57a}$$

where

$$C_{0R}(\lambda_I) = \frac{1}{2} \,, \qquad C_{0I}(\lambda_I) = 0 \,, \tag{4.57b}$$

$$C_{jR}(\lambda_I) = \frac{1}{2} \left[1 + \xi_j + \frac{f\xi_j(1-f)}{(1-f)^2 + \lambda_I^2} \right] , \qquad j = 1, \ldots, N-1 \,, \tag{4.57c}$$

$$C_{jI}(\lambda_I) = -\frac{f\xi_j\lambda_I}{(1-f)^2 + \lambda_I^2} \,, \qquad j = 1, \ldots, N-1 \,. \tag{4.57d}$$

In (4.57) we use the limiting behavior for ξ_j as $\tau \to 0^+$ as given in (4.51).

Similarly, we separate the real and imaginary parts of $F(i\lambda_I)$, where $F(\lambda)$ was defined in (4.48), to obtain that

$$\begin{aligned} F(i\lambda_I) &= \frac{\int_{-\infty}^{\infty} wL_0 \left[L_0^2 + \lambda_I^2 \right]^{-1} w^2 \, dy}{\int_{-\infty}^{\infty} w^2 \, dy} + i \left(\frac{\lambda_I \int_{-\infty}^{\infty} w \left[L_0^2 + \lambda_I^2 \right]^{-1} w^2 \, dy}{\int_{-\infty}^{\infty} w^2 \, dy} \right) \\ &\equiv F_R(\lambda_I) + iF_I(\lambda_I) \,, \end{aligned} \tag{4.58}$$

which determines $g(i\lambda_I)$ from (4.48) as

$$g_j(i\lambda_I) = C_{jR}(\lambda_I) - F_R(\lambda_I) + i\,[C_{jI}(\lambda_I) - F_I(\lambda_I)] \equiv g_{jR}(\lambda_I) + ig_{jI}(\lambda_I)\,. \tag{4.59}$$

In order to calculate $[\arg g_j]_{\Gamma_I^+}$, we require the following properties of $F_R(\lambda_I)$ and $F_I(\lambda_I)$, as established rigorously in Propositions 3.1 and 3.2 of [**106**]:

$$F_R(0) = 1\,; \quad F_R'(\lambda_I) < 0\,, \quad \lambda_I > 0\,; \qquad F_R(\lambda_I) = \mathcal{O}(\lambda_I^{-2})\,, \quad \lambda_I \to +\infty\,, \tag{4.60a}$$

$$F_I(0) = 0\,; \quad F_I(\lambda_I) > 0\,, \quad \lambda_I > 0\,; \qquad F_I(\lambda_I) = \mathcal{O}(\lambda_I^{-1})\,, \quad \lambda_I \to +\infty\,. \tag{4.60b}$$

By using (4.57) and (4.60), we obtain from (4.59) that $g_{0R} < 0$ and $g_{0I} = 0$ at $\lambda_I = 0$, while $g_{0R} > 0$ and $g_{I0} = 0$ as $\lambda_I \to +\infty$. In addition, since $F_I(\lambda_I) > 0$, we conclude that $g_{0I} < 0$ for $\lambda_I > 0$. Therefore, $[\arg g_0]_{\Gamma_I^+} = -\pi$, and hence (4.56) becomes

$$M = N - 1 + \frac{1}{\pi}\sum_{j=1}^{N-1} [\arg g_j]_{\Gamma_I^+}\,. \tag{4.61}$$

The calculation of $[\arg g_j]_{\Gamma_I^+}$ for $j = 1, \ldots, N-1$ is similar, but depends on the range of D. Suppose that $D < D_{c_N}$, where D_{c_N} is the threshold of (4.53), so that $C_{jR}(0) < 1$ for all $j = 1, \ldots, N-1$. Then, from (4.57), (4.60), and (4.59), we calculate that $g_{0R} < 0$ and $g_{0I} = 0$ at $\lambda_I = 0$, while $g_{0R} > 0$ and $g_{I0} = 0$ as $\lambda_I \to +\infty$. In addition, since $F_I(\lambda_I) > 0$ and $C_{0I}(\lambda_I) < 0$, we get $g_{0I} < 0$ for all $\lambda_I > 0$. This gives $[\arg g_j]_{\Gamma_I^+} = -\pi$ for $j = 1, \ldots, N-1$. From (4.61), we then obtain the following result:

Principal Result 4.2.4: *Let $\tau \to 0^+$ and $\epsilon \to 0$. Then, when $D < D_{c_N}$, where D_{c_N} is the threshold of* (4.53)*, the NLEP* (4.47) *has no unstable eigenvalues in Re$(\lambda) > 0$. Therefore, for*

$\tau \to 0^+$, *the threshold* D_{c_N} *gives a necessary and sufficient condition for the stability of the* N*-pulse equilibrium solution* (4.24a) *of* (4.2).

We remark that as D is increased above the threshold D_{c_N} in such a way that $C_{N-1}(0) > 1$ but $C_j(0) < 0$ for $j = 1, \ldots, N-2$, we readily calculate from (4.57), (4.60), and (4.59), that $[\arg g_{N-1}]_{\Gamma_I^+} = 0$ and $[\arg g_j]_{\Gamma_I^+} = -\pi$ for $j = 1, \ldots, N-2$. Therefore, from (4.61) we conclude that $M = 1$, and the only eigenvalue entering the right-half plane is the real eigenvalue corresponding to the competition instability analyzed in §4.2.3. We remark that since τ appears only through the factor $\tau\lambda$, then increasing τ cannot result in a competition instability. Thus, the threshold criterion (4.53) for stability is also valid for a range of $0 < \tau < \tau_0$ for some $\tau_0 > 0$ to be determined.

Next, we show that for $0 < D < D_{cN}$, there are exactly $2N$ unstable eigenvalues in $\mathrm{Re}(\lambda) > 0$ when $\tau > 0$ is sufficiently large, and that these eigenvalues are on the positive real axis in $0 < \lambda < 5/4$. For $\tau \gg 1$, we obtain from (4.50) and (4.41a) that $C_j = \mathcal{O}(\sqrt{\lambda\tau})$ on Γ_R, so that $\lim_{R\to\infty} [\arg g_j]_{\Gamma_R} = \pi/2$. In this way, we obtain in place of (4.56) that

$$M = \frac{5N}{4} + \frac{1}{\pi}\sum_{j=0}^{N-1} [\arg g_j]_{\Gamma_I^+} \ . \tag{4.62}$$

For $\tau \gg 1$ and $\lambda = i\lambda_I$, we obtain from (4.50) and (4.41a) that

$$C_j = \frac{1}{2}\left[1 + \kappa\sqrt{i\tau\lambda_I} + \frac{f\kappa\sqrt{i\tau\lambda_I}}{1 - f + i\lambda_I}\right] , \qquad \kappa \equiv \frac{2}{\beta_0\sqrt{D}} . \tag{4.63}$$

Separating into real and imaginary parts, with $C_j = C_{jR} + iC_{jI}$, we get for $\tau \gg 1$ and $\lambda_I \neq 0$ that

$$C_{jR} = \frac{\kappa\sqrt{\tau\lambda_I}}{2}\frac{|1+i\lambda_I|}{|(1-f)+i\lambda_I|}\cos\left(\frac{\pi}{4}+\theta_0-\theta_1\right)+\frac{1}{2}\,,$$
$$C_{jI} = \frac{\kappa\sqrt{\tau\lambda_I}}{2}\frac{|1+i\lambda_I|}{|(1-f)+i\lambda_I|}\sin\left(\frac{\pi}{4}+\theta_0-\theta_1\right)\,, \tag{4.64a}$$

where θ_0 and θ_1 are defined by

$$\theta_0 = \arctan\left(\lambda_I\right)\,, \qquad \theta_1 = \arctan\left(\lambda_I/(1-f)\right)\,. \tag{4.64b}$$

Since $\lambda_I > 0$, and $0 < f < 1$, then $0 < \theta_0 < \theta_1 < \pi/2$. Notice that $C_{jR} > 0$ for any $\lambda_I > 0$ on this range of θ_0 and θ_1.

For $\tau \gg 1$, we have $g_j \sim ce^{i\pi/4}\sqrt{\lambda_I}$, where $c > 0$ is a real constant, as $\lambda_I \to +\infty$. Therefore, we have $\arg(g_j) = \pi/4$ as $\lambda_I \to +\infty$. Now for $\lambda_I = 0$, we have $g_{jR} < 0$ and $g_{jI} = 0$ when $D < D_{c_N}$, so that $\arg(g_j) = \pi$ when $\lambda_I = 0$. In order to prove that $[\arg g_j]_{\Gamma_I^+} = 3\pi/4$, we must show that $g_{jI} > 0$ whenever $g_{Rj} = 0$. Since $F_R > 0$ and $C_{jR}(\lambda_I) > 0$ for $\lambda_I > 0$, but $C_{jR} = \mathcal{O}(\sqrt{\tau}) \gg 1$ for $\tau \gg 1$, it follows that any root λ_I^* of $g_{Rj} = 0$ must be such that $\lambda_I^* = \mathcal{O}(\tau^{-1}) \ll 1$. Thus, for $\tau \gg 1$, we have $\theta_0 \to 0$ and $\theta_1 \to 0$ as $\lambda_I \to 0$, and so we conclude from (4.64) that $C_{jI} > 0$ with $C_{jI} = \mathcal{O}(1)$ at $\lambda_I^* = \mathcal{O}(\tau^{-1})$. Finally, since $g_{jI} = C_{jI} - F_I$, and $F_I(0) = 0$, we conclude that $g_{jI} > 0$ at any root $\lambda_I^* \ll 1$ of $g_{jR} = 0$. This proves that $[\arg g_j]_{\Gamma_I^+} = 3\pi/4$ for each $j = 0, \ldots, N-1$. Finally, from (4.62) we conclude that $M = 2N$.

To determine more precisely the location of these unstable eigenvalues we proceed as in §4.2.3. For $\tau \gg 1$, and on the positive real axis in $0 < \lambda < 5/4$ we obtain from (4.50) and (4.41a) that $C_j(\lambda)$ is a concave monotone increasing function. Since $C_j(0) < F(0) = 1$ when

$D < D_{c_N}$ for $j = 0, \ldots, N-1$, it follows from the properties of $F(\lambda)$ in (4.49) that for each j, $C_j(\lambda) = F(\lambda)$ must have two roots on the interval $0 < \lambda < 5/4$. We summarize the result as follows:

Principal Result 4.2.5: *Let $\tau \to \infty$ and $\epsilon \to 0$. Then, when $0 < D < D_{c_N}$, where D_{c_N} is the threshold of* (4.53)*, the NLEP* (4.47) *has exactly $2N$ unstable eigenvalues in Re$(\lambda) > 0$. These eigenvalues are located on the real axis in the interval $0 < \lambda < 5/4$.*

Therefore, for the parameter range $0 < D < D_{c_N}$, and by the continuity of the branches of eigenvalues with respect to τ, we conclude that for each $j = 0, \ldots N-1$, there must be a minimum value $\tau_{0j} > 0$ of τ for which the NLEP (4.47) has a complex conjugate pair of eigenvalues at $\lambda = \pm i\lambda_{Ij}^0$, corresponding to each eigenmode in (4.41c). We define the oscillatory stability threshold τ_0 as the minimum of these thresholds, i.e. $\tau_0 = \min_j \tau_{0j}$. Our numerical results show that τ_0 is a Hopf bifurcation point, in the sense that an unstable complex conjugate pair of eigenvalues enters the right half-plane for τ slightly above τ_0. From (4.41c) the $j = 0$ mode corresponds to synchronous pulse amplitude oscillations, while the other modes correspond to asynchronous oscillations in the pulse amplitudes. For the Gierer-Meinhardt model, as studied in [**106**], an ordering principle $\tau_{0j} < \tau_{0j+1}$, $j = 0, \ldots, N-2$ was observed for all values of the parameters tested. That is, the dominant oscillatory instability is that of synchronous oscillations of the pulse amplitudes. In contrast, for all values of the parameter f tested, we find an interval of D in $0 < D < D_{c_N}$ in which this ordering principle is reversed. Thus, the Brusselator admits asynchronous oscillations not observed in previous studies of the stability of pulse solutions. We conjecture that this is due to the activator acting as two separate sources for the inhibitor, necessitating the manipulation (4.45) to obtain the multiplier of the nonlocal

term in the NLEP (4.46). We illustrate asynchronous oscillatory phenomena for two-, three-, and four-pulse examples in §4.2.5.

To determine the smallest value τ_{0j} for which there are two eigenvalues $\lambda = \pm i\lambda_{Ij}^0$ with $\lambda_{Ij}^0 > 0$, on the imaginary axis, and no eigenvalues in the right-half plane, we solve the coupled system $g_{Rj} = g_{Ij} = 0$ given in (4.59) for τ_{0j} and λ_{Ij}^0. In (4.59), $C_{jR}(\lambda_I) = \text{Re}(C_j(i\lambda_I))$ and $C_{jI}(\lambda_I) = \text{Im}(C_j(i\lambda_I))$, where $C_j(\lambda)$ is defined in (4.50) in terms of σ_j as given in (4.41a). The critical value τ_0 is then defined by

$$\tau_0 = \min_j \tau_{0j} \, . \tag{4.65}$$

For given parameters D and f, we used the `MATLAB` function `fsolve()` to solve the system $g_{Rj} = g_{Ij} = 0$ for τ_{0j} and λ_{Ij}^0. To evaluate $F_R(\lambda_I)$ and $F_I(\lambda_I)$ in (4.58), we discretized the operator $[L_0^2 + \lambda_I^2]$ over the interval $-20 < y < 20$ using 500 grid points and used `MATLAB`'s inversion algorithm to solve the boundary value problem. The trapezoidal rule was used to evaluate the integrals in $F_R(\lambda_I)$ and $F_I(\lambda_I)$. Halving the number of grid points, or halving the interval length, did not significantly affect the calculated values of $F_R(\lambda_I)$ and $F_I(\lambda_I)$. In all subsequent plots of τ_{0j} and λ_{Ij}^0, we treat D as the bifurcation parameter and hold f fixed at a particular value. For the values of f tested in the interval $0 < f < 1$, the qualitative behavior of $\tau_{0j}(D)$ remained unchanged.

In Figure 4.2(a), we plot the curves $\tau_{0j}(D)$ for $N = 2$ and $f = 0.5$. The critical value D_{c2} is indicated by the vertical dotted line in the figure. When $D = D_{c2}$, the $j = 1$ curve ends as the corresponding pair of imaginary eigenvalues meet at the origin, as shown in the plot of $\lambda_{Ij}^0(D)$ in Figure 4.2(c). As D increases above D_{c2}, one eigenvalue moves on the real axis into the right-half plane. Because the $j = 0$ mode does not undergo such a bifurcation, the $j = 0$ curve

continues beyond D_{c2} but is not plotted. In general, the jth curve ends when the jth mode becomes unstable to a real eigenvalue crossing into the right-half plane from the origin. In Figure 4.2(b), we magnify the interval in Figure 4.2(a) where the ordering principle $\tau_{01} < \tau_{00}$ holds. For D in this interval, we expect asynchronous oscillations to be the dominant instability. For D to the right of this interval, the familiar ordering principle $\tau_{00} < \tau_{01}$, guaranteeing synchronous oscillatory instabilities, is restored.

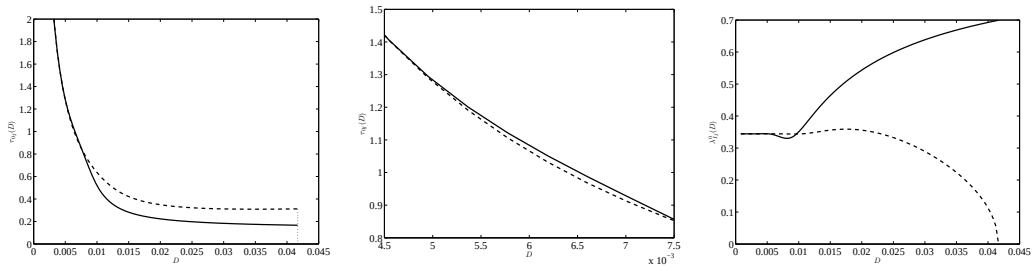

(a) $\tau_{0j}(D)$ for $N = 2$ (b) $\tau_{0j}(D)$ for $N = 2$ closeup (c) $\lambda^0_{Ij}(D)$ for $N = 2$

Figure 4.2. Plots of $\tau_{0j}(D)$ (left and center figures) and $\lambda^0_{Ij}(D)$ (right figure) for $N = 2$ and $f = 0.5$. The critical value $D_{c2} \approx 0.0417$ is indicated by the vertical dotted line. In all figures, the solid and dashed curves correspond to $j = 0$ and $j = 1$, respectively. In the magnified interval shown in the center figure, $\tau_{01} < \tau_{00}$, indicating the possibility of asynchronous oscillations.

In Figure 4.3(a), we show a plot of $\tau_{0j}(D)$ for a three-pulse example with $f = 0.6$. We again plot only the interval $0 < D < D_{c3}$ above which the $j = 2$ curve ceases to exist. In the plot of $\lambda^0_{Ij}(D)$ in Figure 4.3(c), we see that $\lambda^0_{I2} \to 0$ as $D \to D^-_{c3}$. In Figure 4.3(b), the reverse ordering principle is again observed for an interval of D, indicating the possibility of asynchronous oscillations. As similar to the previous two-pulse case, for D to the right of this interval, the usual ordering principle guaranteeing synchronous oscillatory instabilities is restored. The same characteristics of $\tau_{0j}(D)$ and $\lambda^0_{Ij}(D)$ for a four-pulse example with $f = 0.6$ are seen in Figures 4.4(a)-4.4(c).

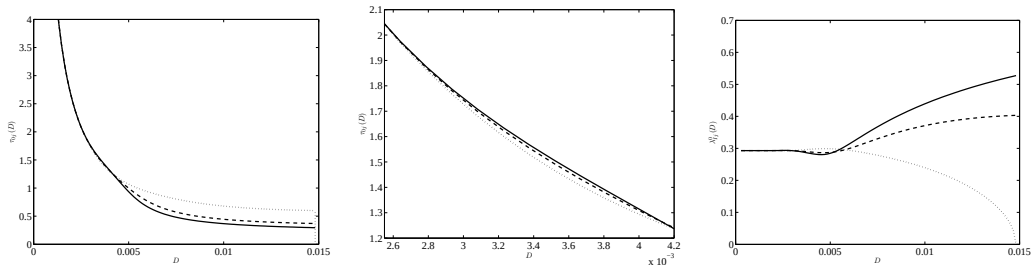

(a) $\tau_{0j}(D)$ for $N = 3$ (b) $\tau_{0j}(D)$ for $N = 3$ closeup (c) $\lambda^0_{Ij}(D)$ for $N = 3$

Figure 4.3. Plots of $\tau_{0j}(D)$ (left and center figures) and $\lambda^0_{Ij}(D)$ (right figure) for $N = 3$ and $f = 0.6$. The critical value $D_{c3} \approx 0.0148$ is indicated by the vertical dotted line. In all figures, the solid, dashed, and dotted curves correspond to $j = 0, 1, 2$, respectively. In the magnified interval shown in the center figure, $\tau_{02} < \tau_{01} < \tau_{00}$.

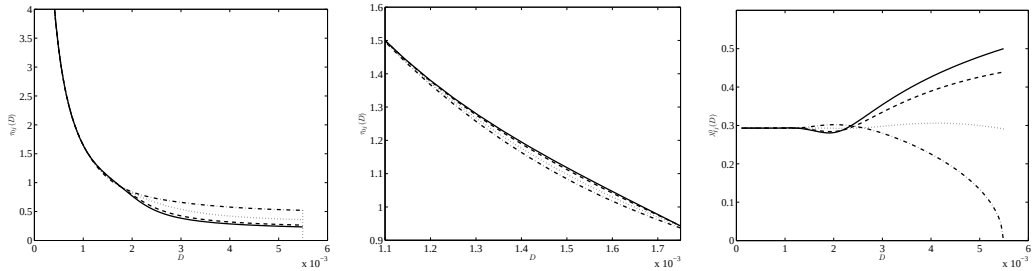

(a) $\tau_{0j}(D)$ for $N = 4$ (b) $\tau_{0j}(D)$ for $N = 4$ closeup (c) $\lambda^0_{Ij}(D)$ for $N = 4$

Figure 4.4. Plots of $\tau_{0j}(D)$ (left and center figures) and $\lambda^0_{Ij}(D)$ (right figure) for $N = 4$ and $f = 0.6$. The critical value $D_{c4} \approx 0.0055$ is indicated by the vertical dotted line. In all figures, the solid, dashed, dotted, and dash-dotted curves correspond to $j = 0, 1, 2, 3$, respectively. In the magnified interval shown in the center figure, $\tau_{03} < \tau_{02} < \tau_{01} < \tau_{00}$.

For the two-pulse example of Figure 4.2 with $f = 0.5$, we trace the paths of the pair of complex conjugate eigenvalues in the right-half plane as τ increases past the Hopf bifurcation value computed in Figures 4.2(a) and 4.2(b). For the two modes $j = 0$ (Figure 4.5(a)) and $j = 1$ (Figure 4.5(b)), we start with the pair $(\tau, \lambda) = (\tau_{0j}(D), \lambda^0_{Ij})$ and solve $g(\lambda) = 0$ in (4.48) for increasingly larger values of τ. For the $j = 0$ mode we take $D = 0.03$ while for the $j = 1$ mode, we take $D = 0.006$ so that in both cases the eigenvalues being tracked are the first ones to cross into the right-half plane. The eigenvalues converge onto the positive real axis when τ is

sufficiently large. As τ is increased further, the eigenvalues split and migrate along the positive axis toward 0 and $\nu_0 = 5/4$ as $\tau \to \infty$, where ν_0 is the principal eigenvalue of the operator L_0.

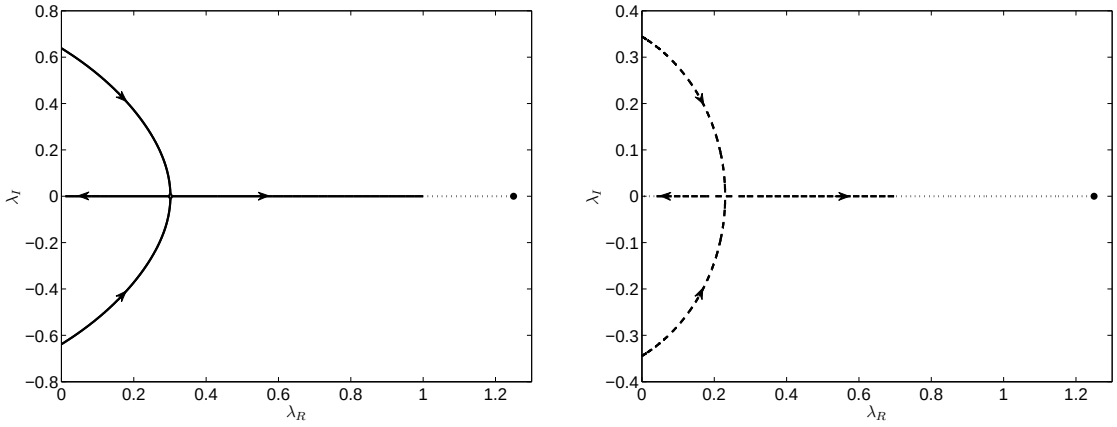

(a) $D = 0.03, j = 0$ (b) $D = 0.006, j = 1$

Figure 4.5. Plots of the paths of $\lambda = \lambda_I + i\lambda_R$ with $N = 2$, and $f = 0.5$ for $(D, j) = (0.03, 0)$ (left) and $(D, j) = (0.006, 1)$ (right) as τ increases past its Hopf bifurcation value $\tau_{0j}(D)$. The arrows denote the direction of traversal for increasing τ. The eigenvalues converge onto the positive real axis when τ reaches some value $\tau_c(D) > \tau_{0j}(D)$. The eigenvalues split, with one tending to 0 and the other tending to $\nu_0 = 5/4$ as $\tau \to \infty$, where ν_0 is the unique positive eigenvalue of the operator L_0.

Two key characteristics shared by Figures 4.2-4.4 are the behaviors of τ_{0j} and λ_{Ij}^0 for small values of D. These figures suggest that $\tau_{0j} \to \infty$ as $D \to 0$ independent of j, while λ_{Ij}^0 approaches a constant value also independent of j. We now provide a simple analytical explanation for this limiting behavior. We remark that this unbounded behavior of τ_{0j} as $D \to 0$ is in marked contrast to the finite limiting behavior as obtained in [**58**] or [**106**] for the Gray-Scott and Gierer-Meinhardt RD models, respectively.

In the limit $D \to 0$, a simple scaling argument shows that $|\mu| \to \infty$, where $\mu = \sqrt{\tau\lambda/D}$. We then readily obtain from (4.41a) that $\sigma_j \to 2$ as $D \to 0$ and that $\beta_0 = \mathcal{O}(D^{-1})$. Therefore,

from (4.50), we get the limiting behavior

$$\begin{gathered} C_j \sim C \equiv \frac{1}{2}\left[1+\alpha z\sqrt{\lambda}+\frac{\alpha f z\sqrt{\lambda}}{1-f+\lambda}\right], \\ z=\sqrt{\tau D}, \quad \alpha=\frac{\alpha^2 v_c^2}{3}, \qquad j=0,\ldots,N-1\,. \end{gathered} \tag{4.66}$$

We set $\lambda = i\lambda_I$, where $\lambda_I > 0$, and then separate (4.66) into real and imaginary parts to get

$$\begin{gathered} C \equiv C_R(\lambda_I) + iC_I(\lambda_I) \equiv \frac{1}{2}\left[1+\frac{\alpha z}{\sqrt{2}}\sqrt{\lambda_I}M_+\right] + i\frac{1}{2\sqrt{2}}\alpha z\sqrt{\lambda_I}M_-\,; \\ M_\pm \equiv \frac{1-f\pm\lambda_I f+\lambda_I^2}{(1-f)^2+\lambda_I^2}\,. \end{gathered} \tag{4.67}$$

Since C is independent of j, it follows that the root $\tau = \tau_{0l}$ and $\lambda_I = \lambda_{Il}$ to the limiting coupled system $C_R(\lambda_I) = F_R(\lambda_I)$ and $C_I(\lambda_I) = F_I(\lambda_I)$ must be independent of j.

For this coupled system to possess a root, it is readily seen that we must have $z = \sqrt{\tau D} = \mathcal{O}(1)$ as $D \to 0$, which implies that $\tau_{0l} = \mathcal{O}(D^{-1})$ as $D \to 0$. We use (4.67) to eliminate z between the coupled system $C_R(\lambda_I) = F_R(\lambda_I)$ and $C_I(\lambda_I) = F_I(\lambda_I)$. In this way, we obtain that λ_{Il} must be a root of

$$H_R(\lambda_I) = H_I(\lambda_I)\,, \tag{4.68a}$$

where $H_R(\lambda_I)$ and $H_I(\lambda_I)$ are defined by

$$H_R(\lambda_I) = \frac{2F_R(\lambda_I)-1}{\lambda_I^2+f\lambda_I+1-f}\,, \qquad H_I = \frac{2F_I(\lambda_I)}{\lambda_I^2-f\lambda_I+1-f}\,. \tag{4.68b}$$

Therefore, for $D \to 0$, we conclude that λ_{Il} depends only on f and is independent of N. The scaling $\tau_{0l} = \mathcal{O}(D^{-1})$ was not observed in the analysis of the Gray-Scott [**58**] or Gierer-Meinhardt models [**106**].

We now prove the existence of a solution $\lambda_{Il} > 0$ to (4.68). We begin by noting that $H_R(0) = (1-f)^{-1} > 0$ and that $H_R(\lambda_I)$ has no poles when $\lambda_I \geq 0$. Also, because $F_R \to 0$ as $\lambda_I \to \infty$, we find from (4.68b) that $H_R \sim -1/\lambda_I^2 < 0$ as $\lambda_I \to \infty$. To show the existence of an intersection between H_R and H_I, there are two cases to consider. The first case is when $0 < f < 2(\sqrt{2}-1)$ so that the denominator of H_I is always positive. Since $F_I(0) = 0 < F_R(0) = 1$, and $F_I(\lambda_I) > 0$ for $\lambda_I > 0$, then by the properties of H_R there must exist a solution to (4.68a). When $2(\sqrt{2}-1) < f < 1$, $H_I(\lambda_I)$ has two poles on the positive real axis at $\lambda_I = \lambda_I^{l,r}$ ordered $0 < \lambda_I^l < \lambda_I^r$ with $\lambda_I^l \to 0^+$ as $f \to 1^-$. Therefore, $H_I \to +\infty$ as $\lambda_I \to \lambda_I^{l-}$. Because $H_R(0) > 0$ and is bounded for all λ_I while $H_I(0) = 0$, there must exist a solution to (4.68a) on the interval $0 < \lambda_I < \lambda_I^l$. This completes the proof of the existence of a root $\lambda_{Il} > 0$ under the scaling $\tau = \mathcal{O}(D^{-1})$ as $D \to 0$. While we have not been able to show analytically that λ_{Il} is unique, we have not observed numerically an example that yields more than one solution to (4.68a).

In Figure 4.6(a), we show the log-log relationship between τ_{0j} and small D for the examples shown in Figures 4.2 - 4.4. Note that in each case, all curves corresponding to modes $j = 0, \ldots, N-1$ are plotted. However, as stated above, τ_{0j} is independent of j for small D and thus the curves are indistinguishable in the plot. In Figure 4.6(b), we plot the N curves of λ_{Ij}^0 as a function of f with D small for $N = 2, 3, 4$. We also plot the solution to (4.68a). Although for each value of N we use a different value of D specified as $D = D_{cN}/10$, all curves are indistinguishable at the resolution allowed by the figure. Because $\lambda_I^l \to 0^+$ as $f \to 1^-$, we expect theoretically that $\lambda_{Il} \to 0^+$ in this limit. Numerically, however, the problem (4.68a) for $1-f$ small becomes ill-conditioned and our numerical solver fails when f is too close to $f = 1$.

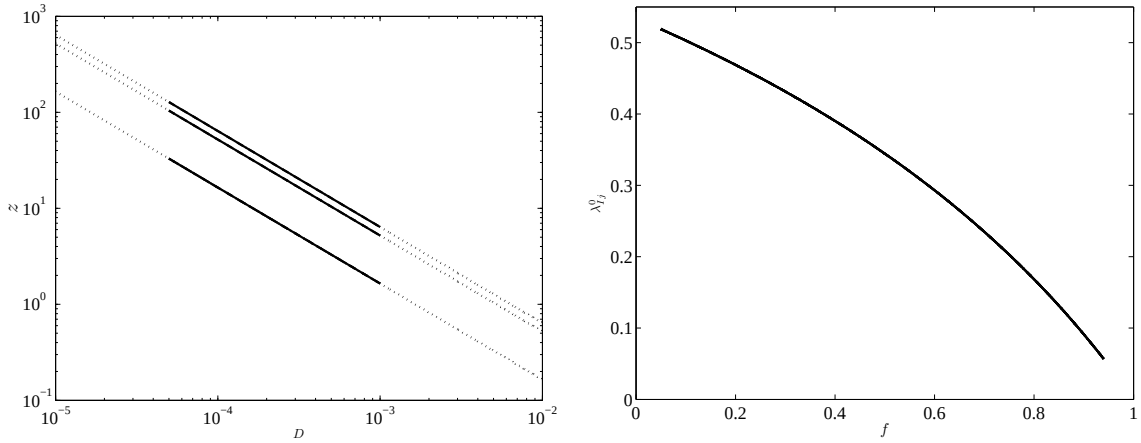

(a) log-log plot of $\tau_{0j}(D)$ for $N = 2, 3, 4$ and $D \ll 1$ (b) λ_{Ij}^0 versus f for $N = 2, 3, 4$ and $D \ll 1$

Figure 4.6. The log-log relationship between τ_{0j} and small D with parameters from Figures 4.2 - 4.4 (left) and λ_{Ij}^0 versus f with D small for $N = 2, 3, 4$ (right). In the left figure, the solid lines are numerically computed solutions of $\tilde{g}_{Rj} = \tilde{g}_{Ij} = 0$, while the dotted lines all have slope -1. The top line corresponds to $N = 2$, $f = 0.5$, the center line to $N = 3$, $f = 0.6$, and the bottom line to $N = 4$ and $f = 0.6$. The different curves of each example corresponding to modes $j = 0, \ldots, N-1$ are indistinguishable. In the right figure, the curves of λ_{Ij}^0 versus f generated by the solution to $\tilde{g}_{Rj} = \tilde{g}_{Ij} = 0$ are plotted, as is the solution to (4.68a). These curves are indistinguishable at the resolution allowed by the figure.

The main limitation of our analysis is that we are unable to determine whether, for each function g_j, a complex conjugate pair of pure imaginary eigenvalues exists at only one value of τ_{0j} for all the ranges of the parameters. Our numerical experiments suggest that for $0 < \tau < \tau_{0j}$ and $D < D_{0cN}$, the pattern is stable. This indicates that our computed thresholds τ_{0j} are the minimun values of τ for which an oscillatory instability occurs.

4.2.5. Numerical Validation

Next, we illustrate the theory presented in §4.2.3 and §4.2.4 regarding competition and oscillatory instabilities of N-pulse equilibria. We solve the Brusselator model without boundary

flux (4.2) numerically using the MATLAB partial differential equations solver `pdepe()` with non-uniformly spaced grid points distributed according to the mapping

$$y = x + \sum_{i=0}^{N-1} \tanh\left[\frac{x - x_i}{2\epsilon}\right]; \qquad -1 - N < y < 1 + N,$$

where x is the physical grid. The initial conditions were taken to be a perturbation of the equilibrium pulse solution of the form

$$u(x,0) = u_e^*(x)\left[1 + \delta \sum_{k=0}^{N-1} d_k e^{-(x-x_k)^2/(4\epsilon^2)}\right], \qquad v(x,0) = v_e^*(x), \tag{4.69}$$

where $\delta \ll 1$ is taken to be 0.002, and d_k is the $(k+1)$th component of the vector $\boldsymbol{d}$ to be defined below. Either 2000 ($\epsilon = 0.005$) or 4000 ($\epsilon = 0.001$) grid points were used to produce the numerical results below. In (4.69), instead of u_e,v_e given in (4.24), we use the true equilibrium u_e^*,v_e^* calculated using small τ starting from the initial conditions u_e,v_e. Because τ does not influence the equilibrium solution, u_e^*, v_e^* may be used as valid initial conditions for any value of τ. We briefly explain the reason for this procedure. With an insufficiently small choice for τ while starting with u_e and v_e as initial conditions, we observe an immediate annihilation of one or more of the pulses. We conjecture that this is due to the inaccuracy of the asymptotic solution associated with the non-zero background of the activator, coupled with the sluggish response of the inhibitor. However, for τ sufficiently small, the inhibitor is able to respond quickly to prevent an annihilation, allowing the system to evolve to a pulse equilibrium state u_e^*, v_e^*.

In (4.69), the choice of the vector $\boldsymbol{d}$ depends on the phenomenon that we illustrate. In computations illustrating competition instabilities, $\boldsymbol{d}$ is taken to be a multiple of $\boldsymbol{v}_{N-1}$, the

eigenvector given in (4.41c) associated with the eigenvalue that first crosses into the right-half plane as D is increased above D_{cN} when τ is sufficiently small. The values of D in the experiments illustrating competition instabilities will be such that only the $j = N-1$ mode is unstable. In computations illustrating oscillatory instabilities, $\boldsymbol{d}$ is taken to be a multiple of the vector $\sum_{j=0}^{N-1} \boldsymbol{v}_j$, with $\boldsymbol{v}_j$ given in (4.41c), which allows for all the modes to be present initially. We track the evolution of the modes through the quantity b_j^{amp}, defined as the amplitude of the oscillations of b_j given by

$$b_j = |\Delta \boldsymbol{u}_m^t \boldsymbol{v}_j| \,, \qquad \Delta \boldsymbol{u}_m \equiv \left(u_{m0} - u_e^*(x_0, 0) \,, \ldots, u_{mN-1} - u_e^*(x_{N-1}, 0)\right)^t ; \quad j = 0, \ldots, N-1 \,, \tag{4.70}$$

allowing clear identification of which modes grow or decay. Here u_{mn} denotes the numerically computed solution at the jth equilibrium pulse location defined by $u_{mj} \equiv u(x_j, t)$ where $x_j = -1 + (2j+1)/N$ with $j = 0, \ldots, N-1$. In all experiments, $\boldsymbol{d}$ is normalized so that $\max_k d_k = 1$.

We consider three experiments with two, three, and four pulses. In each experiment, f is fixed while different combinations of τ and D are used to illustrate the theory for competition and oscillatory instabilities. The results are presented using plots of the amplitude of each pulse $u_{mn} \equiv u(x_n, t)$ versus time. For certain oscillatory examples, we also plot the quantity b_j^{amp} versus time. In our computations, we limit the timescale to much less than $\mathcal{O}(\epsilon^{-2})$ so that the pulses remain approximately stationary over the time intervals shown.

Experiment 1: In this experiment we consider competition and oscillatory instabilities of a two-pulse equilibrium with $f = 0.5$. We begin with an example of competition instability. For

$\epsilon = 0.005$ and $D = 0.043$, in Figure 4.7(a) we plot the initial conditions for u and v on the left and right axes, respectively. Note the non-zero background of u. Using the results depicted in Figure 4.2(a), we calculate that $\tau_0(D) = 0.165$, while using (4.53) we calculate $D_{c2} = 0.0417$. For $\tau = 0.01 < \tau_0(D)$ and $D > D_{c2}$, we expect a competition instability in which one pulse is annihilated with no oscillation in the amplitudes. In Figure 4.7(b), we plot the amplitudes u_{m0} and u_{m1} of the two pulses as a function of time. As suggested by the eigenvector $\boldsymbol{v}_1$ in (4.41c), one pulse annihilates as time increases. Note that the pulse amplitude decays to approximately the value of the non-zero background state.

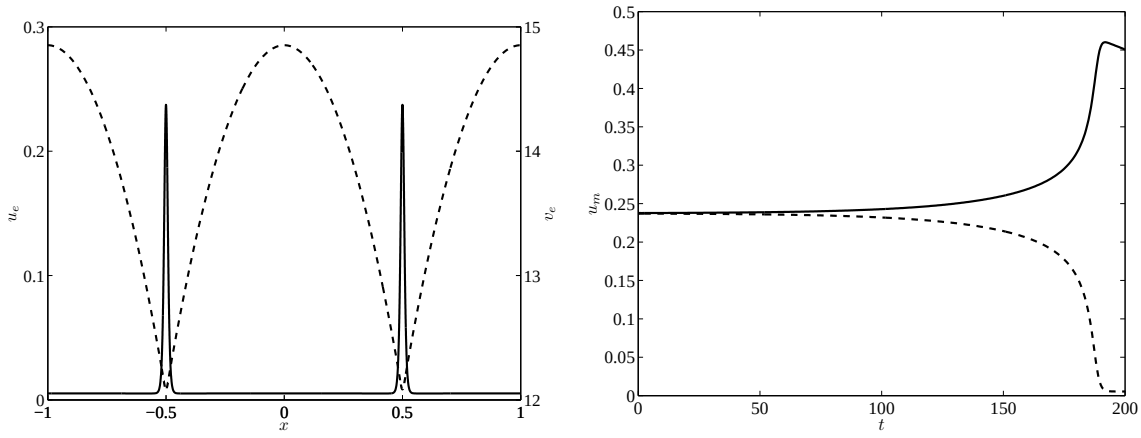

(a) initial condition for u and v

(b) u_m versus t

Figure 4.7. Experiment 1: The left figure is the initial condition for u (solid curve and left axis) and v (dashed curve and right axis) for $N = 2$ with $\epsilon = 0.005$, $f = 0.5$ and $D = 0.043 > D_{c2} = 0.0417$. The right figure shows the amplitudes of the left (solid curve) and right (dashed curve) pulses for $\tau = 0.01$ versus time. The right pulse annihilates as time increases.

We now illustrate oscillatory phenomena. In Figure 4.8(a), we plot the pulse amplitudes when $D = 0.03 < D_{c2}$ and $\tau = 0.17 < \tau_0(D) = \tau_{00} = 0.183$. As expected, no pulse annihilations occur while initial oscillations decay. While the equilibrium is stable to large eigenvalues for this combination of D and τ, we calculate from (4.55) that $D > D_2^* = 0.021$.

Thus, we expect to observe a drift-type instability when $t = \mathcal{O}(\epsilon^{-2})$. Next, for the same value of D, we set $\tau = 0.191 > \tau_0(D)$ so that the synchronous mode undergoes a Hopf bifurcation. The pulse amplitudes are plotted in Figure 4.8(b). As expected, the pulse amplitudes synchronize quickly and oscillate with growing amplitude in time. The eventual annihilation of the pulses suggests that the Hopf bifurcation is subcritical for these parameter values.

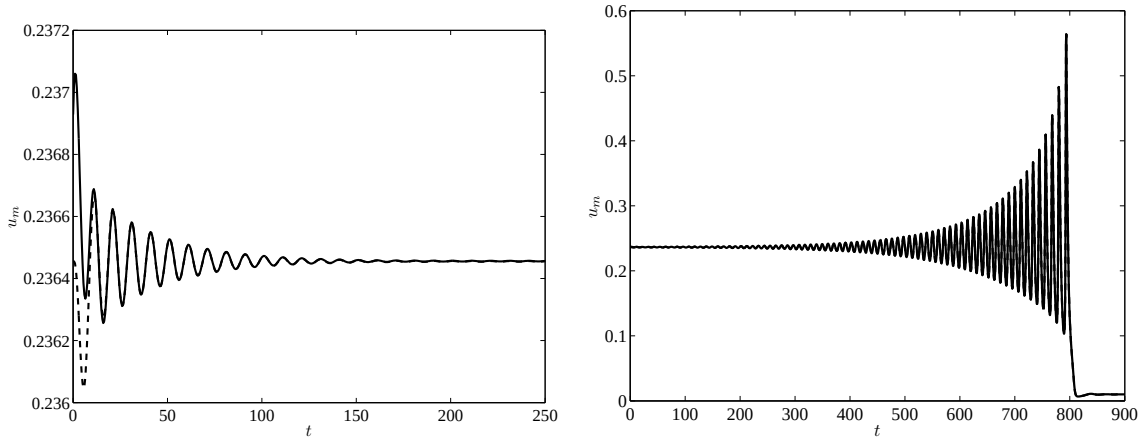

(a) $\tau = 0.17$ (b) $\tau = 0.191$

Figure 4.8. Experiment 1: The left figure is a plot of pulse amplitudes for $N = 2$, $\epsilon = 0.005$, $f = 0.5$, $D = 0.03$, and $\tau = 0.17$. The critical value of τ is $\tau_0(D) = 0.183$. The solid curve is u_{m0} and the dashed curve is u_{m1}. In the right figure, we make a similar plot with $\tau = 0.191 > \tau_0(D)$.

In the next example, we take $\epsilon = 0.001$ and $D = 0.006$. In Figure 4.2(b) we see that for this value of D, the asynchronous oscillatory mode is unstable if $\tau > \tau_0(D) = \tau_{01} = 1.065$ while the synchronous mode is stable if $\tau < \tau_{00} = 1.083$. In Figure 4.9(a), we plot the pulse amplitudes when $\tau = 1.04$ during the initial growth of the oscillations. Note the clear contrast between Figure 4.9(a) and Figure 4.8(b) where the pulses oscillate out of phase in the former and in phase in the latter. In Figure 4.9(b), we show what appears to be regular asynchronous oscillations, suggesting that the Hopf bifurcation may be supercritical for the parameters used.

In Figure 4.9(c) we plot the initial growth of b_1^{amp} and the initial decay of b_0^{amp}, consistent with predictions from analysis. Both modes are present, with the $j = 1$ mode being dominant. We remark that while the numerical threshold in τ is not equal to the theoretical value, we have observed in numerous experiments that agreement with analysis improves as ϵ is decreased.

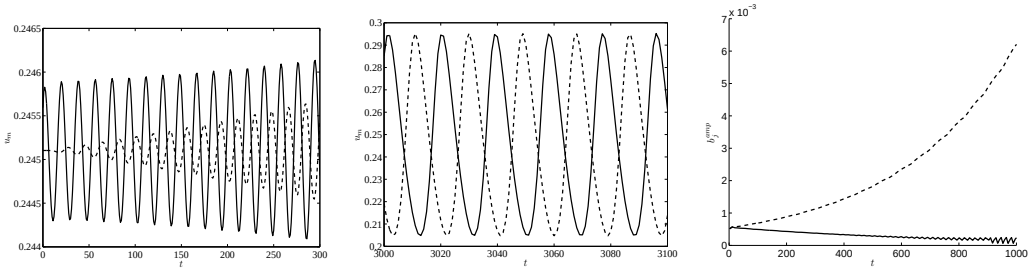

(a) oscillations for small t (b) oscillations for large t (c) b_j^{amp} versus t

Figure 4.9. Experiment 1: In the left figure, we plot pulse amplitudes for the initial growth of asynchronous oscillations. In the center figure, we show the large time behavior of what appears to be regular asynchronous oscillations. The solid (dashed) curve is u_{m0} (u_{m1}). In the right figure, we plot the initial growth and decay of b_1^{amp} (dashed curve) and b_0^{amp} (solid curve). The parameters are $N = 2$, $\epsilon = 0.001$, $f = 0.6$, $D = 0.006$, and $\tau = 1.04$. The threshold value is $\tau_0(D) = \tau_{01} = 1.065$, and corresponds to asynchronous oscillations.

Experiment 2: In this experiment, we consider instabilities of a three-pulse solution with $f = 0.6$. We first consider a competition instability. In Figure 4.10(a), we plot the initial conditions for u and v for $\epsilon = 0.005$ and $D = 0.017 > D_{c3} = 0.0148$. The initial perturbation, according to $\boldsymbol{v}_2$ in (4.41c), increases the amplitude of the first and third pulses while decreasing that of the middle pulse. For $\tau = 0.01 < \tau_0(D) = \tau_{00} = 0.28$, we plot the pulse amplitudes versus time in Figure 4.10(b), observing that the middle pulse annihilates while the other two pulses increase in amplitude. This increase in amplitude, also observed in Figure 4.7(b) of Experiment 1, is expected because the common pulse amplitude increases when the number of pulses decreases

(see (4.17) and (4.24a)). For a perturbation in the $-\boldsymbol{v}_2$ direction we observe the annihilation of the first and third pulses (not shown).

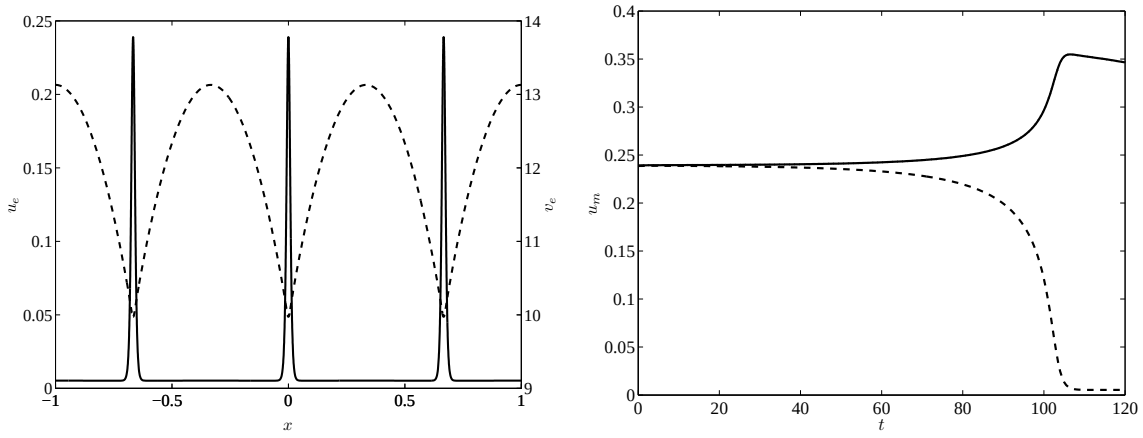

(a) initial conditions for u and v (b) u_m versus t

Figure 4.10. Experiment 2: The left figure is the initial condition for u (solid curve and left axis) and v (dashed curve and right axis) for $N = 3$ with $\epsilon = 0.005$, $f = 0.6$, and $D = 0.017 > D_{c3} = 0.0148$. In the right figure, we plot u_{m0} and u_{m2} (solid curve) and u_{m1} (dashed curve) versus time with $\tau = 0.01$. The second pulse annihilates as time increases.

To illustrate oscillatory behavior, we take $\epsilon = 0.005$ and $D = 0.009$ so that all real eigenvalues lie in the left-half plane if τ is small enough. Using Figure 4.3(a), we calculate $\tau_0(D) = \tau_{00} = 0.3994$. In Figure 4.11(a), we set $\tau = 0.37 < \tau_0(D)$ so that oscillations decay in time. For stability also to small eigenvalues, however, we require $D < D_3^* = 0.011$. In Figure 4.11(b), we set $\tau = 0.42$ so that the pulse amplitudes quickly synchronize and the subsequent oscillations grow in time. As in Experiment 1, we observe the annihilation of the pulses, suggesting that the Hopf bifurcation is subcritical.

We next decrease D to $D = 0.0034$ so that, as suggested by Figure 4.3(b), asynchronous oscillations are the dominant instability. We calculate that $\tau_0(D) = \tau_{02} = 1.518$, $\tau_{01} = 1.544$, and $\tau_{00} = 1.557$. In Figures 4.12(a) and 4.12(b) we plot, respectively, the transient and large

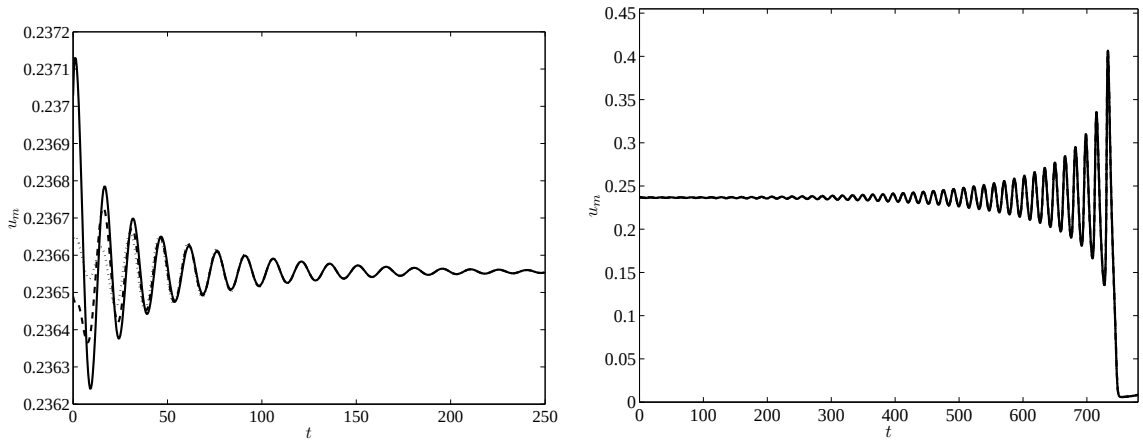

(a) $\tau = 0.37$ (b) $\tau = 0.42$

Figure 4.11. Experiment 2: In the left figure, we plot u_{m0} (solid curve), u_{m1} (dashed curve), and u_{m2} (dotted curve) for $N = 3$, $\epsilon = 0.005$, $f = 0.6$, $D = 0.009$, and $\tau = 0.37$. The right figure is similar except that τ is increased to $\tau = 0.42$. The critical value of τ is $\tau_0(D) = 0.3994$.

time behavior of the pulse amplitudes for $\epsilon = 0.001$ and $\tau = 1.51$. In clear contrast to Figure 4.11(b), the pulse amplitudes oscillate out of phase for both small and large time. In Figure 4.12(b), as the form of the eigenvector $\boldsymbol{v}_2$ in (4.41c) suggests, the first and third pulses oscillate approximately in phase with each other while out of phase with the second pulse. For large time, the oscillations occur within an envelope that oscillates slowly in time relative to the oscillations of the pulse amplitudes. In Figure 4.12(c), we plot the initial growth and decay of b_j^{amp} for all three modes. Consistent with the results depicted in Figure 4.3(b), the $j = 2$ mode grows while the other two modes decay. For large time, all modes are present with the dominant mode being $j = 2$.

Experiment 3: In this experiment, we illustrate instabilities of a four-pulse equilibrium with $f = 0.6$. In Figure 4.13(a), we plot the initial conditions for u and v with $\epsilon = 0.005$ and $D = 0.0057$. We calculate from (4.53) that $D_{c4} = 0.0055 < D$. With $\tau = 0.01 < \tau_0(D) =$

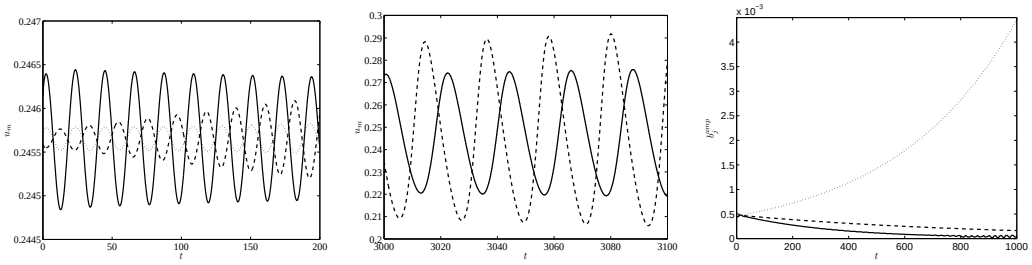

(a) oscillations for small t (b) oscillations for large t (c) b_j^{amp} versus t

Figure 4.12. Experiment 2: In the left and center figures, we plot, respectively, the transient and large time asynchronous oscillations of u_{m0} (solid curve), u_{m1} (dashed curve), and u_{m2} (dotted curve). The first and third pulses oscillate almost in phase for large time. In the right figure, we plot the initial growth and decay of b_j^{amp} for $j = 0$ (solid curve), $j = 1$ (dashed curve), and $j = 2$ (dotted curve). The parameters are $N = 3$, $\epsilon = 0.001$, $f = 0.6$, $D = 0.0034$, and $\tau = 1.51$. The threshold value is $\tau_0(D) = \tau_{02} = 1.518$.

0.2344, we expect an annihilation of one or more pulses without oscillatory behavior. The form of $\boldsymbol{v}_3$ in (4.41c) suggests that the second pulse is the first to annihilate while the fourth pulse decays in amplitude as the other two pulses grow. Once the first annihilation occurs, the resulting three-pulse pattern is no longer in equilibrium and thus evolves according to the dynamics derived in [**97**], and any subsequent annihilations should they occur are beyond the scope of this analysis. In Figure 4.13(b), we plot the pulse amplitudes up to the time of the annihilation of the second pulse.

To show oscillatory phenomena, we take $\epsilon = 0.005$ and $D = 0.004$. Using the data from Figure 4.4(a), we calculate $\tau_0(D) = \tau_{00} = 0.287$. In Figure 4.14(a), we plot the pulse amplitudes for $\tau = 0.27$ so that the equilibrium solution is stable to large eigenvalues. Here, we require $D < D_4^* = 0.00469$ for the equilibrium to also be stable to small eigenvalues. In Figure 4.14(b), we plot the pulse amplitudes for $\tau = 0.31$ so that synchronous oscillations grow in time

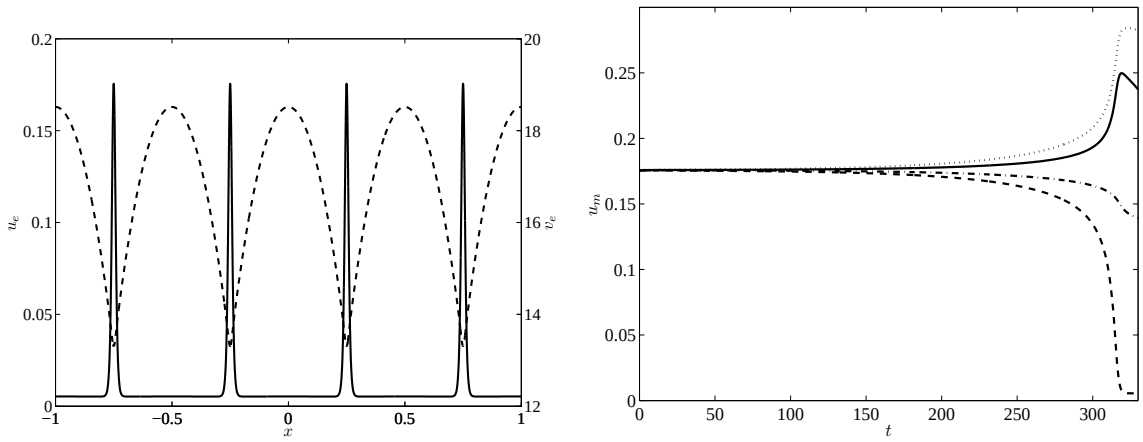

(a) initial conditions for u and v (b) u_m versus t

Figure 4.13. Experiment 3: The left figure is the initial condition for u (solid curve and left axis) and v (dashed curve and right axis) for $N = 4$ with $\epsilon = 0.005$, $f = 0.6$, and $D = 0.0057 > D_{c4} = 0.0055$. In the right figure, we plot u_{m0} (solid curve), u_{m1} (dashed curve), u_{m2} (dotted curve), and u_{m3} (dash-dotted) curve versus time with $\tau = 0.01$. The second pulse annihilates as time increases. All complex eigenvalues are in the stable left-half plane.

until all pulses annihilate. As in Experiment 2, we observe oscillatory behavior subsequent to annihilation.

Lastly, we illustrate asynchronous oscillations with $\epsilon = 0.001$ and $D = 0.0015$. According to the data in Figure 4.4(b), we calculate that $\tau_0(D) = \tau_{03} = 1.084$, $\tau_{02} = 1.098$, $\tau_{01} = 1.112$, and $\tau_{00} = 1.118$. Taking $\tau = 1.06$, we plot the initial growth of asynchronous oscillations in Figure 4.15(a). The form of $\boldsymbol{v}_3$ suggests that the first and fourth pulses oscillate π radians out of phase as should the second and third pulses, while no pulses oscillate in phase. This is shown to be approximately the case for large time in Figure 4.15(b). The initial growth and decay of the quantities b_j^{amp}, shown in Figure 4.15(c), demonstrate the reverse ordering principle of the Hopf bifurcation thresholds predicted by the theory. For large time, all modes are present, with the $j = 3$ mode being dominant.

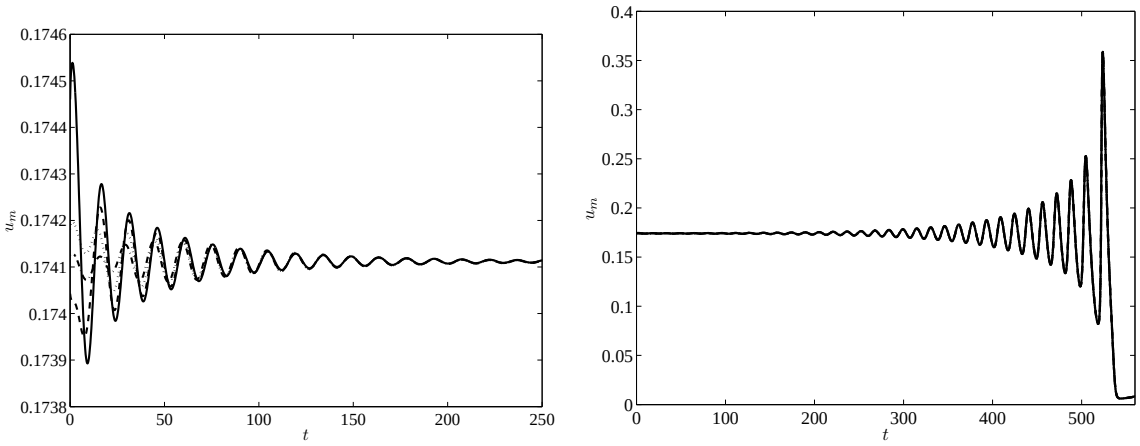

(a) $\tau = 0.27$ (b) $\tau = 0.31$

Figure 4.14. Experiment 3: In the left figure, we plot u_{m0} (solid curve), u_{m1} (dashed curve), and u_{m2} (dotted curve) and u_{m3} (dash-dotted curve) for $N = 4$, $\epsilon = 0.005$, $f = 0.6$, $D = 0.004$, and $\tau = 0.27$. The right figure is similar except $\tau = 0.31$. The critical value of τ is $\tau_0(D) \approx 0.287$.

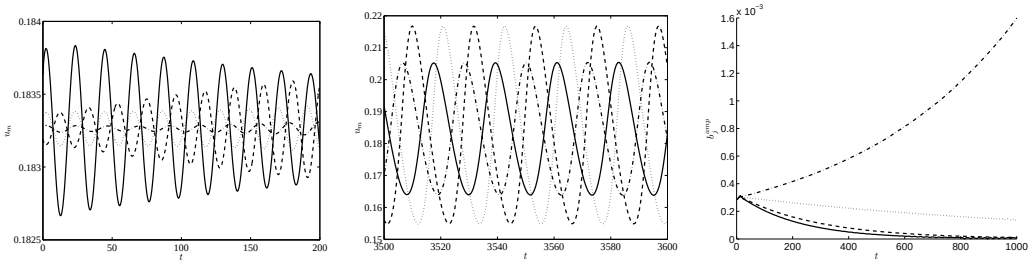

(a) oscillations for small t (b) oscillations for large t (c) b_j^{amp} versus t

Figure 4.15. Experiment 3: In the left and center figures, we plot, respectively, the transient and large time asynchronous oscillations of u_{m0} (solid curve), u_{m1} (dashed curve), u_{m2} (dotted curve), and u_{m3} (dash-dotted curve). For large time, the first and fourth pulses oscillate approximately π radians out of phase, as do the second and third pulses. In the right figure, we show initial growth and decay of b_j^{amp} for $j = 0$ (solid curve), $j = 1$ (dashed curve), $j = 2$ (dotted curve), and $j = 3$ (dash-dotted curve). The parameters are $N = 4$, $\epsilon = 0.001$, $f = 0.6$, $D = 0.0015$, and $\tau = 1.06$. The critical value of τ is $\tau_0(D) = \tau_{03} = 1.084$.

4.3. Stability of Symmetric Two-Pulse Quasi-Equilibria with Boundary Flux

In this section, we analyze dynamically triggered instabilities of symmetric two-pulse quasi-equilibrium solutions to (4.4). In contrast to the equilibrium case studied in §4.2, for which initial conditions were either stable or unstable depending on the "tuning" of the model parameters, dynamically triggered instabilities occur when a pulse pattern, that is initially stable, eventually undergoes an $\mathcal{O}(1)$ timescale instability that is triggered by the slow evolution of the pulses. To study this phenomenon, we first construct a two-pulse quasi-equilibrium solution and derive an equation of motion for the $\mathcal{O}(\epsilon^2)$ slow dynamics of the pulse locations. We then derive an NLEP governing the stability of the quasi-equilibrium solution in terms of the pulse locations. Then, from an analysis of the NLEP we derive criteria for which a stable solution may become unstable as a result of the slow dynamics. We then present numerical examples illustrating the theory. Since general N-pulse quasi-equilibria and their slow dynamics have been studied in [**97**] for the original scaling of the Brusselator model, we omit much of the detail in the construction of the quasi-equilibrium solution.

4.3.1. Construction and Slow Dynamics of the Two-Pulse Quasi-Equilibrium Solution

We seek a symmetric two-pulse quasi-equilibrium solution to (4.4) with pulses centered at $x_1 = -x_0 = \alpha$ with $0 < \alpha < 1$. Since the pulses have equal amplitude, the leading order solution for v in the inner region, as in §4.2.1, is $v \sim v_{cqe}$, where the constant v_{cqe} is to be found. Then, as in §4.2.1, we solve (4.4a) for u in the inner region of the jth pulse to get

$$u \sim \frac{1}{f v_{cqe}} w(y_j)\,, \qquad y_j = \epsilon^{-1}(x - x_j)\,; \qquad j = 0, 1\,,$$

where $w(y)$ is the solution to (4.11). In the outer region $u \sim \epsilon E + \mathcal{O}(\epsilon^2)$. Then, upon representing the terms involving u in (4.4b) as delta masses, we proceed as in §4.2.1 and use (4.12) to obtain that the outer equation for v is

$$\begin{aligned} Dv_{xx} + E + \frac{6}{f v_{cqe}} \left(1 - \frac{1}{f}\right) [\delta(x - x_0) + \delta(x - x_1)] = 0 \,, \\ -1 < x < 1 \,; \qquad v_x(\pm 1) = \pm 1 \,. \end{aligned} \tag{4.71}$$

Integrating (4.71) over the interval $-1 < x < 1$ and applying the boundary conditions, we calculate that

$$v_{cqe} = \frac{6}{f(D+E)} \left[\frac{1}{f} - 1\right] > 0 \,. \tag{4.72}$$

Note that due to the presence of boundary flux, the pulse amplitudes now depend on the inhibitor diffusion coefficient.

Using (4.72) for v_{cqe} in (4.71), we let $v = x^2/2 + \nu(x)$ and solve for $\nu(x)$ in terms of G defined in (4.22) with uniqueness achieved by imposing that $v(x_0) = v(x_1) = v_{cqe}$. In this way, we obtain the following result for the two-pulse quasi-equilibrium solution for u and v:

Principal Result 4.3.1: *Let $\epsilon \to 0$ in* (4.4) *and consider a two-pulse quasi-equilibrium solution with pulses centered at $x_1 = -x_0 = \alpha$ with $0 < \alpha < 1$. Then, the leading order composite solution for u is*

$$u_{qe} \sim \epsilon E + \frac{1}{f v_{cqe}} \left(w\left[\epsilon^{-1}(x + \alpha)\right] + w\left[\epsilon^{-1}(x - \alpha)\right] \right) \,, \tag{4.73a}$$

while the leading order outer solution for v is given by

$$v_{qe} \sim \bar{\nu} + \frac{x^2}{2} + (D + E) \left[G(x; -\alpha) + G(x; \alpha)\right] \,, \tag{4.73b}$$

where G is the Green's function defined in (4.22)*, v_{cqe} is defined in* (4.72)*, and $\bar{\nu}$ is given by*

$$\bar{\nu} \equiv v_{cqe} - (D+E)\left[G(\alpha,-\alpha) + G(\alpha,\alpha)\right] - \frac{\alpha^2}{2}\,. \tag{4.74}$$

To derive the $\mathcal{O}(\epsilon^2)$ slow dynamics of the pulse locations, we introduce the slow time variable $\sigma = \epsilon^2 t$ and retain the next terms in the asymptotic series for the inner solutions of u and v near x_1 as

$$\begin{gathered} u = \frac{1}{f v_{cqe}} w(y_1) + \epsilon U_1(y_1)\,, \qquad v = v_{cqe} + \epsilon V_1(y_1)\,; \\ y_1 = \epsilon^{-1}\left(x - x_1(\sigma)\right)\,, \qquad \sigma = \epsilon^2 t\,. \end{gathered} \tag{4.75}$$

Substituting (4.75) into (4.4), and collecting terms of similar orders, we obtain that

$$L_0 U_1 = -\frac{\dot{x}_1}{f v_{cqe}} w' - E - \frac{w^2}{f v_{cqe}^2} V_1\,, \qquad -\infty < y_1 < \infty\,, \qquad U_1 \to 0 \ \text{ as } \ |y_1| \to \infty\,, \tag{4.76a}$$

$$D V_1'' = -\frac{w}{f v_{cqe}} + \frac{w^2}{f^2 v_{cqe}}\,, \qquad -\infty < y_1 < \infty\,, \qquad V_1' \to v_{qex}(x_1^{\pm}) \ \text{ as } \ y_1 \to \pm\infty\,, \tag{4.76b}$$

where $\dot{x}_1 \equiv dx_1/d\sigma$ and the operator L_0 is defined in (4.37). The limiting condition in (4.76b) comes from matching the gradients of the inner and outer solutions of v. In (4.76a), L_0 has a one dimensional kernel with eigenfunction w'. Thus, the right-hand side of (4.76a) must be orthogonal to w', and consequently

$$-\frac{\dot{x}_1}{f v_{cqe}} \int_{-\infty}^{\infty} (w')^2\, dy - E \int_{-\infty}^{\infty} w'\, dy - \frac{1}{f v_{cqe}^2} \int_{-\infty}^{\infty} w' w^2 V_1\, dy = 0\,.$$

Since w' is odd and $w'w^2 = (w^3)'/3$, we can integrate by parts and use $w \to 0$ as $|y| \to \infty$ to obtain

$$\dot{x}_1 \int_{-\infty}^{\infty} (w')^2 \, dy = \frac{1}{3v_{cqe}} \int_{-\infty}^{\infty} w^3 V_1' \, dy \, . \tag{4.77}$$

Next, we integrate by parts on the right-hand side of (4.77). Using the facts that $\int_0^y w^3(s)\, ds$ is odd and that, by (4.76b), V_1 is even, we calculate that

$$\dot{x}_1 \int_{-\infty}^{\infty} (w')^2 \, dy = \frac{1}{6v_{cqe}} \int_{-\infty}^{\infty} w^3 \, dy \, [V_1'(\infty) + V_1'(-\infty)] \, . \tag{4.78}$$

Finally, since $\frac{\int_{-\infty}^{\infty} w^3 \, dy}{\int_{-\infty}^{\infty} (w')^2 \, dy} = 6$, we can apply the limiting conditions for V_1 in (4.76b) to reduce (4.78) to

$$\dot{x}_1 = \dot{\alpha} = \frac{1}{v_{cqe}} \left[v_{qex}(x_1^+) + v_{qex}(x_1^-) \right] \, . \tag{4.79}$$

To calculate the right-hand side of (4.79), we use (4.73b) and (4.22). We summarize the result as follows:

Principal Result 4.3.2: *Consider the quasi-equilibrium solution* (4.73) *of* (4.4) *with pulses centered at* $x_1 = -x_0 = \alpha$ *for* $0 < \alpha < 1$. *Then, for* $\epsilon \to 0$, *the pulses drift with speed* $\mathcal{O}(\epsilon^2)$ *according to the ODE*

$$\frac{d\alpha}{dt} \sim \epsilon^2 \mathcal{H}(\alpha) \, ; \qquad \mathcal{H}(\alpha) \equiv \frac{1}{v_{cqe}} \left[1 + \frac{E}{D} - \frac{2\alpha E}{D} \right] \, , \tag{4.80}$$

where v_{cqe} *is defined in* (4.72). *The equilibrium locations of the pulses are at* $\pm\alpha_e$ *where* $\mathcal{H}(\alpha_e) = 0$, *which yields*

$$\alpha_e = \frac{1}{2} + \frac{D}{2E} \, . \tag{4.81}$$

Due to the imposed boundary flux, these equilibrium locations are not at the symmetry locations $\pm 1/2$ *of the no boundary flux system studied previously in* §*4.2. From (4.81), we observe that for the equilibrium locations to be inside the domain, we must have that* $D/E < 1$*. Since* $\mathcal{H}'(\alpha_e) < 0$*, the equilibrium points of the ODE are always stable. Note that* (4.80) *predicts an exponential approach to the equilibrium. In [**78**], it was shown that the approach under the influence of subdiffusion is algebraic in time.*

We limit our study to the parameter range where the inequality $D/E < 1$ is satisfied. We note that the equilibrium is stable under the dynamics (4.80), which was derived under the assumption that $x_0 = -x_1$. That is, the equilibrium (4.81) is stable only to perturbations that preserve this symmetry. For the equilibrium to be stable to any perturbation, including to those that break the symmetry, the parameters D, E and f must satisfy the condition (cf. [**97**])

$$\frac{1-f}{Ef^2} < \frac{1}{24}\frac{E}{D}\left[1+\frac{D}{E}\right]^3 . \tag{4.82}$$

The criterion (4.82), as derived in [**97**], is the condition that must be satisfied for a two-pulse symmetric equilibrium solution to be stable to eigenvalues of $\mathcal{O}(\epsilon^2)$. The stability with respect to the large eigenvalues with $\lambda = \mathcal{O}(1)$ as $\epsilon \to 0$ is considered below.

4.3.2. Derivation of the NLEP

In this subsection, we derive the NLEP governing the stability of quasi-equilibrium solutions on an $\mathcal{O}(1)$ timescale. Since this NLEP has the same form as in (4.47), differing only in the coefficient of the nonlocal term, we focus mainly on the derivation of the new coefficient. In §4.3.3, we calculate a value α_c such that the quasi-equilibrium solution is unstable to a competition instability when $\alpha < \alpha_c$. Thus, a competition instability is dynamically triggered if the

condition $\alpha_e < \alpha_c < \alpha(0) < 1$ holds. For then, $\alpha(t)$ will dip below α_c on its approach to its equilibrium state α_e. In §4.3.4, we calculate the Hopf bifurcation thresholds as a function of α, analogous to those calculated in §4.2.4, and we find that dynamically triggered oscillatory instabilities can also occur.

We linearize about the quasi-equilibrium solution by writing $u = u_{qe} + e^{\lambda t}\Phi$ and $v = v_{qe} + e^{\lambda t}\Psi$. Substituting this into (4.4), we then follow the same procedure as used in (4.26)–(4.47). Aside from replacing $\beta_0 = 6(f^2 v_c^2 D)^{-1}$ by $\beta = 6(f^2 v_{cqe}^2 D)^{-1}$ in (4.39), the only difference lies in the matrix $\mathcal{G}^{(\mu)}$ due to the pulses not being located at $x = \pm 1/2$. That is, instead of the matrix $\mathcal{G}^{(\mu)}$, we now have the matrix

$$\mathcal{G}_\alpha^{(\mu)} \equiv \begin{pmatrix} G^{(\mu)}(-\alpha,-\alpha) & G^{(\mu)}(-\alpha,\alpha) \\ G^{(\mu)}(\alpha,-\alpha) & G^{(\mu)}(\alpha,\alpha) \end{pmatrix}, \tag{4.83}$$

where $G^{(\mu)}$ satisfies (4.32). Notice that since $x_1 = -x_0$, then $\mathcal{G}_\alpha^{(\mu)}$ is a symmetric matrix with constant row sum. Thus, the eigenvectors are in the directions $(1,1)^t$ and $(1,-1)^t$. To calculate the eigenvalues of $\mathcal{G}_\alpha^{(\mu)}$, we proceed as in [**94**] and write $\mathcal{G}_\alpha^{(\mu)} = \mathcal{B}_\alpha^{-1}/\mu$, where $\mathcal{B}_\alpha$ is given in Section 2 of [**94**] as

$$\mathcal{B}_\alpha \equiv \begin{pmatrix} d_\alpha & f_\alpha \\ f_\alpha & d_\alpha \end{pmatrix}; \qquad d_\alpha \equiv \coth(2\mu\alpha) + \tanh\left[\mu(1-\alpha)\right], \tag{4.84}$$

$$f_\alpha \equiv -\operatorname{csch}(2\mu\alpha).$$

Here μ is defined in (4.30). The eigenvalues $\sigma_0^{(\alpha)}$ and $\sigma_1^{(\alpha)}$ of $\mathcal{B}_\alpha$ and the corresponding eigenvectors $\boldsymbol{v}_0$ and $\boldsymbol{v}_1$ are

$$\begin{aligned} \sigma_0^{(\alpha)} &= \tanh(\mu\alpha) + \tanh\left[\mu(1-\alpha)\right]\,; \qquad \boldsymbol{v}_0^t = (1,1), \\ \sigma_1^{(\alpha)} &= \coth(\mu\alpha) + \tanh\left[\mu(1-\alpha)\right]\,; \qquad \boldsymbol{v}_1^t = (1,-1)\,. \end{aligned} \tag{4.85}$$

The eigenvalues κ_j of the matrix $\mathcal{G}_\alpha^{(\mu)}$ are then given by $\kappa_j = 1/(\mu\sigma_j^{(\alpha)})$, for $j = 0, 1$. In terms of $\sigma_j^{(\alpha)}$, we obtain the following NLEP:

Principal Result 4.3.3: *Let $\epsilon \to 0$ and consider the two-pulse symmetric quasi-equilibrium solution as given in* (4.73)*. The stability of this quasi-equilibrium solution to $\mathcal{O}(1)$ timescale instabilities is determined by the spectrum of the NLEP in* (4.47)*, where χ_j is replaced by $\chi_j^{(\alpha)}$, defined as*

$$\begin{gathered} \chi_j^{(\alpha)} = \frac{2}{1+\mu\sigma_j^{(\alpha)}/\beta}\left[1 + \frac{f\mu\sigma_j^{(\alpha)}}{f\beta - (1+\lambda)\left(\beta + \mu\sigma_j^{(\alpha)}\right)}\right], \qquad j = 0, 1\,; \\ \beta \equiv \frac{(D+E)^2 f^2}{6D\,(1-f)^2}\,. \end{gathered} \tag{4.86}$$

The discrete eigenvalues of (4.47a) *are the roots of the transcendental equations $g_j^{(\alpha)}(\lambda) = 0$, where*

$$g_j^{(\alpha)}(\lambda) \equiv C_j^{(\alpha)}(\lambda) - F(\lambda)\,, \qquad C_j^{(\alpha)}(\lambda) \equiv \frac{1}{\chi_j^{(\alpha)}(\lambda)}\,. \tag{4.87}$$

Here $F(\lambda)$ is defined in (4.48)*, and $C_j^{(\alpha)}(\lambda)$ is given by*

$$C_j^{(\alpha)}(\lambda) = \frac{1}{2}\left[1 + \xi_j + \frac{f\xi_j}{1+\lambda-f}\right], \qquad \xi_j \equiv \frac{\mu\sigma_j^{(\alpha)}}{\beta}\,. \tag{4.88}$$

4.3.3. Dynamically Triggered Competition Instabilities

Next, we look for roots to (4.87) on the positive real axis. The analysis here is similar to that in §4.2.3. We first consider the case where $\tau = 0$. To find real positive roots of $g_j^{(\alpha)}(\lambda)$ as $\tau \to 0$, we let $\mu \to 0$ in (4.85) to obtain that $\xi_0 \to 0$ and $\xi_1 \to (\alpha\beta)^{-1}$ as $\tau \to 0$. Then, from (4.87) and (4.88), we have that $C_0^{(\alpha)} = 1/2 < 1$, so that the synchronous mode $(1,1)^t$ mode is always stable when $\tau = 0$. Here we have used the properties (4.49) for $F(\lambda)$. Alternatively, when $\tau = 0$, we have from (4.88) that

$$C_1^{(\alpha)}(\lambda) = \frac{1}{2}\left[1 + \xi_1 + \frac{f\xi_1}{1+\lambda-f}\right], \qquad \xi_1 \equiv 1/(\alpha\beta)\,. \tag{4.89}$$

Since $C_1^{(\alpha)}(\lambda)$ is a positive decreasing function of λ while $F(\lambda)$ has the properties in (4.49), then $g_1^{(\alpha)}$ has a unique positive real root if $C_1^{(\alpha)}(0) > 1$ and no roots if $C_1^{(\alpha)}(0) < 1$. A winding number argument similar to that used in §4.2.3 can be used to show that no other roots exist in the right-half plane. This leads to the following stability criteria:

Principal Result 4.3.4: *For $\tau = 0$, consider the quasi-equilibrium solution* (4.73) *to* (4.4) *with pulses centered at $x = \pm\alpha$ for $0 < \alpha < 1$. The solution is stable on an $\mathcal{O}(1)$ timescale if and only if*

$$\alpha > \alpha_c\,; \qquad \alpha_c \equiv \frac{6D(1-f)}{(D+E)^2 f^2}\,. \tag{4.90}$$

If the inequality in (4.90) *is reversed, the quasi-equilibrium profile is unstable to one real positive eigenvalue corresponding to the $(1,-1)^t$ mode, which conserves the sum of the amplitudes of the pulses. Note that if $D \ll 1$ but $D \gg \mathcal{O}(\epsilon^2)$, we have that $\alpha_c \sim 6D(1-f)/(E^2 f^2) \ll 1$ so that the region of stability spans almost the entire range $0 < \alpha < 1$. Also, from* (4.90)*, we see that $\alpha_c \sim \mathcal{O}(D^{-1})$ as $D \to \infty$.*

As discussed earlier, a two-pulse quasi-equilibrium solution can undergo a dynamic competition instability whenever $\alpha_e < \alpha_c < 1$. By using the expression for α_e in (4.81), we have the following result:

Principal Result 4.3.5: *The quasi-equilibrium solution in* (4.73) *with a rightmost initial pulse location* $\alpha(0)$ *satisfying* $\alpha(0) > \alpha_c$ *will undergo a dynamic competition instability at some time* $t > 0$ *when* $\alpha_e < \alpha_c < 1$. *These inequalities hold when*

$$\frac{1}{12}\frac{E}{D}\left[1+\frac{D}{E}\right]^3 < \frac{1-f}{Ef^2} < \frac{1}{6}\frac{E}{D}\left[1+\frac{D}{E}\right]^2 . \tag{4.91}$$

The region described by (4.91) is plotted in Figure 4.16. Above the dotted curve a competition instability occurs starting at $t = 0$ for any $\alpha(0)$, while below the solid curve the two-pulse quasi-equilibrium solution is stable to the large eigenvalues and there is no competition instability for any $\alpha(0)$ with $\alpha(0) > \alpha_e$.

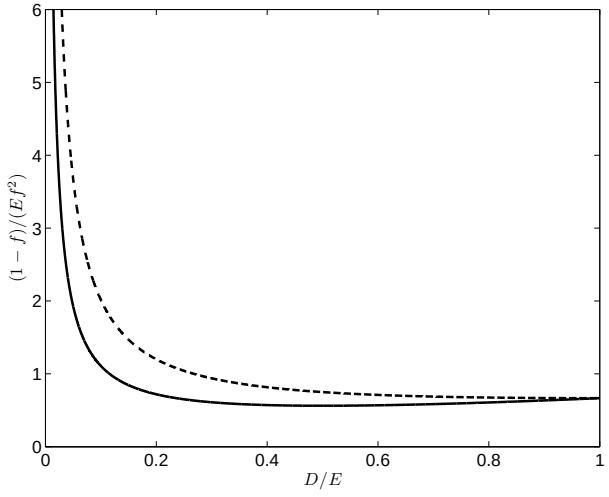

Figure 4.16. The region between the two curves is the parameter space in which a dynamic competition instability is possible for a two-pulse pattern with initial state $\alpha(0)$ with $\alpha_e < \alpha(0) < 1$. The horizontal axis is on the range $0 < D/E < 1$ for which a two-pulse equilibrium solution exists.

By comparing the lower bound of (4.91) with (4.82), we conclude that for $\tau = 0$ the two-pulse equilibrium solution is stable if and only if it is stable to the small eigenvalues in the limit $\tau \to 0$. The result is written as:

Principal Result 4.3.6: *The equilibrium solution in* (4.73) *with* $\alpha = \alpha_e$ *is stable with respect to the large eigenvalues but unstable with respect to the small eigenvalues when*

$$\frac{1}{24}\frac{E}{D}\left[1+\frac{D}{E}\right]^3 < \frac{1-f}{Ef^2} < \frac{1}{12}\frac{E}{D}\left[1+\frac{D}{E}\right]^3 . \tag{4.92}$$

It is stable with respect to the small eigenvalues when (4.82) *holds.*

For the case $\tau > 0$, it is difficult, owing to the non-monotonicity of the curves $C_j^{(\alpha)}(\lambda)$, to obtain explicit results that count the number of positive real eigenvalues in the right half-plane. However, the following (less precise) results are readily proved.

Principal Result 4.3.7: *Suppose that* $\tau \geq 0$ *and that* $0 < \alpha < \alpha_c$. *Then, the NLEP in Principal Result 3.3 admits at least one real positive eigenvalue. Hence, the quasi-equilibrium pattern in unstable. Alternatively, suppose that* $\alpha_c < \alpha < 1$. *Then, for* $\tau > 0$ *sufficiently large, the NLEP in Principal Result 3.3 admits four real positive eigenvalues.*

To prove the first statement, we note that $C_1^{(\alpha)}(0) > 1$ when $\alpha < \alpha_c$. Therefore, the curves $C_1^{(\alpha)}(\lambda)$ and $F(\lambda)$ must have at least one intersection in $\lambda > 0$ when $\tau \geq 0$. To prove the second statement we notice that $C_j^{(\alpha)}(0) < 1$ when $\alpha > \alpha_c$ for $j = 0, 1$ and that $C_j^{(\alpha)}(\lambda) = \mathcal{O}\left(\sqrt{\tau\lambda}\right)$ for $\lambda > 0$ when $\tau \gg 1$. It follows from the concavity of $C_j^{(\alpha)}(\lambda)$ in the large τ limit and the convexity of $F(\lambda)$ (see properties (4.49)) that for both $j = 0$ and $j = 1$, there are two intersection points of $C_j^{(\alpha)}(\lambda) = F(\lambda)$ on $0 < \lambda < 5/4$.

4.3.4. Dynamically Triggered Oscillatory Instabilities

For the parameter range $\alpha_c < \alpha < 1$, we calculate the threshold τ_0 for which the NLEP has a complex conjugate pair of eigenvalues on the imaginary axis. More specifically, we calculate the values $\tau = \tau_{0j}(\alpha)$ such that $g_j^{(\alpha)} = 0$ has a pair of complex conjugate solutions $\lambda = \pm i\lambda_{Ij}^0(\alpha)$ on the imaginary axis. The quantity

$$\tau_0(\alpha) = \min(\tau_{00}, \tau_{01})\,, \tag{4.93}$$

is then defined to be the Hopf instability threshold. As in §4.2.4, either the $j = 0$ mode, which corresponds to synchronous oscillations, or the $j = 1$ mode, which corresponds to asynchronous oscillations, can be the dominant instability, depending on the value of α. In contrast, for the GM and GS models studied in [**94**] the synchronous mode was always the dominant instability. Using the numerical procedure used to produce the Hopf bifurcation curves of §4.2.4, we solve $g_j^{(\alpha)}(i\lambda_I) = 0$ to obtain curves $\tau_{0j}(\alpha)$ and $\lambda_{Ij}^0(\alpha)$.

Treating α as the independent variable, we fix D and E and generate Hopf curves for values of f in the interval $f_c < f \leq 0.9$, where $\alpha_c = 1$ when $f = f_c$. In Figure 4.16, this corresponds to a vertical traversal from the dotted curve down toward the D/E-axis. Results are presented on a semi-log plot for three ratios of D/E. In Figures 4.17(a) - 4.17(c), we take $E = 1$ and $D = 0.2, 0.4$ and 0.6. Similar plots were made (not shown) for the same ratios of D/E but with $D = 1$ and $E = 5, 2.5, 1.67$, yielding qualitatively similar plots. For values of α where the curves are solid, the synchronous mode is the dominant instability ($\tau_0 \equiv \tau_{00}$), whereas for the portions of the curves where they are dashed, the asynchronous mode is dominant ($\tau_0 \equiv \tau_{01}$). The curves are ordered such that for a given α, $\tau_0(\alpha)$ increases with increasing f. We end the

plot for $\alpha < \alpha_c$, that is, values of α for which the τ_{01} curve does not exist; the corresponding complex conjugate imaginary eigenvalues approach the origin as $\alpha \to \alpha_c^+$ the same way that $\lambda_{I1}^0 \to 0$ as $D \to D_{c2}^-$ as discussed in §4.2.4. The equilibrium location α_e is denoted by a dot; in the absence of a dot, the condition $\alpha_e < \alpha_c$ is satisfied and a dynamic competition instability is possible. In Figure 4.17(a), τ_{00} and τ_{01} are almost equal for α sufficiently near unity, and the breaks in the curves appear to be due to differences in decimal places beyond the precision of the solver.

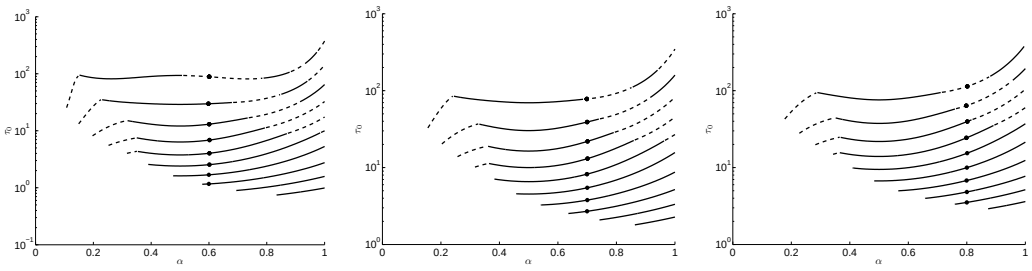

(a) $D = 0.2$, $E = 1$ (b) $D = 0.4$, $E = 1$ (c) $D = 0.6$, $E = 1$

Figure 4.17. Plot of τ_0 versus α for various f with $E = 1$ and $D = 0.2$ (left), $D = 0.4$ (center) and $D = 0.6$ (right). The extent of the curves in α increases in f, as does the value of τ_0 for any given α. For α where the curves are solid (dashed), the dominant instability is the synchronous (asynchronous) mode. The dot denotes the equilibrium location α_e; for curves without a dot, a dynamic competition instability is possible. The values of f are as follows: left figure: $f = 0.6181$, 0.6494, 0.6808, 0.7121, 0.7434, 0.7747, 0.8060, 0.8374, 0.8687, 0.9000; center figure: $f = 0.6772$, 0.7019, 0.7267, 0.7514, 0.7762, 0.8010, 0.8257, 0.8505, 0.8752, 0.9000; right figure: $f = 0.6980$, 0.7204, 0.7429, 0.7653, 0.7878, 0.8102, 0.8327, 0.8551, 0.8776, 0.9000.

For a given α, the quasi-equilibrium is stable (unstable) when τ is below (above) the curve. Thus, because the pulse motion from (4.80) is directed monotonically towards the equilibrium location, dynamic oscillatory instabilities are only possible when either the slope of τ_0 is negative when $\alpha < \alpha_e$ or positive when $\alpha > \alpha_e$. From Figures 4.17(a) - 4.17(c), we see that for f near f_c, the only possibility for a dynamic oscillatory instability is when the initial pulse

locations satisfy $\alpha(0) > \alpha_e$ and τ satisfies $\tau_0(\alpha_e) < \tau < \tau_0(\alpha(0))$ (or $\tau_0(\alpha_c) < \tau < \tau_0(\alpha(0))$ if $\alpha_e < \alpha_c$), leading to the triggering of synchronous pulse oscillations at some $t > 0$ as $\alpha \to \alpha_e^+$. For larger f, a similar scenario is possible for asynchronous oscillations. For still larger f, synchronous oscillations may be triggered when the initial pulse location satisfies $\alpha(0) < \alpha_e$. This may occur after passage through a region of instability to asynchronous oscillations. In the next section, we illustrate these scenarios by numerically solving the full PDE system (4.4).

4.3.5. Numerical Validation

We now illustrate five different scenarios involving pulse dynamics with parameters used to generate curves in Figure 4.17(a). For clarity, we reproduce the curves in Figure 4.18 on which we qualitatively annotate the dynamics of $\alpha(t)$ for each run. Below, we present the results of each run by plotting the pulse amplitudes u_m and pulse locations x_j versus time, produced by solving (4.4) with 4000 grid points using `MATLAB`'s `pdepe()` solver. In all runs, we took $\epsilon = 0.005$, $D = 0.2$ and $E = 1$, with f and τ being varied between the runs. The initial conditions are treated in the same way as described in §4.2.5, where the quasi-equilibrium solution in (4.73) is taken as the initial conditions, and a small value of τ is used to solve forward in time until a true quasi-equilibrium solution is reached. While the time required for the initiation process is small compared to ϵ^{-2}, the pulses still drift during this time. As such, appropriate compensations were made in the initial conditions so that the pulse locations were in their desired locations at the end of the initiation. All values for the initial pulse locations $\alpha(0)$ quoted below refer to their locations at the end of the initiation.

In Run 1, we take $\alpha(0) = 0.85$, $f = 0.6494$, and $\tau = 1.05 < \tau_0(\alpha(0))$ so that the quasi-equilibrium is initially stable at $t = 0$. However, as indicated in Figure 4.18, our theory predicts

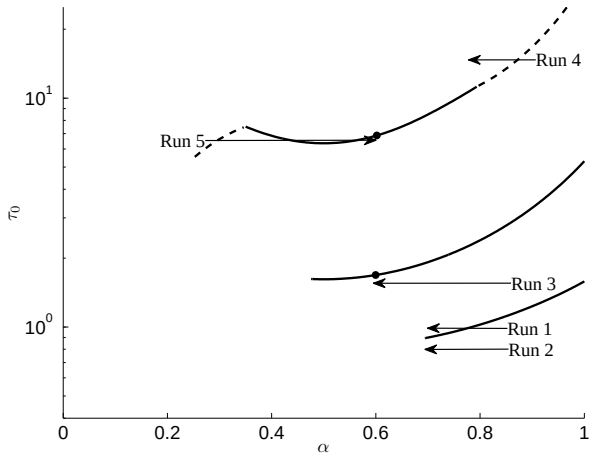

Figure 4.18. Hopf stability curves for (bottom to top) $f = 0.6494$, 0.7121, and 0.806. The arrows indicate the evolution of $\alpha(t)$, while the height of the arrows is only indicative of the value of τ used in the runs. Runs 1 and 2 are associated with the lowest curve, Run 3 with the middle curve, and Runs 4 and 5 with the top curve. Solid curves indicate that $\tau_0 \equiv \tau_{00}$ (synchronous mode) while dashed curves indicate that $\tau_0 \equiv \tau_{01}$ (asynchronous mode). The curves are cut off on the left at $\alpha = \alpha_c$. The equilibrium point $\alpha_e = 0.6$ is indicated by a dot when the condition $\alpha_e > \alpha_c$ is satisfied.

that a dynamic synchronous oscillatory instability is triggered at some $t > 0$ when α decreases below the synchronous stability threshold indicated by the solid curve in this figure. That is, for some time $t > 0$, the condition $\tau > \tau_0(\alpha(t))$ is satisfied, at which time the solution becomes unstable to synchronous oscillations. In Figure 4.19(a) we show the amplitudes of the two pulses, which are indistinguishable, after the onset of the synchronous Hopf instability. The pulses annihilate before α reaches α_c, implying that the annihilation was not due to a competition instability. In Figure 4.19(b), we show a favorable comparison between the slow time evolution of the location of the pulses and the dynamics in (4.80) before the time of annihilation.

With the initial conditions and the other parameters unchanged, for Run 2 we decrease τ to $\tau = 0.8$ so that the Hopf stability threshold is not crossed at any point in the dynamics. However, because $\alpha_e < \alpha_c$, a competition instability occurs as $\alpha(t)$ decreases below α_c. This scenario is

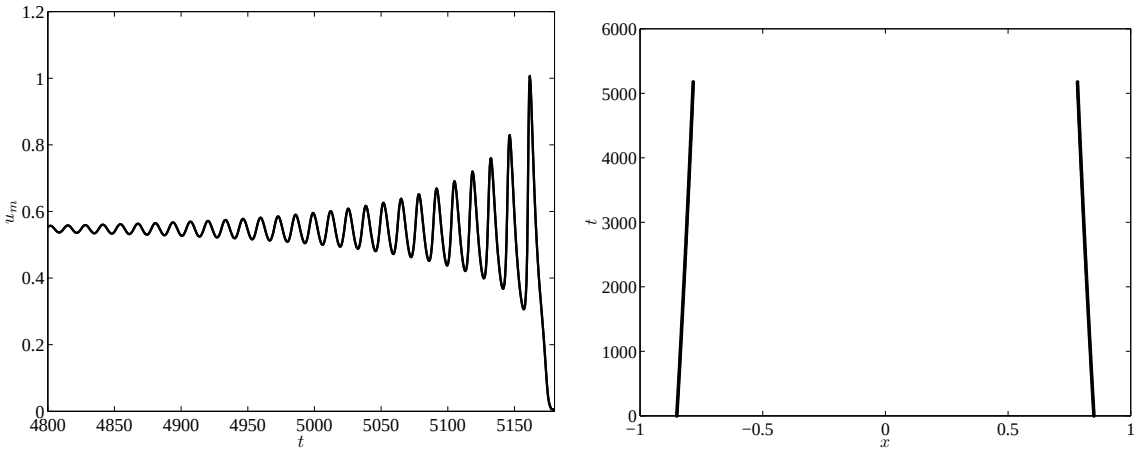

(a) u_m versus t (b) x_j versus t

Figure 4.19. Run 1: Dynamic synchronous oscillatory instability for $\epsilon = 0.005$, $D = 0.2$, $E = 1$, $f = 0.6494$, $\tau = 1.05$, and $\alpha(0) = 0.85$. In the left figure, synchronous oscillations of the pulse amplitudes grow in time at the onset of instability and annihilate at some later time. In the right figure, we show a comparison between the evolution of the pulse locations and the dynamics (4.80). They are indistinguishable in this plot.

illustrated in Figure 4.18. In Figure 4.20(a), we show the annihilation of one of the pulses after the threshold $\alpha(t) < \alpha_c$ is crossed. In Figure 4.20(b), we show a favorable comparison between the numerical pulse dynamics and that predicted by (4.80) up to the time of the annihilation of the right pulse. After the annihilation, the remaining pulse evolves according to the one-pulse dynamical result of [**97**].

In Run 3, we keep τ unchanged but increase f to $f = 0.7121$ so that $\alpha_c < \alpha_e$ and τ remains below $\tau_0(\alpha)$ for all values of α in the interval $(\alpha_e, \alpha(0))$. Thus, no dynamic instabilities occur, and the pulses evolve monotonically to their equilibrium locations at $\alpha_e = 0.6$. The motion of the pulses, along with the dynamics (4.80), are shown in Figure 4.20(c).

In Run 4, we take $\alpha(0) = 0.91$, $f = 0.806$, and $\tau = 15 < \tau_0(\alpha(0))$. This run is similar to Run 1 except that a dynamic asynchronous instability is triggered instead of a synchronous instability. This scenario is shown in Figure 4.18; for some $t > 0$, $\alpha(t)$ will satisfy $\tau > \tau_0(\alpha(t))$,

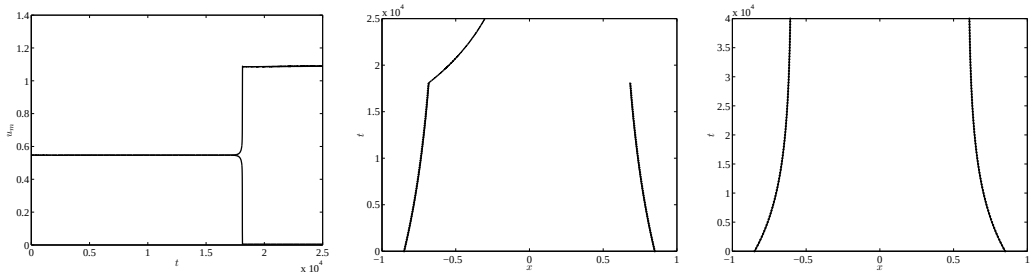

(a) u_m versus t, $\alpha_e < \alpha_c$ (b) x_j versus t, $\alpha_e < \alpha_c$ (c) x_j versus t, $\alpha_e > \alpha_c$

Figure 4.20. Runs 2 and 3: The left and center figures (Run 2) are plots of the pulse amplitudes and locations versus time in the case of a dynamic competition instability for $\epsilon = 0.005$, $D = 0.2$, $E = 1$, $f = 0.6494$, $\tau = 0.8$, and $\alpha(0) = 0.85$. In the right figure (Run 3), f is increased to $f = 0.7172$ so that no instabilities are triggered and the pulses approach the equilibrium location $\alpha_e = 0.6$.

initiating an asynchronous instability. For this run, we perturbed the initial condition as in (4.69), where $d_0 = 1$ and $d_1 = -1$ in accordance with the eigenvector associated with the asynchronous mode. While the perturbation initially decayed and appeared to be unnoticeable by the time the pulses approached the asynchronous instability threshold, enough of the initial perturbation remained to trigger the asynchronous instability. Without the initial perturbation, a synchronous instability developed due to the nearby synchronous instability threshold (not shown in Figure 4.18).

In Run 5, we keep the parameters as in Run 4, except we set $\alpha(0) = 0.28$ and $\tau = 6.6$ so that $\tau > \tau_0(\alpha(0)) = \tau_{01}$. Thus, the solution starts above the asynchronous stability threshold but gains stability as $\alpha(t)$ increases towards α_e. However, before reaching α_e, a loss of stability to synchronous oscillations occurs before stability is regained after $\alpha(t)$ drifts across the zone of synchronous instability. The evolution through the zones of stability and instability is depicted in Figure 4.18. In Figures 4.22(a) and 4.22(b), we show the pulse amplitudes and locations versus time for the entire duration of the dynamics. Note that the pulses evolve according to

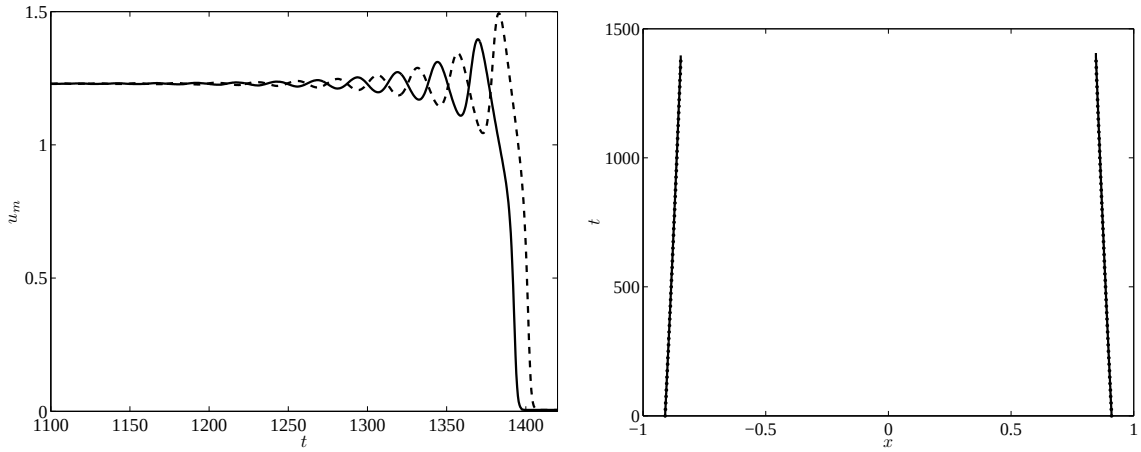

(a) u_m versus t (b) x_j versus t

Figure 4.21. Run 4: Dynamic asynchronous oscillatory instability for $\epsilon = 0.005$, $D = 0.2$, $E = 1$, $f = 0.806$, $\tau = 15$, and $\alpha(0) = 0.91$. In the left figure, asynchronous oscillations of the left (solid) and right (dashed) pulse amplitudes grow in time at the onset of instability and annihilate at some later time. In the right figure, we show a comparison between the evolution of the pulse locations and the dynamics (4.80) up to the time of annihilation.

(4.80) even when $\alpha(t)$ is in an unstable region. Figure 4.22(a) shows the triggering of two distinct types of instabilities, each of which are eventually extinguished as time increases. The first of these instabilities, as previously mentioned, is to the asynchronous mode and is magnified in Figure 4.22(c). The initial conditions were perturbed in the same way as in Run 4. After an initial growth in the amplitude of asynchronous oscillations, the pulse amplitudes approach their quasi-equilibrium value as they move into the zone of stability. At a later time, shown in Figure 4.22(d), the pulses move into a zone of synchronous instability where the amplitude of synchronous oscillations grow. These oscillations decay as the pulses move out of the unstable region and towards their equilibrium locations. Note that frequency of synchronous oscillations is approximately four times that of the asynchronous oscillations, which is consistent with our calculations (not shown). In other experiments, it was observed that starting too far above the

asynchronous stability curve led to an annihilation of one of the pulses. Further, the movement of the pulses through a zone of instability without annihilating may be facilitated by ϵ sufficiently large; for small ϵ where the times spent in unstable regions are significantly longer, annihilation events may occur.

Finally, we note that all of these experiments involve only $\mathcal{O}(1)$ instabilites. For numerical computations involving instabilities to $\mathcal{O}(\epsilon^2)$ eigenvalues, see [**97**].

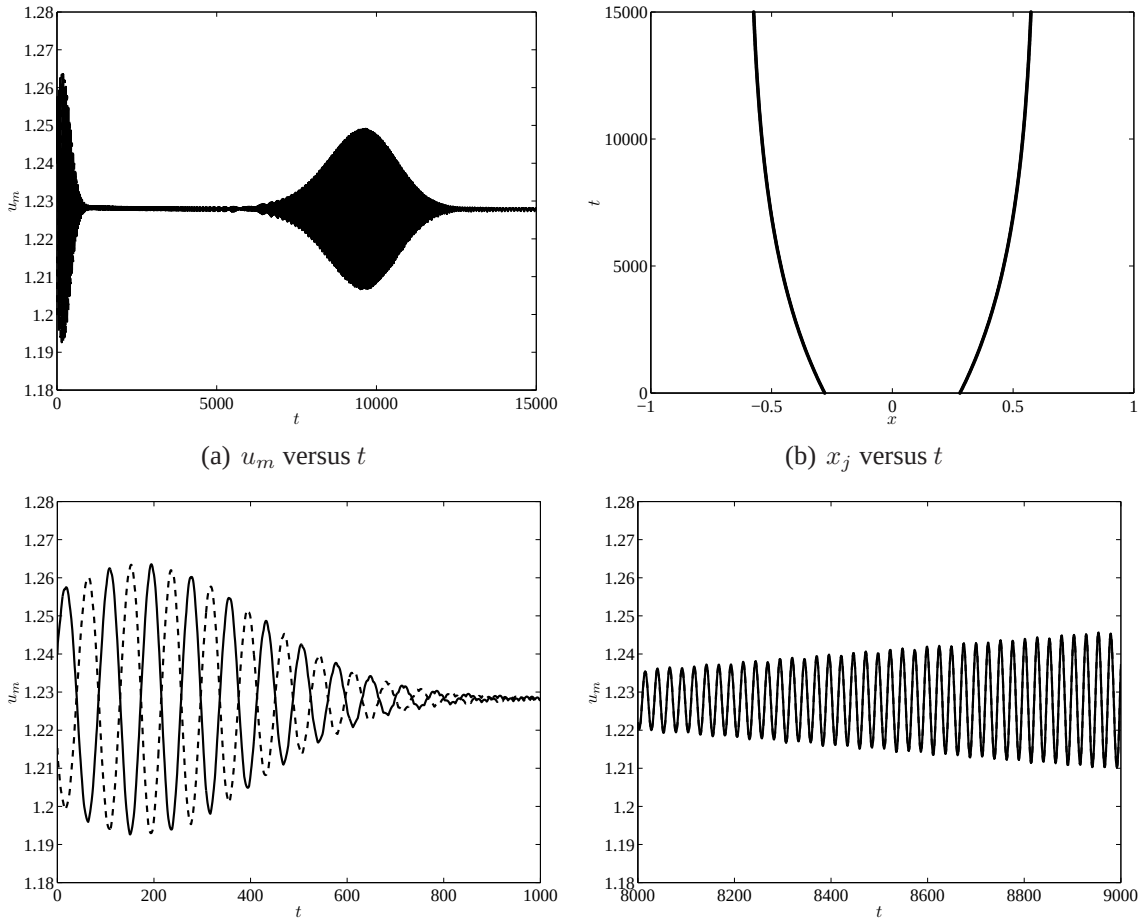

(a) u_m versus t

(b) x_j versus t

(c) u_m versus t, first instability: asynchronous

(d) u_m versus t, second instability: synchronous

Figure 4.22. Run 5: Synchronous and asynchronous instabilities for $\epsilon = 0.005$, $D = 0.2$, $E = 1$, $f = 0.806$, $\tau = 6.6$, and $\alpha(0) = 0.28$. The top left figure shows the pulse amplitudes as the pulses move through zones of stability and instability and eventually to their equilibrium locations (top right). The first instability is to the asynchronous mode (bottom left) and the second instability is to the synchronous mode (bottom right). In the bottom left figure, the solid (dashed) curve is the amplitude of the left (right) pulse. In the bottom right figure, the pulse amplitudes are indistinguishable.

4.4. Discussion

We have analyzed the stability of localized pulse patterns for two closely related singularly perturbed RD systems with Brusselator kinetics. The derivation of the NLEP for the Brusselator

is more intricate than in previous stability analyses of pulse patterns for the GM and GS models [**58**, **102**, **106**], owing to the non-trivial background state for the activator and the existence of two nonlocal terms arising from the $\mathcal{O}(\epsilon^{-1})$ coefficient in (4.2b) and (4.4b). A combination of rigorous and numerical analysis was used to obtain stability thresholds from this NLEP, and the results have been confirmed with full numerical simulations of the PDE systems. For (4.4), an NLEP stability theory is applied to a quasi-steady two-pulse evolution, and our results show the existence of dynamically triggered instabilities depending on the parameter regime.

For both Brusselator models (4.4) and (4.2), our NLEP stability results show that as τ increases above a threshold, a Hopf bifurcation triggers either a synchronous or an asynchronous oscillation in the pulse amplitudes. The nature of the oscillation depends on the parameter values of f and D, and for (4.4), also on the inter-pulse distance. Our full numerical simulations of the PDE systems confirm the two modes of oscillation. Furthermore, our numerical results suggest that the synchronous instability, which leads to the annihilation of pulses, is subcritical, while the asynchronous instability is supercritical. The existence of robust asynchronous pulse amplitude oscillations observed in our analysis of the Brusselator model has not been reported in NLEP stability studies of other RD (cf. [**58**, **106**]).

A key open problem, suggested by our results, is to perform a weakly nonlinear theory on the Brusselator model, and on related RD systems with pulse solutions, to analyze whether pulse amplitude oscillations are sub- or super-critical.

Another interesting open problem is to try to extend the pulse-splitting analysis of [**30**, **59**, **72**] to analyze a similar pulse-splitting phenomena for the Brusselator model (4.2) that occurs in the regime whe f approaches unity. Starting from a one-pulse quasi-equilibrium state, in Fig. 4.23 we show numerical results computed from (4.2) for the paramater set $\epsilon = 0.01$, $A = 0$,

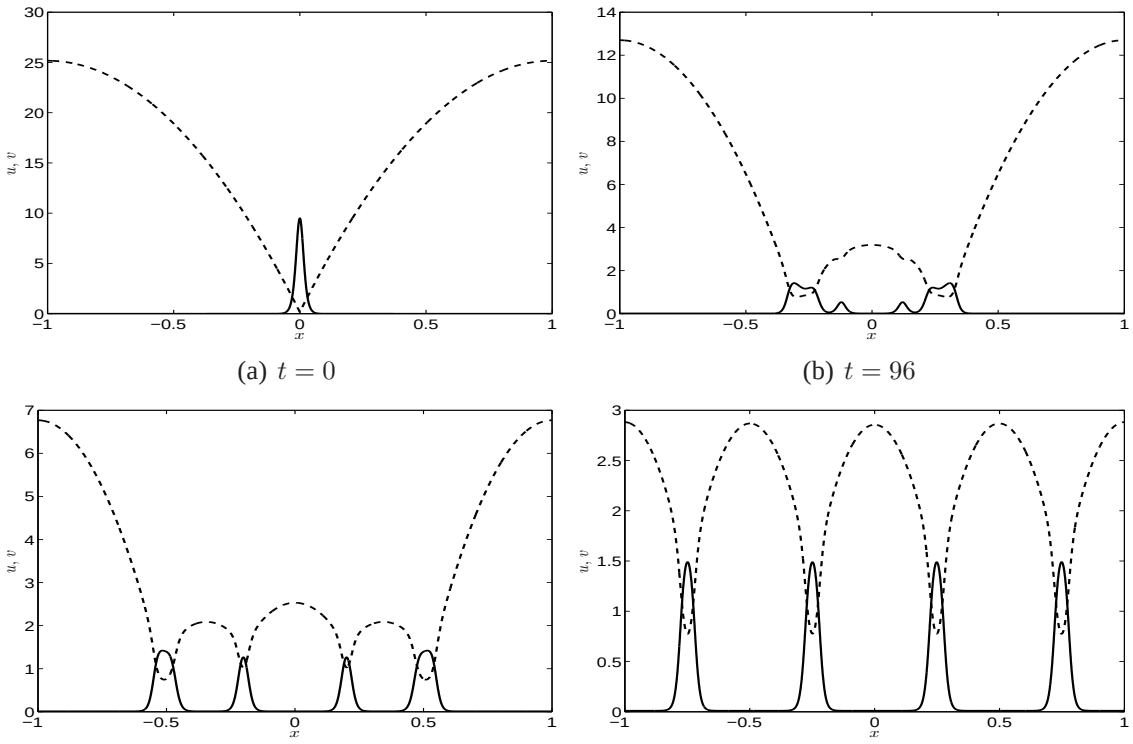

Figure 4.23. Self-replication of a pulse for (4.2) with $\epsilon = 0.01$, $A = 0$, $D = 0.02$, $f = 0.95$, and $\tau = 0.001$. The solid curve is u while the dotted curve is v.

$D = 0.02$, $f = 0.95$, and $\tau = 0.001$. Such a pulse-splitting behavior has not been reported previously for the Brusselator model.

One may also analyze (4.2) in a two dimensional spatial domain, where localized spot patterns undergo either self-replication, competition, or oscillatory, instabilities depending on the parameter regime. The determination of phase diagrams in parameter space for these instabilities is critical for characterizing dynamic bifurcations of localized spot patterns. Finally, it may be interesting to apply the techniques of Chapters 3 and 4 to the models of follicle formation in the skin developed in [**20**, **70**]. A reaction-diffusion system was used to model the epidermis, while a mechanochemical system was used to model the dermis. Small amplitude spatially

periodic solutions of one system was taken a source for the other through a simple coupling term. A large amplitude study may be possible with a singularly perturbed reaction-diffusion system in which a bulk feed of the inhibitor is supplied by the mechanochemical system. The spatially varying inhibitor feed may result in pinning of pulses in the reaction-diffusion system away from their usual equilibrium locations.

Bibliography

[1] P. Assemat, A. Bergeon, E. Knobloch, *Spatially Localized States in Marangoni Convection in Binary Mixtures*, Fluid Dynamics Research **40**, (2008), pp. 852–876.

[2] D. Avitabile, D. J. B. Lloyd, J. Burke, E. Knobloch, B. Sandstede, *To Snake or Not to Snake in the Planar SwiftHohenberg Equation*, SIAM J. Appl. Dyn. Syst., **9**(3), (2010), pp. 704–733.

[3] I. Barrass, E. J. Crampin, P. K. Maini, *Mode Transitions in a Model Reaction-Diffusion System Driven by Domain Growth and Noise*, Bull. Math. Biol., **68**, (2006), pp. 981–995.

[4] M. Beck, J. Knobloch, D. J. B. Lloyd, B. Sandstede, T. Wagenknecht, *Snakes, Ladders, and Isolas of Localised Patterns*, SIAM J. Math. Anal., **41**, (2009), 936–972.

[5] D. Bensimon, B.I. Shraiman, V. Croquette, *Nonadiabatic Effects in Convection*, Phys. Rev. **A38**, (1988), pp. 5461–5464.

[6] A. Bergeon, J. Burke, E. Knobloch, I. Mercader, *Eckhaus Instability and Homoclinic Snaking*, Phys. Rev. E **78**, 046201 (2008).

[7] U. Bortolozzo, M. G. Clerc, S. Residori, *Local Theory of the Slanted Snaking Bifurcation Diagram*, Phys. Rev. E, **78**, 036214 (2008).

[8] C .J. Budd, R. Kuske, *Localised Periodic Patterns for the Non-Symmetric Generalized Swift-Hohenberg Equation*, Physica D, **208**, (2005), pp. 73-95.

[9] J. Burke, *Ph.D. Thesis*, University of California, Berkeley, (2008).

[10] J. Burke, E. Knobloch, *Localized States in the Generalized Swift-Hohenberg Equation*, Phys. Rev. E **73**, 056211 (2006).

[11] J. Burke, E. Knobloch, *Snakes and ladders: Localized States in the SwiftHohenberg Equation*, Phys. Lett. A, **360**, (2007), pp. 681–688.

[12] J. Burke, E. Knobloch, *Homoclinic Snaking: Structure and stability*, Chaos, **17**, 037102 (2007).

[13] A. R. Champneys, E. Knobloch, Y.-P. Ma, T. Wagenknecht, *Homoclinic Snakes Bounded by a Saddle-Centre Periodic Orbit*, To appear in SIAM J. Appl. Dyn. Sys., (2012).

[14] S. J. Chapman, G. Kozyreff, *Exponential Asymptotics of Localised Patterns and Snaking Bifurcations Diagrams*, Physica D., **238**, (2009), pp. 319–354.

[15] W. Chen, M. J. Ward, *Oscillatory Instabilities and Dynamics of Multi-Spike Patterns for the One-Dimensional Gray-Scott Model*, Europ. J. Appl. Math **20**(2), (2009), pp. 187–214.

[16] W. Chen, M.J. Ward, *Localized Spot Patterns in the Two-dimensional Gray-Scott Model: Part I; Spot Dynamics and Self-Replication*, submitted, SIAM J. Appl. Dyn. Sys., October 2009.

[17] P. Coullet, C. Riera, C. Tresser, *Stable Static Localized Structures in One Dimension*, Phys. Rev. Lett., **84**(14), (2000), pp. 3069–3072.

[18] P. Coullet, C. Riera, C. Tresser, *Qualitative Theory of Stable Stationary Localized Structures in One Dimension*, Prog. Theor. Phys. **139**, (2000), pp. 46–58.

[19] E.J. Crampin, E.A. Gaffney, P.K. Maini, *Reaction and Diffusion on Growing Domains: Scenarios for Robust Pattern Formation*, Bull. Math. Biol., **61**, (1999), pp. 1093–1120.

[20] G. C. Cruywagen, J. D. Murray, *On a Tissue Interaction Model for Skin Pattern Formation*, J. Nonlinear. Sci. **2**, (1992), pp. 217–240.

[21] A. De Wit, *Spatial Patterns and Spatiotemporal Dynamics in Chemical Systems*, Adv. Chem. Phys., **109**, (1999), pp. 435–513.

[22] A. De Wit, D. Lima, G. Dewel, P. Borckmans, *Spatiotemporal Dynamics Near a Codimension-Two Point*, Phys. Rev. E **54**(1), (1996), pp. 261–271.

[23] A. D. Dean, P. C. Matthews, S. M. Cox, J. R. King, *Exponential Asymptotics of Homoclinic Snaking*, Nonlinearity, **24**, (2011), 3323.

[24] D. del-Castillo-Negrete, *Fractional Diffusion Models of Nonlocal Transport*, Phys. Plasmas, **13**, 082308 (2006).

[25] D. del-Castillo-Negrete, B. A. Carreras, V. E. Lynch, *Fractional Diffusion in Plasma Turbulence*, Phys. Plasmas, **11**(8), (2004), pp. 3854–3864.

[26] E. J. Doedel, A. R. Champneys, T. Fairgrieve, Y. Kuznetsov, B. Oldeman, R. Paffenroth, B. Sandstede, X. Wang, and C. Zhang. Auto07p: Continuation and Bifurcation Software for Ordinary Differential Equations. Technical report, Concordia University, 2007.

[27] A. Doelman, R. A. Gardner, T. J. Kaper, *Large Stable Pulse Solutions in Reaction-Diffusion Equations*, Indiana U. Math. J., **50**(1), (2001), pp. 443–507.

[28] A. Doelman, W. Eckhaus, T. J. Kaper, *Slowly-Modulated Two-Pulse Solutions in the Gray-Scott Model I: Asymptotic Construction and Stability*, SIAM J. Appl. Math., **61**(3), (2000), pp. 1080–1102.

[29] A. Doelman, W. Eckhaus, T. J. Kaper, *Slowly Modulated Two-Pulse Solutions in the Gray–Scott Model II: Geometric Theory, Bifurcations, and Splitting Dynamics*, SIAM J. Appl. Math., **66**(6), (2001), pp. 2036–2062.

[30] A. Doelman, R. A. Gardner, T. J. Kaper, *Stability Analysis of Singular Patterns in the 1D Gray-Scott Model: A Matched Asymptotic Approach*, Physica D, **122**, (1998), pp. 1–36.

[31] A. Doelman, T. Kaper, *Semistrong Pulse Interactions in a Class of Coupled Reaction-Diffusion Equations*, SIAM J. Appl. Dyn. Sys., **2**(1), (2003), pp. 53–96.

[32] A. Doelman, T. J. Kaper, K. Promislow, *Nonlinear Asymptotic Stability of the Semistrong Pulse Dynamics in a Regularized Gierer-Meinhardt Model*, SIAM J. Math. Anal., **38**(6), (2007), pp. 1760–1787.

[33] S. –I. Ei, M. Mimura, M. Nagayama, *Pulse–pulse Interaction in Reaction–diffusion systems*, Physica D, **165**, (2002), pp. 176–198.

[34] S. –I. Ei, Y. Nishiura, K. –I. Ueda, *2^n-Splitting or Edge-Splitting? - A Manner of Splitting in Dissipative Systems* -, Japan J. Indust. Appl. Math., **18**, (2001), pp. 181–205.

[35] S. Fedotov, *Non-Markovian Random Walks and Nonlinear Reactions: Subdiffusion and Propagating Fronts*, Phys. Rev. E, **81**, 011117 (2010).

[36] E. A. Gaffney, N. A. M. Monk, *Gene Expression Time Delays and Turing Pattern Formation Systems*, Bull. Math. Biol., **68**, (2006), pp. 99–130.

[37] A. Gierer, H. Meinhardt, *A Theory of Biological Pattern Formation*, Kybernetic, **12**, (1972), pp. 30–39.

[38] A. A. Golovin, B. J. Matkowsky, V. A. Volpert, *Turing Pattern Formation in the Brusselator Model with Superdiffusion*, SIAM J. Appl. Math., **69**(1), (2008), pp. 251–272.

[39] D. Gomila, A. Scroggie, W. Firth, *Bifurcation Structure of Dissipative Solitons*, Physica D **227**, (2007), pp. 70–77.

[40] Y. Hayase, *Collision and Self Replication of Pulses in a Reaction Diffusion System*, J. Phys. Soc. Jpn., **66**(9), (1997), pp. 2584–2587.

[41] B. I. Henry, T. A. M. Langlands, S. L. Wearne, *Anomalous Diffusion with Linear Reaction Dynamics: From Continuous Time Random Walks to Fraction Reaction-Diffusion Equations*, Phys. Rev. E, **74**, 031116 (2006).

[42] S. M. Houghton, E. Knobloch, *Homoclinic Snaking in Bounded Domain*, Phys. Rev. E **80** 026210 (2009).

[43] S. M. Houghton, E. Knobloch, *The Swift-Hohenberg Equation with Broken Cubic-Quintic Nonlinearity*, Phys. Rev. E, **84**, 016204 (2011).

[44] R. Hoyle, *Pattern Formation: An Introduction to Methods*, Cambridge University Press, Cambridge, (2006).

[45] D. Iron, M.J. Ward, *A Metastable Spike Solution for a Nonlocal Reaction-Diffusion Model*, SIAM J. Appl. Math., **60**(3), (2000), pp. 778–802.

[46] D. Iron, M. J. Ward, *The Dynamics of Multi-Spike Solutions for the One-Dimensional Gierer-Meinhardt Model*, SIAM J. Appl. Math., **62**(6), (2002), pp. 1924–1951.

[47] D. Iron, M. J. Ward, J. Wei, *The Stability of Spike Solutions to the One-Dimensional Gierer-Meinhardt Model*, Physica D, **150**(1-2), (2001), pp. 25–62.

[48] D. Iron, J. Wei, M. Winter, *Stability Analysis of Turing Patterns Generated by the Schnakenberg model*, J. Math. Biol., **49**(4), (2004), pp. 358–390.

[49] W. Just, M. Bose, S. Bose, H. Engel, E. Scöll, *Spatiotemporal Dynamics Near a Supercritical Turing-Hopf Bifurcation in a Two-Dimensional Reaction-Diffusion System*, Phys. Rev. E, **64**, 026219 (2001).

[50] H. –C. Kao, E. Knobloch, *Weakly Subcritical Stationary Patterns: Eckhaus Instability and Homoclinic Snaking*, Phys. Rev. E **85**, 026211 (2012).

[51] B.S. Kerner, V.V. Osipov, *Self-organization in Active Distributed Media: Scenarios for the Spontaneous Formation and Evolution of Dissipative Structures*, Sov. Phys.-Usp. **33**, (1990), pp. 679–719.

[52] B. S. Kerner, V. V. Osipov, *Autosolitions: A New Approach to Problem of Self-Organization and Turbulence*, Kluwer Academic Publishers, Dordrecht, (1994).

[53] H. Kidachi, *On Mode Interactions in Reaction Diffusion Equation with Nearly Degenerate Bifurcations*, Prog. Theor. Phys., **63**(4), (1980), pp. 1152–1169

[54] J. Klafter, A. Blumen, M. F. Shlesinger, *Stochastic Pathway to Anomalous Diffusion*, Phys. Rev. A, **35**(7), (1987), pp. 3081–3085.

[55] E. Knobloch, *Spatially Localized Structures in Dissipative Systems: Open Problems*, Nonlinearity, **21**, (2008), T45–T60.

[56] J. Knobloch, T. Wagenknecht, *Homoclinic Snaking Near a Heteroclinic Cycle in Reversible Systems*, Physica D, **206**, (2005), pp. 82–93.

[57] T. Kolokolnikov, T. Erneux, J. Wei, *Mesa-type Patterns in the One-dimensional Brusselator and Their Stability*, Physica D, **214**, (2006), pp. 63–77.

[58] T. Kolokolnikov, M. J. Ward, J. Wei, *The Existence and Stability of Spike Equilibria in the One-Dimensional Gray-Scott Model: The Low Feed Rate Regime*, Studies in Appl. Math., **115**(1), (2005), pp. 21–71.

[59] T. Kolokolnikov, M. J. Ward, J. Wei *The Existence and Stability of Spike Equilibria in the One-Dimensional Gray-Scott Model: The Pulse-Splitting Regime*, Physica D., **202**(3-4), (2005), pp. 258–293.

[60] T. Kolokolnikov, M.J. Ward, J. Wei, *Slow Translational Instabilities of Spike Patterns in the One-Dimensional Gray-Scott Model*, Interfaces and Free Boundaries, **8**(2), (2006), pp. 185–222.

[61] T. Kolokolnikov, M.J. Ward, and J. Wei, *Spot Self-Replication and Dynamics for the Schnakenburg model in a Two-Dimensional Domain*, J. Nonlinear Sci. **19**(1), (2009), pp. 1–56.

[62] T. Kolokolnikov, M. J. Ward, J. Wei, *The Stability of Steady-State Hot-Spot Patterns for a Reaction-Diffusion Model of Urban Crime*, DCDS-B, submitted, (2011), (34 pages).

[63] G. Kozyreff, *Localized Turing Patterns in Nonlinear Optical Cavities*, Physica D **241**, (2012), pp. 939–946.

[64] T. A. M. Langlands, B. I. Henry, S. L. Wearne, *Anomalous Diffusion with Multispecies Linear Reaction Dynamics*, Phys. Rev. E, **77**, 021111 (2008).

[65] C. S. Lin, W. M. Ni, I. Takagi, *Large Amplitude Stationary Solutions to a Chemotaxis System*, J. Diff. Eq., **72**, (1988), pp. 1–27.

[66] D. J. B. Lloyd, B. Sandstede, D. Avitabile, A. R. Champneys, *Localized Hexagon Patterns of the Planar SwiftHohenberg Equation*, SIAM J. Appl. Dyn. Sys, **7**(3), (2008), pp.1049–1100.

[67] Y. –P. Ma, J. Burke, E. Knobloch, *Defect-mediated snaking: A New Growth Mechanism for Localized Structures*, Physica D, **329**, (2010), pp. 1867–1883.

[68] P. K. Maini, J. Wei, M. Winter, *Stability of Spikes in the Shadow Gierer-Meinhardt System with Robin Boundary Conditions*, Chaos **17**, 037106 (2007).

[69] B.A. Malomed, A.A. Nepomnyashchy, M.I. Tribelsky, *Domain Boundaries in Convection Patterns*, Phys. Rev. **A42**, (1990), pp. 7244–7263.

[70] L. J. Shaw, J. D. Murray, *Analysis of a Model for Complex Skin Patterns*, SIAM J. Appl. Math., **50**(2), (1990), pp. 628–648.

[71] R. Metzler, J. Klafter, *The Random Walk's Guide to Anomalous Diffusion: A Fractional Dynamics Approach*, Phys. Rep. 339 (2000), **1**, pp. 1–77.

[72] C. B. Muratov, V. V. Osipov, *Static Spike Autosolitons in the Gray-Scott Model*, J. Phys. A: Math. Gen., **33**, (2000), pp. 8893–8916.

[73] C. B. Muratov, V. V. Osipov, *Stability of the Static Spike Autosolitons in the Gray–Scott Model*, SIAM J. Appl. Math., **62**(5), (2002), pp. 1463–1487.

[74] Y. Nec, *Spike-Type Solutions to One Dimensional Gierer-Meinhardt Model with Lèvy Flights*, Stud. Appl. Math., (2012), published online.

[75] Y. Nec, A.A.Nepomnyashchy, *Linear Stability of Fractional Reaction-Diffusion Systems*, Math. Model. Nat. Phenom., **2**(2), (2007), pp. 77–105.

[76] Y. Nec, A.A.Nepomnyashchy, *Turing Instability of Anomalous Reaction-Anomalous Diffusion Systems*, European J. Appl. Math., **19**, (2008), pp. 329–349.

[77] Y. Nec, A. A. Nepomnyashchy, A. A. Golovin, *Oscillatory Instability in Super-Diffusive Reaction-Diffusion Systems: Fractional Amplitude and Phase Diffusion Equations*, EPL, **82**, 58003 (2008).

[78] Y. Nec, M. J. Ward, *Dynamics and Stability of Spike-Type Solutions to a One Dimensional Gierer-Meinhardt Model with Sub-Diffusion*, Physica D, **241**, (2012), pp. 947-963

[79] G. Nicolis, I. Prigogine, *Self-Organization in Nonequilibrium Systems*, Wiley, New York, 1977.

[80] Y. Nishiura, *Far-From Equilibrium Dynamics, Translations of Mathematical Monographs*, Vol. **209**, AMS Publications, (2002), Providence, Rhode Island.

[81] Y. Nishiura, T. Teramoto, K. Ueda, *Scattering and Separators in Dissipative Systems*, Phys. Rev. E **67**, 056210 (2003).

[82] Y. Nishiura, D. Ueyama, *A Skeleton Structure of Self-Replicating Dynamics*, Physica D, **130**, (1999), pp. 73–104.

[83] K.B. Oldham, J. Spanier, The Fractional Calculus, Academic Press, New York, 1974.

[84] J. E. Pearson, *Complex Patterns in a Simple System*, Science, **216**, (1993), pp. 189–192.

[85] B. Pena, C. Perez-Garcia, *Stability of Turing Patterns in the Brusselator Model*, Phys. Rev. E., **64**, 056213 (2001).

[86] R. Peng, M. Wang, *Pattern Formation in the Brusselator System*, J. Math. Anal. Appl., **309**(1), (2005), pp. 151–166.

[87] R. Peng, M. Yang, *On Steady-State Solutions of the Brusselator-Type System*, Nonlinear Analysis: Theory, Methods, and Appl., **71**(3-4), (2009), pp. 1389–1394.

[88] Y. Pomeau, *Front Motion, Metastability and Subcritical Bifurcations in Hydrodynamics*, Physica D, **23**, (1986), pp. 3–11.

[89] F. Saguès, V. P. Shkilev, I. M. Sokolov, *Reaction-Subdiffusion Equations for the $A \rightleftharpoons B$ Reaction*, Phys Rev. E, **77**, 032102 (2008).

[90] B. Sandstede, A. Scheel,*Defects in Oscillatory Media: Toward a Classification*, SIAM J. Appl. Math., **3**(1), (2004), pp. 1–68.

[91] C. P. Schenk, M. Or-Guil, M. Bode and H. Purwins, *Interacting Pulses in Three-Component Reaction-Diffusion Systems on Two-Dimensional Domains*, Phys. Rev. Lett., **78**(19), (1997), pp. 3781–3784.

[92] M. B. Short, A. L. Bertozzi, P. J. Brantingham, *Nonlinear Patterns in Urban Crime - Hotpsots, Bifurcations, and Suppression*, SIAM J. Appl. Dyn. Sys., **9**(2), (2010), pp. 462–483.

[93] I. M. Sokolov, M. G. Schmidt, F. Saguès, *Reaction-Subdiffusion Equations*, Phys. Rev. E, **73**, 031102 (2006).

[94] W. Sun, M. J. Ward, R. Russell, *The Slow Dynamics of Two-Spike Solutions for the Gray-Scott and Gierer-Meinhardt Systems: Competition and Oscillatory Instabilities*, SIAM J. Appl. Dyn. Sys., **4**(4), (2005), pp. 904–953.

[95] A.M. Turing, *The Chemical Basis of Morphogenesis*, Philos. Trans. R. Soc. London Ser. B, **237**, (1952), pp. 37-72.

[96] J. C. Tzou, A. Bayliss, B. J. Matkowsky, V. A. Volpert, *Interaction of Turing and Hopf Modes in the Superdiffusive Brusselator Model Near a Codimension Two Bifurcation Point*, Math. Model. Nat. Phenom., **6**(1), (2011), pp. 87–118.

[97] J. C. Tzou, A. Bayliss, B. J. Matkowsky, V. A. Volpert, *Stationary and Slowly Moving Localized Pulses in a Singularly Perturbed Brusselator Model*, European J. Appl. Math., **22**(5), (2011), pp. 423–453.

[98] J. C. Tzou, B. J. Matkowsky, V. A. Volpert, *Interaction of Turing and Hopf modes in the Superdiffusive Brusselator Model*, Appl. Math. Lett. **22**, (2009), 1432–1437.

[99] P. .P. Vako, X. Z. Zhang, *Finite Domain Anomalous Spreading Consistent with First and Second Laws*, Commun. Nonlinear Sci. Numer. Simul., **15**, (2010), pp. 3455–3470.

[100] V. K. Vanag, *Waves and Patterns in Reaction Diffusion Systems. Belousov-Zhabotinsky Reaction in Water-in Oil Microemulsions*, Phys.-Usp. **47**, (2004), pp. 923–941.

[101] V. K. Vanag, I. R. Epstein, *Localized Patterns in Reaction-Diffusion Systems*, Chaos, **17**(3), 037110 (2007).

[102] H. Van der Ploeg, A. Doelman, *Stability of Spatially Periodic Pulse Patterns in a Class of Singularly Perturbed Reaction-Diffusion Equations*, Indiana Univ. Math. J., **54**(5), (2005), pp. 1219–1301.

[103] M. J. Ward, D. McInerney, P. Houston, D. Gavaghan, P. Maini, *The Dynamics of Pinning of a Spike for a Reaction Diffusion System*, SIAM. J. Appl. Math., **62**(4), (2002), pp. 1297–1328.

[104] M. J. Ward, J. Wei, *Asymmetric Spike Patterns for the One-Dimensional Gierer-Meinhardt Model: Equilibria and Stability*, European J. Appl. Math., **13**(3), (2002), pp. 283–320.

[105] M. J. Ward, J. Wei, *The Existence and Stability of Asymmetric Spike Patterns for the Schnakenberg Model*, Studies in Appl. Math., **109**(3), (2002), pp. 229–264.

[106] M. J. Ward, J. Wei, *Hopf Bifurcations and Oscillatory Instabilities of Spike Solutions for the One-Dimensional Gierer-Meinhardt Model*, J. Nonlinear Sci. **13**(2), (2003), pp. 209–264.

[107] M.J. Ward, J. Wei, *Hopf Bifurcations and Oscillatory Instabilities of Spike Solutions for the One-Dimensional Gierer-Meinhardt Model*, J. Nonlinear Sci. **13(2)**, (2008), pp. 209–264.

[108] J. Wei, *On Single Interior Spike Solutions for the Gierer-Meinhardt System: Uniqueness and Spectrum Estimates*, Europ. J. Appl. Math., **10**(4), (1999), pp. 353–378.

[109] J. Wei, *Existence and Stability of Spikes for the Gierer-Meinhardt System*, book chapter in *Handbook of Differential Equations, Stationary Partial Differential Equations*, **5** (M. Chipot ed.), Elsevier, (2008), pp. 489–581.

[110] R. Wittenberg, P. Holmes, *The Limited Effectiveness of Normal Forms: A Critical Review and Extension of Local Bifurcation Studies of the Brusselator PDE*, **100**, (1997), pp. 1–40.

[111] A. Yadav, S. M. Milu, W. Horsthemke, *Turing Instability in Reaction-Subdiffusion Systems*, Phys Rev. E, **78**, 026116 (2008).

[112] L. Yan, M. Dolnik, A.M. Zhabotinsky, I.R. Epstein, *Pattern Formation Arising From Interaction Between Turing and Wave Instabilities*, J. Chem. Phys., **117**, (2002), pp. 7259–7265.

APPENDIX A

Coefficients of Amplitude Equations near the C2THP

The coefficients of the amplitude equations in (2.2) are as follows:

$$\gamma = -\frac{1}{2}\,\frac{E^2\left(-\mu\sqrt{1+E^2}+\sqrt{1+E^2}E^2\rho+\mu\right)}{\left(\sqrt{1+E^2}-1\right)^2\sqrt{1+E^2}}\,,$$

$$g = -\frac{1}{18}\,\frac{\left(8\,E^4-17\,E^2-21\,E^2\sqrt{1+E^2}+8\,\sqrt{1+E^2}+8\right)E^2}{(1+E^2)\left(\sqrt{1+E^2}-1\right)^3}\,,$$

$$\lambda = -\frac{E^2}{\left(14\,E^2+5\,E^4-10\,E^2\sqrt{1+E^2}+8-8\,\sqrt{1+E^2}\right)(1+E^2)^{3/2}\left(\sqrt{1+E^2}-1\right)}\Bigg[$$

$$-17\,E^6+E^2\sqrt{1+E^2}\left(4E^4+27E^2+32\right)-43\,E^4-40\,E^2+16\left(\sqrt{1+E^2}-1\right)\Bigg]\,,$$

$$\zeta = 2\,\frac{\left(\sqrt{1+E^2}-1\right)^2}{E^2+1-\sqrt{1+E^2}}\,,$$

$$\nu = \frac{1}{2}\,\mu\,,$$

$$\beta_r = \frac{1}{2}\,\frac{E^2+2}{1+E^2}\,,$$

$$\beta_i = \frac{1}{6}\,\frac{4\,E^4-7\,E^2+4}{(1+E^2)\,E}\,,$$

$$\delta_r = -\frac{\left(4\,E^6-33\,E^4\sqrt{1+E^2}+72\,E^4-94\,E^2\sqrt{1+E^2}+124\,E^2-56\,\sqrt{1+E^2}+56\right)E^4}{\left(14\,E^2+5\,E^4-10\,E^2\sqrt{1+E^2}+8-8\,\sqrt{1+E^2}\right)\left(\sqrt{1+E^2}-1\right)^2(1+E^2)^{3/2}}\,,$$

$$\delta_i = -\frac{E^3}{\left(14\,E^2+5\,E^4-10\,E^2\sqrt{1+E^2}+8-8\,\sqrt{1+E^2}\right)\left(\sqrt{1+E^2}-1\right)^2\left(1+E^2\right)^{3/2}}\Bigg[$$

$$12\,E^6\sqrt{1+E^2}-44\,E^6+67\,E^4\sqrt{1+E^2}-94\,E^4+58\,E^2\sqrt{1+E^2}-58\,E^2-8+8\,\sqrt{1+E^2}\Bigg]\,,$$

$$\kappa_r = \frac{E^2+1-\sqrt{1+E^2}}{E^2}\,,$$

$$\kappa_i = \frac{\sqrt{1+E^2}-1}{E}\,.$$

APPENDIX B

Scaling Analysis of the Brusselator Model

In this appendix we outline the scaling analysis of [**97**] for the existence of pulses to (3.2). For $\epsilon_0 \to 0$, U has an inner scale U_{inn} near a pulse and an outer scale U_{out} away from a pulse. In contrast, V has only one scale across the interval, which is induced by the boundary feed so that $V = \mathcal{O}(\mathcal{A}_0)$. In order to obtain a homoclinic solution characterizing the pulse profile, we require in the inner region near a pulse that $U_{\text{inn}}^2 V \sim U_{\text{inn}}$. Therefore, $U_{\text{inn}} = \mathcal{O}\left(\mathcal{A}_0^{-1}\right)$.

Next, since U is localized, we require from (3.2b) that $DV_{xx} \sim \int_{-1}^{1} VU^2\,dx$. Since the integrand has an $\mathcal{O}(\epsilon_0)$ support near a pulse, this yields that $\mathcal{A}_0 \sim \epsilon_0/\mathcal{A}_0$, which implies that $\mathcal{A}_0 = \mathcal{O}(\epsilon_0^{1/2})$. Consequently, we conclude that $U_{\text{inn}} = \mathcal{O}(\epsilon_0^{-1/2})$ and $V_{\text{inn}} = \mathcal{O}(\epsilon_0^{1/2})$. Finally, from (3.2b) we must balance the scales of DV_{xx} and BU across $-1 < x < 1$, which yields that $U_{\text{out}} = \mathcal{O}(\epsilon_0^{1/2})$, and consequently $\mathcal{E}_0 = \mathcal{O}(\epsilon_0^{1/2})$ from (3.2a).

Therefore, we will consider (3.2) in the parameter regime where $\mathcal{A}_0 = \epsilon_0^{1/2} A_0$ and $\mathcal{E}_0 = \epsilon_0^{1/2} E_0$ for some non-negative $\mathcal{O}(1)$ constants A_0 and E_0. We also give an alternate scaling for the $A_0 = 0$ case.

First, we introduce the rescaled $\mathcal{O}(1)$ variables u and v and the new temporal variable σ, defined by

$$U = \epsilon_0^{-1/2} u_c u\,, \qquad V = \epsilon_0^{1/2} v_c v\,, \qquad t = T\sigma\,.$$

From (3.2), we then obtain the system

$$\frac{1}{T(B_0+1)}u_\sigma = \left(\frac{\epsilon_0}{\sqrt{B_0+1}}\right)^2 u_{xx} + \frac{\epsilon_0 E_0}{u_c(B_0+1)} - u + \frac{u_c v_c}{B_0+1}vu^2\,, \tag{B.1a}$$

$$\frac{\sqrt{B_0+1}}{u_c^2 T}v_\sigma = \frac{D_0\sqrt{B_0+1}}{u_c^2}v_{xx} + \frac{\sqrt{B_0+1}}{\epsilon_0}\left(\frac{B_0}{u_c v_c}u - vu^2\right)\,. \tag{B.1b}$$

Choosing $T = 1/(B_0+1)$ and $u_c v_c = B_0$ in (B.1), and defining the new parameters ϵ, D, E, f, and τ as

$$\begin{aligned} \epsilon &\equiv \frac{\epsilon_0}{\sqrt{B_0+1}}\,, \qquad D \equiv \frac{D_0\sqrt{B_0+1}}{u_c^2}\,, \\ E &\equiv \frac{E_0}{u_c\sqrt{B_0+1}}\,, \qquad f \equiv \frac{B_0}{B_0+1}\,, \qquad \tau \equiv \frac{(B_0+1)^{3/2}}{u_c^2}\,, \end{aligned} \tag{B.2}$$

we obtain the system

$$u_\sigma = \epsilon^2 u_{xx} + \epsilon E - u + fvu^2\,, \qquad -1 < x < 1\,, \qquad u_x(\pm 1,\sigma) = 0\,, \tag{B.3a}$$

$$\tau v_\sigma = D v_{xx} + \frac{1}{\epsilon}\left(u - vu^2\right)\,, \qquad -1 < x < 1\,, \qquad v_x(\pm 1,\sigma) = \pm A_0/v_c\,, \tag{B.3b}$$

valid for $A_0 \geq 0$. If $A_0 > 0$, we choose $v_c = A_0$ so that $u_c = B_0/A_0$. Replacing the time variable σ with t in (B.3), the Brusselator model with asymptotically small boundary feed of the inhibitor is written in the form (4.4) where σ is replaced by t, and ϵ, f, E, D and τ are defined in terms of the original variables by (4.5).

Alternatively, if $A_0 = 0$, we may choose $u_c = E_0/\sqrt{B_0+1}$ so that $v_c = B_0\sqrt{B_0+1}/E_0$, resulting in the parameter E in (B.2) and (B.3) being unity. In this case, the Brusselator model with no flux boundary conditions is (4.2) where ϵ, f, D, and τ are as defined in (4.3).

APPENDIX C

Exponentially Slow Evolution of a Single Pulse When $E = 0$ and $A > 0$

In §3.3, the analysis predicted that for the single-pulse case with $E = 0$ and $A > 0$, the pulse would remain stationary for all time regardless of its position in the domain. However, as we will show below, the single-pulse solution is in fact only metastable; the eigenvalue problem linearized around this solution admits an eigenvalue that is exponentially small but positive. We further find that the exponentially small eigenvalue is the principle eigenvalue, that is, the eigenvalue with the largest real part. Following closely the analysis of [**45**] for a particular limit of the Gierer-Meinhardt model, we begin by first casting (3.3) in the form of a nonlocal reaction-diffusion system and linearizing around the quasi-equilibrium solution. We then analyze the resulting nonlocal eigenvalue problem and derive an asymptotic expression for the exponentially small (positive) eigenvalue. Numerical methods will be used to confirm the analysis as well as to show that no other eigenvalues have positive real parts. Finally, we derive an ODE for the exponentially slow dynamics of the center of the pulse, which we confirm by numerically solving (3.3). Because the following analysis and arguments are similar to those in [**45**], we omit much of the detail.

For the purpose of the following analysis, it is convenient to consider a re-scaled form of (3.3). We introduce the new variables and parameters

$$u = \epsilon^{-1/2}\frac{B}{A}U\,, \qquad v = \epsilon^{1/2}AV\,, \qquad t = \frac{1}{B+1}\tau\,, \qquad \epsilon = \sqrt{B+1}\epsilon_0\,,$$

resulting in

$$U_\tau = \epsilon_0^2 U_{xx} + \epsilon_0 E_0 - U + fVU^2\,, \qquad U_x(\pm 1,\tau) = 0\,, \tag{C.1a}$$

$$\sigma V_\tau = \mathcal{D} V_{xx} + \frac{1}{\epsilon_0}(U - VU^2)\,, \qquad V_x(\pm 1,\tau) = \pm 1\,, \tag{C.1b}$$

where

$$f = \frac{B}{B+1}\,, \qquad E_0 = \frac{EA}{B\sqrt{B+1}}\,, \qquad \mathcal{D} = D\sqrt{B+1}\frac{A^2}{B^2}\,, \qquad (B+1)^{3/2}\frac{A^2}{B^2}\,.$$

We will consider the case where $E_0 = 0$ in (C.1a).

We assume as before that U has a localized solution of width $O(\epsilon_0)$ while V to leading order is equal to the constant $\bar{V}$ in the inner region and varies on an $O(1)$ length-scale in the outer region. Then in the outer region, treating functions of U as multiples of delta functions, (C.1b) must satisfy the Fredholm condition

$$\bar{V} = \frac{2\mathcal{D}\epsilon_0 + \int_{-1}^{1} U(x)\,dx}{\int_{-1}^{1} U^2(x)\,dx}\,.$$

Then solving for the leading order solution of V in the outer region and matching it to the constant leading order inner solution, we write (C.1) as a nonlocal reaction-diffusion system

$$U_\tau = \epsilon_0^2 U_{xx} - U + fVU^2\,, \qquad U_x(\pm 1,\tau) = 0\,, \tag{C.2a}$$

$$V = |x - x_0| + \frac{2\mathcal{D}\epsilon_0 + \int_{-1}^{1} U(x)\,dx}{\int_{-1}^{1} U^2(x)\,dx}\,, \tag{C.2b}$$

where we have set $E_0 = 0$. The leading order quasi-equilibrium solution is then

$$U_E(x;x_0) = \frac{1}{fV_0} u_c\left(\frac{x-x_0}{\epsilon}\right)\,; \qquad u_c(y) \equiv \frac{3}{2}\text{sech}^2\left(\frac{y}{2}\right)\,, \tag{C.3a}$$

$$V_E(x;x_0) = |x-x_0| + V_0\,; \qquad V_0 \equiv \frac{3(1-f)}{\mathcal{D}f^2}\,, \tag{C.3b}$$

where x_0 is the center of the pulse.

To derive the eigenvalue problem, we linearize (C.2) around U_E and V_E by introducing perturbations ϕ and η according to

$$U = U_E(x;x_0) + e^{\lambda t}\phi(x)\,, \tag{C.4a}$$

$$V = V_E(x;x_0) + e^{\lambda t}\eta\,, \tag{C.4b}$$

where η is a constant. Substituting (C.4) into (C.2a), we obtain the following nonlocal eigenvalue problem

$$L_{\epsilon_0} \equiv \epsilon_0^2\phi_{xx} + (-1+2u_c)\phi + \frac{1}{6\epsilon_0}u_c^2\int_{-1}^{1}\left[f - 2u_c\left(\frac{x-x_0}{\epsilon_0}\right)\right]\phi(x)\,dx = \lambda\phi\,, \qquad \phi_x(\pm 1) = 0\,, \tag{C.5}$$

where we have used (C.4) in (C.2b) to compute η in terms of ϕ. Eqn. (C.5) may also be obtained by substituting (C.4) into (C.1), where η would then be computed in terms of ϕ by applying the Fredholm alternative to the linearized equation for η. We note that (C.5) is similar to the NLEP considered in [**45**], differing only in the nonlocal term.

If (C.5) was posed on an infinite domain, $\phi = u_c'$ would be an eigenfunction corresponding to $\lambda = 0$. This is the translation mode. On a finite domain, u_c' fails to satisfy the equation

and boundary conditions by exponentially small terms as $\epsilon_0 \to 0$. Thus, we expect that L_{ϵ_0} has an exponentially small eigenvalue and also that ϕ_1 is exponentially close to u_c'. In order for the single-pulse solution to be metastable, however, we require that all other eigenvalues have negative real parts. This is where the nonlocal term of (C.5) becomes important; as argued in [**45**] (and references therein), (C.5) without the nonlocal term has an $O(1)$ positive real eigenvalue that is exponentially close to $5/4$. This was confirmed numerically by discretizing the local part of L_{ϵ_0} using the second order difference approximation of the second derivative with grid spacing Δx and computing the eigenvalues of the resulting matrix $\mathcal{A}^{\Delta x}$. To add the contribution of the nonlocal part of L_{ϵ_0}, we used the trapezoidal rule also with grid spacing Δx to approximate the integral term, constructing the matrix $\mathcal{B}^{\Delta x}$. Computing the eigenvalues of $\mathcal{A}^{\Delta x} + \mathcal{B}^{\Delta x} \equiv \mathcal{C}^{\Delta x}$, we found that, aside from the expected small (positive) eigenvalue, all eigenvalues had negative real parts, regardless of the value of f between 0 and 1. Thus, the small eigenvalue is the principle eigenvalue of (C.5).

The analysis required to estimate the exponentially small eigenvalue λ_1 corresponding to the eigenfunction $\phi_1(x)$ is similar to that performed in [**45**]. As such, we only show the steps that are specific to this problem. We first give Lagrange's identity for $(v, L_{\epsilon_0} u)$, where $(u, v) = \int_{-1}^{1} uv\, dx$:

$$(v, L_{\epsilon_0} u) = \epsilon^2 (u_x v - v_x u)\Big|_{-1}^{1} + (u, L_{\epsilon_0}^* v), \tag{C.6a}$$

$$L_{\epsilon_0}^* v \equiv \epsilon_0^2 v_{xx} + (-1 + 2u_c)v + \frac{1}{6\epsilon_0}(f - 2u_c) \int_{-1}^{1} u_c^2 v\, dx. \tag{C.6b}$$

We now multiply (C.5) by u_c' and integrate over $-1 < x < 1$, to obtain

$$\lambda_1(u_c', \phi_1) = -\epsilon_0 u_c'' \phi_1|_{-1}^{1} + (\phi_1, L_{\epsilon_0}^* u_c'), \tag{C.7}$$

where we have applied (C.6a) to the $(u_c', L_{\epsilon_0}\phi_1)$ term and used $\phi_{1x}(\pm 1) = 0$ to eliminate the boundary terms involving ϕ_{1x}. The terms in (C.7) are the same as those in [**45**], with the exception being that the nonlocal part of the adjoint operator $L_{\epsilon_0}^*$ is different. However, the term involving $L_{\epsilon_0}^*$ was shown to be exponentially negligible in [**45**]; if the same were true in (C.7), we may conclude that the eigenpair λ_1, ϕ_1 is the same as that found in [**45**] to within exponentially negligible terms. To show this, we first calculate $L_{\epsilon_0}^* u_c'$. Since u_c' is a solution of the local part of $L_{\epsilon_0}^*$,

$$L_{\epsilon_0}^* u_c' = \frac{1}{6\epsilon_0}(f - 2u_c)\int_{-1}^{1} u_c^2 u_c'\, dx \tag{C.8}$$

$$\sim 12(f - 2u_c)\left(e^{-\frac{3}{\epsilon_0}(1-x_0)} - e^{-\frac{3}{\epsilon_0}(1+x_0)}\right), \tag{C.9}$$

where we have used that

$$u_c(y) \sim 6e^{\mp y} \text{ as } y \to \pm\infty. \tag{C.10}$$

To estimate $(\phi_1, L_{\epsilon_0}^* u_c')$, we first recall that ϕ_1 is exponentially close to u_c', differing only in exponentially small boundary layer terms required to satisfy the no-flux boundary conditions. That is,

$$\phi_1(x) \sim C_1 u_c'\left(\frac{x - x_0}{\epsilon_0}\right) + e.s.t,$$

where C_1 is a normalizing constant, and $e.s.t$ denotes exponentially small terms. Thus, by integrating and applying (C.10), it can be shown that the term

$$(\phi_1, L^*_{\epsilon_0} u_c') = 12\left(e^{-\frac{3}{\epsilon_0}(1-x_0)} - e^{-\frac{3}{\epsilon_0}(1+x_0)}\right)\int_{-1}^{1}(f-2u_c)\phi_1\,dx \tag{C.11}$$

is exponentially smaller than the other two terms in (C.7), leading to the result

$$\lambda_1 = 60\left(e^{-\frac{2}{\epsilon_0}(1+x_0)} + e^{-\frac{2}{\epsilon_0}(1-x_0)}\right). \tag{C.12}$$

As a check, we see from (C.11) that $(\phi_1, L^*_{\epsilon_0} u_c')$ is exponentially smaller than $O(e^{-3/\epsilon_0})$, while $\lambda_1 = O(e^{-2/\epsilon_0})$. Thus, the term in (C.11) is indeed exponentially negligible. Result (C.12) was confirmed by calculating the eigenvalues of the matrix $\mathcal{C}^{\Delta x}$. Eigenvalues were computed using grid spacings of Δx, $2\Delta x$ and $4\Delta x$ so that Richardson extrapolation could be applied twice to increase the accuracy required for small ϵ. The agreement between (C.12) and the numerical computations is shown in Figure C.1. It should not be surprising that (C.12) is the same expression as that obtained in [**45**]; the NLEP in [**45**] has the same local terms while the nonlocal terms in both NLEP's contribute terms exponentially smaller than the exponential terms in (C.12), and thus in both cases have an exponentially negligible effect on the eigenpair λ_1, ϕ_1.

Since the linearization around the single-pulse quasi-equilibrium solution yields a principle eigenvalue that is positive but exponentially small as $\epsilon_0 \to 0$, we expect the pulse to evolve on an exponentially slow time-scale. As in the calculation of λ_1, the nonlocal term in (C.5) is insignificant and we thus recover the same result for the motion of the pulse as in [**45**]:

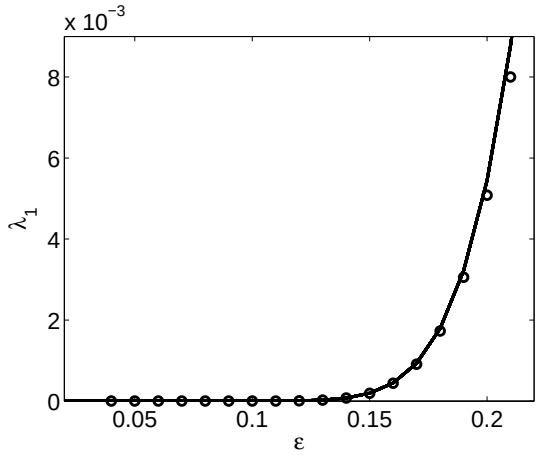

Figure C.1. Plot λ_1 versus ϵ, where the solid line is the asymptotic estimate (C.12) and the circles are from numerical computations.

$$\frac{dx_0}{d\tau} = 60\epsilon_0 \left(e^{-\frac{2}{\epsilon_0}(1-x_0)} - e^{-\frac{2}{\epsilon_0}(1+x_0)} \right),$$

or in terms of the original variables t, B and ϵ,

$$\frac{dx_0}{dt} = 60\epsilon\sqrt{B+1} \left(e^{-\frac{2\sqrt{B+1}}{\epsilon}(1-x_0)} - e^{-\frac{2\sqrt{B+1}}{\epsilon}(1+x_0)} \right). \tag{C.13}$$

Thus, for $x_0 \neq 0$, the pulse drifts toward the nearest boundary instead of toward $x = 0$, the latter of which was observed when $E > 0$. The result (C.13) is compared to a numerical solution of (3.3) in Figure C.2, the results of which were verified by grid refinement. We note that the numerical solution is extremely sensitive to the ratio $\sqrt{B+1}/\epsilon$, and for values of the ratio either too large or too small, the match is not as close.

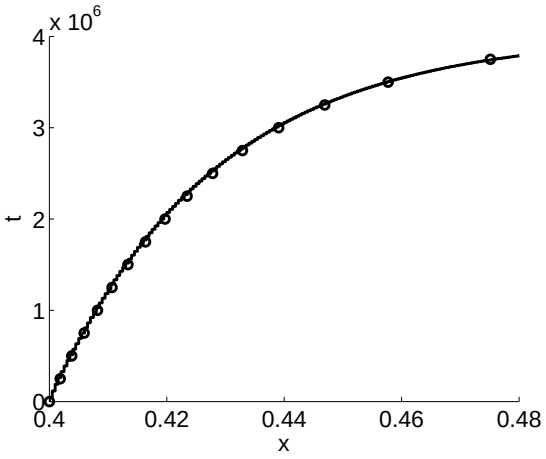

Figure C.2. Comparison of asymptotic and numerical results for exponentially slow dynamics of a single pulse starting at $x_0 = 0.4$ for parameters $\epsilon = 0.082$, $A = 2$, $B = 1$, $D = 1$, and $E = 0$. The solid line (circles) represent the numerical (asymptotic) result.